

**Synthesis, Purification, Characterization and Application of
Discretely Functionalized Gold Nanoparticles**

CHAK, Chun Pong

A Thesis Submitted in Partial Fulfillment of
the Requirements for the Degree of
Doctor of Philosophy
in
Chemistry

The Chinese University of Hong Kong
August 2011

UMI Number: 3504740

All rights reserved

INFORMATION TO ALL USERS

The quality of this reproduction is dependent on the quality of the copy submitted.

In the unlikely event that the author did not send a complete manuscript and there are missing pages, these will be noted. Also, if material had to be removed, a note will indicate the deletion.



UMI 3504740

Copyright 2012 by ProQuest LLC.

All rights reserved. This edition of the work is protected against unauthorized copying under Title 17, United States Code.



ProQuest LLC.
789 East Eisenhower Parkway
P.O. Box 1346
Ann Arbor, MI 48106 - 1346

Thesis/Assessment Committee

Professor Yu, Chai-Mei Jimmy (Chair)
Professor Leung, Cham Fai Ken (Thesis Supervisor)
Professor Shing, Kung Ming Tony (Thesis Co-supervisor)
Professor Lam, Sik Lok Sherlock (Committee Member)
Professor Lee, Cronin (External Examiner)

Dedicated to My Family

And

My Love

Table of Content

Table of content.....	i
Acknowledgements.....	v
Abstract.....	vi
Abbreviations.....	x
Publications related to this thesis.....	xiii

Introduction and Background

Chapter One – Introduction of Gold Nanoparticles

1.1 Introduction.....	1
1.2 Chemical synthesis of gold nanoparticles (AuNPs)	
1.2.1 One-phase synthesis of citrate-coated AuNPs (Turkevich Method).....	4
1.2.2 Two-phase synthesis of alkanethiolate-coated AuNPs (B Brust-Schiffrin Method).....	6
1.2.3 Miscellaneous methods.....	8
1.3 Functionalization of AuNPs	
1.3.1 Ligand place exchange reaction.....	11
1.3.2 In situ mixing of binary ligands during synthesis.....	13
1.3.3 Chemical post-functionalization.....	14
1.4 Surface plasmon resonance (SPR) of AuNPs	
1.4.1 General properties of gold assemblies and self-assembling monolayer (SAM).....	16
1.4.2 Detection of molecules on the SAM of gold <i>via</i> SPR changes.....	17
1.4.3 Making network of AuNPs with gold SAM to increase sensitivity of SPR detection.....	19
1.5 Characterization of AuNPs	
1.5.1 Spectroscopic methods.....	20
1.5.2 Microscopic methods.....	20
1.5.3 Miscellaneous characterization methods	21
1.6 Applications	
1.6.1 Catalysis.....	22
1.6.2 Sensors of DNA, antigens, aptamers, enzymatic reactions and other small molecules	23
1.6.3 Ions sensors.....	24
1.6.4 Fingerprint detector.....	25
1.6.5 Miscellaneous applications.....	26

Chapter Two – Discretely Functionalized AuNPs

2.1 Synthesis of discretely mono-functionalized AuNPs	
2.1.1 Covalent solid-phase supported synthesis.....	28
2.1.2 Electrostatic solid-phase supported synthesis.....	32
2.1.3 Single polymer chain protection synthesis.....	33
2.1.4 Solution-phase synthesis followed by separation.....	35
2.1.5 Miscellaneous methods.....	37
2.2 Synthesis of discretely di-functionalized AuNPs.....	39
2.3 Characterization methods of discretely functionalized AuNPs.....	41
2.4 Potential applications of the discretely functionalized AuNPs.....	44
2.5 Aims and scopes of the project.....	46

Results and Discussions

Chapter Three – Synthesis and Purification of Discretely Mono-Functionalized AuNPs

3.1 General considerations.....	48
3.2 Molecular recognition between crown ether and ammonium salt	
3.2.1 The origin of recognition.....	51
3.2.2 Formation of pseudorotaxane and binding constant measurement.....	52
3.3 Synthesis and characterization of supramolecular precursors	
3.3.1 Preparation of ammonium ligand.....	56
3.4 Synthesis, characterization and theoretical calculation of <i>n</i> -butanethiolate-coated AuNPs.....	58
3.5 Synthesis of discretely mono-functionalized AuNPs and characterization	
3.5.1 Solid-phase support polymer and site isolation effect.....	63
3.5.2 Synthetic route of mono-functionalized AuNPs.....	64
3.5.3 Stepwise characterization of the synthesis.....	65
3.6 Purification of discretely mono-functionalized AuNPs by iron oxide nanoparticles and characterization	
3.6.1 General considerations.....	79
3.6.2 Preparation of the amine functionalized iron oxide nanoparticles.....	80
3.6.3 Preparation of the crown ether-decorated iron oxide nanoparticles.....	80
3.6.4 Purification route of mono-functionalized AuNPs by magnetic separation.....	82
3.6.5 Stepwise characterization of purification process.....	84
3.7 Instrumental characterization of discretely mono-functionalized AuNPs	
3.7.1 FT-IR spectroscopy and far-IR spectroscopy.....	92
3.7.2 X-ray photoelectron spectroscopy.....	94

3.7.3 UV/visible absorption spectroscopy.....	95
3.7.4 High resolution transmission electron microscopy.....	96
3.8 Characterization of discretely mono-functionalized AuNP <i>via</i> formation of supramolecular dimers and trimers with bis- and tris- crown ether linkers	
3.8.1 General considerations.....	97
3.8.2 Synthesis of bis-crown ether linker.....	98
3.8.3 Synthesis of tris-crown ether linker.....	99
3.8.4 Formation of AuNPs supramolecular dimers and trimers.....	100
3.8.5 Computational models of the AuNPs supramolecular dimers and trimers....	108
3.8.6 Control experiments.....	112
3.9 Section conclusion.....	115

Chapter Four – Superficial Application of Discretely Functionalized AuNPs

4.1 Surface plasmon resonance characterization - General considerations.....	116
4.2 Device fabrication.....	119
4.3 General instrumental setup.....	120
4.4 Synthesis and characterization of precursor.....	123
4.5 Self-assembling monolayer of crown ether on gold surface.....	124
4.6 SPR characterization of self-assembling and disassembling process	
4.6.1 <i>n</i> -butanethiolate coated AuNPs.....	126
4.6.2 Purified discretely mono-functionalized AuNPs.....	127
4.6.3 Crude AuNPs from the synthetic process.....	131
4.6.4 Randomly functionalized AuNPs.....	135
4.7 Atomic force microscopy.....	139
4.8 Purification of mono-functionalized AuNP from crude mixture	
4.8.1 Quantification study.....	141
4.9 Section conclusion.....	143

Chapter Five – Applications as Short Base-pairing DNA Sensors

5.1 General considerations.....	145
5.2 Synthesis of the mono-maleimide functionalized AuNPs.....	148
5.3 Synthesis of the mono-ssPrimer functionalized AuNPs and <i>ds</i> DNA–AuNP dimers.....	149
5.4 Synthesis of random-ssPrimer functionalized AuNPs and <i>ds</i> DNA–AuNP random structures.....	152
5.5 Melting temperature analysis.....	154
5.6 TEM characterization of <i>ds</i> DNA–AuNP structures.....	163
5.7 Section conclusion.....	165

Chapter Six –Conclusion and Outlook.....	166
Chapter Seven – Experimental Procedures	
7.1 General information.....	168
7.2 Experimental procedures.....	173
References.....	190
Appendix	
List of spectra.....	A1

Acknowledgements

I would like to give my sincere thanks to God which give me life on Earth to do research and sincere thanks are also given to my supervisor, Prof. Ken Cham-Fai Leung for his encouragement, continuous guidance and useful suggestions during my M.Phil.–Ph.D. projects. He is a kind professor with a great patience and forgiveness. Thanks are also given to Prof. Christopher H. K. Cheng for his support for the projects and helpful comments.

I would like to thank my family, especially my mother, for their endless support and love. Thanks are also given brothers and sisters in church, especially Ms. Iris Siu, Mr. Jacky Cheung and Ms. Sandy Tsang for their support, love in Christ and prayers throughout my whole study life. Thanks are also given to my dear friend Ms. Agnes Chat.

Lastly, I would like to thank my seniors, Dr. Siu-Yin Cheung, Dr. Chui-Man Lo, Dr. Kwun-Ngai Lau, Mr. Chun-Ho Wong for their suggestions and teaching. Thanks are also given to my previous and present fellow group members, including Prof. Shouhu Xuan, Mr. Long-Ho Chau, Ms. Wing-Yan Wong, Mr. Siu-Fung Lee, Mr. Kwok-Wai Ho and Mr. Cheuk-Ting Chung for their helpful discussion and support.

May 2011

Chun-Pong Chak

Center of Novel Functional Molecules

Institute of Molecular Functional Materials

Department of Chemistry

The Chinese University of Hong Kong

Hong Kong S.A.R, China

Abstract

In this thesis, it describes the synthesis, purification, characterization and applications of mono-amine functionalized gold nanoparticles (AuNPs) with an average diameter of 2 nm. Mono-amine functionalized AuNPs were synthesized by employing the ON/OFF switchable recognition between ammonium salt and dibenzo[24]crown-8 in acid/base condition together with the site isolation effect based on a solid phase supported polystyrene Wang resin. The crude mono-amine functionalized AuNPs were purified by magnetic separation using dibenzo[24]crown-8-coated superparamagnetic iron oxide nanoparticles *via* pH-switchable pseudorotaxane formation. The purified product as well as the intermediates during synthesis was characterized by infrared (IR) and X-ray photoelectron spectroscopies (XPS). The mono-amine functionality of the AuNPs was characterized by the formation of the novel supramolecular dimers and trimers, titrating with *bis*-dibenzo[24]crown-8 and *tris*-dibenzo[24]crown-8. Furthermore, transmission electron microscopy (TEM) images show that there were significant amounts of AuNP supramolecular dimers in the solutions and that there were both AuNP dimers and trimers in the supramolecular trimer solutions. The trimers observed under the TEM were triangular or near-linear shapes. Moreover, UV/visible spectroscopic analysis of the supramolecular AuNP dimer and trimer solutions in different ratios

between the crown ether linker and AuNPs demonstrated a gradual appearance of the two distinct plasmonic resonance bands at 620 and ~700 nm.

The discretely mono-amine functionalized AuNPs could be simultaneously purified and detected by a real-time surface plasmon resonance (SPR) with organic solvent-compatible microfluidic device/instrumentation. The discretely functionalized AuNPs could be assembled and disassembled on the surface of dibenzo[24]crown-8 coated gold plate *via* pH-switchable pseudorotaxane formation and dethreading in the microfluidic device. The monovalent attachment and detachment of AuNPs on gold surface gave real-time plasmonic signals which were successfully monitored by SPR. Furthermore, the self-assembly and disassembly processes of crude AuNPs and randomly functionalized gold nanoparticles were also monitored by SPR. The SPR results revealed that the crude and randomly functionalized AuNPs possessed different self-assembling and disassembling properties so that the mono-amine discretely functionalized AuNPs could be purified and simultaneously obtained with a SPR real time signal. The randomly functionalized AuNPs possessed incomplete disassembly during the pH-switching processes. Such observations together with the complete pH-switching of mono-functionalized AuNPs on gold surface were also characterized by atomic force microscopy (AFM).

The discretely functionalized AuNPs were further explored as a probe for DNA sensing. Mercapto-oligonucleotides were immobilized to the mono-amine AuNPs through thiol-maleimide click reactions with a hetero-bifunctional linker. Two types of primer (5 base pairs) were functionalized onto the AuNPs. These DNA-AuNPs hybridized complementarily with the sequence of the pathogenicity island of vancomycin-resistant *Enterococcus faecalis* so as to detect its presence. The DNA–AuNP detection was operated in organic solvents—*N,N'*-dimethylformamide (DMF), chloroform, and trace amount of water with sodium chloride and characterized by UV/visible absorption spectroscopy. UV/visible absorption of the system at 521 nm was monitored for the DNA hybridization. The melting temperature (T_m) studies were performed with different solvent system ratios, different alignments (*tail-to-tail* and *head-to head*) of AuNPs and different amounts of sodium chloride. The T_m was found to be higher with increasing salt concentrations and increasing ratios of chloroform to DMF. Moreover, the T_m was found to be similar with different alignments (*tail-to-tail* and *head-to-head*) of AuNPs which were different from the randomly functionalized gold nanoparticles that reported previously in the literature.

摘要

本論文敘述了直徑大小約兩納米的單一胺功能化金納米粒子之合成、純淨、表徵分析及其應用。單一胺功能化金納米粒子的合成利用了有機銨鹽與二苯-24-冠-8 在酸鹼情況下的份子識別之開關與固態支持的聚苯乙烯樹脂之功能組位置孤立效應。合成之後的金納米粒子通過能以酸鹼開關的偽輪烷機制，經二苯-24-冠-8 功能化的超順磁性之氧化鐵納米粒子的磁性分離所純淨。經純淨之單一胺功能化金納米粒子以及在合成過程中的反應中間體經紅外線光譜及 X 射線光電子能譜進行了表徵分析。其單一胺功能化通過與二-二苯-24-冠-8 和三-二苯-24-冠-8 滴定構成之新穎超份子二聚體及三聚體而展現。在穿透式電子顯微鏡觀察下，二聚體之溶液中含有大量超份子金納米粒子二聚體，而三聚體之溶液中則有超份子金納米粒子二聚體及三聚體。三聚體的形狀有三角形及類直線形。另外，不同滴定比例之冠醚與金納米粒子經紫外及可見光譜之分析下慢慢的展現了兩個突出之等離子共振峰，其峰值為於 620 及~ 700 nm。

單一胺功能化金納米粒子亦可經實時表面等離子共振、耐有機溶液之微流控儀器被同時純淨及表徵分析。單一胺功能化金納米粒子能在微流控儀器內之二苯-24-冠-8 功能化的金版表面經酸鹼開關的偽輪烷機制所聚合與拆卸，而整個聚合與拆卸經過了實時表面等離子共振所描繪。另一方面，未經純淨之單一胺功能化及多胺功能化金納米粒子亦經過了實時表面等離子共振所描繪，結果發現此兩類金納米粒子在經酸鹼開關的偽輪烷機制下擁有不同之聚合與拆卸的特

性，從而令單一胺功能化金納米粒子得以完全純淨及通過微流控儀器所獲得。而多胺功能化金納米粒子擁有不完全之偽輪烷拆卸的特性，此觀察與單一胺功能化金納米粒子擁有完全之偽輪烷拆卸的特性得到了原子力顯微鏡的引證。

單一胺功能化金納米粒子進一步用作脫氧核糖核酸之感應器。透過一個雙功能連結份子寡核苷酸硫醇與單一胺功能化金納米粒子進行了硫醇-順丁烯二醯亞胺點擊化學而結合。兩類不同的引物 (每個引物擁有 5 個鹼基對)與單一胺功能化金納米粒子分別結合。此兩類不同的引物所共同組成之脫氧核糖核酸排列與抗萬古黴素的糞腸球菌致病性島脫氧核糖核酸的排列是相互補充的。所組成之脫氧核糖核酸-金納米粒子在有機溶液(二甲基甲酰胺, 三氯甲烷及極少量之氯化鈉水溶液)下經紫外及可見光譜所分析。在紫外及可見光譜中, 521 nm 的波峰是用作以觀察脫氧核糖核酸的雜交。其融解溫度 (T_m) 在不同之溶液比例、不同的金納米粒子排列形式 (尾對尾以及頭對頭)以及不同分量之氯化鈉水溶液被分析。分析後發現其融解溫度在提升氯化鈉水溶液之濃度及三氯甲烷對二甲基甲酰胺之比例會上升。另一方面, 其融解溫度在不同的金納米粒子排列形式 (尾對尾以及頭對頭)中沒有太大的分別, 此等發現與文獻中多功能化之金納米粒子有所不同。

Abbreviations and Acronyms

2-D	Two-dimensional	EtOAc	Ethyl acetate
3-D	Three-dimensional	EtOH	Ethanol
Å	Ångström	Fmoc	9-Fluorenylmethoxy-carbonyl
°C	Degree Celsius		
λ_{\max}	Peak absorption wavelength	g	Gram
δ	Chemical shift	h	Hour(s)
% T	Transmittance percentage	Hz	Hertz
calcd	Calculated	HR	High resolution
AE-HPLC	Anion exchange, high performance liquid chromatography	IBCF	Isobutylchloroformate
AFM	Atomic force microscopy	IR	Infra-red
APTES	Aminopropyltriethoxysilane	<i>J</i>	Coupling constant
ATP	Adenosine-5'-triphosphate	K	Kelvin
AuNP(s)	Gold nanoparticle(s)	K_a	Binding constant
Boc	<i>tert</i> -butyloxycarbonyl	L	Liter(s)
CCD	Charged-coupled device	LAH	Lithium aluminium hydride
d	Day(s); doublet (spectral)	Lys	L-lysine
DB24C8	Dibenzo[24]crown-8	μ	Micro
DCC	<i>N,N'</i> -dicyclohexylcarbodiimide	m	Multiplet (spectral); Meter(s); milli-
DCM	Dichloromethane	M	Molar(moles per liter)
Dde	1-(4,4-dimethyl-2,6-dioxocyclohexylidene) ethyl	M_w	Molecular weight
DMAP	4-dimethylaminopyridine	M^+	Parent molecular ion
DMF	<i>N,N</i> -dimethylformamide	MeCN	Acetonitrile
DNA	Deoxyribonucleic acid	mL	Milliliter(s)
<i>ds</i>	Double-stranded	MeNO ₂	Nitromethane
EDCI	1-ethyl-3-(3-dimethylamino-propyl) carbodiimide methiodide	MeOH	Methanol
EDX	Energy-dispersive X-ray spectroscopy	MHz	Megahertz
ESI	Electrospray ionization	min	Minute(s)
		mM	Millimole(s) per liter
		mmol	Millimole(s)
		m.p.	Melting point
		MRI	Magnetic resonance imaging
		MS	Mass spectrometry
		<i>m/z</i>	Mass-to-charge ratio
		nm	Nanometer(s)

NMR	Nuclear magnetic resonance	SPDP	3-(2-pyridyldithio) propionic acid
NOESY	Nuclear overhauser effect spectroscopy	SPP	Surface plasmon polariton
<i>p</i>	<i>para</i>	SPR	Surface plasmon resonance
PDMS	Polydimethylsiloxane	<i>ss</i>	Single-stranded
PDP	Pyridyldithio propionate	<i>t</i>	Triplet (spectral); <i>tert</i>
PEGA	Poly(ethylene glycol) acrylamide copolymer	T_m	Melting temperature (DNA)
<i>p</i> FBn	4-fluorobenzyl	TEM	Transmission electron microscopy
ppm	Part(s) per million	TEOS	Tetraethylorthosilicate
PS	Polystyrene	TFA	Trifluoroacetic acid
q	Quartet (spectral)	TGA	Thermogravimetric analysis
R	Substituent(s)	THF	Tetrahydrofuran
RNA	Ribonucleic acid	TLC	Thin-layer chromatography
s	Singlet (spectral); Second(s)	TMS	Trimethylsilyl
SAM	Self-assembling monolayer	UV	Ultraviolet
SAXS	Small-angle X-ray scattering	vis	Visible
SPIO	Superparamagnetic iron oxide nanoparticles	XPS	X-ray photoelectron spectroscopy
		XRD	X-ray powder diffraction

Publications Originated from the Work of this Thesis

1. Chak, C. P.; Xuan, S. H.; Mendes, P. M.; Yu, J. C.; Cheng, C. H. K.; Leung, K. C. F., "Discrete Functional Gold Nanoparticles: Hydrogen Bond-Assisted Synthesis, Magnetic Purification, Supramolecular Dimer and Trimer Formation", *ACS Nano* **2009**, *3*, 2129-2138.
2. Leung, K. C. F.; Chak, C. P.; Lo, C. M.; Wong, W. Y.; Xuan, S.; Cheng, C. H. K., "pH-Controllable Supramolecular Systems", *Chem. Asian. J.* **2009**, *4*, 364-381.
3. Wang, H. H.; Wang, Y. X. J.; Leung, K. C. F.; Au, D. W. T.; Xuan, S. H.; Chak, C. P.; Lee, S. K. M.; Sheng, H.; Zhang, G.; Qin, L.; Griffith, J. E.; Ahuja, A. T., "Durable Mesenchymal Stem Cell Labelling by Using Polyhedral Superparamagnetic Iron Oxide Nanoparticles", *Chem. Eur. J.* **2009**, *15*, 12417-12425.
4. Leung, K. C. F.; Wang, Y. X. J.; Wang, H. H.; Xuan, S. H.; Chak, C. P.; Cheng, C. H. K. "Biological and Magnetic Contrast Evaluation of Shape-Selective Mn-Fe Nanowires" *IEEE Trans. Nanobiosci.* **2009**, *8*, 192-198.
5. Chak, C. P.; Chau, L. H.; Wu, S. Y.; Ho, H. P.; Li, W. J.; Mendes, P. M.; Leung, K. C. F., "Simultaneous Purification and Surface Plasmon Resonance Characterization of Mechanoresponsive, Discretely Functionalized Gold Nanoparticles", *J. Mater. Chem.* **2011**, *21*, 8317-8323.
6. Chak, C. P.; Lai, J. M. Y.; Sham, K. W. Y.; Cheng, C. H. K.; Leung, K. C. F., "DNA Hybridization of Pathogenicity Island of Vancomycin-Resistant *Enterococcus faecalis* with Discretely Functionalized Gold Nanoparticles in Organic Solvent Mixtures", *RSC Adv.*, in press.
7. Wang, Y. X. J.; Quercy-Jouvet, T.; Wang, H. H.; Li, A. W.; Chak, C. P.; Xuan, S. H.; Shi, L.; Wang, D. F.; Lee, S. F.; Leung, P. C.; Lau, C. B. S.; Fung, K. P.;

- Leung, K. C. F., "Efficacy and Durability in Direct Labeling of Mesenchymal Stem Cells Using Ultrasmall Superparamagnetic Iron Oxide Nanoparticles with Organosilica, Dextran, and PEG Coatings", *Materials* **2011**, *4*, 703-715.
8. Chak, C. P.; Xuan, S.; Leung, K. C. F., "Synthesis, Magnetic Purification and Characterization of Monovalent Amine-Functional Gold Nanoparticles", *Abstract of "The Sixteenth Symposium on Chemistry Postgraduate Research in Hong Kong" 2009*, Hong Kong SAR, China, p. I-25.
9. Chak, C. P.; Xuan, S.; Leung, K. C. F., "Supramolecular Synthesis and Magnetic Purification of Discrete Functional Gold Nanoparticles", *Abstract of "The Seventeenth Symposium on Chemistry Postgraduate Research in Hong Kong" 2010*, Hong Kong SAR, China, p. I-34.
10. Chak, C. P.; Leung, K. C. F., "Simultaneous Purification and Surface Plasmon Resonance Characterization of Mono-functionalized Gold Nanoparticles", *Abstract of "The Eighteenth Symposium on Chemistry Postgraduate Research in Hong Kong"*, **2011**, Hong Kong SAR, China, p. I-32.

Chapter 1 – Introduction of Gold Nanoparticles

1.1 Introduction

Nanotechnology which involves gold nanoparticles, gains much attention for its wide applications in chemistry, physics, engineering and biology. It can be reflected by a dramatic increase in the number of publications related to gold nanoparticles during the last fifteen years (Figure 1-1). The word “nanoparticles” refer to clusters of atoms or molecules having an overall size of 1–100 nanometer. There are two general approaches to produce nanoparticles, namely *top down* and *bottom up* methods.^{1a-c}

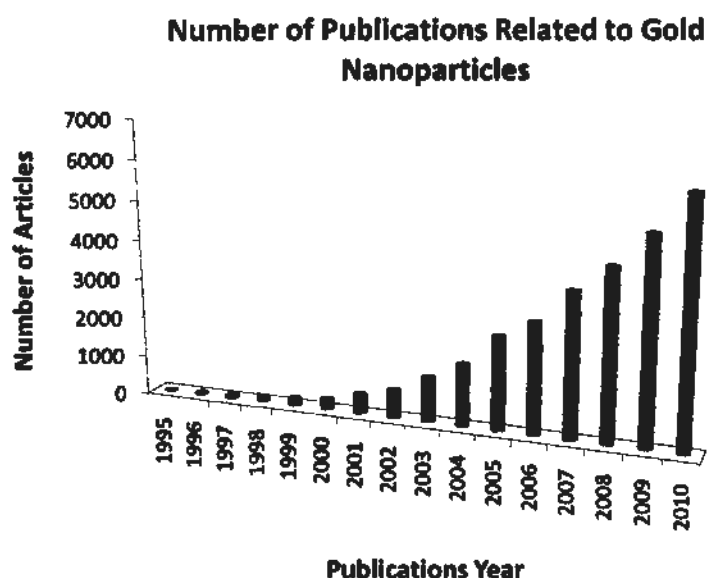


Figure 1-1. Number of publications related to AuNPs (by December 2010), Source: SciFinder Scholar; keyword: gold nanoparticles.

Top down approach involves the removal or division of a bulk material into its nanostructure.^{1a2} Photolithography, electron beam lithography are examples for producing nanostructures by *top down* approach. For the lithographic methods,

however, expensive instruments are required and large amount of materials could be wasted by repeated number of steps.^{1a,2}

Bottom up approach involves the assembly of atoms, generated by reduction of ions, to give the desired nanostructure.^{1a} Since the size of an atom is about 1 Å (1 Å equals to 0.1 nm), the construction of nanostructure from ångström scale into nanoscale structure is somewhat more common and effective than the *top down* approach. Such approach involves the termination of nanocluster growth from atoms in the presence of a capping agent. The size and shape of the nanostructures can be controlled by using different capping agents, reducing agents, reaction time and techniques.^{1a,2}

Examples for producing nanostructures by *bottom up* approach are chemical, sonochemical, thermal and photochemical methods. For photochemical method, UV irradiation^{3a-e} and near-IR laser^{3e} can be used to produce gold nanoparticles in the presence^{3a-c} or absence^{3d,e} of small gold nanoparticle seeds. For UV irradiation, the size of gold nanoparticles (5-120 nm) can be controlled by the ratio of ligands or seeds and gold salt. For near-IR irradiation, the size of gold nanoparticles (1-200 nm) can be tuned by the time of irradiation. For sonochemical method,^{4a,b} the reduction rate of gold salt in aqueous medium can be controlled by the ultrasonic intensity, solution temperature and reaction flask position in sonicator, hence controlling the

size of the gold nanoparticles. For thermal method,⁵ gold nanoparticles with surfactant can be subjected to thermolysis to give gold nanoparticles with an increased size.

For the above-mentioned methods, chemical synthesis of gold nanoparticles was perhaps more popular because a wider range of capping ligands with different functional groups can be used.

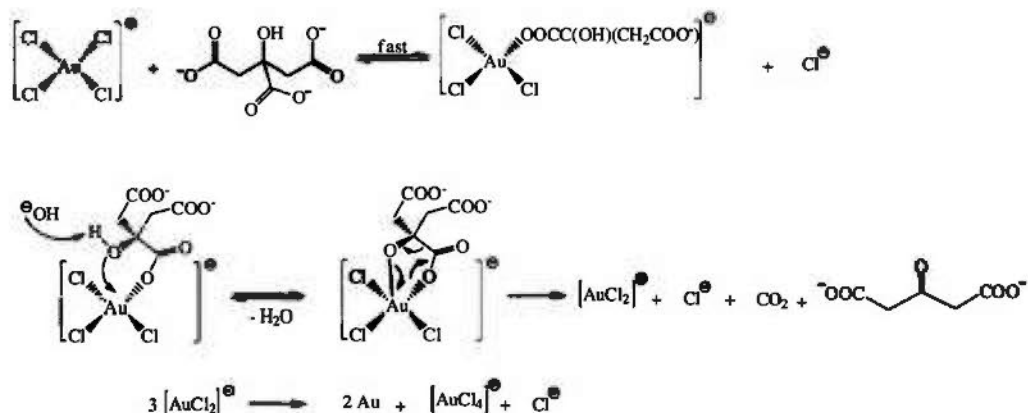
1.2 Chemical synthesis of gold nanoparticles (AuNPs)

In general, gold nanoparticles are synthesized by a reduction of tetrachloroaurate in solution whereas gold(III) ions are reduced to gold(0) atoms. The gold atoms then rapidly nucleate and grow into nano-scaled particles.^{1c,2}

1.2.1 One-phase synthesis of citrate-coated AuNPs (Turkevich Method)

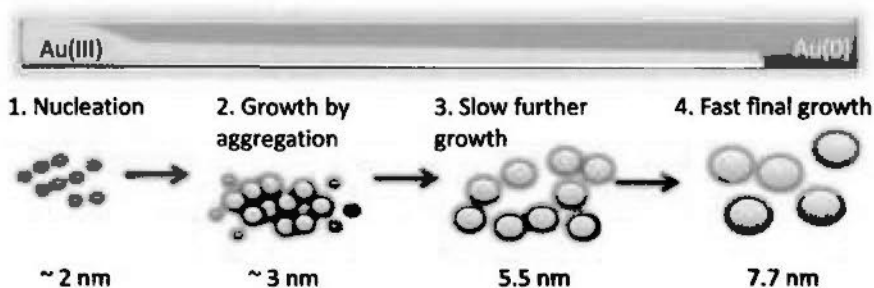
The synthesis of citrate-coated AuNPs can be dated back to 1951 by Turkevich.^{6a} Gold(III) salt and citrate solution were stirred in water, and that the gold salt was reduced by citrate at 100 °C, yielding AuNPs with a diameter about 20 nm. Such method was modified by Frens in 1973 to give AuNPs of 16 to 147 nm.^{6b} The ratio of gold to citrate, temperature, and the order of addition of reagents determined the size of the AuNPs.

For instance, tetrachloroaurate solution was heated to 100 °C in a double-walled reactor with a thermostat bath. The solution was stirred vigorously and the mantle provided a homogenous temperature distribution within the reaction mixture. While the solution was boiling, preheated trisodium citrate solution was added to the solution. The solution was then cooled and extracted to give the citrate-coated AuNPs. The concentration of citrate solution added during the synthesis determined the size of AuNPs. The general mechanism of forming AuNPs has been studied which is shown as follow:^{6c}



Scheme 1. Mechanism of formation of citrate-coated AuNPs.^{6c}

In recent years, the Turkevich method has been modified, whereas the minimum size of the AuNPs obtained by this method at 75 °C can be 7.7 nm.^{6d} The formation processes of AuNPs have been monitored by small-angle X-ray scattering (SAXS) and X-ray absorption near-edge spectroscopy (XANES) (Scheme 2). Moreover, it was reported that the formation of AuNPs can also be achieved at room temperature with the aid of ultra-violet irradiation technique.^{3d}



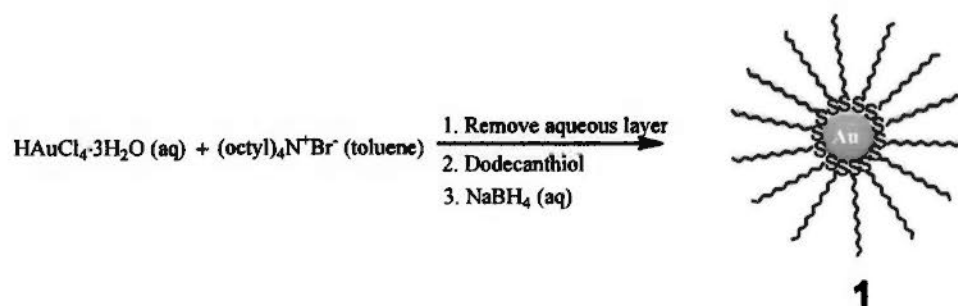
Scheme 2. Formation of citrate-coated AuNPs by a modified Turkevich method.^{6d}

This method is commonly used to prepare larger AuNPs with loosely bound citrate ligand on the gold surface, thereby feasible for post-functionalization.^{1g}

1.2.2 Two-phase synthesis of alkanethiolate-coated AuNPs (Brust-Schiffrin Method)

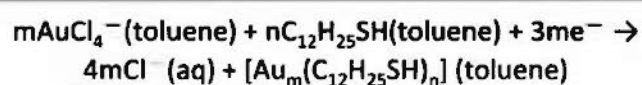
The two-phase synthesis of alkanethiolate-coated AuNPs has been reported by Brust and Schiffrin in 1994 (Scheme 3).^{7a,b} Since the alkanethiolate-coated AuNPs are found to be more thermally stable and air stable with higher monodispersity with controlled size ranging from 1.5 to 5.2 nm, the discovery of the two-phase synthesis method has a great influence in synthesizing AuNPs.

For instance, tetrachloroaurate was transferred to toluene using tetraoctylammonium bromide as phase transfer reagent. The organic layer was obtained and stirred vigorously with the addition of dodecanethiol, followed by the addition of sodium borohydride solution, to give the alkanethiolate-coated AuNPs. The obtained AuNPs can be isolated and redissolved in organic solvents without irreversible aggregation and decomposition.

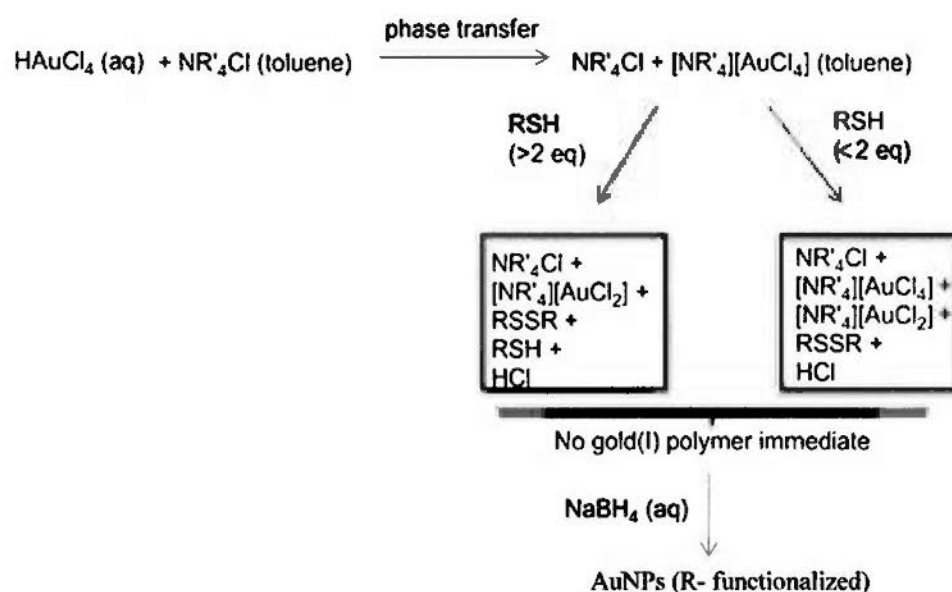


Scheme 3. Synthetic scheme of alkanethiolate-coated AuNPs by Brust-Schiffrin method.

The general mechanism of formation of AuNPs is proposed in 1994 by Brust which is shown as follow:^{7a}



From the above equations, the gold(III) ions are reduced by electrons generated from sodium borohydride to give the AuNPs. Later it is then proposed that there should be a formation gold(I) polymer after addition of dodecanethiol.^{7c}



However, Lennox^{7d} later found, in the above mechanism, by ¹H NMR spectroscopy that the thiol reduced gold(III) to gold(I) chloride but there should not be gold(I) polymer formation as an intermediate except there exist excess water or polar

solvents. Moreover, it is found that the ligands attached on AuNPs are in thiolate $[\text{Au}_m(\text{C}_{12}\text{H}_{25}\text{S})_n]$ rather than in thiol $[\text{Au}_m(\text{C}_{12}\text{H}_{25}\text{SH})_n]$.^{7e}

The size of the AuNPs can be tuned by the ratio of thiol to gold salt, and the rate of sodium borohydride addition. A large thiol to gold salt molar ratio results in smaller nanoparticles. Moreover, fast addition of sodium borohydride and at low temperature will give smaller nanoparticles with better dispersity.^{7f}

The alkanethiolate-coated AuNPs obtained in this method are more stable because the gold–sulfur bonds are relatively strong due to the soft character of gold and sulfur.^{1g} However, the gold–sulfur bond can be broken and exchanged with another sulfur-containing ligand under certain conditions which are described in Section 1.3.1.

1.2.3 Miscellaneous methods

There are several methods to synthesize AuNPs including the Martin method, seeding method and dendritic method, etc. With the advance of nanochemistry nowadays, more synthetic methods with improved particle's monodispersity and size control are expected to be discovered.

Martin method⁸ was discovered in 2010, the AuNPs were prepared in “stabilizer-free” form by reduction of tetrachloroaurate in water and modified to give dodecanethiolate-coated AuNPs (Figure 1-2). The whole synthetic process takes

place in approximately ten minutes. Sodium borohydride was mixed in 1.0 M sodium hydroxide solution for several hours, while the tetrachloroaurate has been stored in 1.0 M hydrochloric acid for several months. The two solutions were mixed. The obtained AuNPs possess a size ranging from 3.2 to 5.2 nm by controlling the borohydride anion to hydroxide anion ratio. The AuNPs were proposed to be stabilized by the boron-based anion and hence, the AuNPs are effectively exchanged by thiol in the presence of a phase transfer reagent. Acetone was added to the water and then hexane. Dodecanethiol was then added to the hexane layer and the AuNPs will be functionalized by dodecanethiol by vigorous shaking of the two-phase mixture.

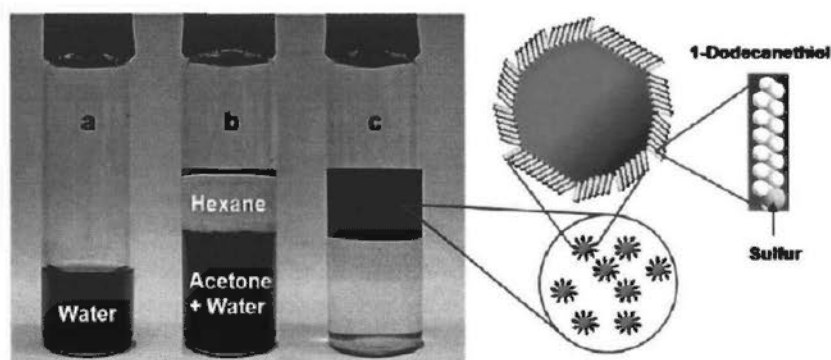


Figure 1-2. Synthesis of dodecanethiolate-coated AuNPs by Martin method. a) “Stabilizer-free” AuNPs were synthesized in water; b) AuNPs were mixed with acetone and hexane; c) dodecanethiol was added to hexane layer and vigorous shaking was applied (obtained from Ref. 8).

Seeding method^{9a-c} is also popular in synthesizing large AuNPs. A relatively strong reducing agent, such as sodium borohydride, was used to synthesize small spherical gold seeds. The seeds were then added to a grow solution which contains

gold salts and surfactant. Then, a weaker reducing agent, ascorbic acid, was added to reduce the gold(III) ions to gold(I) ions. The gold(I) ions then induce a catalyzed reduction on the surface on the gold seeds. However, the growth of gold seeds is believed to be a kinetic process, so the size and shape of the nanoparticles are difficult to be controlled.

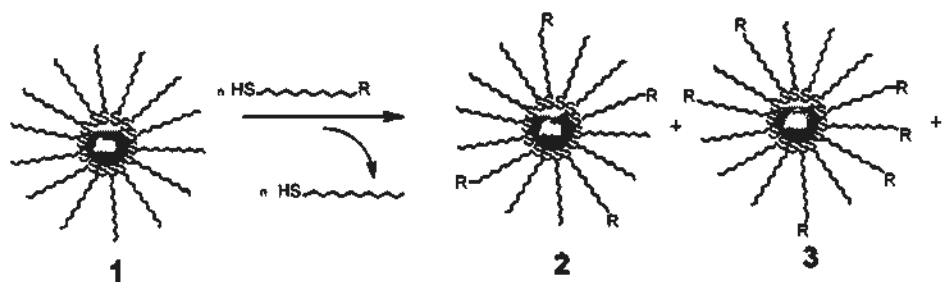
Dendritic method¹⁰ employs the use of dendrimer to synthesize AuNPs. Dendrimers are capable to encapsulate gold metal ions by electrostatic and various supramolecular interactions based on azide, amine, alcohol or carboxylic acid groups at the dendrimers interior. Recently, azide-functionalized dendrimers have been used to prepare dendrimer-coated AuNPs rendering a tunable AuNPs size from 1.8 to 42 nm. There are several advantages of using dendrimers as capping agents for synthesis. The dendrimer arm can prevent nanoparticle aggregation for better size control, and that the peripheral groups on dendrimers can be easily post-functionalized into other moieties for different applications. However, the disadvantage may be accounted for the multiple-step and time-consuming synthesis of dendrimers with high generations.

1.3 Functionalization of AuNPs

AuNPs can be functionalized with one or more types of functional groups suitable for various applications.

1.3.1 Ligand place exchange reaction

To begin with, known amount of different functional thiols can be added to the alkanethiolate-coated AuNPs **1** in an organic solvent, e.g., toluene with stirring for 48-60 hours at room temperature,^{11a} to facilitate ligand place exchange reactions on gold surface. A portion of original thiolate on the gold surface will be displaced by the new thiols added to the mixture (Scheme 4). However, the number of functional groups displaced on each AuNPs is unknown, only an average number of functional groups can be determined.

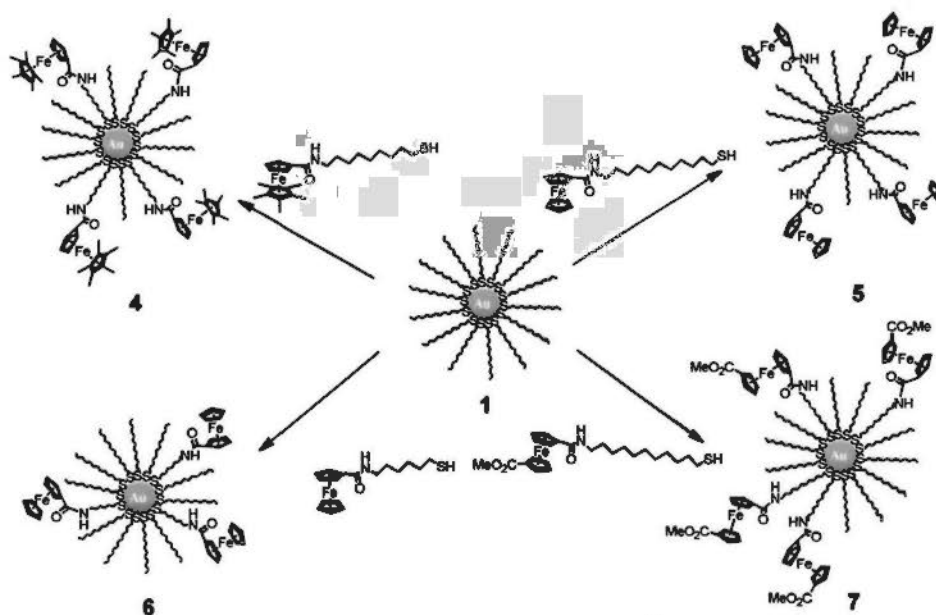


Scheme 4. Place exchange reaction of alkanethiolate-coated AuNPs with the addition of n molar R -functionalized thiol to replace n molar dodecanthiol from the AuNPs.

There are lots of examples of ligand place exchange reactions. In particular, the alkanethiolate-coated AuNPs **1** can be functionalized with different numbers of ferrocene-alkanethiol compounds (**4** to **7**) via place exchange reactions in dichloromethane for 2 days at room temperature (Scheme 5).^{11b,c} The resulting

ferrocene-containing AuNPs are capable to detect anions (H_2PO_4^- and HSO_4^-).^{11b,c}

The place exchange reactions can also take place at elevated temperature (> 60 °C) in a short period of time.^{11d} The mechanism involves the partially or fully dissociated Au–S bond and followed by nucleophilic displacement during the place exchange reaction.^{11a}



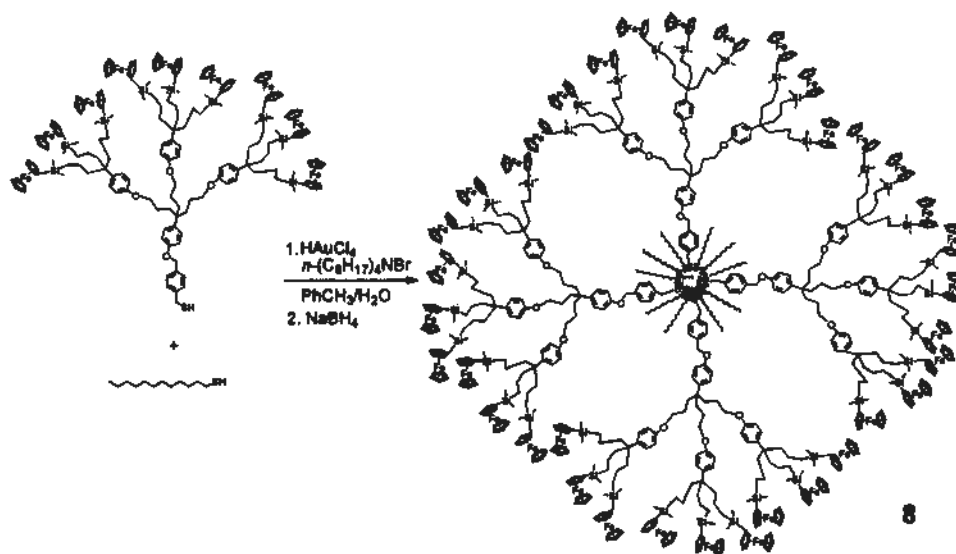
Scheme 5. Place exchange reactions of ferrocene-alkanethiol compounds with dodecanethiol in dodecanethiolate-coated AuNPs.^{11b}

Such ligand exchange reactions can be extended to the citrate-coated AuNPs, the citrate ligands are relatively more labile than thiolate ligand. Hence, citrate-coated AuNPs can be easily functionalized by the addition of any functional thiols. For example, mercaptoalkyloligonucleotides were added to 13 nm citrate-coated AuNPs to undergo ligand exchange reaction to give mercaptoalkyloligonucleotides-functionalized AuNPs^{12a} with stronger Au–S bonds.

Similar ligand place exchange reactions are used commonly,^{12b-e} to produce functionalized AuNPs for sensing applications, which are described in Section 1.6.2. The ligand replacement reactions also work for the citrate replacement by acetone and iodine.^{13a,b}

1.3.2 *In situ* mixing of binary ligands during synthesis

Functionalization of AuNPs can also be achieved by mixing two or more types of ligands during the *in situ* synthesis of AuNPs. For example, dendron-fucntionalized AuNPs **8** can be prepared in mixing the mercaptodendron with dodecanethiol and gold salt, followed by the addition of sodium borohydride (Scheme 6).^{14a} Such *in situ* method is efficient based on the fact that steric bulky dendrons are not capable for place exchange reaction with good yield.



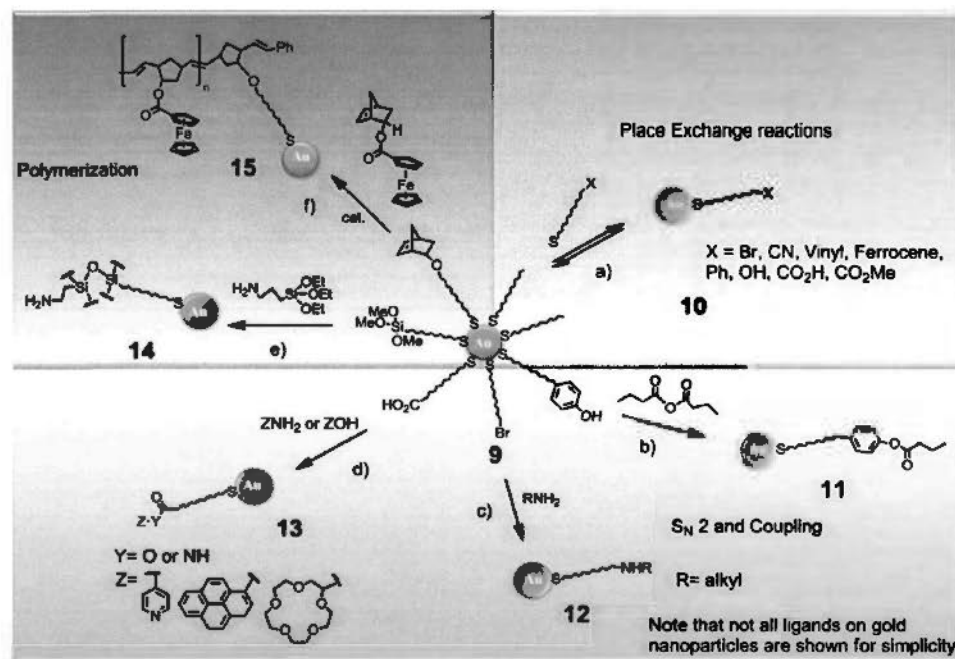
Scheme 6. *In situ* mixing of binary thiol ligands during synthesis of AuNPs.^{14a}

Another example is the synthesis of binary ligand-coated, ripped AuNPs for

the preparation of di-functionalized AuNPs. The binary mixing of 1-nonanethiol and 4-methylbenzenethiol with gold salt and followed by the addition of sodium borohydride yields the ripped AuNPs.^{14b} Synthetic details of di-functionalized AuNPs are discussed in Section 2.2.

1.3.3 Chemical post-functionalization

Chemical reactions of functionalized AuNPs **9** (Scheme 7)^{15a} such as polymerizations to give **14** and **15**,^{15b} nucleophilic substitutions to give **11** and **12**,^{11a} place exchange reactions to give **10**,^{15c} coupling reactions to give **13**,^{15d} and photo-induced reactions^{15e} are also feasible to further functionalize AuNPs.



Scheme 7. Several chemical reactions on the surface of AuNPs. a) Place exchange reactions; b-d) nucleophilic and coupling reactions; e-f) polymerizations.^{15a}

1.4 Surface plasmon resonance (SPR) of AuNPs

The surface plasmon resonance (SPR) band of the AuNPs is due to the collective oscillations of electron clouds at the surface of the nanoparticles correlated with the electromagnetic field of the incoming light.^{1g} When the wavelength of light is much greater than the size of nanoparticles, the continuous electron bands of gold become discrete² and the free d-electrons in metal will oscillate.^{1a} The electron density in the particles is polarized to one surface and oscillates in resonance with the frequency of light when the wave front of light passes.

Hence, the color of the AuNPs in the absence of any other dyes or colored materials in solution originates from the SPR of the AuNPs. The SPR absorption band can be observed in the visible region around 520 nm and depends on the size, shape, interparticle distance and nature of the protecting organic shell and environment changes.^{16a-c}

The SPR properties were discovered and studied in 1908 by Mie.^{1g} Combining with recent reports on Mie's theory,^{16d-f} it showed that the SPR should be absent with core size of nanoparticles less than 2 nm. Also, the ligand shell will change the refractive index and will cause a shift in SPR band. Moreover, the SPR band will be red-shifted if the interparticle distance decreases. However, it will be negligible when the interparticle distance is greater than the average diameter of the nanoparticles.^{16g-i}

Moreover, the refractive index and also the SPR band will be affected by different solvents.^{16a} Hence, by changing the above parameters, the shifts of SPR band can be detected by UV/visible absorption spectroscopy. The observable of such changes provides wide applications for detection of specific molecules, which are discussed in Section 1.6.^{12a,20a-h}

1.4.1 General properties of gold assemblies and self-assembling monolayer (SAM)

A gold thin film coated with monolayer of surface ligand is regarded as a gold self assembling monolayer (SAM). AuNPs, gold(I) thiolate polymer and thiolate SAM possess different structures as well as different oxidation states of gold atoms (Figure 1-3).² Alkanethiolate gold SAM can be prepared easily by direct immersion of a gold thin film into alkanethiol in organic solvent for several hours thereby Au-S bonds will be formed.

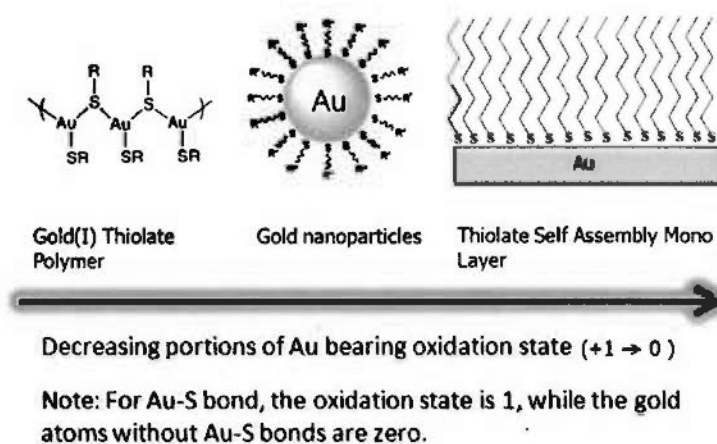


Figure 1-3. Structural difference between gold(I) thiolate polymer, AuNPs and thiolate SAM.²

Bottom layer of gold atoms in SAM are in oxidation state of zero and regarded

as bulk gold which do not exhibit localized surface plasmon resonance as AuNPs do.¹⁶ However, there is surface plasmon polaritons (SPPs) observed for the SAM of gold thin film in a certain instrumental setup condition.^{17a-f} The SPPs refer to a fluctuation of electron density at the interface between the gold thin film coupled with electromagnetic waves^{17a-c} which is non-radiative in nature^{17b,d} and presents as propagating wave.^{1f} The electromagnetic surface oscillations can be only coupled to photons with a prism, grating or spatially localized scattering center so that the momentum mismatch can be resolved.^{17b} The SPPs depend on the medium of solution on the gold thin film which alters the refractive index, and hence, the surface plasmon wave absorption peak will be shifted upon a change of solvent and substrates on the gold thin film.^{17e} Therefore, the SPPs changes of gold thin film has been used in applications for detection of biomolecules.^{17g,h,n-p}

1.4.2 Detection of molecules on the SAM of gold via SPR changes

Instrumental setup of the SPPs usually employs a total internal reflection (TIR) in the right prism under the glass coated with ~50 nm metallic thin film (Figure 1-4a).^{1f,17e,f,m} When light is reflected from the gold film, there will be an absorption signal (decrease in intensity) as it coupled with conducting electrons. An evanescent wave will be generated which decays exponentially into the solution on the surface of gold thin film. The SPPs resonance is measured by the minimum point of the

intensity curve,^{1f} which is highly sensitivity to the refractive index of sample solutions as previously mentioned (Figure 1-4b). When there are substrate immobilizations, reactions or change of solvent system, the angle of reflection of the light will be altered and will be recorded by the charged-coupled device (CCD), which corresponds to the shift of the minimum point of the intensity curve. The maximum distance of detection of samples in the solution is about 200 nm from the metallic thin film, enabling the detection of surface attachments and modifications of the gold thin film.^{1f} However, this method is restricted by the concentration and molecular weight of the molecules being detected. The sensitivity of the detection of 20 kDa protein is about 1- 10 nM.^{1f}

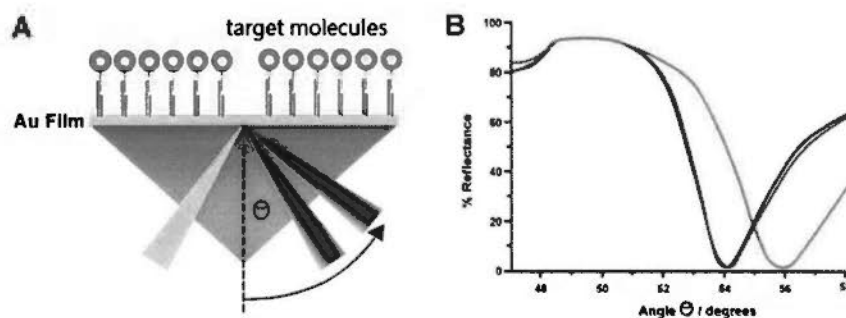


Figure 1-4. a) Instrumental setup of SPPs detection of gold thin film utilizing TIR alignment. When the target molecules was added, there will be change in angle θ which can be detected by CCD; b) a graph of angle changes can be plotted with different analytes added (obtained from Ref. 1f).

1.4.3 Making network of AuNPs with gold SAM to increase sensitivity of SPR detection

Since AuNPs possess high polarizability^{17f} and localized SPR effect, they exhibit strong interactions with the gold thin film SPPs,^{17a,e-f} which will increase the intensity of the resultant field.^{17f} The absorption of SPPs resonance will be altered by the size of AuNPs on the gold thin film. The larger the size of the AuNPs, the greater the angle derivate upon change in medium.¹⁷ⁱ Such coupling effect is also distance-dependent, as the distance of nanoparticles and the gold thin film varies.^{17a,f} Moreover, the gold nanoparticle enhancement to SPPs sensitivity of gold thin film was reported, with a 1000-fold increased sensitivity for oligonucleotides detection.^{17j} The detection utilizing AuNPs can be simply achieved by electrostatic,^{17e} biotin-streptavidin interactions,^{17j} gold-thiol formation^{17k} and direct hybridization by DNA,^{17l} etc, to the target molecules or the ligand layer on the gold thin film.

1.5 Characterization of AuNPs

AuNPs can be characterized by various spectroscopic, microscopic and alternative methods.

1.5.1 Spectroscopic methods

Nuclear magnetic resonance (NMR),^{18a} Fourier-transform infra-red (FT-IR),^{18b} ultra-violet/visible (UV/Vis) spectroscopies^{16a-i} can be used to provide structural information of the ligand integrity of the AuNPs. Spectroscopies can provide structural information of organic shell as in organic compounds, except the ligands atom near the gold core will give a broad signal in NMR spectroscopies so that the integration of protons will be affected. FT-IR spectroscopies can provide information of functional group identities of the ligands. UV/Visible spectroscopies can be used to monitor the surface plasmon resonance absorption of the AuNPs.

X-ray photoelectron spectroscopy (XPS)^{15a} and energy-dispersive X-ray spectroscopy (EDX)^{18c} can provide elemental information on the gold and/or other atoms ratio of the gold nanoparticle composites. Laser desorption ionization mass spectroscopy can provide information on molecular weight with or without ligands.^{18d}

1.5.2 Microscopic methods

The most popular technique used to characterize AuNPs is the high resolution

transmission electron microscopy (HRTEM).^{18e} Nanosized gold core can be observed visually. An electron beam is transmitted to and interacts with the sample, since AuNPs possess dense electron clusters, which can be deposited as dark contrast in the TEM image. Scanning tunneling microscopy (STM),^{18f} atomic force microscopy (AFM)^{18f} can be used to scan the surface and also give information of core dimension and surface of the nanoparticles.

1.5.3 Miscellaneous characterization methods

Thermogravimetric analysis (TGA)^{15a} can also give information of the gold core's dimension in the aid of calculations. Ligand-coated AuNPs can be analyzed by TGA instruments whereas all organic ligands will be decomposed to give free bulk gold. The percentage of organic matters in the nanoparticles can be analyzed as weight loss. Other techniques like small-angle X-ray scattering (SAXS),^{18f} X-ray diffraction,^{18f} etc, are also used to determine the size and composition of AuNPs.

1.6 Applications

Many applications can be utilized with AuNPs. In this section, some of the important applications will be introduced, such as catalysis, biosensors, ion sensors, fingerprint detector and miscellaneous applications.

1.6.1 Catalysis

AuNPs can catalyze the CO oxidation in the presence of other metal or metal hydroxide. For instance, gold cluster $\text{Au}_9\text{PPh}_3(\text{NO}_3)_3$ dispersed in Mn, Fe, Co, Ni, Cu or copper hydroxide can catalyze the oxidation of CO even below 0 °C or at -70 °C.^{19a} The activity of CO oxidation is also high with AuNPs deposited on Fe_2O_3 ,^{19b} and other metal oxides. The activity increases with decrease in size of AuNPs which can be attributed to the valence bond density state of AuNPs. A synergistic mechanism occurred at the AuNPs-metal oxide interface, CO will be adsorbed onto an adjacent site of metal oxide which is occupied by pre-adsorbed oxygen molecules. The reaction will involve an intermediate carbonate species which will decompose to CO_2 upon desorption.^{19c}

N-imidazole-functionalized-thiolate AuNPs can also catalyze the cleavage of dinitrophenyl acetate in methanol-water solution with a faster rate than acetyl-*N*-methylhistamine.^{19d} Alkanethiolate-coated AuNPs with hexanediene functionality can coordinate to RuCl_3 , which can catalyze the heterogenous

polymerization of norbornene.^{19e}

1.6.2 Sensors of DNA, antigens, aptamers, enzymatic reactions and other small molecules

Biosensors utilizing AuNPs have been widely reported, most of them utilize the surface plasmon resonance changes upon the existence of the target molecules.^{12a,20a-e}

A representative example of DNA sensors will be discussed.

AuNPs (13 nm) have been used for 30 base pairs DNA target detection (Figure 1-5).^{12a} The AuNPs were functionalized by 5'- or 3'- mercaptoalkyloligonucleotides (28 base pairs each). When a target DNA is present in the solution, these two gold-oligonucleotide chains can be hybridized with the target DNA by aligning continuously the 15 base pairs each in the two gold-oligonucleotide chains. Hence, the AuNP-oligonucleotide structures will be aggregated so that the interparticle distance will decrease significantly, resulting in a change of surface plasmon resonance. Such SPR changes can be observed visually by spotting the solution on the C₁₈ thin layer chromatography plate. When the interparticle distance was smaller than the nanoparticle size (aggregation induced by target DNA), the color was blue. In contrast (no aggregation), the color was red. This application can be used to detect even single base pair mismatch by conducting the DNA annealing experiments compared to those without mismatch at different temperatures.

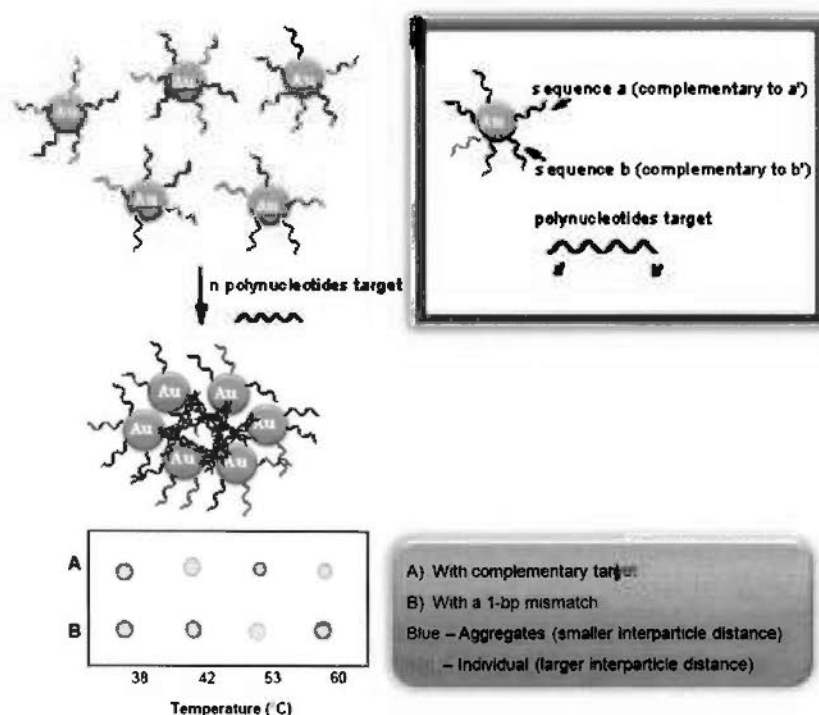


Figure 1-5. DNA sensors which utilize AuNPs. AuNPs are functionalized with two types of DNA which are complementary to different parts of target DNA. Upon target DNA addition, AuNPs become aggregated and the SPR red shift to give a blue color which can be visualized by C_{18} TLC. DNA with a base pair mismatch can be also detected by melting temperature studies.^{12a}

Similar techniques which utilize the changes of SPR upon decrease in interparticle distance of AuNPs, have been reported in detection of antigens,^{20a} aptamers,^{20b,c} monitoring enzymatic reactions,^{20d} and other chemical compounds like melamine via hydrogen bonding recognition to AuNPs.^{20e}

1.6.3 Ion sensors

Ion sensors with AuNPs also employ the SPR band shift mechanism when target ions are present. AuNPs can be functionalized with 11-mercaptopundecanoic acid, whereas the presence of toxic transition metal cations such as lead, cadmium and mercury

ions will possess a color change of AuNPs from red to blue.^{21a} Crown ethers such as [15]crown-5 can be functionalized to the AuNPs for selective detection of potassium ions over sodium, lithium, cesium, ammonium and calcium ions.^{21b} Anions such as adenosine-5'-triphosphate anions (ATP^{2-}) and H_2PO_4^- , HSO_4^- can be detected by ferrocene-functionalized AuNPs^{11b,c} (See also Section 1.3.1). The presence of the target anions with the ferrocene-functionalized AuNPs will possess a change in the redox profile of ferrocene. The addition of H_2PO_4^- gives a new voltammetric wave at a less positive potential with a difference of 220 mV. The voltammetric wave of the ferrocene will be disappeared when the added anions become saturated. The addition of HSO_4^- will give a smaller potential shift of 40 mV. The dendritic ferrocene-functionalized AuNPs are also capable to detect H_2PO_4^- and ATP^{2-} over HSO_4^- and Cl^- by observing their voltammetric redox profiles.

1.6.4 Fingerprint detector

AuNPs can be used to detect fingerprint²¹ which is beneficial to forensic sciences. A volunteer's finger can be dipped into an antibody-coated AuNPs solution, so that the AuNPs will bind to the fingerprint by supramolecular recognition with antigens in human sweat in the fingerprint, leading to a fluorescence visualization (Figure 1-6A).^{22a} Fingerprints which were immobilized on a substrate, can also be detected by depositing citrate-coated AuNPs at low pH.^{22b,c} Then, physical developers such as

gold or silver can be added to enhance the visualization of the AuNP immobilized fingerprints (Figure 1-6b).

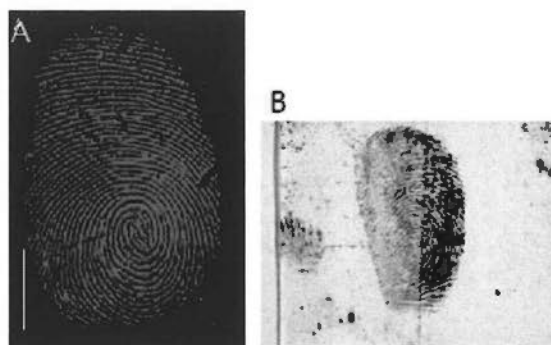


Figure 1-6. Fingerprint detection by AuNPs. a) Fluorescence image of volunteers' fingerprint pattern (Obtained from Ref. 22a); b) visual images of fingerprint stained on polypropylene (Obtained from Ref. 22b).

1.6.5 Miscellaneous applications

There are still numerous applications of AuNPs in various fields. Drug delivery and gene transfection are hot research fields.^{23a-c} For example, platinum-based anticancer drugs can be attached on the AuNPs via supramolecular interactions so that it demonstrates better cytotoxicity than the drug alone and can be transferred directly to the lung cancer cell nucleus.^{22b} Charge-reversal polyelectrolytes-coated AuNPs are also feasible to enhance gene delivery and siRNA silencing.^{23c} The charge-reversal polyelectrolytes-coated AuNPs can disrupt the endosome and release the pharmaceutical reagents easily and modified by the target ligands so that the gene transfection and siRNA silencing can take place.

Chapter Two – Discretely Functionalized AuNPs

As mentioned in the previous chapter, AuNPs are usually post-modified with multiple functional groups for various specific applications. However, the exact number of functional groups on each AuNP is generally unknown whereas only an average number of functional groups of all AuNPs can be analyzed and reported. It is still a challenge to synthesize AuNPs with a discrete number of functional groups since there are multiple reactive sites on AuNPs in a close proximity. For example, a 2 nm AuNP possesses approximately 100 surface ligands.^{24a} Place exchange reactions or *in situ* mixing of binary ligands during synthesis would inevitably give mixtures of nanoparticles with multiple functional groups in different ratios for each nanoparticle even with careful stoichiometric control.^{24b} Hence, the as-synthesized AuNPs are randomly functionalized. These nanoparticles are expected to form large aggregates with undefined structures and properties, and sometimes with poor reproducibility.^{24b} Therefore, discretely functionalized AuNPs have great potentials to be investigated as precisely defined structures for specific applications. Moreover, there are only few literatures reported for preparing discretely functionalized AuNPs.

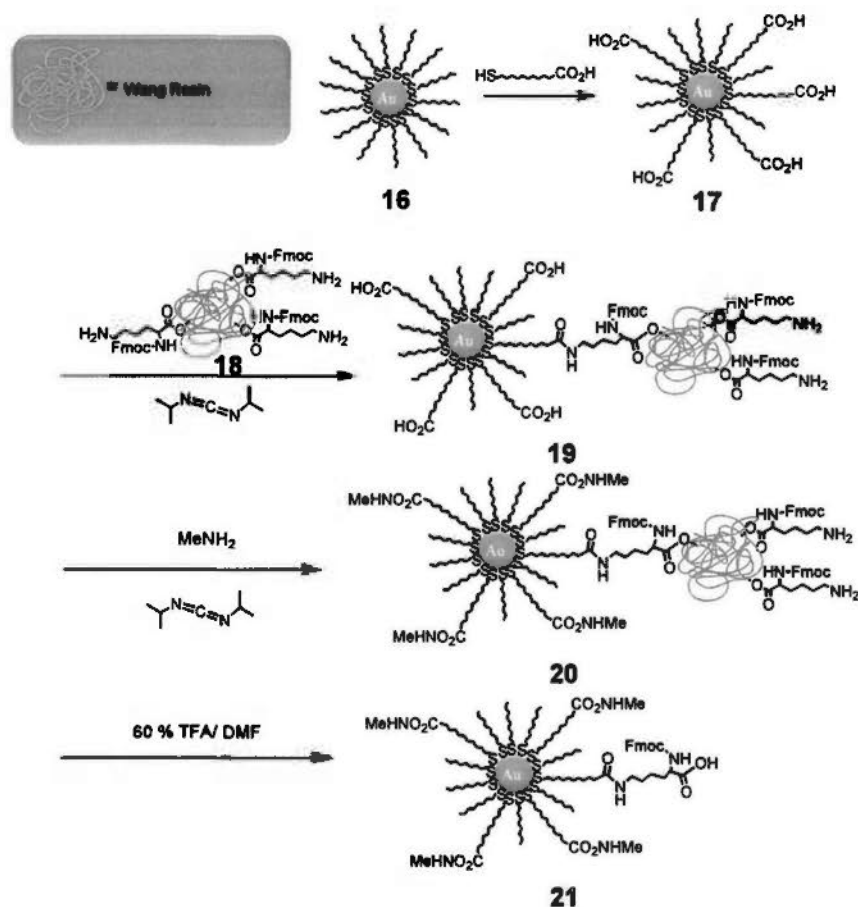
2.1 Synthesis of discretely mono-functionalized AuNPs

A discretely mono-functionalized AuNPs refers to a single AuNP which contains a single reactive functional group (e.g., -OH, -NH₂, -CO₂H, etc.) and many other non-reactive groups (e.g., alkyl chains). There are several reported methods in synthesizing discretely mono-functionalized AuNPs.

2.1.1 Covalent solid-phase supported synthesis

Covalent solid-phase supported synthesis of discretely mono-functionalized AuNPs has been reported in 2004 by Jacobson *et al.*^{25a} and Huo *et al.*^{25b} Generally, polystyrene Wang resin with controlled functional group density was used as the solid-phase support. One hydroxyl functional group of the resin per nm³ was from 9 to 20, hence, it allows only one ~2 nm AuNP to react with the functional moiety of the resin. This process is called “site isolation effect”, excess AuNPs can be washed away *via* the solid-phase synthesis. Finally, mono-functionalized AuNPs can be obtained by a covalent cleavage between the resin and the functionalized AuNP.

On the other hand, Jacobson employed the Fmoc-Lys(Dde) polystyrene Wang Resin with 0.54 mmol/g functional groups density as the solid-phase support (Scheme 8).



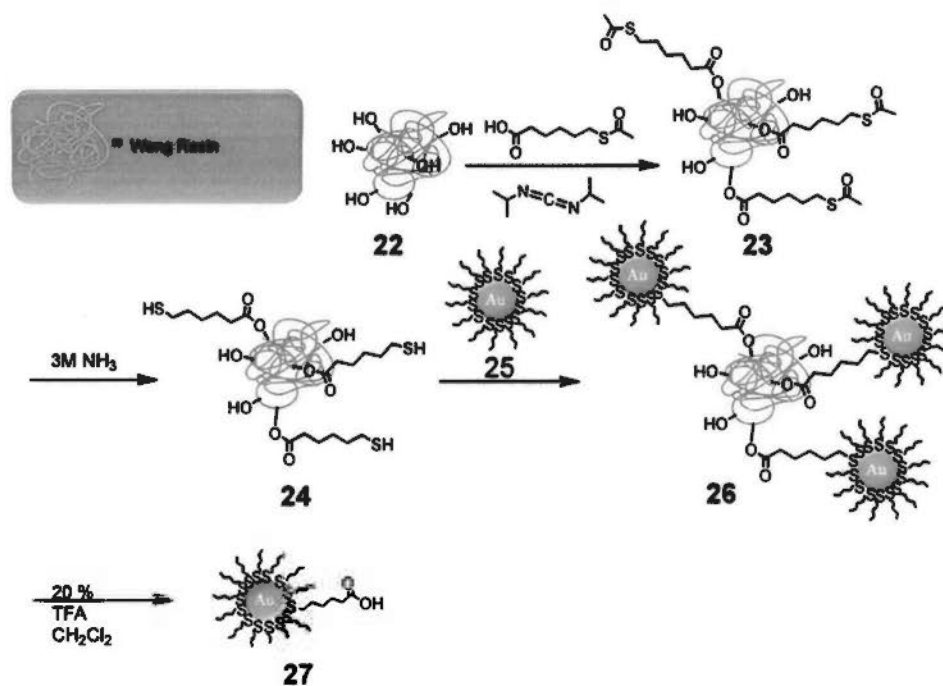
Scheme 8. The covalent solid-phase supported synthesis of mono-Lys-functionalized AuNPs.^{25a}

Carboxylic acid randomly functionalized AuNPs (2 nm) **17** were obtained by a specific place exchange reaction of octanethiolate-coated AuNPs **16** with 11-mercaptoundecanoic acid. For the solid support, the Dde protected amine was deprotected by hydrazine hydrate with a base. The amine groups in the resin **18** are far away from each other giving a volume approximately 9 nm^3 , which is sufficient for the coupling reaction with a 2 nm nanoparticle. The amine group of the resin and one of the carboxylic acid groups on AuNPs are then coupled to form amide in the

presence of 1,3-diisopropylcarbodiimide to afford **19**. After a washing procedure to remove an excess of nanoparticles, the free, residual carboxylic acid groups of the AuNP were protected by methamine to give **20**. Finally, the Fmoc-protected Lys-monofunctionalized AuNPs **21** were obtained by a cleavage of the ester group of resin with trifluoroacetic acid with 10 % yield. The total yield of the reactions can be increased by using a better swelling polymer, e.g., poly(ethylene glycol)acrylamide copolymer (PEGA) based resin. The overall yield was found to be 25 %. However, the Lys functional groups density was 0.05 mmol/g, which is much lower than the Wang resin to prevent the random functionalization of AuNPs in highly swelling polymer conditions.

On the other hand, Huo *et al.* employed the Wang resin **22** with hydroxyl functional groups density 1.4–3.2 mmol/g as a solid-phase supported polymer (Scheme 9). 6-Mercaptohexanoic acid was coupled with hydroxyl groups on the resin by 1,3-diisopropylcarbodiimide to give **23**, followed by deprotection of acetyl groups to afford **24**. The thiol groups on the resin **24** were found to possess 20 nm³ spaces for allowing a 2 nm AuNP to react. Then, 2.8 nm *n*-butanethiolate-coated AuNPs **25** were added to the resin for a place exchange reaction with the thiol on the resin. After that, trifluoroacetic acid (20 % in dichloromethane) was added to cleave the mono-carboxylic acid-functionalized AuNPs. The crude product **27** was then

purified using centrifuge and size exclusion chromatography and the yield of reaction was about 33 %.



Scheme 9. The covalent solid-phase supported synthesis of mono-carboxylic acid-functionalized AuNPs.^{25b}

A more detailed study on the covalent solid-phase supported synthesis was reported by altering the resin with different ligand loading of hydroxyl groups to thiol groups, and place exchange reactions solvents.^{25c} It was found that a more flexible resin (JandaJel) with higher swelling properties give lower yield of mono-functionalized AuNPs (Figure 2-1). However, the site isolation effect will be diluted in this case. A large surface area (with a lower functional groups density) was required for place exchange reactions since the volume for place exchange reaction of nanoparticle decreased with higher swelling property of resins. For the choice of

solvents in place exchange reaction, a hexane/dichloromethane mixture was used in the reactions to increase the purity of the mono-functionalized AuNPs. Since hexane will decrease the swelling properties of the resin, the multiple attachments of thiols to the same nanoparticle were avoided. The purity of the mono-functionalized AuNPs will be higher. With different ligand loadings, the yield of mono-functionalized AuNPs can be increased with a higher ratio of hydroxyl groups, so that there are fewer chances for multi-functionalization of the nanoparticles.

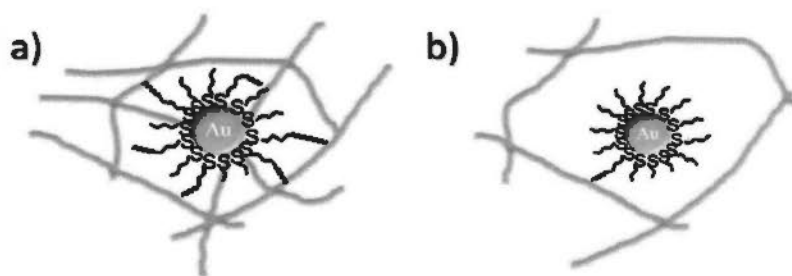
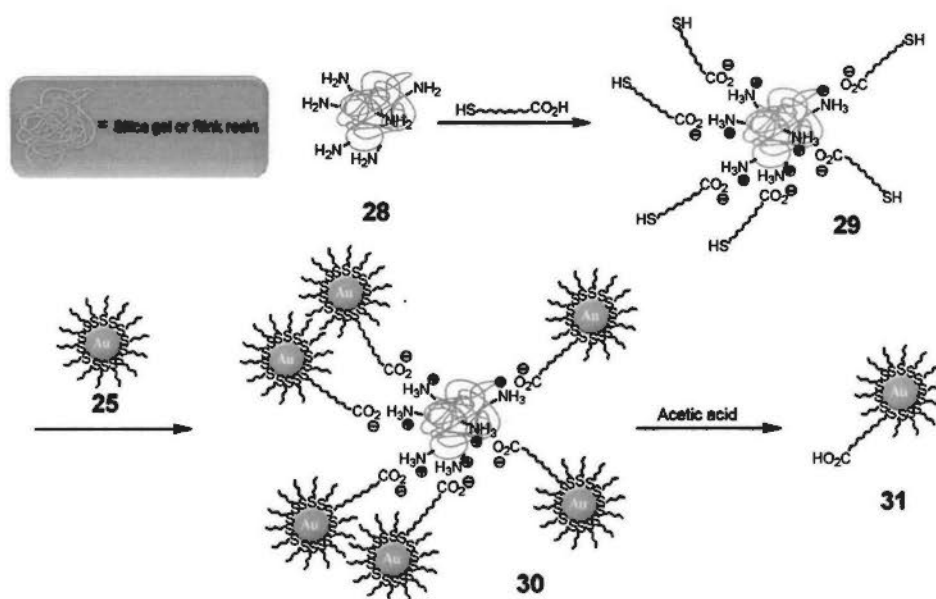


Figure 2-1. a) Multi-functionalized AuNPs will be obtained in a more swelled polymer; b) mono-functionalized AuNPs will be obtained in a more rigid polymer.^{25c}

2.1.2 Electrostatic solid-phase supported synthesis

Electrostatic solid-phase supported synthesis of mono-functionalized AuNPs has been reported in 2006.²⁶ Amino-functionalized silica gel and polystyrene Rink resin **28** (with amino functional groups) were used as the solid-phase support polymer (Scheme 10). The amino-functionalized silica gel has a low nitrogen content of 2.1 %. 11-Mercaptoundecanoic acid was added to the silica gel, so that proton transfer was facilitated by electrostatic interactions between the negatively charged carboxylates with the positive charged amino groups on the resin **29**. Then, 2.2 nm

n-butane-coated AuNPs **25** were added to undergo place exchange reaction. Finally, the mono-carboxylic acid-functionalized AuNPs can be obtained by the addition of acetic acid, followed by purification using a centrifugation and size exclusion chromatography. Similar protocol was found to be worked for the polystyrene Rink resin. The isolated yield was about 60–90 %.

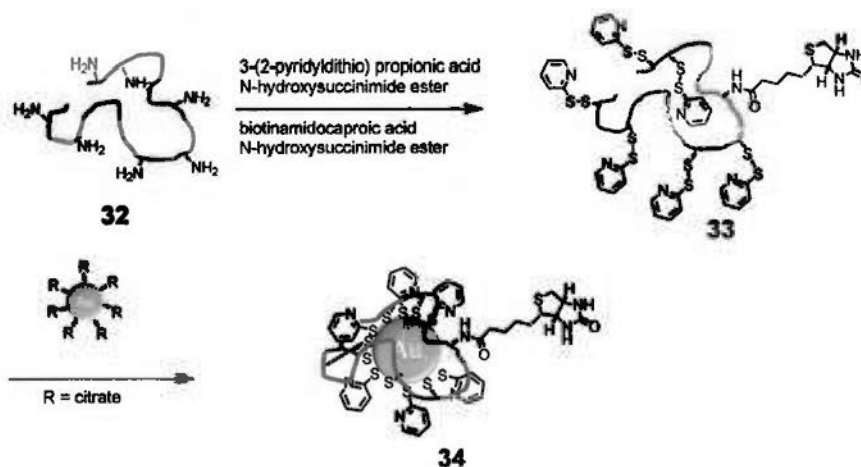


Scheme 10. The electrostatic solid-phase supported synthesis of mono-carboxylic acid-functionalized AuNPs.²⁶

2.1.3 Single polymer chain protection synthesis

There are two methods which utilize a single polymer chain protection to synthesize mono-functionalized AuNPs. They are the pre-organized-polymer method and the post-polymerization method. For the pre-organized-polymer method, a single polymer chain was functionalized with various functional groups before the self-assembly to the AuNPs. For the post-polymerization, the monomer-coated

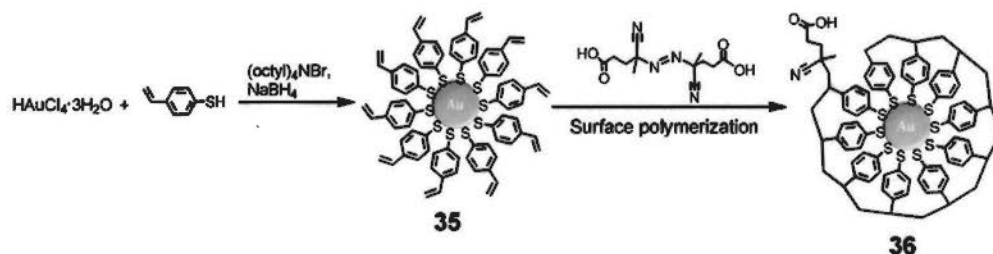
AuNPs underwent free radical polymerization and that the initiator was finally attached to the front of the polymer, so that a single functional group can be obtained.



Scheme 11. The single polymer chain protection synthesis of AuNPs. The polymer was modified by biotin unit before the attachment of polymer to AuNPs.^{27a}

The pre-organized-polymer method have been reported in 2004 (Scheme 11),^{27a} a 2000 kDa aminodextran polymer **32** was functionalized with pyridyldithio propionate (PDP) and biotin, through a coupling reaction with *N*-hydroxysuccinimide esters of 3-(2-pyridyldithio) propionic acid (SPDP) and biotinamidocaproic acid to give polymer **33**. The reaction conditions and concentrations are tuned so that only 1.05 dextran molecules were reacted with a 15 nm citrate-coated AuNP. The disulfide groups on the dextran polymer were then self-assembled on the AuNPs. It was found that each dextran molecule possesses 15 biotin units, 11987 non-functionalized glucose units, and 336 pyridine unit. Hence, the AuNPs **34** were regarded as monodextran-functionalized with various functional

groups.



Scheme 12. The single polymer chain protection synthesis of AuNPs. AuNPs were functionalized with monomers with vinyl groups, then the surface radical polymerization took place by the addition of initiator.^{27b}

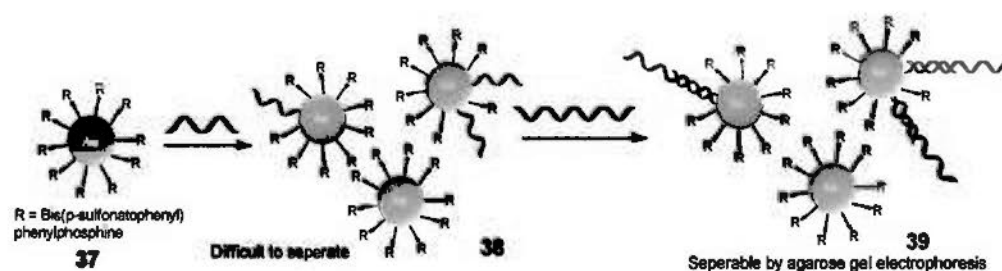
For the post-polymerization, it has been reported in 2007 utilizing the free radical polymerization of vinyl groups on the AuNPs **35** surface (Scheme 12).^{27b} AuNPs with 2–5 nm were functionalized with 4-vinylthiophenol. Then, the polymerization of vinyl groups was initiated by 4,4'-azobis(4-cyanopentanoic acid) at 80 °C, leaving a single carboxylic acid group on the surface of the AuNPs **36**. The free radical polymerization was stabilized by the presence of the cationic tetra-*n*-octylammonium bromide to prevent polymerizations between more than one nanoparticle, since it will incorporate into the ligand shell of the AuNPs and that the positively charged AuNPs repel each other. Moreover, the rate of the polymerization was a fast process compared to the decomposition rate of the initiator, so that it is unlikely to start polymerization on the same nanoparticle by two initiators.

2.1.4 Solution-phase synthesis followed by separation

A careful stoichiometric control of ligand ratio can produce a mixture of functionalized AuNPs. This mixture can be purified to obtain solely the

mono-functionalized AuNPs.^{24a,25b,26,28} Mono-functionalizations of small gold nanocluster with core diameter 0.8 nm and 1.4 nm were achieved by stoichiometric control of ligand ratio followed by purification of ion exchange chromatography.^{24a} There were only 7 phosphor ligands on the surface of 0.8 nm gold nanoclusters, while there were only 12 phosphor ligands on the surface of 1.4 nm gold nanoclusters. Hence, the stoichiometric control and purification were quite convenient as the number of ligands on the gold nanoclusters was small, while it became more difficult when the size of nanoparticles increases.

However, with the advancement in the purification technique developed in the recent years, the mono-functionalized AuNPs can be obtained by ions exchange chromatography, size exclusion chromatography and gel electrophoresis, etc, after the solution phase synthesis of the mixtures of the AuNPs. The separation process is easier for the size and a large difference in the overall charge between each oligo-AuNPs.



Scheme 13. Resolution of agarose gel electrophoresis can be increased by hybridization of 15 base pair DNA on AuNPs with 70 base pair DNA.^{28c}

Gel permeation chromatography^{25b,26} can be used to separate ~2 nm mono- and

multi-carboxylic acid-functionalized AuNPs synthesized by solid-phase support polymers. Agarose gel electrophoresis^{28a,b} was reported to be able to separate mono-, di- and tri-functionalized 5 nm and 20 nm AuNPs respectively with DNA of 40 and 70 base pairs. Mono-functionalized AuNPs with short DNA can only be purified by the incorporation of complementary long base pair DNA to the mono-functionalized AuNPs **39** (Scheme 13).^{28c} Anion exchange, high performance liquid chromatography (AE-HPLC)^{28a} was employed to separate 15 base-pair DNA mono-, di- and tri-functionalized 20 nm AuNPs with high resolution (Figure 2-2).

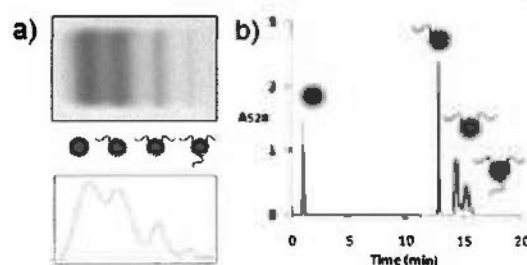
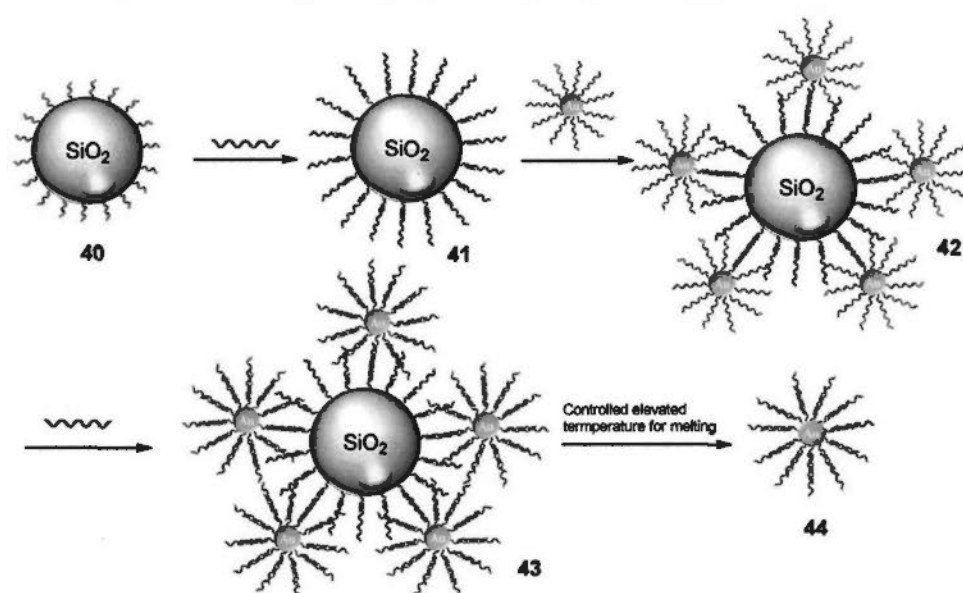


Figure 2-2. a) Agarose gel electrophoresis; b) AE-HPLC purification of 70-base polyT DNA which conjugated to 5 nm AuNP. The resolution of products was found to be better for AE-HPLC (obtained from Ref. 28a).

2.1.4 Miscellaneous methods

Mono-functionalization of AuNPs can also be achieved by utilizing bigger microparticles as the support surface for functionalization (Scheme 14).²⁹ Silica dioxide microparticles (400 nm) were modified by 7 base-pair DNA (**40**) which were then hybridized with 27 base pairs DNA to give **41**. Then, 13 nm AuNPs functionalized with 12 base-pair DNA, which was complementary to other end of the 27 base pairs DNA, were hybridized on the silica dioxide microparticles (**42**). After

that, the remaining DNA functional groups on AuNPs were hybridized by a complementary DNA (43). Finally, as the distances of the hybridized DNA from AuNPs to silica dioxide microparticles were different, they possess different melting points. The 7 base-pair DNA on silica dioxide microparticles melted before the melting of the 12 base pairs DNA on AuNPs. Hence, mono-DNA-functionalized AuNPs can be obtained by increasing the temperature carefully.



Scheme 14. The asymmetric functionalization of AuNPs with DNA by silica microparticles.²⁵

2.2 Synthesis of discretely di-functionalized AuNPs

The synthesis of di-functionalized AuNPs is also a challenge. A precise control of reaction conditions is required since only two of the functional groups on the AuNPs have to be replaced or reacted. DNA di-functionalized AuNPs were usually obtained as side products by purification through gel electrophoresis or AE-HPLC from the side reactions of place exchange reactions as mentioned in previous section. The direct synthesis of di-functionalized AuNPs is somewhat very difficult and only a literature was reported. Hetero-ligand-coated AuNPs with ripples and ordered structures reported³⁰ can undergo simple place exchange reaction to give the di-functionalized AuNPs.^{14b} AuNPs with ripple and ordered structure were synthesized from the *in situ* mixing of 1-nonanethiol and 4-methylbenzenethiol during synthesis. Owing to the nature of the two ligands (length and intermolecular forces), the AuNPs with ripples and ordered structure can be obtained by tuning the ratio of these two ligands. These ligands coated on the AuNPs were found to have the same tilt angles and directions, relative to the normal of surface so that the intermolecular forces (π - π interactions and Van der Waals' forces) were maximized. Therefore, there will be two singularities at the two opposite ends of the AuNPs for such alignments of ligands in spherical AuNPs (Figure 2-3). The two singularities were expected to be unstable for reactions since they have non-equilibrium tilt angle

and are not stabilized by the intermolecular interactions with neighbor ligands. Hence, a simple place exchange reaction on the two singularities can be undergone to obtain di-functionalized AuNPs in a short reaction time.

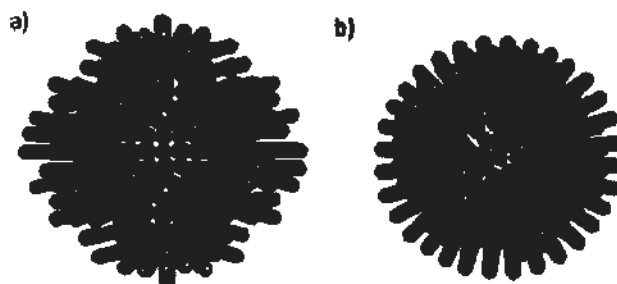
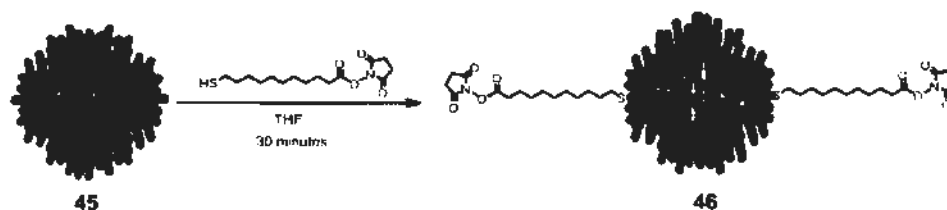


Figure 2-3. a) Side view; b) top view of the hetero-ligand-coated AuNPs with ripples and ordered structure. Two types of ligand are labeled with different color. Purple color: 1-nonanethiolate; green color: 4-methylbenzenethiolate.^{14b}

For instance, excess 11-mercaptopundecanoic acid *N*-hydroxysuccinimide ester was added to the binary ligand-coated AuNPs with ripples and ordered structure. Then, the reaction mixture was stirred for 30 minutes at room temperature (Scheme 15) and that the reaction was quenched by the addition of water to induce a precipitation which was filtered over a Sephadex column.

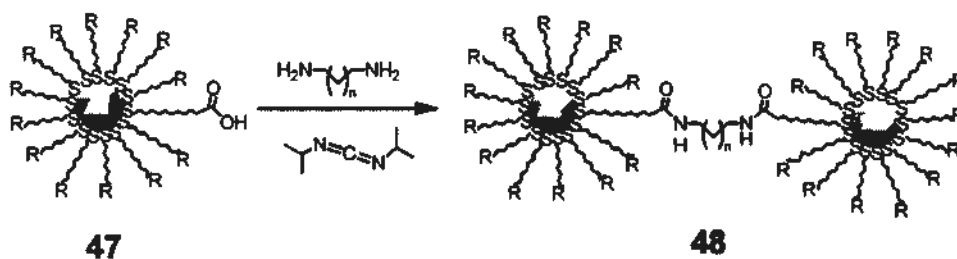


Scheme 15. The synthesis of di-functionalized AuNPs by simple place exchange reaction with 11-mercaptopundecanoic acid *N*-hydroxysuccinimide ester.^{14b}

2.3 Characterization methods of discretely functionalized AuNPs

Characterization of discretely functionalized AuNPs is somewhat difficult. FT-IR and UV/visible spectroscopies can only give characteristic peaks of functional groups or SPR band. While NMR can provide proton environments of the ligand shell, however, it was found that the distance of atoms from the gold core is an important factor which affects the broadening of the signals. Hence, it is difficult to compare the integration of the protons within the AuNPs.^{18a} XPS can provide elemental information, however, it has some limitations such as the relative sensitivity and signal-to-noise ratio. The most important limitation of the above methods is the quantitative study which can only assume that the size of the AuNPs is mono-dispersed.²⁶

Perhaps the most commonly used method to characterize discretely functionalized AuNPs is the formation of dimers by coupling reactions which can be observed by using transmission electron microscopy (Scheme 16).



Scheme 16. Coupling reaction of mono-carboxylic acid-functionalized AuNPs with diamine.

For instance, mono-carboxylic acid-functionalized AuNPs can couple with

ethylenediamine^{25a,26} or diaminoheptane^{25b,27b} by coupling agent such as 1,3-diisopropylcarbodiimide to give dimers of AuNPs which can be revealed in their TEM images (Figure 2-4).

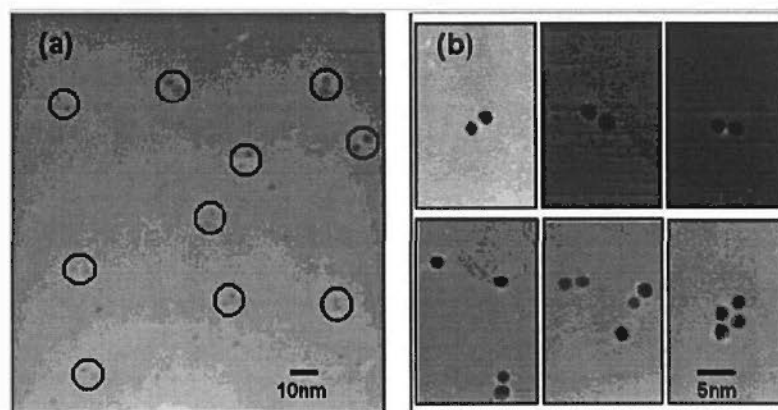
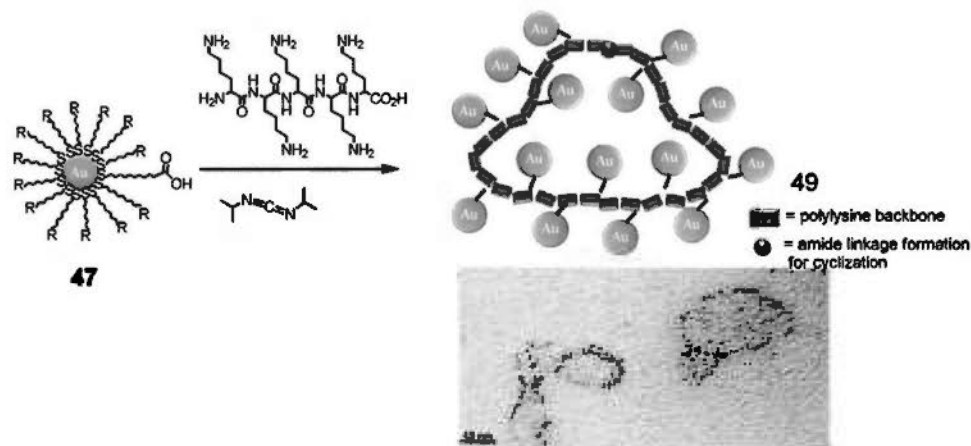


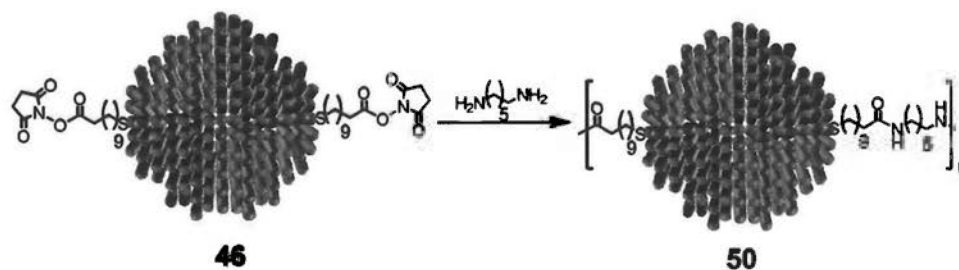
Figure 2-4. TEM images of AuNPs dimers after coupling reaction of mono-carboxylic acid-functionalized AuNPs with diamine. a) Images with lower magnification; b) images with higher magnification. (obtained from Ref. 25a)

Mono-carboxylic acid-functionalized AuNPs can also be coupled with polylysine (>30 kDa) to give a necklace structure (Scheme 17).³¹ The AuNPs reacted with the branching amine groups in the presence of 1,3-diisopropylcarbodiimide. The carboxylic acid and amine on the main chain backbone of lysine coupled together to form a necklace structure.



Scheme 17. The formation of necklace by the coupling reaction of mono-carboxylic acid-functionalized AuNPs and polylysine. TEM image obtained from Ref. 31.³¹

Di-functionalized AuNPs can also be characterized in TEM by the addition of 1,6-diaminohexane to form a polymer chain (Scheme 18).^{14b} The polymerization took place in a two-phase environment whereas the polymer precipitated in the interface of the two phases.



Scheme 18. The polymerization of di-functionalized AuNPs.^{14b}

The characterization utilizing formation of dimers or polymer in TEM images may not give a 100 % quantification of the mono-functionalized or di-functionalized AuNPs. The percentage of dimer over monomer can be estimated from a TEM image over a large area by counting the average number of particles.

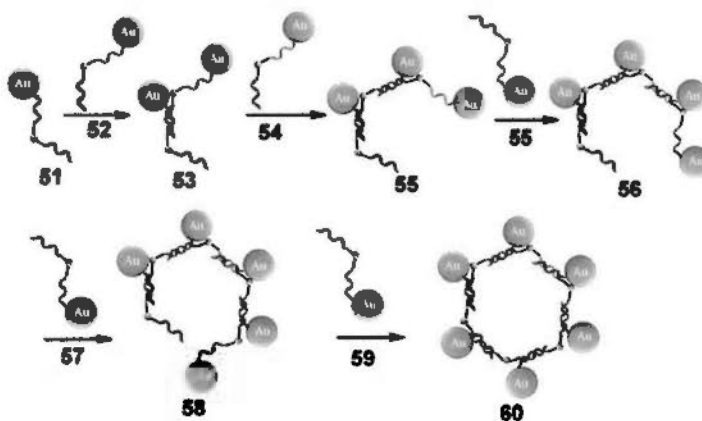
2.4 Potential applications of the discretely functionalized AuNPs

Since discretely functionalized AuNPs contain a known number of specific ligand(s) or functional group(s) for molecular recognition or further derivatization. Quantitative measurements in sensing applications should be able to improve and open the way to quantitative, single molecule detection.³²

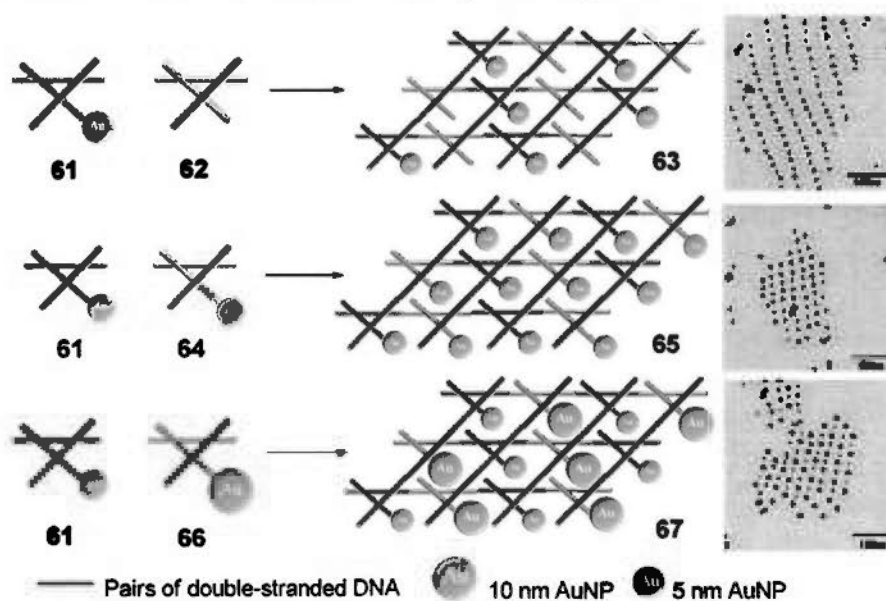
Furthermore, AuNP dimers,^{25a,b,26,27b,33a} trimers³³ and straight chain polymers^{14b,31} can be obtained by a rational linkage of discretely functionalized AuNPs as mentioned before, while they are difficult to be obtained using randomly functionalizing AuNPs due to bulkiness and multiple reaction sites on AuNPs. Such dimers, trimers or polymers may have potential applications in single molecule scattering spectroscopies,³⁴ and surface enhanced Raman spectroscopy (SERS)³⁵ with ultra-sensitivity for single molecule detection.

Moreover, discretely functionalized AuNPs already have been used in construction of special architectures, utilizing groups of mono-DNA-functionalized AuNPs.^{28b,c,36a,b} Special structures such as DNA-hexagon with one AuNP on each edge (Scheme 19),^{36a} DNA-triangle encapsulating one AuNP in each triangle (Scheme 20),^{36b} were reported. These scaffolds have potential biological applications in functionalizing with biological macromolecules. Moreover, such ordered arrays of AuNPs may be useful in nanoelectronic field as the AuNPs can act as single electron

transistors, from which AuNPs have to be linked in complicated circuit and logic gates.^{24a,37}



Scheme 19. The formation of DNA hexagon utilizing mono-functionalized AuNPs.^{35a}



Scheme 20. Formation of multiple DNA triangles encapsulating one AuNP in each triangle, TEM images obtained from Ref. 28b.

2.5 Aims and scopes of the thesis project

The primary aim of the thesis project is to synthesize novel discretely monoamine-functionalized AuNPs using supramolecular (crown ether–ammonium ligand) interactions and solid-phase supported synthesis with stepwise characterization by spectroscopies. This novel method results in improved yields and better control of ON/OFF switching by the formation of pseudorotaxane AuNPs for place exchange reactions. This method is better than the covalent and electrostatic solid-phase supported synthesis of mono-functionalized AuNPs.

Another aim of the project is to purify the discretely mono-functionalized AuNPs using crown ether-coated magnetic iron oxide nanoparticles. Such purification utilizing magnetic nanoparticles is facile, fast and efficient, compared to the traditional chromatographic separation and electrophoresis processes.

Discretely mono-functionalized AuNPs are expected to possess serendipitous properties compared to the randomly functionalized AuNPs. Our aim is to explore the differences of surface self-assembly between the two types of nanoparticles.

Another purpose of the project is to develop a method of simultaneous purification and surface plasmon resonance characterization of mono-functionalized AuNPs, which can be achieved by SPR detection using a crown ether-coated SAM of gold thin film in the microfluidic device. The difference behavior between randomly

functionalized AuNPs and mono-functionalized AuNPs in ON/OFF switching of pseudorotaxane can be observed by SPR changes. The mono-functionalized AuNPs can be purified and characterized using such method and device settings.

Finally, the mono-functionalized AuNPs are applied as sensors for short base pair DNAs. Melting curves of the DNA–AuNP system in organic solvents are studied. It has also been the first reported system for DNA sensors of AuNPs in organic solvents utilizing short base pair DNA as target. The DNA–AuNP system utilizing the randomly functionalized AuNPs will also be studied in comparison with the mono-functionalized AuNPs. The chosen target DNA was the pathogenicity island of vancomycin-resistant *Enterococcus faecalis*, hence, such application is potentially applicable in quantitative biosensing at extremely low concentrations.

Chapter Three – Synthesis and Purification of Discretely Mono-Functionalized AuNPs

3.1 General Considerations

In this chapter, supramolecular motif-assisted, solid-phase-supported synthesis of novel discretely functionalized AuNPs and their magnetic purification are discussed. Solid-phase-supported synthesis is convenient and efficient because the solid resin can be easily filtered off which reduces the effort in separation of starting materials. Also, a resin with a specific functional group density provides specific reactive spaces for mono-functionalization of AuNPs, known as the site isolation effect as described in chapter 2. Therefore, the solid-phase-supported synthesis provides several advantages over solution phase synthesis, mainly to reduce the formation of larger portions of randomly functionalized AuNPs. Moreover, different from previous reports,²⁵ the synthesis of mono-functionalized AuNPs involves harsh conditions in the form of covalent bond formation and cleavage which reduce the yield and purity of the mono-functionalized AuNPs.

Supramolecular chemistry³⁸ involves molecular recognition which can be used to efficiently construct novel functional molecules, such as molecular switches, molecular motors,^{39a} artificial molecular muscles,^{39b} and molecular elevators, etc.^{39c} Moreover, the applications of supramolecular chemistry to the development of

organic–inorganic hybrid materials with improved functionalities have been reported in recent years.^{1b} For instance, heterosupramolecular approaches provides the enhancement of recognition and sensing on material surface, the building of reversible nanometer-sized networks and 3-D architectures and the incorporation of biometric and gated chemistry in hybrid nanomaterials.^{39d} The combination of supramolecular chemistry and inorganic nanomaterials can lead to fine-tuning of materials and open up future, novel applications. Therefore, it is expected that the use of supramolecular-based, solid-phase support has several advantages such as ON/OFF switching of supramolecular moieties in mild condition which results in better yield and higher endurance towards stability of AuNPs during the synthesis.

Though an electrostatic-based synthesis of discretely functionalized AuNPs has been reported,²⁶ the system only comprises electrostatic interactions that is single directional and relatively weak in interacting with the resin. Hence, the additional ligands for place exchange reaction would be inevitably detached and extremely sensitive to the solvent, concentration and temperature. It will lead to the formation of a higher portion of randomly functionalized AuNPs as in solution phase synthesis.

Therefore, dibenzo[24]crown-8-modified (DB24C8-modified) solid-phase support is chosen because the crown ether–ammonium ligand pseudorotaxane formation comprises multiple hydrogen bonds, ion-dipole interactions and π - π

interactions. Multivalent assemblies between the molecular recognition motifs to form pseudorotaxane are feasible *via* a self-sorting process. These interactions reduce the chances of accidental release of the ligands which is more stable when compared to the electrostatic based system. While the ligands can be released easily by addition of base to the system, such system possesses a better control of ON/OFF switching of the pseudorotaxane which results in improved yield and purity of the as-synthesized mono-functionalized AuNPs.

The mono-functionalized AuNPs obtained can be easily purified by magnetic separation using DB24C8-coated magnetic iron oxide nanoparticles. Magnetic nanoparticles are used since the products can be separated using magnetic separation, which is facile and efficient. Again, the attachment and detachment of the AuNPs on magnetic nanoparticles can be achieved by adding acid/base to the supramolecular system. All these advantages overwhelm the use of traditional, complicated, expensive and time-consuming chromatographic methods to purify the mono-functionalized AuNPs.

Finally, the solid-phase support resin and magnetic nanoparticles are recyclable and reusable, so that they can be versatile tools for synthesis and purification of this type of discretely functionalized nanoparticles.

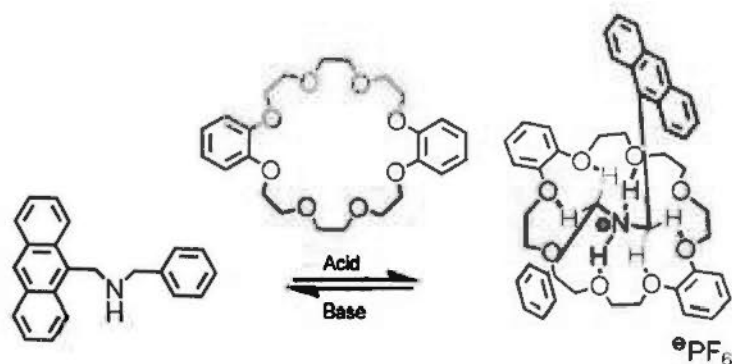
3.2 Molecular recognition between crown ether and ammonium salt

3.2.1 The origin of recognition

The molecular recognition between crown ether and ammonium ligands has been well documented.^{39e-i} DB24C8 interacts with ammonium ligands by various supramolecular interactions (Scheme 21). For instance, the supramolecular species possesses multiple and strong $[N^+-H\cdots O]$ and $[N^+C-H\cdots O]$ hydrogen bonds in several directions. Moreover, there are π - π interactions between the aromatic moieties in crown ether and ammonium ligands. Furthermore, there are ion-dipole interactions between ammonium cation and the neutral crown ether.

The ammonium ligands will slip into the DB24C8 ring to form a pseudorotaxane which can be reversibly disassociated and associated by addition of base or acid as stimuli, respectively. By increasing the polarity of the solvent system, at elevated temperature, or dilution, the pseudorotaxane can be dissociated.

The reversible assembly and disassembly of pseudorotaxane can apply in several applications with control-release properties, such as drug delivery or nanovalves.^{39j,k} In contrast, a rotaxane with bulky stoppers cannot be dissociated into its starting components.



Scheme 21. Reversible assembly and disassembly of pseudorotaxane by adding acid/base to the system. Two types of hydrogen bonds within the pseudorotaxane were shown.^{39e}

3.2.2 Formation of pseudorotaxane and binding constant measurement

The formation of pseudorotaxane can be confirmed by 2-D NOESY NMR spectroscopy, while the binding constant between the self-assembly of **68** (DB24C8-CO₂Me) with an ammonium ligand **69**·HPF₆ can be measured by ¹H-NMR spectroscopy.

In order to determine the binding constant and pseudorotaxane formation in the DB24C8-modified Wang's resin **76** with the ammonium ligand **69** for place exchange reaction in 6:1 dichloromethane to acetonitrile solvent system, a set of control pseudorotaxane was employed. **68** (DB24C8-CO₂Me) and **69**·HPF₆ were chosen for study. **68** was used instead of **70**^{41a-c} (DB24C8-CO₂H), since **68** and **76** both have an ester bond linkage in crown ether side arm and that carboxylic acid group may interfere the hydrogen bonds of the system. **68** and **69** were expected to form pseudorotaxane **68** ⊃ **69**·HPF₆ in 1:1 ratio as reported in literatures.^{39f-i}

Since the formation of pseudorotaxane is equilibrium, there are some free

crown ether and ammonium ligands left unbounded in the solution, while there is some crown ether and ammonium ligands bounded to each other to form pseudorotaxane. Hence, the integration ratio of bounded and unbounded systems can be used to calculate the binding constant for slowly exchanged complex.

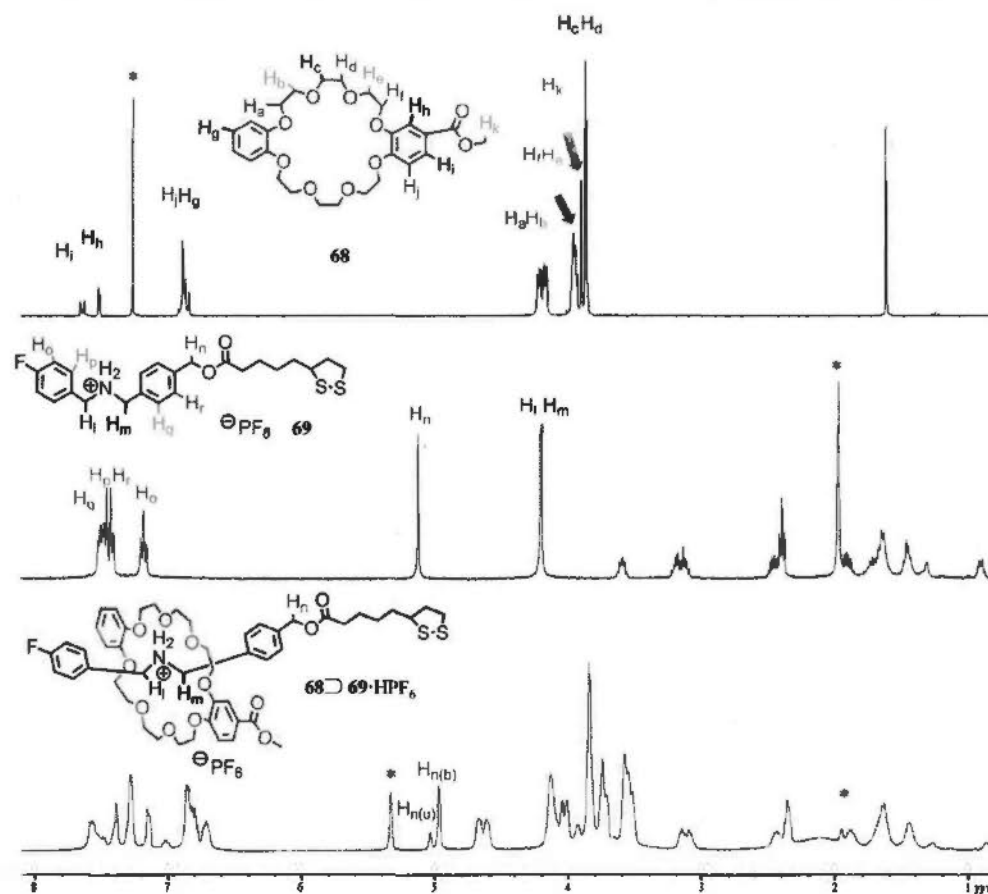


Figure 3-1. ^1H NMR spectra of DB24C8- CO_2Me **68**; ammonium ligand **69**; and the pseudorotaxane **68** \supset **69**· HPF_6 . (*) represents the residual solvent signal, (u) represents unbounded ligand and (b) represents bounded ligand.

The binding constant (K) of an equimolar ratio of components to form a pseudorotaxane can be determined by ^1H NMR (Figure 3-1) using the following equations:³⁸

$$[C] = \frac{n}{n+m} [H]_0 \quad \dots\dots\dots(1)$$

$$K = \frac{[C]}{([H]_0 - [C])^2} \quad \dots\dots\dots(2)$$

where $[H]_0$ represents the initial host concentration; $[C]$ represents the complex concentration in equilibrium; m and n represent the integration of the peak for complex and host respectively.

The initial concentration of host and guest are equal to 20.29 mM. By substituting the initial the concentration of host as well as the integration ratio of complex and host into equation (1), the equilibrium concentration of complex is calculated as 15.35 mM. Then, the binding constant is calculated using the equation (2), as 652 M^{-1} .⁴⁰

2-D NOESY NMR spectroscopy is capable to determine the proton-proton correlation through space. If the ammonium ligand slips into the crown ether, there will be correlation signals in both sides of spectra for hydrogen atoms in close proximity interacting with each other through space.

As shown in the 2-D NOESY NMR spectrum (Figure 3-2) of the pseudorotaxane **68** \supset **69**·HPF₆, there are proton-proton correlations through space, which indicates the formation of pseudorotaxane **68** \supset **69**·HPF₆. Cross peaks are observed for benzyl proton (H_n) with protons in ethylene glycol chain (H_{a-f}). Benzyl protons (H_i) and (H_m) are also coupled with ethylene glycol chain (H_{a-f}). The aromatic protons of DB24C8-CO₂Me **68** and that of ammonium ligand **69**·HPF₆ are also coupled through space. Meanwhile, it is worth to note that the chemical shift of

benzyl proton (H_n) of the ammonium thread is significantly different upon the formation of the pseudorotaxane from which both peaks coexist. On the other hand, the benzyl protons (H_i) and (H_m) should have coupled with ethylene glycol chain (H_{a-f}) to give two sets of peaks, however, the chemical shift of H_i and H_m in the pseudorotaxane overlapped with (H_i) and (H_m) of the unbounded state.

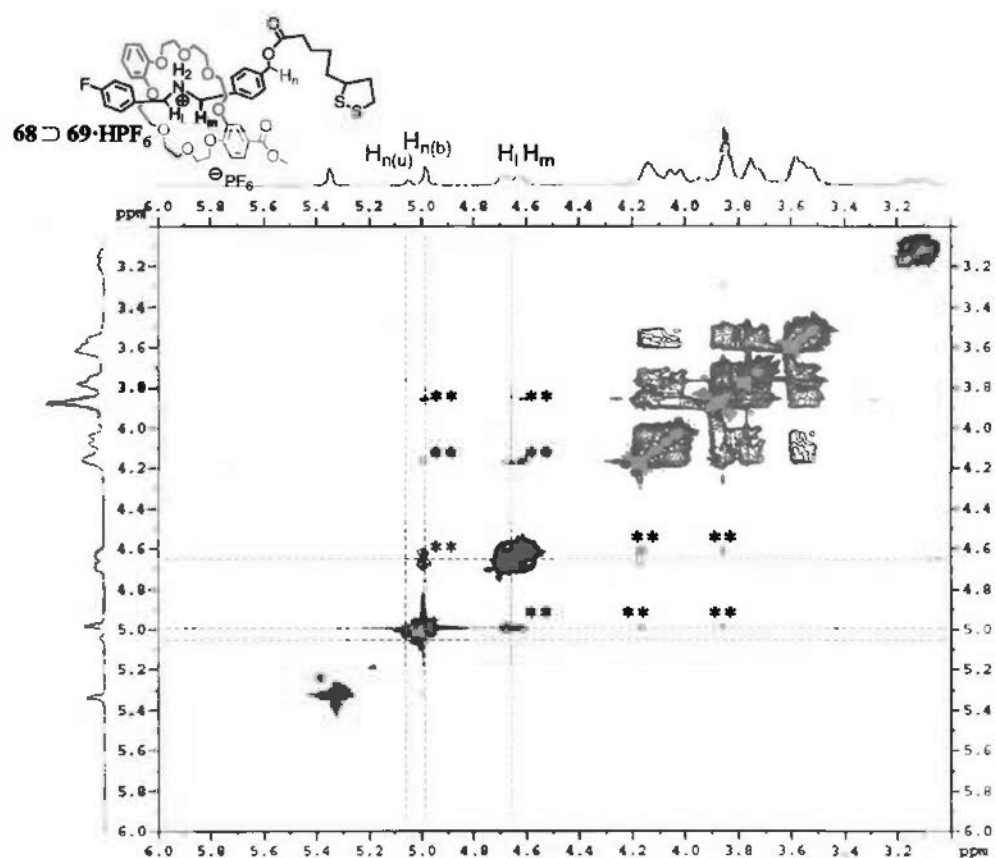


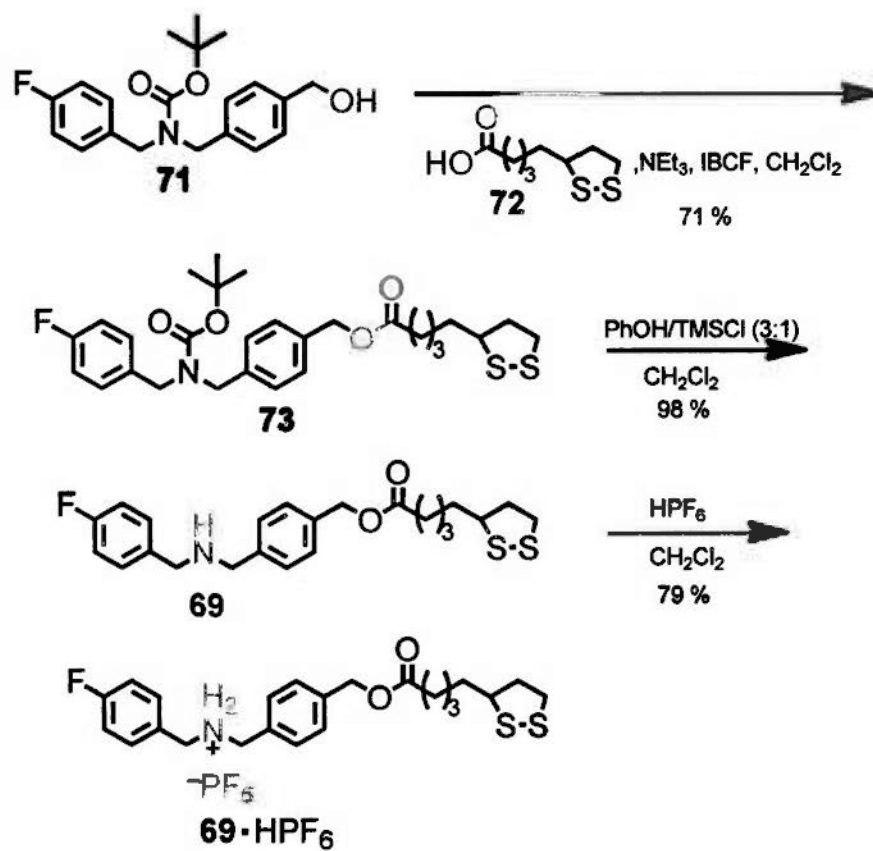
Figure 3-2. 2-D NOESY ^1H NMR spectrum of the formation of pseudorotaxane $68 \rightleftharpoons 69 \cdot \text{HPF}_6$ from 68 and $69 \cdot \text{HPF}_6$. Red (*) represents solvent peak, black (**) represents correlation peaks.

3.3 Synthesis and characterization of supramolecular precursors

3.3.1 Preparation of ammonium ligand

The ammonium ligand **69**·HPF₆ was chosen to functionalize AuNPs because it possesses two aromatic groups that are relatively not bulky, which enable the formation of pseudorotaxane by a threading assembly with multiple supramolecular interactions. Moreover, in contrast to thiols, lipoic ester moiety was chosen because it does not form higher-order disulfide dimers or polymers during the synthesis in the presence of small amount of oxygen. The length of lipoic ester moiety is longer than *n*-butanethiolate on the gold surface, so that the disulfide moiety will be place-exchanged with a *n*-butanethiolate without (1) the blocking by bulkiness of side ligands, and (2) jeopardizing the pseudorotaxane structure.

The synthetic scheme is shown in Scheme 22. Lipoic acid **72** was first reacted with isobutylchloroformate (IBCF) to give mixed anhydride of lipoic carbonate, then it was reacted with the alcohol **71**^{39j} to form a lipoic ester **73** in 71 % yield. Deprotection of **73** by phenol/trimethylchlorosilane (PhOH/TMSCl) with 3:1 ratio in dichloromethane affords the amine **69** in 98 % yield. Finally, the amine was protonated by the addition of hexafluorophosphoric acid to give the ammonium thread **69**·HPF₆.

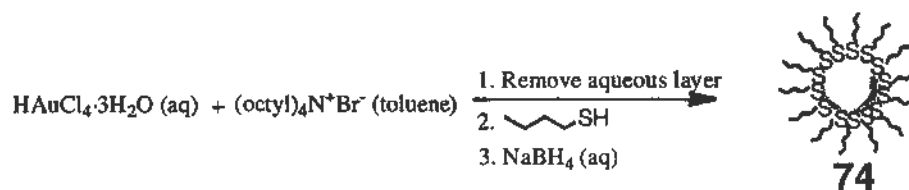


Scheme 22. The synthetic route of ammonium thread $69 \cdot \text{HPF}_6$, which is the precursor of the pseudorotaxane $68 \supset 69 \cdot \text{HPF}_6$.

3.4 Synthesis, characterization and theoretical calculation of *n*-butanethiolate-coated AuNPs

n-Butanethiolate coated AuNP was chosen as the precursor material to synthesize the mono-functionalized AuNPs, the length of *n*-butanethiolate is shorter than the commonly used dodecanethiolate, so that it is less bulky for easier place exchange reaction within the solid-phase supported synthesis. Dodecanethiolate-coated AuNPs should increase the chance of multi-functionalization due to its bulkiness and long pathway required for entry of thiol to be exchanged. The synthesis of *n*-butanethiolate coated AuNPs can be achieved simply by using a slightly modified Brust-Schiffrin method (Scheme 23).^{25b,c,26}

To synthesize the AuNPs, tetrachloroaurate, which was dissolved in aqueous solution, was transferred to toluene using tetraoctylammonium bromide as a phase transfer reagent. The organic layer was collected and then stirred vigorously with the addition of *n*-butanethiol, followed by a quick addition of sodium borohydride aqueous solution, giving the *n*-butanethiolate-coated AuNPs. The obtained organic layer was evaporated at reduced pressure and room temperature. Excess ethanol was added to the AuNPs with stirring so that all AuNPs were precipitated. The solution was then stored at 4 °C overnight and filtered with a membrane with a 0.25 μm pore size. The AuNPs were washed with cold ethanol several times to remove excess *n*-butanethiol. The AuNPs 74 were collected and dried in vacuum.



Scheme 23. The synthetic scheme of *n*-butanethiolate coated AuNPs 74.

n-Butanethiolate coated AuNPs 74 were characterized by TEM, FT-IR and TGA.⁴² TEM images showed that the size of nanoparticles was about 2–2.5 nm (Figure 3-3). FT-IR spectrum of the AuNPs showed that there were absorption peaks of alkane C–H stretching, corresponding to the *n*-butane groups in 2870, 2922, 2954 cm^{-1} and terminal CH_3 symmetrical deformation at 1376 cm^{-1} .

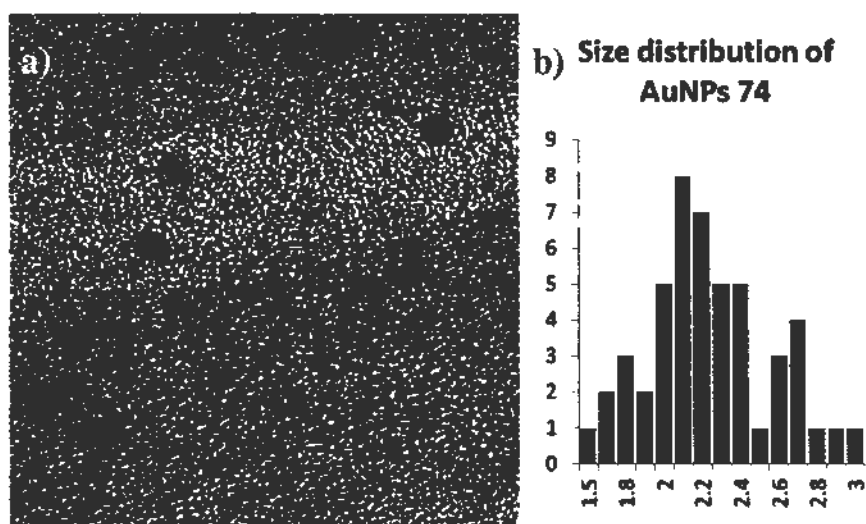


Figure 3-3. a) The TEM image of *n*-butane-thiolate coated AuNPs 74.; b) the size distribution of the AuNPs 74 by counting 50 nanoparticles in TEM images.

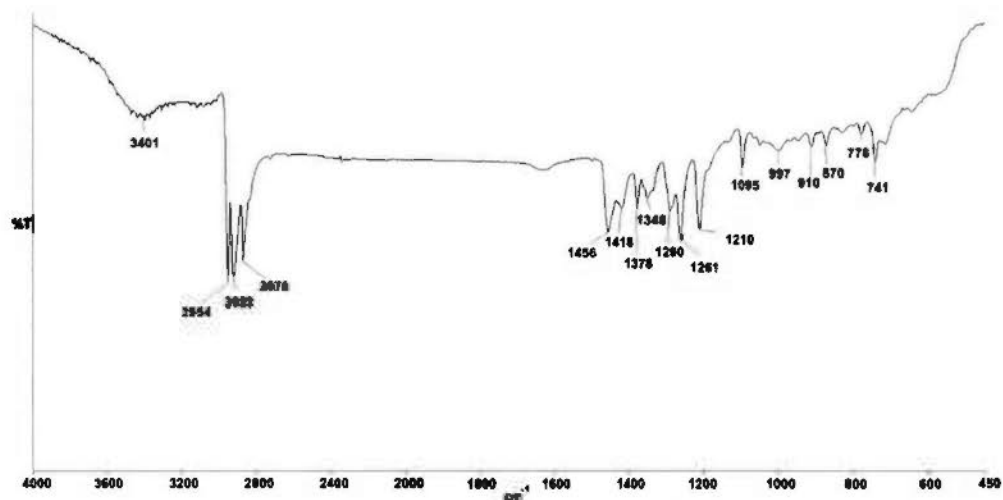


Figure 3-4. FT-IR spectrum of *n*-butanethiolate coated AuNPs 74.

TGA result (Figure 3-5) shows that there was about 11.05 % weight loss from 136.5–198.1 °C, such loss referred to the decomposition of *n*-butanethiolate ligands.

There was more-or-less no further weight loss above 200 °C.

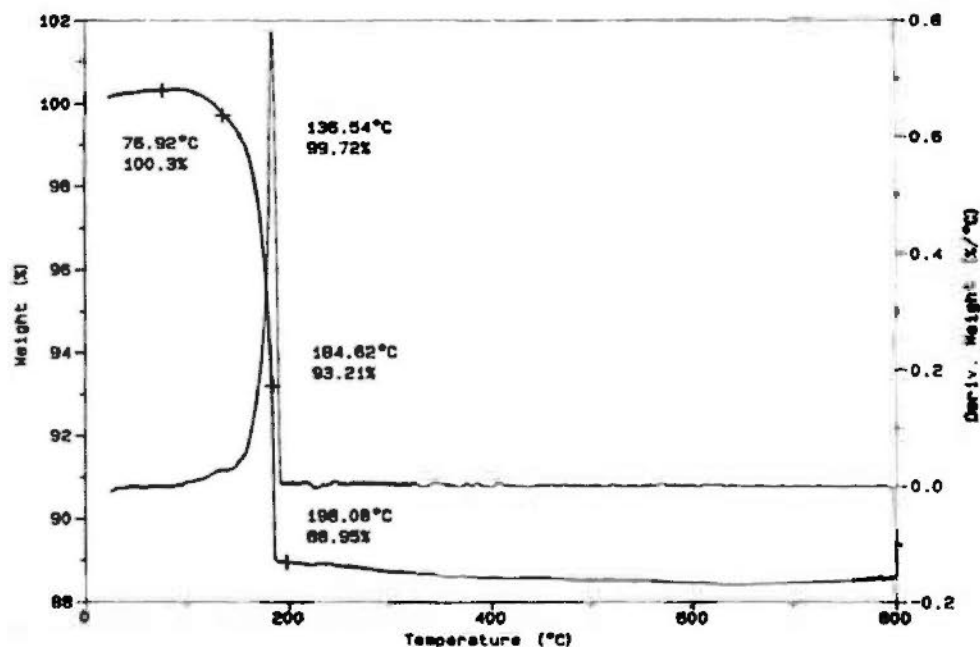


Figure 3-5. TGA result of *n*-butanethiolate coated AuNPs 74.

The percentage of organic matters in the AuNPs obtained in TGA results can be used to estimate the size of AuNPs, number of ligands on the nanoparticles and the cluster size of the gold core (Table 3-1). The calculations based on modeling of the dodecanethiolate AuNPs^{7f} were modified to render for *n*-butanethiolate coated AuNPs 74. Noticeably, there are several assumptions for the calculations. First, all AuNPs are completely monodispersed. Second, all AuNPs should possess the same amount of organic matters.

Table 3-1. Theoretical calculation of properties of *n*-butanethiolate coated AuNPs 74.

No. of Au Atoms (Shape)	R_{core} nm	No. of surface atoms	Surface area, nm ²	Calculated TGA %organic	No. of chains	R_{total} nm
79 (TO ⁺)	0.7	60	8.3	17.88	38	1.2
116 (TO ⁺)	0.7	78	11.36	17.14	53	1.2
140 (TO ⁺)	0.8	96	11.43	14.63	53	1.3
201 (TO)	0.9	128	15.22	13.79	71	1.4
225 (TO ⁺)	1.0	140	15.19	12.5	71	1.5
309 (CO)	1.1	162	19.64	11.88	92	1.6
314 (TO ⁺)	1.0	174	19.46	11.6	91	1.6
459 (TO ⁺)	1.2	234	24.34	10.11	114	1.7
586 (TO)	1.2	272	28.94	9.45	135	1.7
807 (TO ⁺)	1.4	348	34.86	8.38	163	1.9
976 (TO)	1.5	390	40.02	7.98	187	2.0
1289 (TO)	1.6	482	47.22	7.2	221	2.1
2406 (TO)	2.0	752	69.86	5.78	326	2.5
2951 (TO ⁺)	2.2	876	79.44	5.39	371	2.7
4033 (TO)	2.4	1082	97	4.84	453	2.9
4794 (TO ⁺)	2.6	1230	108.3	4.56	506	3.1
6266 (TO)	2.8	1472	128.7	4.16	601	3.3

CO = cuboctahedron; TO = ideal truncoctahedron (all sides equal); TO⁺ = truncoctahedron in which ($0 < n - m \leq 4$), where *n* is the number of atoms between (111) facets and *m* is the number of atoms between (111) and (100) facets; TO⁻ = truncoctahedron in which ($-4 \leq n - m < 0$, $m > 1$).

Surface area, number of surface atoms, number of chains on the surface of nanoparticles and radius of core are intrinsic properties due to the shape and number of atoms of gold in the gold nanoclusters. For instance, there are six 5 * 5 square

faces and eight equilateral triangular faces having edges of five gold atoms in the 309 cuboctahedron gold nanoclusters. Hence, the surface area should be $6 [(5 * 0.288)^2] + 8 [0.5 * (5 * 0.288)^2 \sin 60^\circ] = 19.64 \text{ nm}^2$. Note that the diameter of one gold atom is 0.288 nm and the first term in surface area calculation is from the square faces whereas the second term is from the triangular faces. The number of alkanethiolate ligand chains can be determined by the surface area of AuNPs divided by the surface area footprint of alkanethiolate 0.214 nm^2 .⁴³ Then, the TGA percentage of organic matters can be calculated since the molecular weight of ligand, the number of ligand chains and the number of gold atoms in nanoclusters are known. Hence, the following equation can be used to calculate the TGA percentage of organic matters:

$$\text{Calculated \% organic matter} = \frac{M_w(\text{ligand}) * \text{No. of ligand chain}}{M_w(\text{ligand}) * \text{No. of ligand chain} + M_w(\text{gold}) * \text{No. of gold atoms}} \dots (3)$$

where M_w represents the molecular weight of the respective substrates.

The experimental TGA percentage of organic matters was found to be about 11.1 %, which is closer to calculated 11.6 % organic matters in 314 gold nanoclusters. From Table 3-1, the theoretical core size of the AuNPs is 2.0 nm, the number of surface atoms is 174 and the number of ligand chain was about 91. All these properties of the AuNPs are important for applications utilizing AuNPs. Note that the TGA data can only provide its average composition since the nanoparticles are not completely mono-dispersed.

3.5 Synthesis of discretely mono-functionalized AuNPs and characterization

3.5.1 *Solid-phase support polymer and site isolation effect*

Polystyrene Wang resin 75 (PS Wang resin, poly(4-(4-vinylbenzyloxy)benzyl alcohol with hydroxyl groups density 1.0–1.5 mmol/g) was used as the solid-phase support polymer and it was commonly used in solid-phase peptide chemistry.^{44a} The hydroxyl groups resin was used because it can be coupled with carboxylic acid to form ester linkage without side reactions.

PS Wang resin can be swelled and dispersed in various solvents, however, the extent of the swelling differs in different solvents. The resin should be completely swelled before solid-phase reaction take place otherwise it will result in poor accessibility of reaction sites with slow reaction rates.^{44b} A good solvent should give a swelling volume of greater than 5-fold, thereby allowing better reaction yield and rate.^{44b}

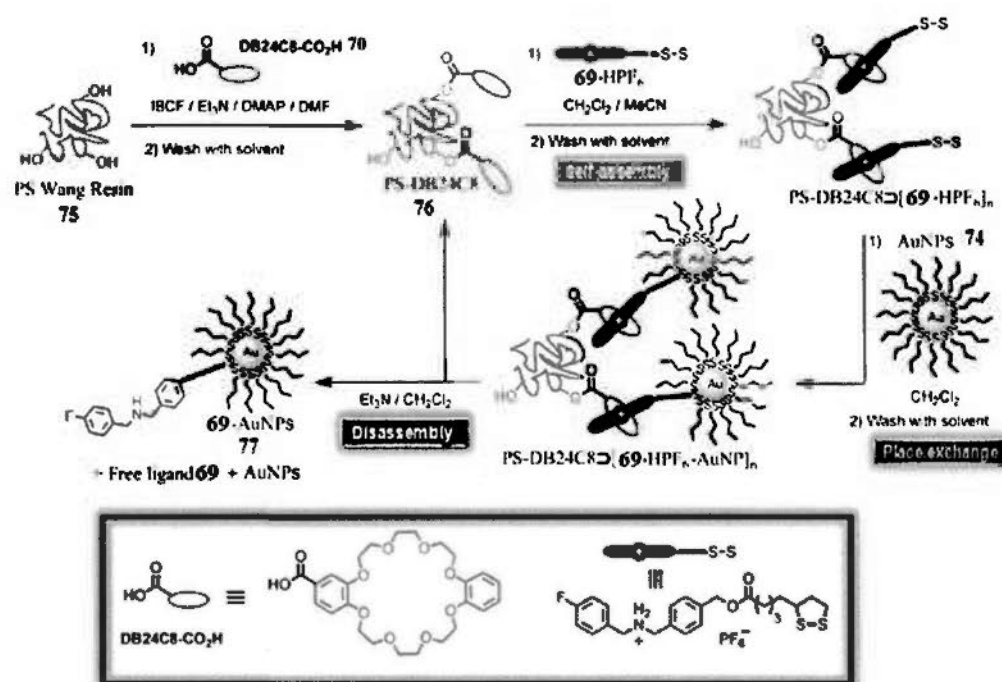
PS Wang resin 75 with particle size of 100–200 mesh and a hydroxyl group density of 1.0–1.5 mmol/g has a rough hydroxyl density of 1.05 g/cm³.^{44c} This resin swells in dichloromethane and expand 5–10 times of its original volume. We assume 10 times of expansion occurred at 40 °C.^{25b,42} Thus, there is approximately one hydroxyl group per 12.7 nm³ resin in dichloromethane solution. Hence, each hydroxyl groups are sufficiently distant from each other in terms of space and

volume. This site isolation effect allows one 2 nm AuNP reacting with one reactive functional group of the resin.

3.5.2 Synthetic route of mono-functionalized AuNPs

The general scheme for synthesizing the mono-functionalized AuNPs is shown in

Scheme 24.⁴²



Scheme 24. Synthetic route of mono-functionalized AuNPs 77.

Briefly, DB24C8-CO₂H 70^{41a-c} was treated with isobutylchloroformate (IBCF) to form anhydride in DMF *in situ* prior to the addition of PS Wang resin 75 to give the DB24C8-decorated resin 76 (PS-DB24C8) in 77 % yield. Then, 76 was swelled in a CH₂Cl₂/MeCN (6:1) mixture, dibenzylamine-disulfide ligand 69-HPF₆ was added to self-assemble⁴⁵ with the crown ether moiety of 76 to give PS-DB24C8-(69-HPF₆)_n.

[69·HPF₆]_n. Then, a slightly excess of AuNPs (AuNPs with average core size of 2 nm, 74) was added to the poly(pseudorotaxane) structure PS-DB24C8 ⊃ [69·HPF₆]_n, the disulfide in 69 on the resin will place-exchange with butanethiolate, so that the AuNPs will be immobilized to afford the PS-DB24C8 ⊃ [69·HPF₆·AuNP]_n. The crown ether moieties are distant from each other by site isolation effect, each self-assembled disulfide ligand most likely reacted with only one AuNP. Finally, PS-DB24C8 ⊃ [69·HPF₆·AuNP]_n was incubated with triethylamine solution in dichloromethane to deprotonate of all ammonium ions into amines. Hence, the crown ether lost its hydrogen-bonded binding affinity towards the amine and the AuNPs 77 (69·AuNP) was separated out from the solid resin. The solution isolated after the deprotonation step not only contained AuNPs 77 but also might contain unreacted, physisorbed AuNPs 74, the unreacted amine ligand 69 and the multi-functionalized AuNPs (69_n-AuNP). The mixture was then vacuum dried and washed by cold ethanol to remove the unreacted amine ligand 69, and then it was subjected to an effective and efficient purification by magnetic nanoparticles.

3.5.3 Stepwise characterization of the synthesis

In the first step of reaction, i.e. the coupling reaction of DB24C8-CO₂H 70 with the PS Wang resin 75 to give 76 (PS-DB24C8), the yield of the reaction was determined by ¹H NMR spectroscopy following the below procedure.

76 (PS-DB24C8) was filtered after the reaction and washed with dichloromethane several times. Then, a known amount (5.4 μL) of nitromethane was added to the filtrate as an internal standard, so that ^1H NMR can be used to determine the yield of reaction.

The yield was simply determined using the integration ratio of the methyl-protons in nitromethane and the benzene proton as shown in Figure 3-6. The NMR signal at δ 4.31 refers to the three protons of CH_3NO_2 with integration of 100.0000, the peak at δ 7.71–7.73 refers one aromatic proton H_a , with an integration of 117.2578. By calculating the ratio of integration to the mole ratio of the standard to **70** with the correction of number of protons involved, the amount of **70** (DB24C8- CO_2H) in the filtrate was found to be 0.3485 mmol. Therefore, the yield of the reaction was found to be 77 %.

The site isolation effect will become stronger after the coupling reactions, hence, the average space for one DB24C8 crown ether should become 13.6 nm^3 in the resin. Hence, the site isolation effect allows one 2 nm AuNPs reacting with one reactive functional group in the resin.

Interestingly, the reaction was found to be unsuccessful when the solvent was changed to dichloromethane instead of DMF. It was found that no ester bond formed (FT-IR) and 100 % of **70** (NMR) was recovered. It may be attributed to the strong

hydrogen bondings between hydroxyl groups within the resin in dichloromethane, which reduce the rate of reaction and site accessibility.

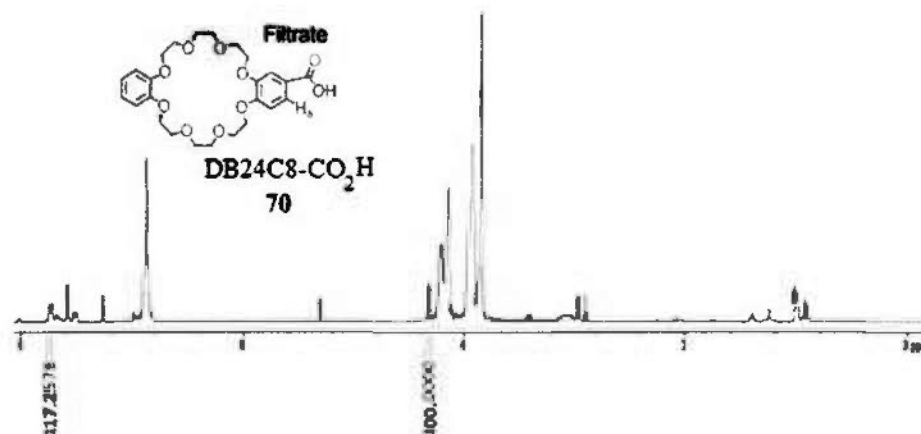


Figure 3-6. ¹H NMR spectrum of the filtrate from the coupling reaction of 70 with PS Wang resin 84. (Number of scan = 16)

The whole synthetic processes of mono-functionalized AuNPs mixture were characterized step-by-step by FT-IR spectroscopy, far-IR spectroscopy and X-ray photoelectron spectroscopy (XPS).⁴²

The FT-IR spectra of the intermediates — PS Wang resin 75, 76 (PS-DB24C8), PS-DB24C8 ⊃ [69·HPF₆]_n, PS-DB24C8 ⊃ [69·HPF₆·AuNP]_n and 77 (69-AuNP) were obtained (Figure 3-7).⁴² For the FT-IR spectrum of PS Wang resin 75 (Figure 3-7a), there are three main IR absorptions,⁴⁶ they are the O-H stretching (~3400 cm⁻¹), alkane C-H stretching (2920 and 2960 cm⁻¹) and aromatic absorptions (~1600, 1200–1500, and ~900 cm⁻¹), which show the presence of hydroxyl groups, polystyrene alkane backbone and benzyl aromatic rings respectively. For the FT-IR

spectrum of PS-DB24C8 **76** (Figure 3-7b),⁴⁷ the absorption peaks in the spectrum are similar to the PS Wang resin **75** except for the appearance of a sharp absorption at 1741 cm^{-1} which corresponds to the C=O absorption. It indicated that there is new ester linkage formation after the coupling reaction between the DB24C8-CO₂H **70** with the PS Wang resin **75**. For the FT-IR spectrum of PS-DB24C8 \supset [**69**·HPF₆]_n (Figure 3-7c), the ligand **69**·HPF₆ interacted with the crown ether moiety in the resin, it was proven by the appearance of two new sets of IR modes at $\sim 3230\text{--}3260\text{ cm}^{-1}$ (N⁺-H stretching) and 840 cm^{-1} (*para*-substituted aromatic C-H). Moreover, the transmission percentage (% T) of C=O absorption at 1735 cm^{-1} increased, which showed that the self-assembly of the ester-containing ligand **69**·HPF₆ on the **76** (PS-DB24C8) to form poly(pseudorotaxane) PS-DB24C8 \supset [**69**·HPF₆]_n was successful. The FT-IR spectrum of PS-DB24C8 \supset [**69**·HPF₆·AuNP]_n (Figure 3-7d) was similar to that of PS-DB24C8 \supset [**69**·HPF₆]_n (Figure 3-7c). However, there is a new absorption peak at 249 cm^{-1} observed, which correspond to Au-S absorption,⁴⁸ in PS-DB24C8 \supset [**69**·HPF₆·AuNP]_n when comparing the far-IR spectrum of PS-DB24C8 \supset [**69**·HPF₆]_n (Figure 3-8a) with PS-DB24C8 \supset [**69**·HPF₆·AuNP]_n (Figure 3-8b). It indicated that there was successful immobilization of AuNPs onto PS-DB24C8 \supset [**69**·HPF₆]_n structure to form PS-DB24C8 \supset [**69**·HPF₆·AuNP]_n structure. The detailed assignments of FT-IR and far-IR spectra of PS Wang resin **75**,

76 (PS-DB24C8), PS-DB24C8 \supset [69-HPF₆]_n and PS-DB24C8 \supset [69-HPF₆-

AuNP]_n are displayed in Table 3-2.

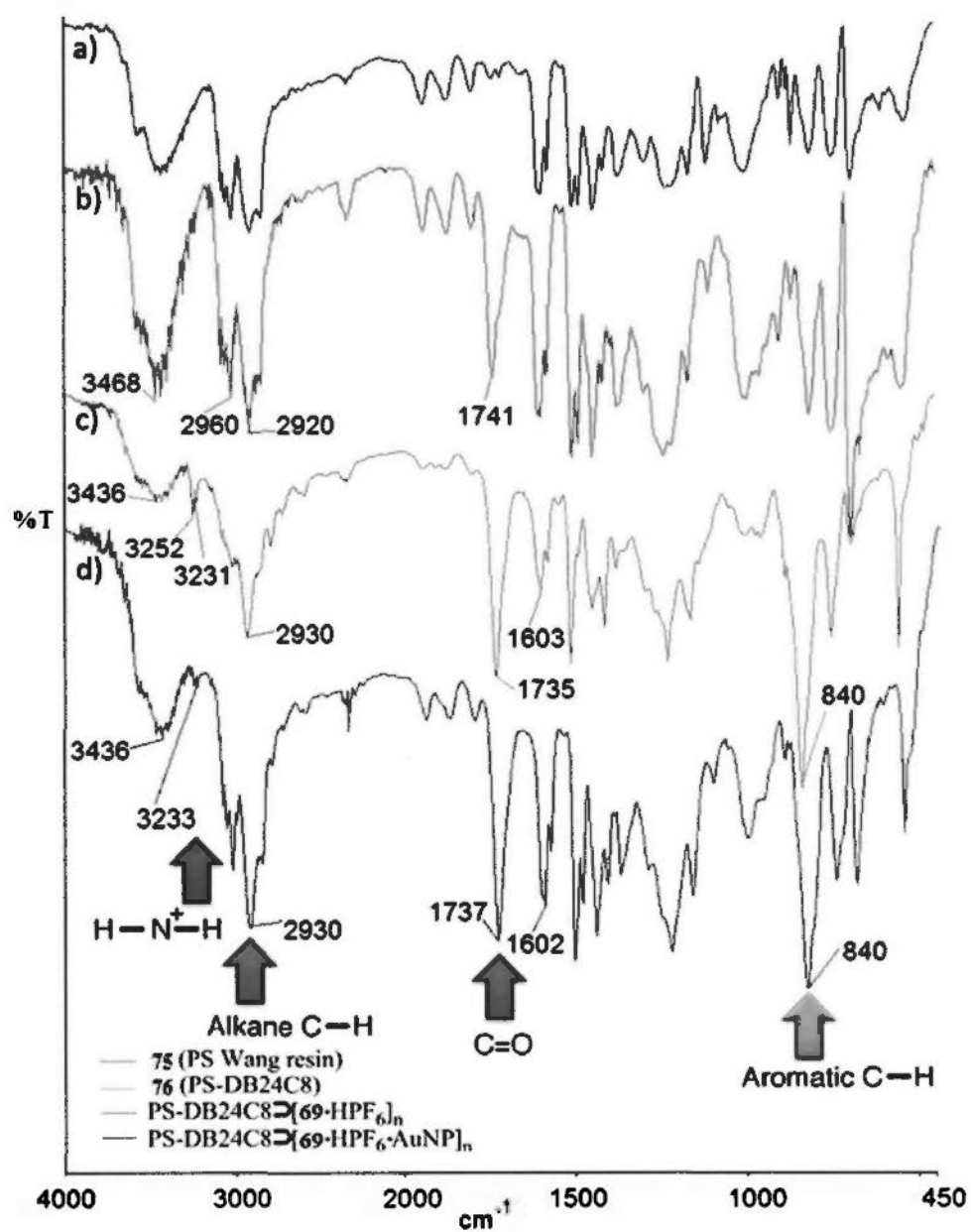


Figure 3-7. FT-IR spectra of a) PS Wang resin 75; b) 76 (PS-DB24C8); c) PS-DB24C8 \supset [69-HPF₆]_n and d) PS-DB24C8 \supset [69-HPF₆·AuNP]_n.

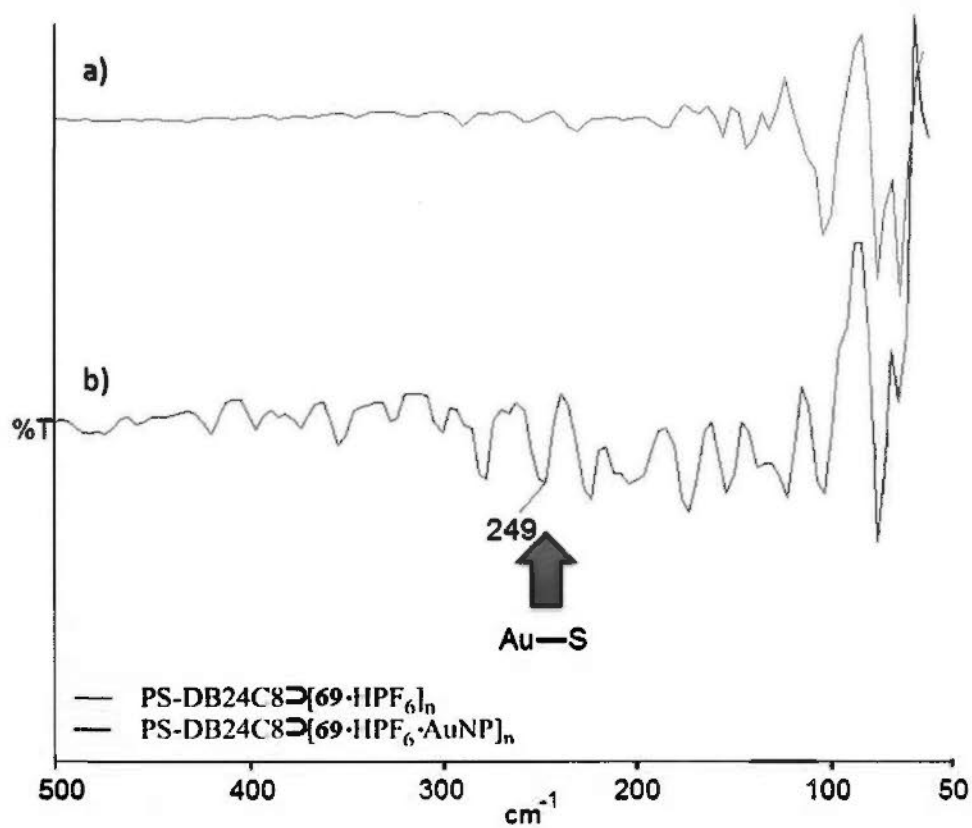
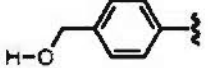
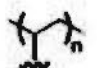
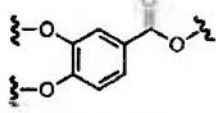
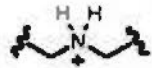

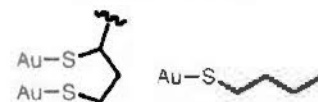


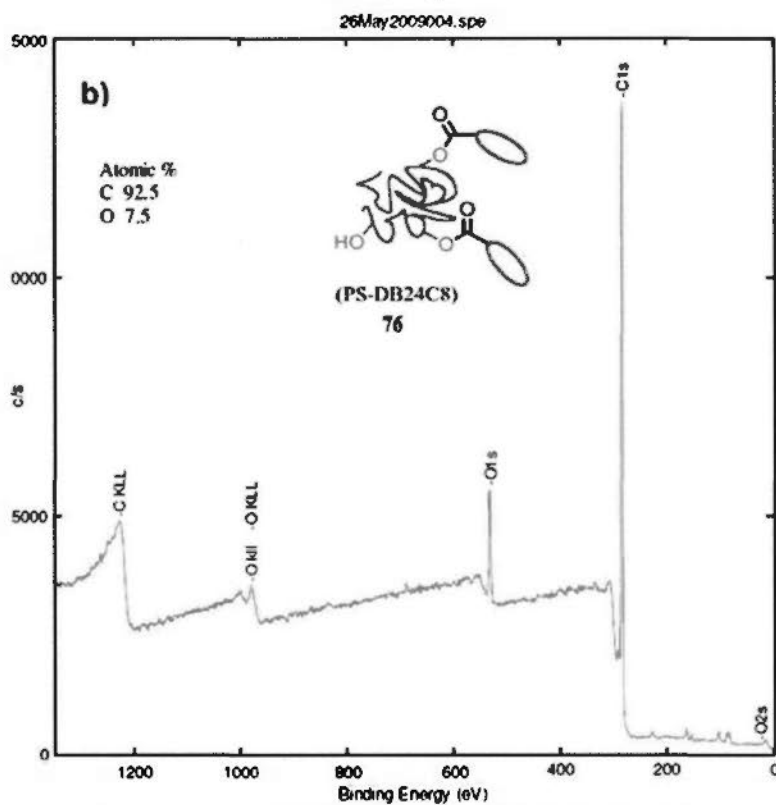
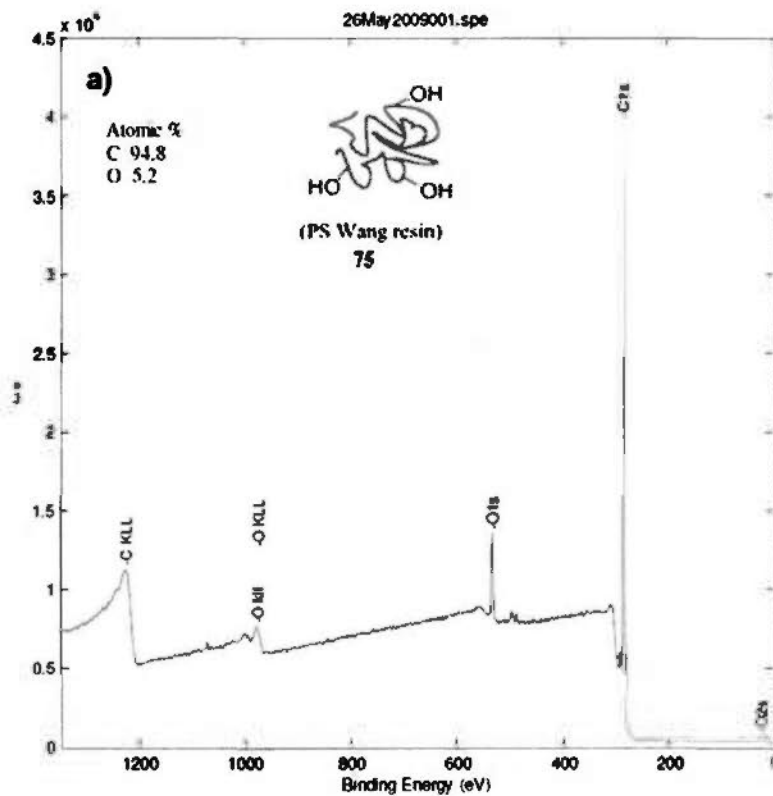
Figure 3-8. FT-IR spectra of a) PS-DB24C8 ⊃ [69-HPF₆]_n and b) PS-DB24C8 ⊃ [69-HPF₆·AuNP]_n.

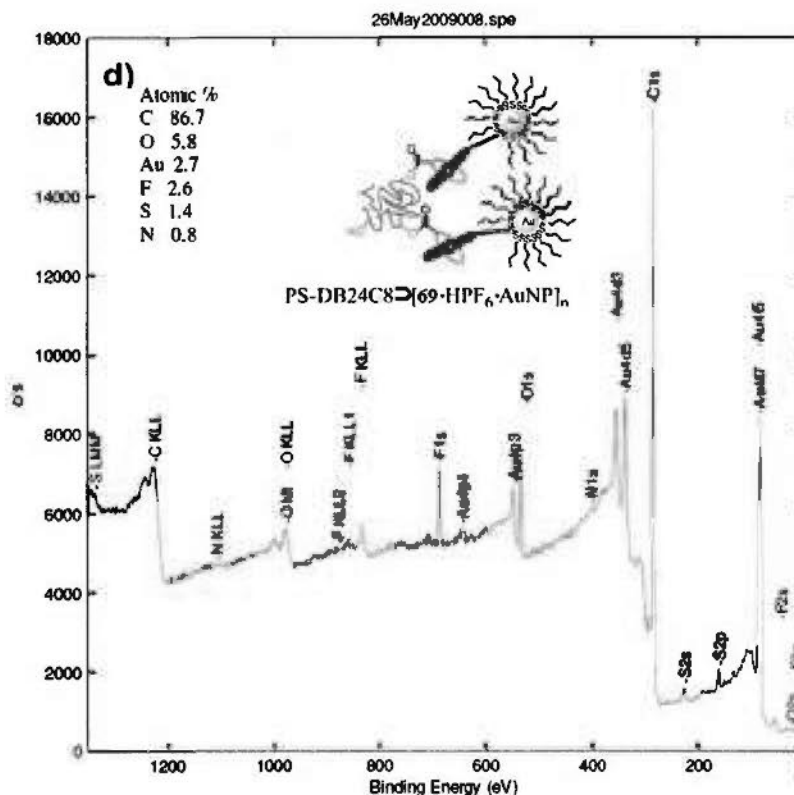
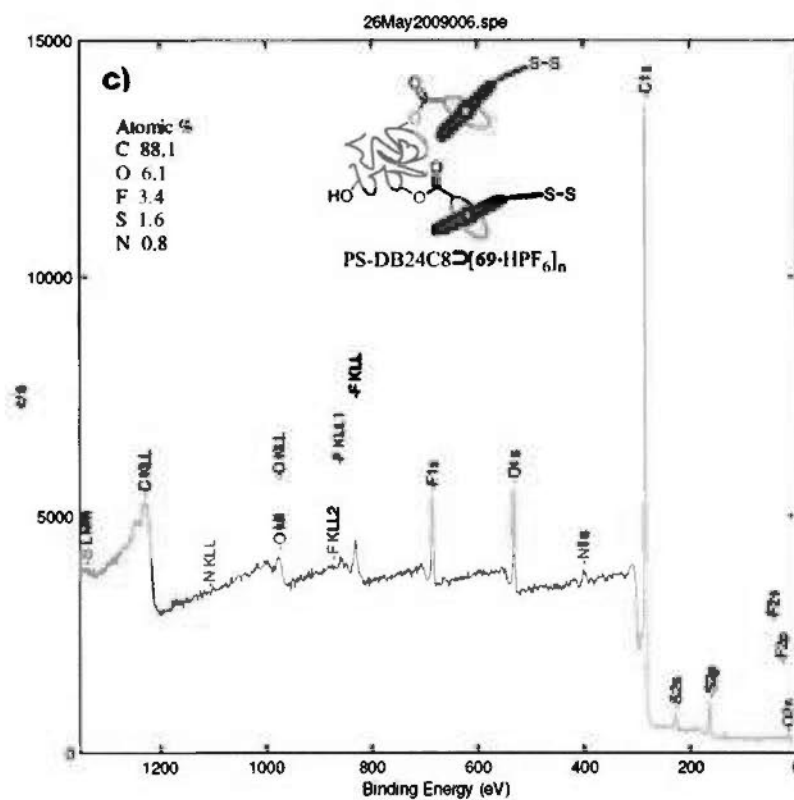
Table 3-2. Overview of assignments of FT-IR and far-IR absorption peaks of PS Wang resin 75; 76 (PS-DB24C8); PS-DB24C8 \supset [69-HPF₆]_n and PS-DB24C8 \supset [69-HPF₆·AuNP]_n.

compound/structure	wavenumber (cm ⁻¹)	assignment
PS Wang resin 75	~3400 (s)	O-H stretching 
	2920 (s), 2960 (s)	alkane C-H stretching 
	~1600 (m)	aromatic overtone
	~1200-1500 (m)	aromatic C-H bending
	~900 (w)	aromatic out-of-plane C-H bending
PS-DB24C8 76	~3400 (s)	O-H stretching
	2920 (s), 2960 (s)	alkane C-H stretching
	1741 (s)	C=O absorption 
	~1600 (m)	aromatic overtone
	~1200-1500 (m)	aromatic C-H bending
PS-DB24C8 \supset [69-HPF ₆] _n	~900 (w)	aromatic out-of-plane C-H bending
	~3400 (s)	O-H stretching
	~3230-3260 (w)	N ⁺ -H stretching 
	2930 (s)	alkane C-H stretching
	1735 (s)	C=O absorption
	~1600 (m)	aromatic overtone
	~1200-1500 (m)	aromatic C-H bending
	~900 (w)	aromatic out-of-plane C-H bending
	840 (s)	<i>para</i> -substituted aromatic C-H 
	PS-DB24C8 \supset [69-HPF ₆ ·AuNP] _n	~3400 (s)
~3230-3260 (w)		N ⁺ -H stretching
2930 (s)		alkane C-H stretching
1737 (s)		C=O absorption
~1600 (m)		aromatic overtone

~1200-1500 (m)	aromatic C-H bending
~900 (w)	aromatic out-of-plane C-H bending
840 (s)	<i>para</i> -substituted aromatic C-H
	Au-S absorption
249 (w)	

The XPS spectra of PS Wang resin **75**, **76** (PS-DB24C8), PS-DB24C8 \square [69•HPF₆]_n, PS-DB24C8 \square [69•HPF₆•AuNP]_n and **77** (69-AuNP) were also obtained (Figure 3-9). XPS analysis of PS Wang resin **75** (Figure 3-9a) and **76** (PS-DB24C8) (Figure 3-9b) showed the presence of carbon and oxygen. However, the XPS spectrum of PS-DB24C8 \square [69•HPF₆]_n showed additional peaks at 685 eV (F 1s), 400 eV (N 1s) and 162 eV (S 2p), which indicated the self-assembly of the ammonium ligand 69•HPF₆ onto the DB24C8 moiety on the **76** (PS-DB24C8) to form PS-DB24C8 \square [69•HPF₆]_n. For XPS spectra of PS-DB24C8 \square [69•HPF₆•AuNP]_n (Figure 3-9c), it consists of the characteristic peaks for gold 86 eV (Au 4f_{5/2}) and 83 eV (Au 4f_{7/2}) in addition to the characteristic peaks of fluorine, nitrogen and sulfur of the ligand.





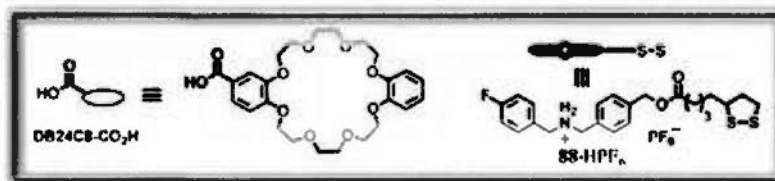


Figure 3-9. XPS spectra of a) PS Wang resin **75**; b) **76** (PS-DB24C8); c) PS-DB24C8 \supset [69·HPF₆]_n and d) PS-DB24C8 \supset [69·HPF₆·AuNP]_n.

Color changes in solution were also observed during the whole synthetic processes. As the Wang resin possesses a lower density and insoluble in dichloromethane and acetonitrile, the resin will disperse on the upper portion of solvent upon standing for several minutes, while the resin will be dispersed in whole solvent upon vigorous mechanical shaking. The color of the solvent and resin can be observed easily, thereby characterizing the stage of reactions. When the PS-DB24C8 \supset [69·HPF₆]_n was dispersed in solvent upon standing, the resin was yellow and deposited on the upper portions of solvent (Figure 3-10a). When the resin was shaken vigorously, the resin was dispersed well in the solvent with yellow color (Figure 3-10b). Then, the AuNPs **74** were added to undergo place exchange reaction, the resin became black in color and was then filtered after incubation. When the resin was dispersed again in solvent with vigorous shaking to give PS-DB24C8 \supset [69·HPF₆·AuNP]_n, the color of whole solution turned black (Figure 3-10c). Subsequently, the color of solvent at the bottom became colorless while the color of resin was still black upon standing (Figure 3-10d), which indicated the AuNPs have been immobilized with the ligand 69·HPF₆ that self-assembled on the crown ether

moiety of the resin. After that, triethylamine was added to deprotonate the ammonium ligand in the AuNPs **77**, the whole solution was still black (Figure 3-10e). The color of solvent in the bottom became brown while the color of resin became paler in color upon standing (Figure 3-10f). It indicated that the AuNPs has been disassembled from the resin due to the deprotonation of the ligand **69**·HPF₆ in the AuNPs, and the lost of binding affinity of crown ether and ligand. The final resin became yellow which indicated that no AuNPs were attached and can be reused for the next preparation cycle.

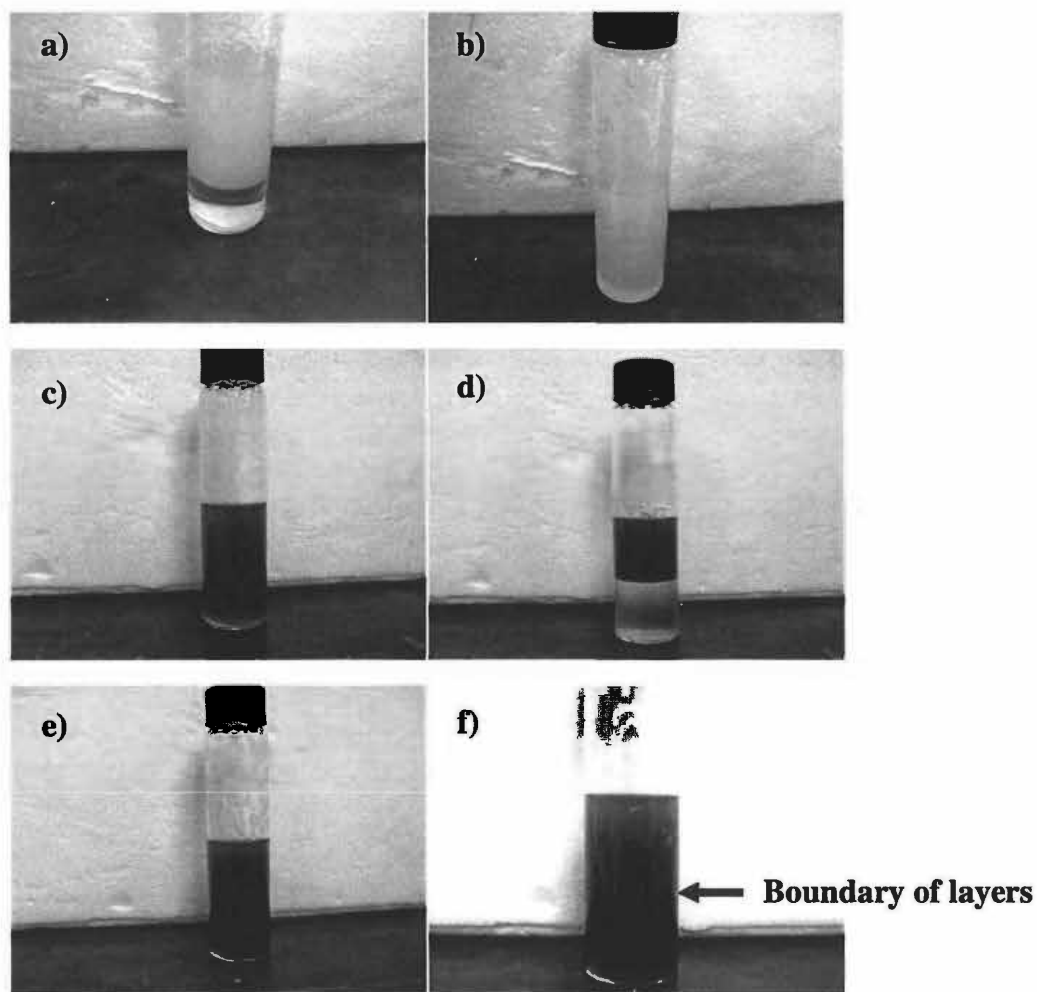


Figure 3-10. Photographs of a) PS-DB24C8 \supset [69-HPF₆]_n upon standing; b) PS-DB24C8 \supset [69-HPF₆·AuNP]_n after vigorous shaking; c) PS-DB24C8 \supset [69-HPF₆·AuNP]_n after vigorous shaking; d) PS-DB24C8 \supset [69-HPF₆·AuNP]_n upon standing; e) after addition of triethylamine to PS-DB24C8 \supset [69-HPF₆·AuNP]_n and vigorous shaking; f) after addition of triethylamine to PS-DB24C8 \supset [69-HPF₆·AuNP]_n upon standing.

3.6 Purification of discretely mono-functionalized AuNPs by iron oxide nanoparticles and characterization

3.6.1 General considerations

Superparamagnetic iron oxide nanoparticles (SPIO)⁴⁹⁻⁵² have been widely used in biomedical field and catalysis. It can be a good candidate as magnetic resonance imaging (MRI) agent and can be used for cell labeling. The iron oxide nanoparticles that functionalized with DB24C8 at the peripheries were used to purify the mono-functionalized AuNPs. Iron oxide nanoparticles of core about 200 nm with a uniform silica coating and amine peripheral functional groups was decorated with DB24C8-CO₂H **70** by amide linkage. When a magnet was put under the containers with SPIO nanoparticles, the magnetic nanoparticles would be attracted by the magnetic field and stucked on the wall surface near the magnet. Therefore, magnetic separation can be used to separate the desired compounds, which selectively bounded supramolecularly to the DB24C8-coated SPIO nanoparticles, from bulk mixtures by successive washing and magnetic separating procedures.

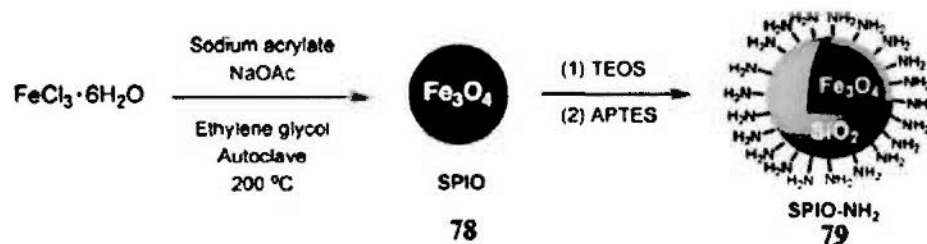
Mono-functionalized AuNPs with amine functional group can be protonated and self-assembled onto the DB24C8 moieties of SPIO nanoparticles. Hence, magnetic separation to purify the mono-functionalized AuNPs was feasible.

Moreover, the SPIO nanoparticles were found to be compatible with a dilute acid (i.e., trifluoroacetic acid, H-TFA) and a dilute base (i.e., triethylamine).

Therefore, iron oxide nanoparticles can be readily used to purify the mono-functionalization AuNPs by ON/OFF switching of pseudorotaxane process.

3.6.2 Preparation of the amine functionalized iron oxide nanoparticles

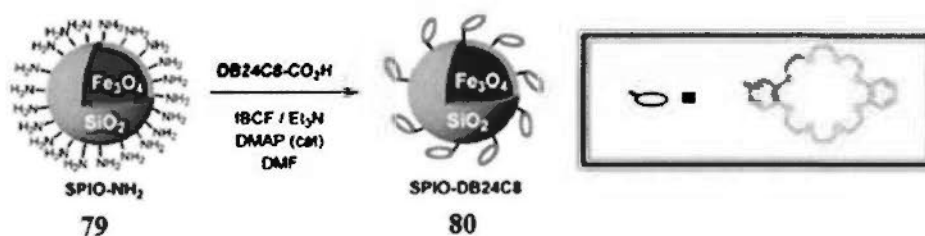
Superparamagnetic iron oxide nanoparticles were prepared by a solvothermal reaction.⁵¹ Iron(III) chloride hexahydrate was mixed with sodium acrylate, sodium acetate and ethylene glycol with stirring which was subjected to heating at 200 °C. The obtained SPIO nanoparticles **78** were dispersed in ethanol and possessed the structures of Fe₃O₄. The resulted nanoparticles can be coated by a layer of tetraethylorthosilicate (TEOS) and then a layer of aminopropyltriethoxysilane (APTES) to give SPIO nanoparticles **79** core/shell structures with an average core diameter of 200 nm (Scheme 25).



Scheme 25. Synthetic scheme of the amine functionalized SPIO nanoparticles **79**.

3.6.3 Preparation of the crown ether-decorated iron oxide nanoparticles

The amine functionalized SPIO nanoparticles can be decorated with DB24C8 by coupling reaction with DB24C8-CO₂H **70** via mixed anhydride formation by isobutylchloroformate (Scheme 26).



Scheme 26. The synthetic scheme of crown ether decorated SPIO nanoparticles **80**.

The residue from the coupling reaction by magnetic separation was collected whereas the amount of the crown ether decorated on the iron oxide was determined from the reaction yield, which was calculated from the ^1H NMR spectrum. The yield was determined simply using the integration ratio of the methyl protons in nitromethane and the benzene proton as shown in Figure 3-11. The signal at δ 4.31 ppm refers to the three protons of CH_3NO_2 with integration of 100.0000, the peak at δ 7.71–7.73 ppm refers to an aromatic proton (H_a), with integration of 248.6338. By calculating the ratio of integration to the mole ratio of the standard to **70** with the correction of number of protons involved, the amount of DB24C8- CO_2H **70** in the residue was found to be 0.739 mmol. Therefore, the reaction yield was determined as 74 %. Hence, the amount of crown ether decorated on the iron oxide nanoparticles was 2.20 mmol/g of iron oxide nanoparticles.

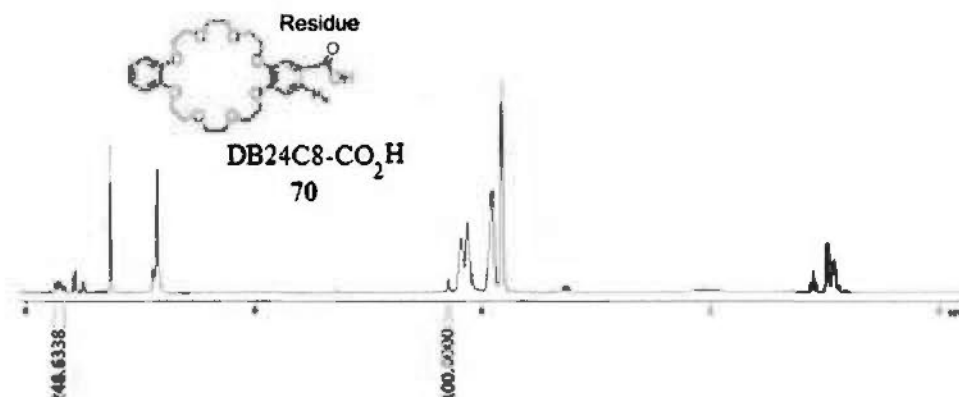
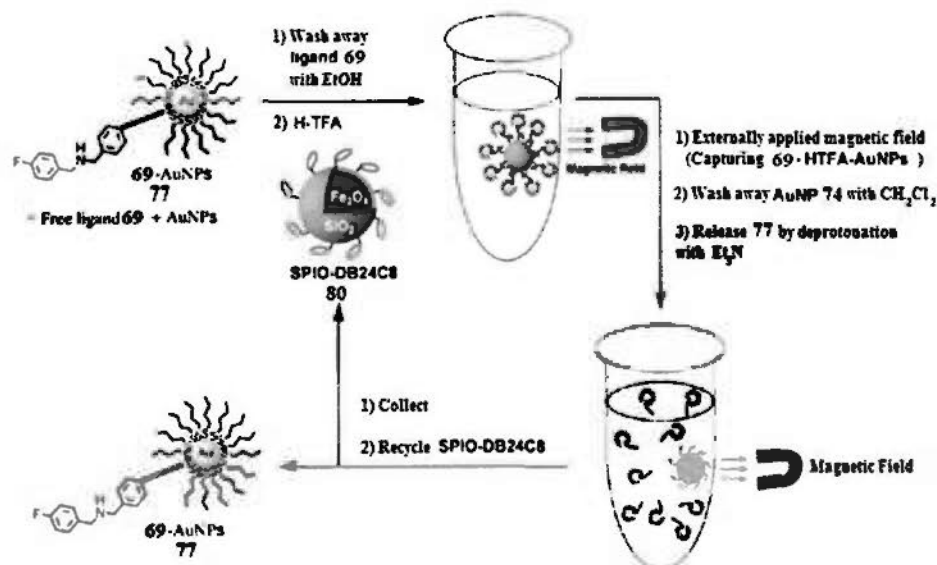


Figure 3-11. ^1H NMR spectrum of the filtrate from the coupling reaction of **70** with amine functionalized iron oxide nanoparticles **80**. (Number of scan = 16)

3.6.4 Purification route of mono-functionalized AuNPs by magnetic separation

The general scheme for the purification of mono-functionalized AuNPs is shown in

Scheme 27.



Scheme 27. Purification of mono-functionalized AuNPs **77** by DB24C8-coated SPIO nanoparticles **80**.

The crude mono-functionalized AuNPs obtained from the supramolecular solid-phase supported synthesis was dried and washed with cold ethanol at $0\text{ }^\circ\text{C}$. It

was found that the ligand **69** could be effectively washed away without jeopardizing the AuNPs related structures. The resulting AuNP solution mixture which contained the mono-functionalized AuNPs **77** and non-functionalized AuNPs **74** was re-dispersed in dichloromethane and treated with trifluoroacetic acid (H-TFA). Therefore, only the amine groups in the mono-functionalized AuNPs were protonated and self-assembled onto the crown ether moiety in SPIO-DB24C8 **80** by forming the pseudorotaxane superstructures to give SPIO-DB24C8 \supset [**69**·HPF₆·AuNP]_n. Then, an external magnetic field was applied, so that all the magnetic nanoparticles, together with the self-assembled mono-functionalized AuNPs, were magnetically attracted to the wall of the containers. Any excess and unreacted non-functionalized AuNPs **74** were washed away. The washing steps and magnetic separation were repeated to ensure that all unreacted AuNPs **74** were washed away. While the magnetic field was still applied on SPIO-DB24C8 \supset [**69**·HTFA·AuNP]_n, it was subjected to a base treatment with triethylamine to deprotonate all ammonium ions into amines, so that the purified mono-functionalized AuNPs **77** (**69**-AuNP) can be obtained. The iron oxide nanoparticles **80** (SPIO-DB24C8) can be recycled and reused. The purification process was repeated 5–7 times to give conversion yields of 3.0 mg of **77** (**69**-AuNP) per gram of PS Wang resin **75** (–OH density = 1.0–1.5 mmol/g) and 2.3 mg of **77** (**69**-AuNP) per gram of **76** (PS-DB24C8) (–DB24C8

density ~ 1.0 mmol/g). The yield is near quantitative after several repeated purification steps.

3.6.5 Stepwise characterization of purification process

The whole purification process was characterized by FT-IR, EDX with TEM imaging. Moreover, the whole purification process can also be monitored by color change of the solution.

From the FT-IR spectrum of **79** (SPIO-NH₂) (Figure 3-12a), there were characteristic peaks of 3401 cm⁻¹, 1092 cm⁻¹ and 588 cm⁻¹ which corresponded to the amine N-H stretching, Si-O and Fe-O absorption, respectively. For the FT-IR spectrum of **80** (SPIO-DB24C8) (Figure 3-12b), the amide absorption peak at 1629 cm⁻¹ was in higher intensity than that of **79**, which indicated there was amide formation after the crown ether was coupled to the amine on the iron oxide periphery. The characteristic peaks of 1093 cm⁻¹ and 586 cm⁻¹ corresponded to Si-O and Fe-O absorption, respectively. From the FT-IR spectrum of SPIO-DB24C8 \square [69-HTFA-AuNP]_n (Figure 3-12c), the absorption peaks from the ligand 69-HTFA were hardly observed since the size ratio of SPIO nanoparticles was much larger than the AuNPs. The content of iron oxide coating was also dominant in their IR absorption signals with characteristic peaks of 1095 cm⁻¹ and 587 cm⁻¹, corresponding to Si-O and Fe-O absorption, respectively.

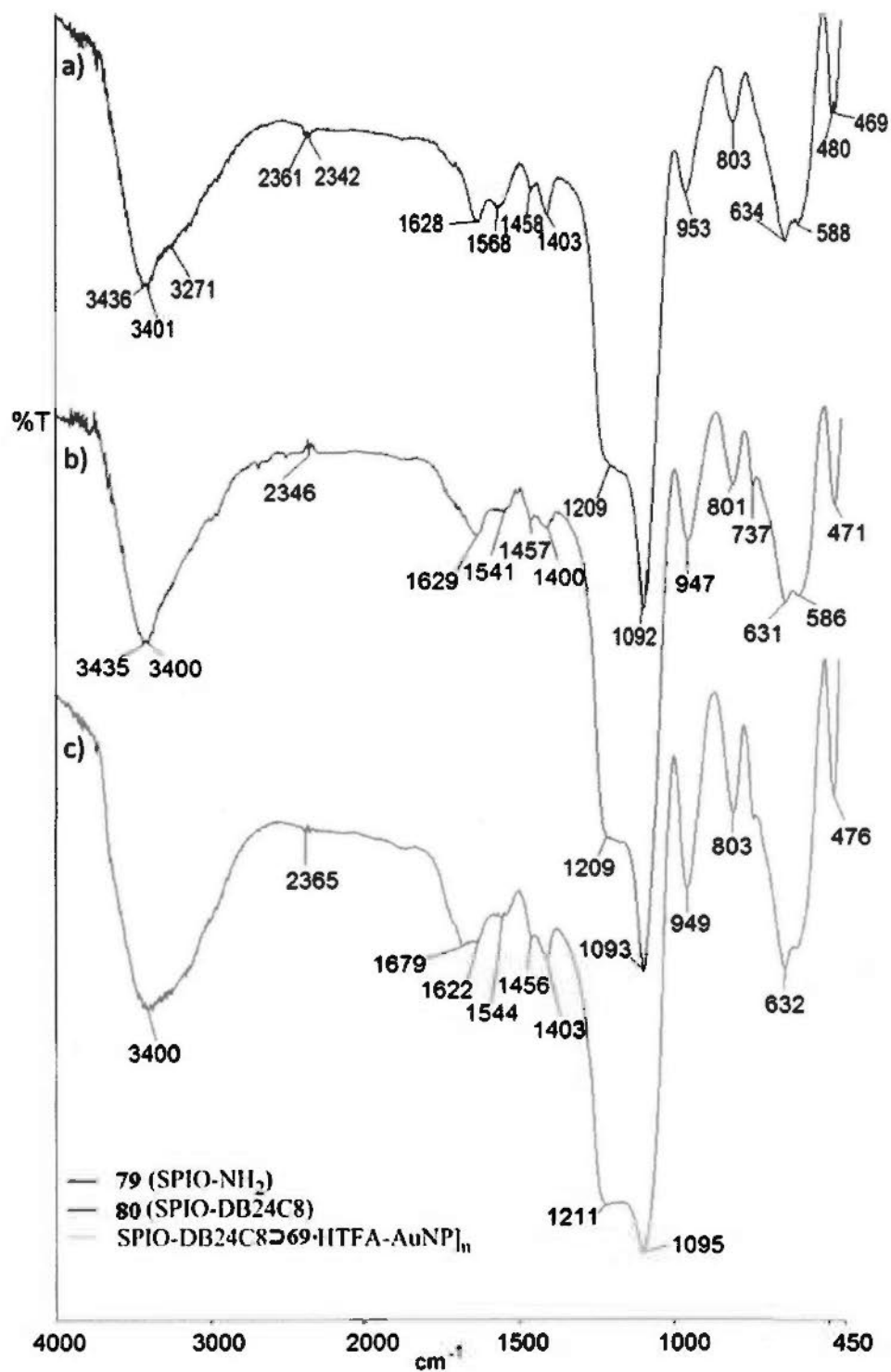


Figure 3-12. FT-IR spectra of a) 79 (SPIO-NH₂); b) 80 (SPIO-DB24C8); c) SPIO-DB24C8@[69-HTFA-AuNP]_n.

The purification processes were also monitored by characterizing the respective nanostructures obtained at different purification steps by TEM. Figure 3-13a shows the typical **80** (SPIO-DB24C8) microsphere with diameter about 200 nm. After the self-assembling process of mono-functionalized AuNPs **77** on the crown ether moiety of the SPIO nanoparticles, the nanostructures of SPIO-DB24C8 \supset [**69**·HTFA·AuNP]_n was obtained. TEM (Figure 3-12b-e) images showed that there were smaller AuNPs (2 nm) well deposited on the periphery of the **80** (SPIO-DB24C8) microspheres. After the successive washing and magnetic separation process, triethylamine was added to release the mono-functionalized AuNPs **77**, the TEM of remaining SPIO nanoparticles showed that there were no AuNPs deposited (Figure 3-12f). It showed that such process of ON/OFF switching of pseudorotaxane chemistry of mono-functionalized AuNPs **77** was complete and the SPIO nanoparticles can be recycled and reused.

Energy dispersive X-ray (EDX) spectroscopy were also performed for the elemental analysis of **80** (SPIO-DB24C8) microsphere (Figure 3-13a), SPIO-DB24C8 \supset [**69**·HTFA·AuNP]_n before (Figure 3-13b) and after the base treatment (Figure 3-13c). The results show the presence of Cu (from copper grid), Fe, O, C and Si in all the spectra corresponded to the iron oxide nanoparticles and organic matters. Moreover, there was characteristic peak of Au in 2–3 keV and 8–10

keV region in SPIO-DB24C8 \supset [69-HTFA·AuNP]_n, which is different from the EDX spectra of **80** (SPIO-DB24C8) and SPIO-DB24C8 \supset [69-HTFA·AuNP]_n after the base treatment. Hence, it proved again the complete ON/OFF switching of mono-functionalized AuNPs **77** pseudorotaxane by acid/base condition on the crown ether modified SPIO nanoparticles.

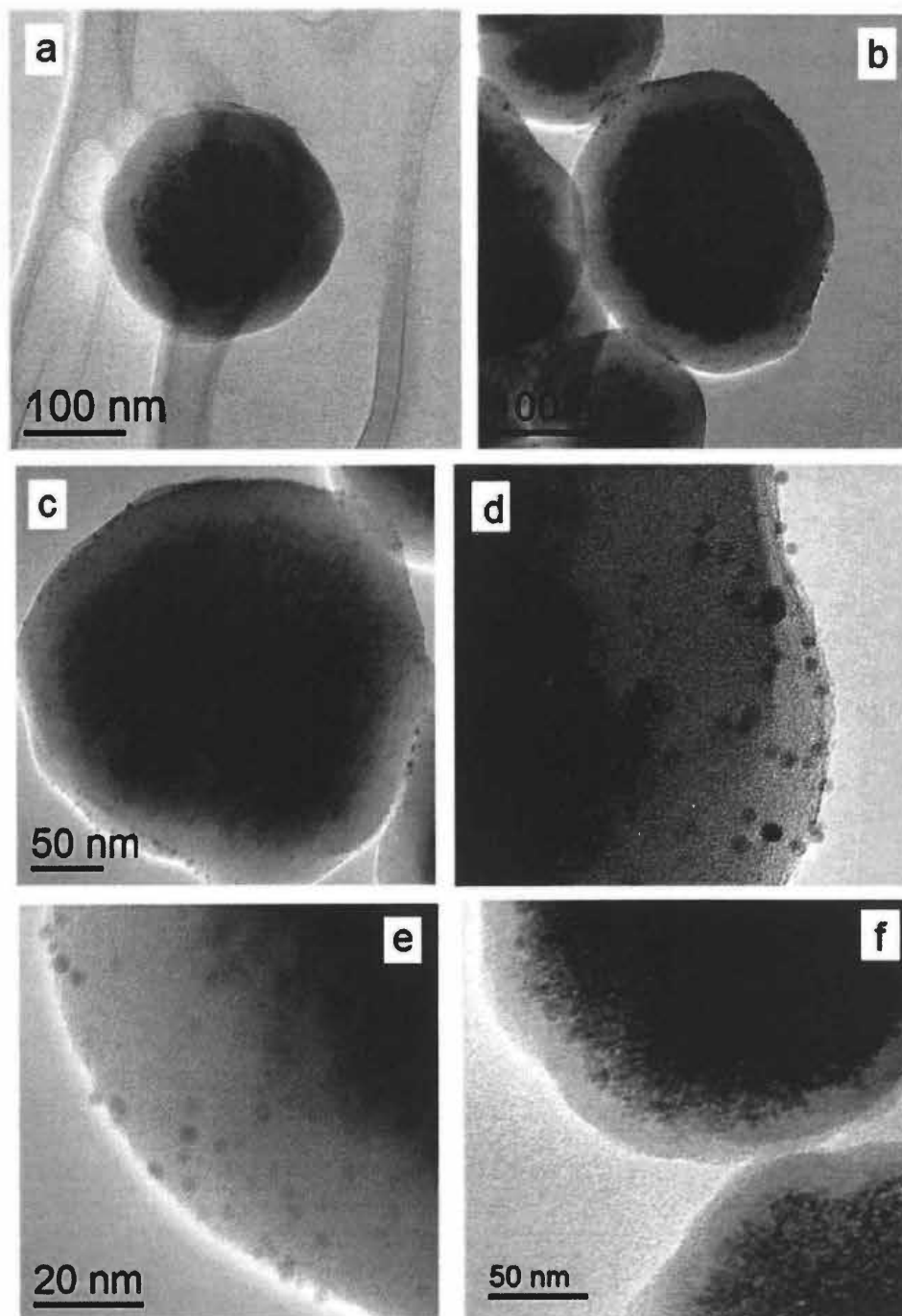
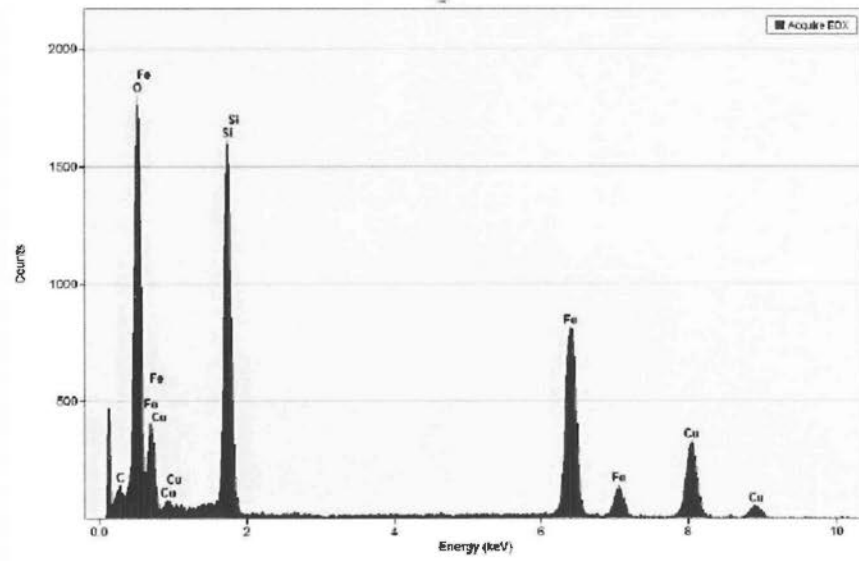
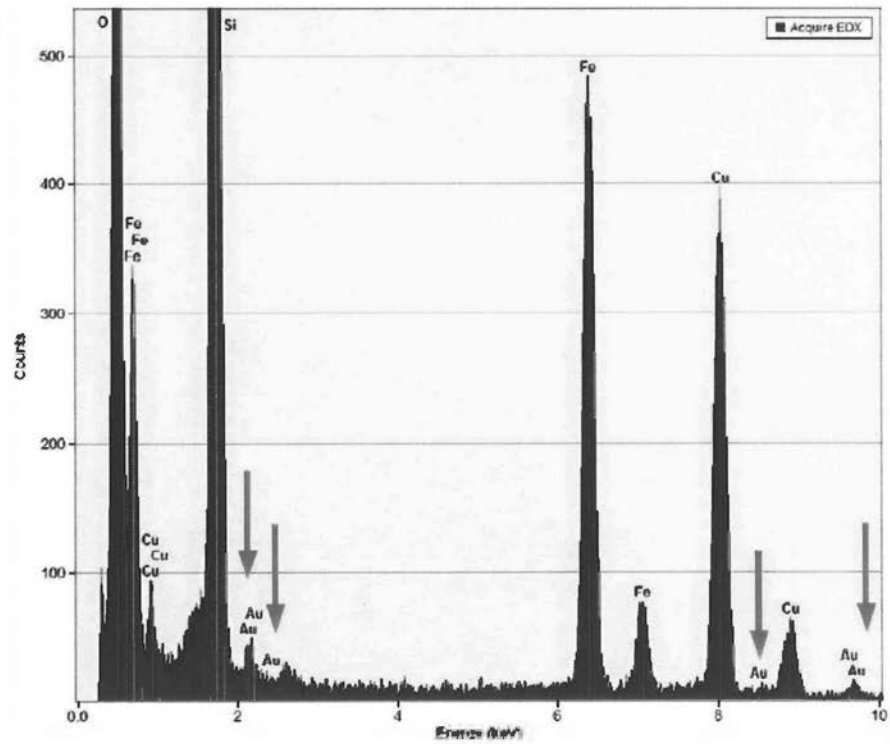


Figure 3-12. TEM images of a) **80** (SPIO-DB24C8); b,c) SPIO-DB24C8 \supset [69-HTFA-AuNP]_n with lower magnification; d,e) SPIO-DB24C8 \supset [69-HTFA-AuNP]_n with higher magnification and f) the remaining **80** (SPIO-DB24C8) nanoparticles after base treatment of SPIO-DB24C8 \supset [69-HTFA-AuNP]_n.

a)



b)



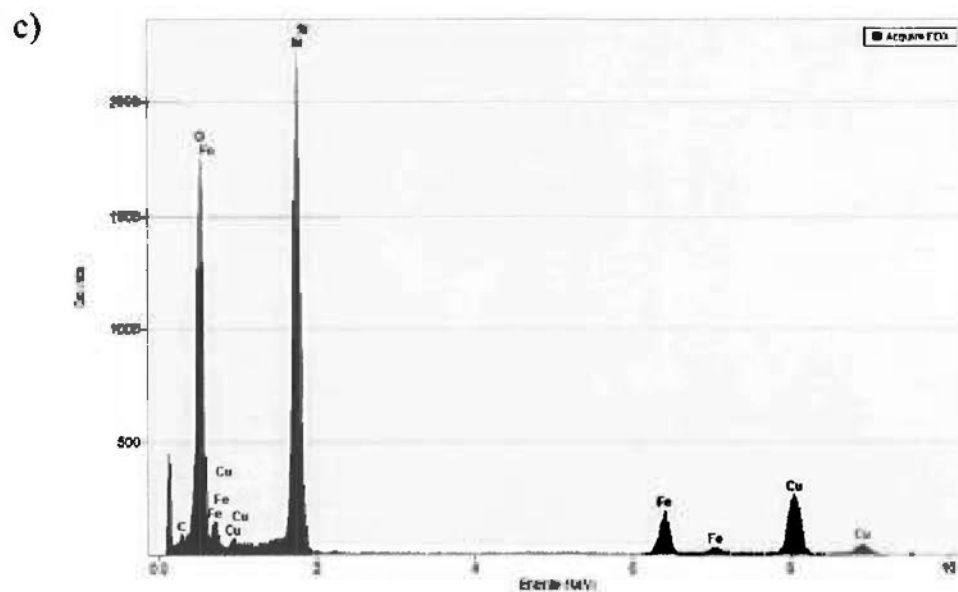


Figure 3-13. EDX spectra of a) **80** (SPIO-DB24C8); b) SPIO-DB24C8 \supset [69-HTFA·AuNP]_n; c) the remaining **80** (SPIO-DB24C8) nanoparticles after base treatment of SPIO-DB24C8 \supset [69-HTFA·AuNP]_n.

Color changes of solution were also observed during the magnetic purification process. The iron oxide nanoparticles will be magnetically attracted to the wall of the reaction vial upon applying a magnetic field. The nanoparticle **80** (SPIO-DB24C8) was ultrasonically dispersed in dichloromethane to give a brown solution (Figure 3-14a). Self-assembling of AuNPs to **80** (SPIO-DB24C8) nanoparticle solution gave SPIO-DB24C8 \supset [69-HTFA·AuNP]_n with a black solution (Figure 3-14b). After several successive washing processes to remove the unreacted AuNPs, the upper portion of solution upon the magnetic separation became clear (Figure 3-14c), which indicated that all unreacted AuNPs were washed away. The re-dispersed solution was subjected to a base treatment whereas a magnetic

separation gave a brown solution on the upper portion of the solution (Figure 3-14d), indicating the release of AuNPs into the bulk solution.

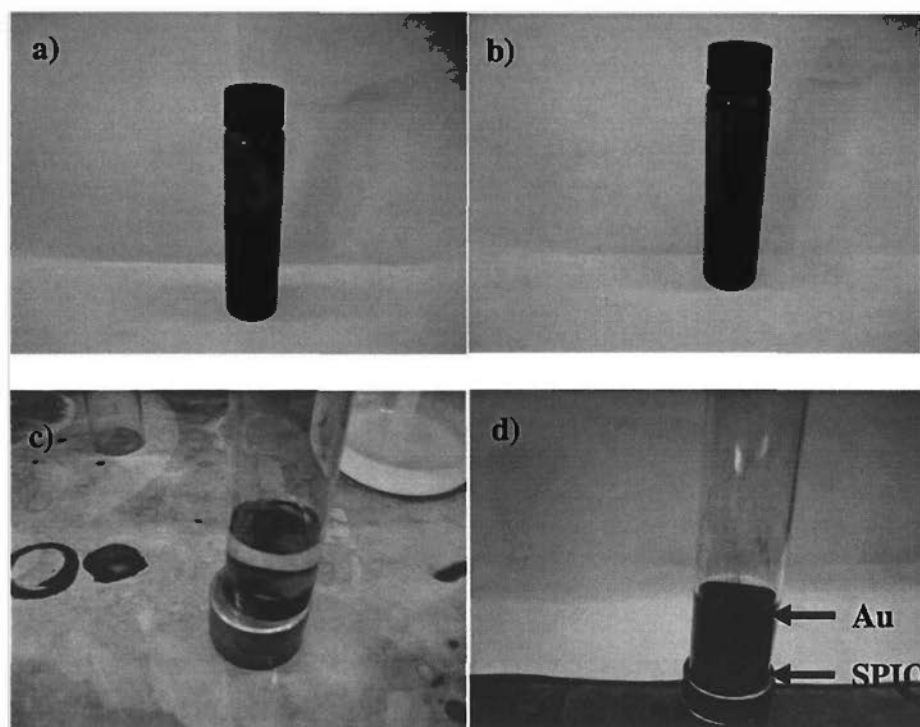


Figure 3-14. Photographs of a) **80** (SPIO-DB24C8); b) SPIO-DB24C8 \supset [69-HTFA·AuNP]_n; c) SPIO-DB24C8 \supset [69-HTFA·AuNP]_n under magnetic field (the third times washing process); d) SPIO-DB24C8 \supset [69-HTFA·AuNP]_n after the base treatment and under magnetic field.

3.7 Instrumental characterization of discretely mono-functionalized AuNPs

3.7.1 FT-IR spectroscopy and far-IR spectroscopy

After the magnetic purification steps of AuNPs, the purified mono-functionalized AuNPs **77** (**69**-AuNP) were subjected to FT-IR and far-IR analyses. Major absorption peaks were observed (Figure 3-15a,b) at $\sim 3400\text{ cm}^{-1}$ (N-H stretching), 2852 and 2925 cm^{-1} (alkane C-H stretching), 1733 cm^{-1} (C=O absorption), 1600 cm^{-1} (aromatics overtone), 1384 cm^{-1} (CH_3 symmetrical deformation from *n*-butanethiolate ligands), 804 cm^{-1} (*para*-substituted aromatic C-H), 249 and 250 cm^{-1} (Au-S absorption). The absorption peaks of C-H asymmetric and symmetric methylene stretching vibration are shifted to lower wavenumbers from 2920 to 2852 cm^{-1} and from 2960 to 2925 cm^{-1} .⁵³ Among these observed major IR absorption peaks, the secondary amine ($\text{R}_2\text{N-H}$) bending, ($\text{R}_2\text{N}^+-\text{H}$) stretching, C-S and S-S absorption peaks are too weak to be observed.

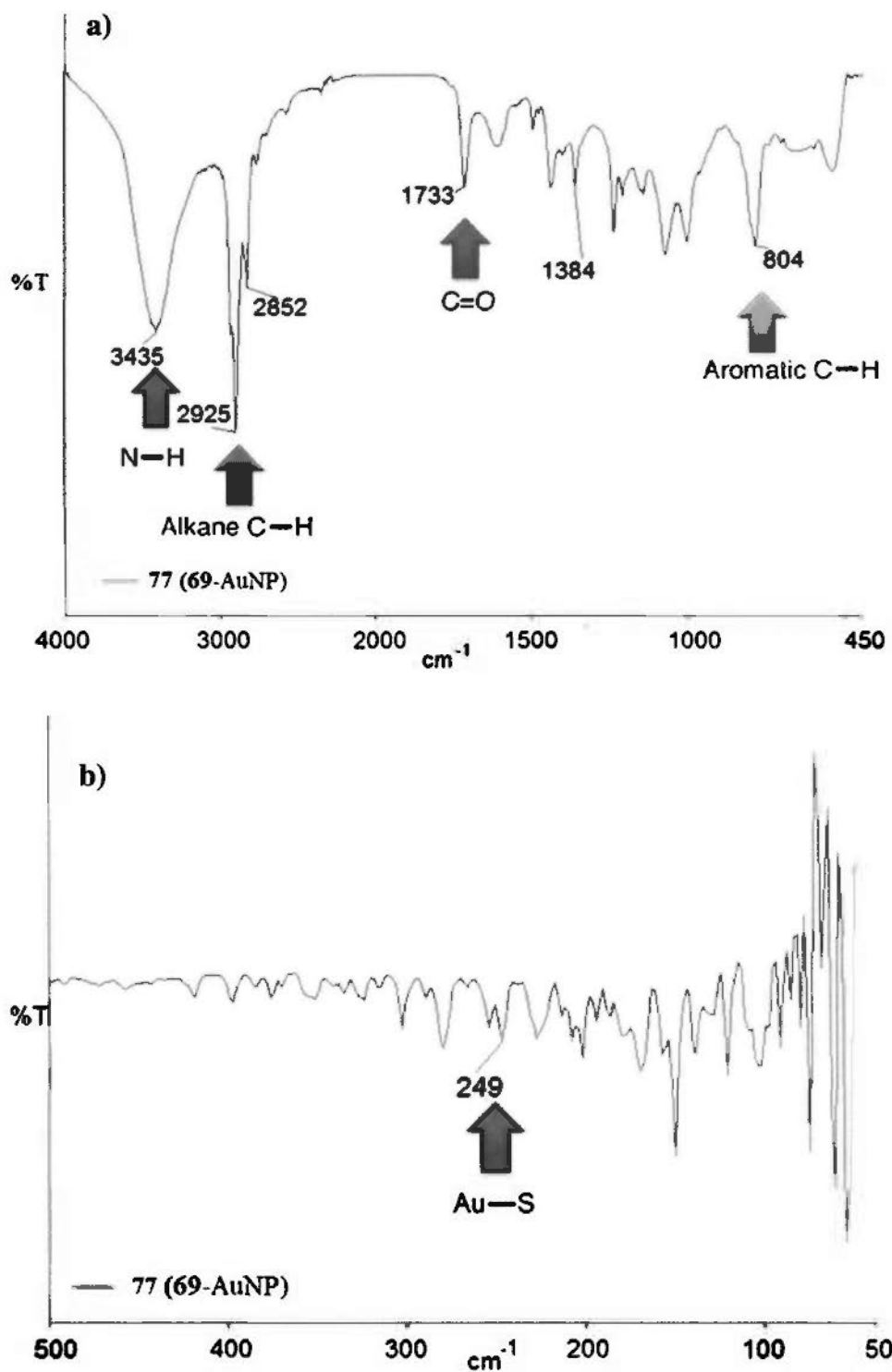


Figure 3-15. a) FT-IR spectrum and b) far-IR spectrum of mono-functionalized AuNPs 77 (69-AuNP).

3.7.2 X-ray photoelectron spectroscopy

For XPS spectra of **77** (69-AuNP) (Figure 3-16), it renders the characteristic peaks for gold 86 eV (Au 4f_{5/2}) and 83 eV (Au 4f_{7/2}) in addition to the characteristic peaks of fluorine, nitrogen and sulfur of the ligand corresponding to the ligand **69**.

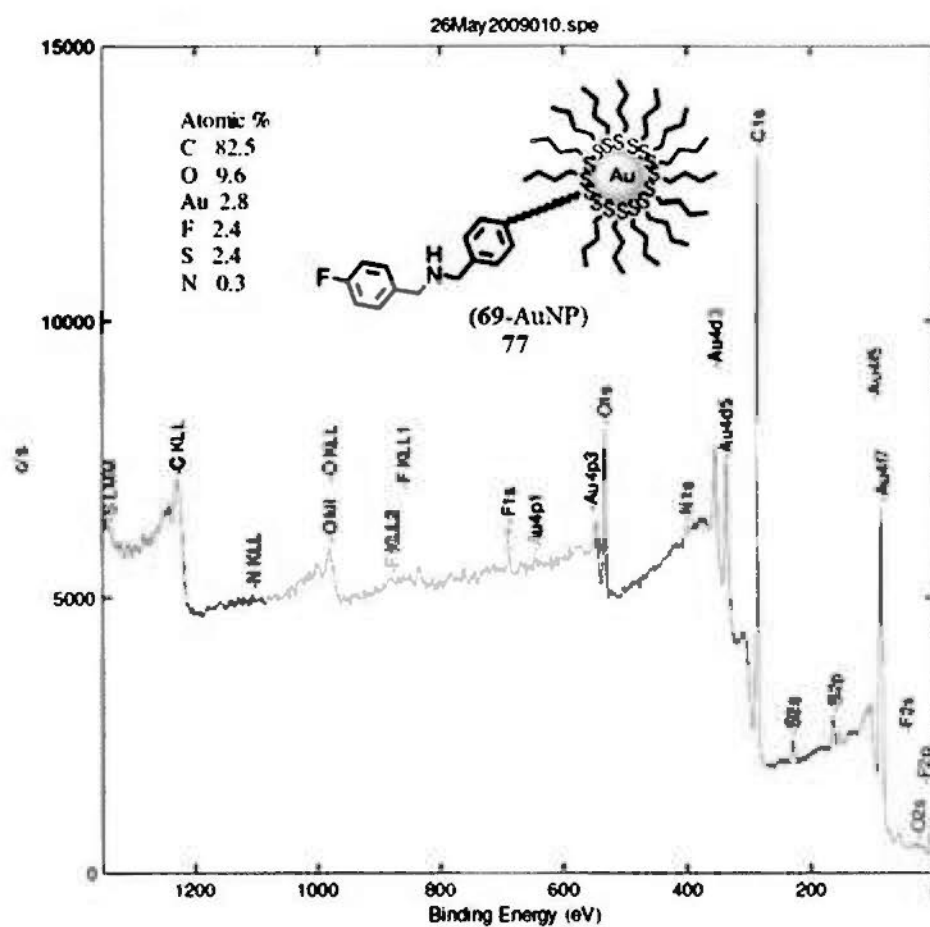


Figure 3-16. XPS spectrum of **77** (69-AuNP).

3.7.3 UV/visible absorption spectroscopy

The UV/visible absorption spectra of AuNPs **74**, mono-functionalized AuNPs **77** (**69**-AuNP) and the ligand **69** are shown in Figure 3-17. The AuNPs **74** and mono-functionalized AuNPs **77** (**69**-AuNP) possess a plasmon resonance absorption peak at about 520 nm.^{12a,15a,33b,48b} Moreover, there is an absorption peak at about ~260 nm in the spectra of ligand **69** and mono-functionalized AuNPs **77** (**69**-AuNP), but not found in spectrum of AuNPs **74**. Hence, the mono-functionalized AuNPs **77** should be consisted of the ligand **69**.

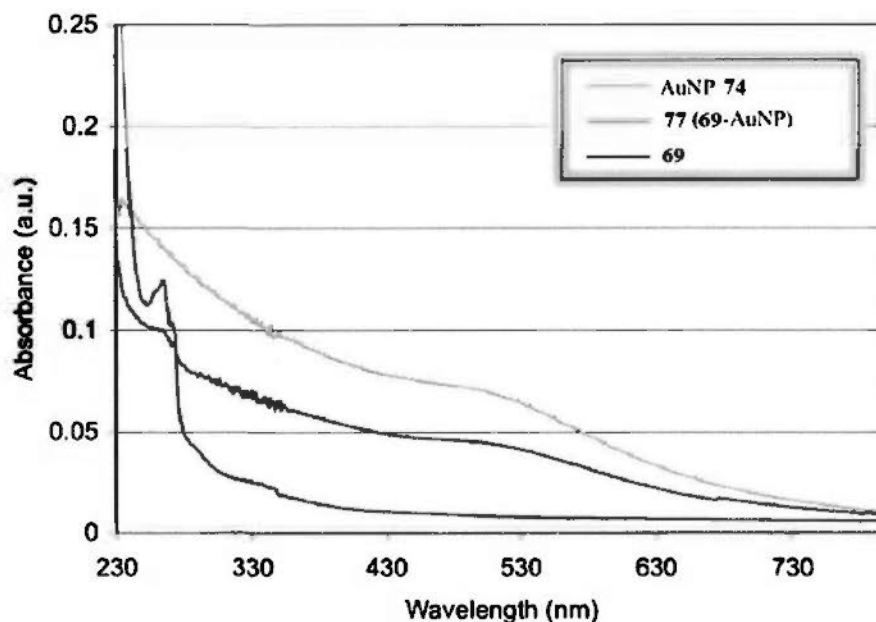


Figure 3-17. Stacked UV/visible spectra (CH_2Cl_2 , 298 K) of AuNP **74**, **77** (**69**-AuNP) and the ligand **69** with concentration of ~0.20 mg/mL in CH_2Cl_2 .

3.7.4 High resolution transmission electron microscopy

The TEM image of mono-functionalized AuNPs **77** (**69**-AuNP) (Figure 3-18) reveals that the mono-functionalized AuNPs (with average core diameter of 2 nm) did not form aggregates.

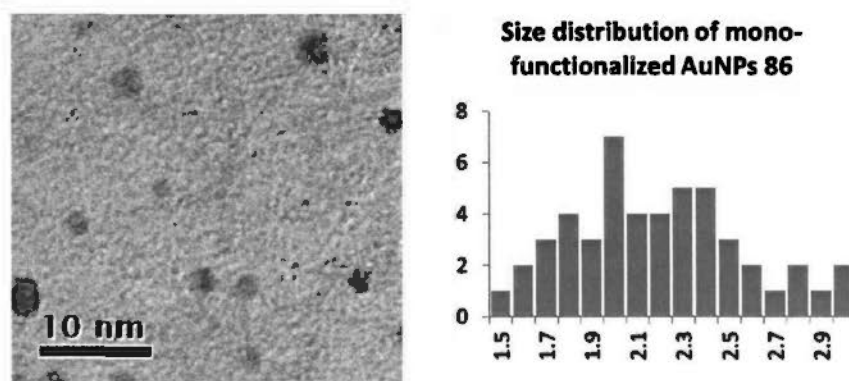


Figure 3-18. a) TEM images of **77** (**69**-AuNP); b) the size distribution of the mono-functionalized AuNPs **77** by counting 50 nanoparticles in TEM images.

3.8 Characterization of discretely mono-functionalized AuNP *via* formation of supramolecular dimers and trimers with bis- and tris- crown ether linkers

3.8.1 General considerations

Generally, the purified mono-functionalized AuNPs should be self-assembled to form dimers and trimers in the presence of divalent linkers and trivalent linkers, respectively. These dimeric or trimeric AuNP nanostructures can be visualized in TEM images and characterized by a change in their UV/visible absorption spectra. Such change in UV/visible absorption can only be observed when the interparticle distance becomes smaller than the average diameter of the AuNPs upon formation of dimers or trimers, so the SPR effect of the AuNPs induces a shift in UV/visible absorption (See section 1.4 and 1.6).

If the AuNPs contains any higher-ordered functionalization (e.g., di-functionalized, tri-functionalized, etc), the self-assemblies with divalent or trivalent linkers should possess aggregations rather than specific dimeric or trimeric structures. The aggregated AuNP nanostructures can be easily observed in their TEM images.

Therefore, a divalent linker BisDB24C8 **82** and a trivalent linker TrisDB24C8 **86** were synthesized in order to help characterizing the mono-functionalized AuNPs **77** by forming supramolecular AuNP dimers and trimers, respectively. The resulted nanostructures are novel supramolecular AuNPs dimers and trimers which are also

acid/base switchable. The use of such supramolecular systems has several advantages over the covalent dimerization in terms of (1) a milder condition of reversible formation and disassembly of the pseudorotaxane dimers and trimers; and (2) a readily available amine reactivity of the mono-functionalized AuNPs.

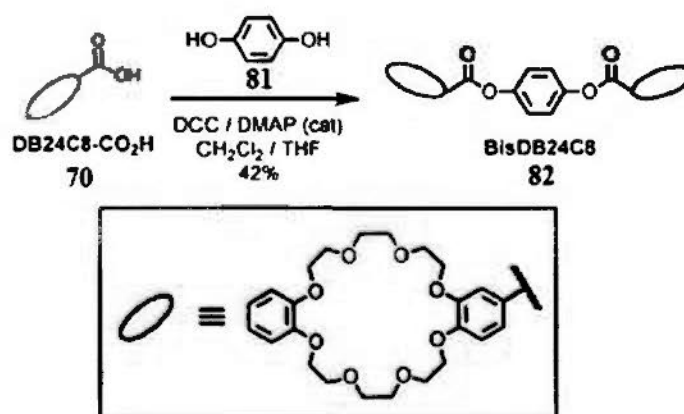
The design of the divalent and trivalent linkers should be well addressed so that the supramolecular dimer and trimer nanostructures should possess interparticle distances similar or smaller than the average diameter of the individual AuNPs. Thus, the SPR band shift can be observed by using UV/visible spectroscopy. Several computational models of the AuNPs supramolecular dimers and trimers were created in order to estimate the respective supramolecular nanostructures and their interparticle distances (See Section 3.8.5).

3.8.2 Synthesis of bis-crown ether linker

In order to minimize the interparticle distance of AuNPs, the divalent linker should be short and rigid to reduce a large variation of interparticle distance due to conformational changes. Bis-crown ether linker was chosen since it is necessary to form the supramolecular dimers by molecular recognition of dibenzylammonium and dibenzo crown ether.

BisDB24C8 **82** was synthesized by the coupling reaction of DB24C8-CO₂H **70** with hydroquinone **81** by *N,N'*-dicyclohexylcarbodiimide (DCC) in 42 % yield

(Scheme 28). Hydroquinone core was chosen since the resulted compound should be in planar and rigid. Then, the conformation changes of the linker can be minimized, and that the major conformation changes should be originated from the AuNPs alignments.



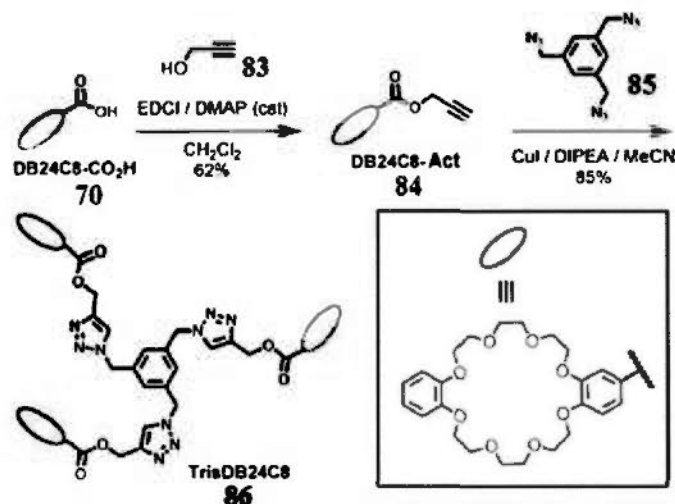
Scheme 28. The synthetic scheme of divalent linker **82** BisDB24C8.

3.8.3 Synthesis of tris-crown ether linker

Owing to the difficulties to purify the relatively polar crown ether-containing compounds and the low yield of coupling reactions with three crown ethers by ester formation, an efficient and simple “click” chemistry approach⁵⁴ was adopted to synthesize the tris-crown ether linker. The resulted linker can be precipitated out from acetonitrile in quantitative yield without any complicated purification.

DB24C8-CO₂H **70** was first coupled with propargyl alcohol **83** by 1-ethyl-3-(3-dimethylaminopropyl)carbodiimide (EDCI) to afford the DB24C8-Act **84** in 62 % yield. The TrisDB24C8 **86** was then synthesized from the copper(I)

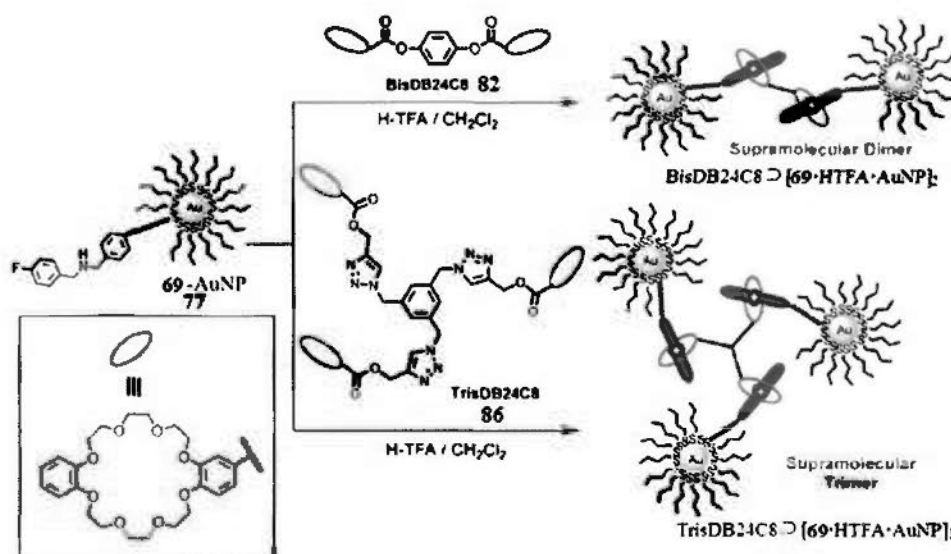
catalyzed 1,3-dipolar cycloaddition (click) reaction of DB24C8-Act **84** and tris(azidomethyl)benzene **85** to give the TrisDB24C8 **86** in 85 % yield (Scheme 29).



Scheme 29. The synthetic scheme of trivalent linker **86** TrisDB24C8.

3.8.4 Formation of AuNPs supramolecular dimers and trimers

The general scheme for formation of supramolecular AuNP dimers and trimers is shown in Scheme 30. The purified mono-functionalized AuNPs **77** were first protonated by trifluoroacetic acid in dichloromethane, which was then either mixed with BisDB24C8 **82** or TrisDB24C8 **86** to give the respective supramolecular dimers BisDB24C8 \supset [**69**·HTFA·AuNP]₂ or supramolecular trimers TrisDB24C8 \supset [**69**·HTFA·AuNP]₃).



Scheme 30. The formation of supramolecular dimers and trimers using the BisDB24C8 **82** and TrisDB24C8 **86**.

The amount of the BisDB24C8 **82** and TrisDB24C8 **86** required for exact stoichiometric ratio for self-assembling with the mono-functionalized AuNPs **77** were difficult to be achieved. Hence, several titration experiments were performed with different ratios of **77** and the linkers (w/w).

For the formation of supramolecular dimers, the ratios of mixing the mono-functionalized AuNPs **77** with BisDB24C8 **82** were 1:1, 2:1 and 3.5:1 (w/w). For the mixing ratio with 1:1 (w/w) of the mono-functionalized AuNPs **77** with BisDB24C8 **82**, the UV/visible spectrum showed that the absorption increased in intensity and completely shifted to 620 nm and ~700 nm (Figure 3-19a). The red-shifted absorption peaks corresponded to the formation of AuNPs aggregates resulting in decrease of the interparticle distance. When the amount of mono-functionalized

AuNPs **77** increased with the BisDB24C8 **82** (w/w = 2:1 and 3.5:1), the plasmonic absorption band at ~700 nm disappeared with the appearance of new red-shifted local absorption peaks at about 580 nm. It indicated that there were still modest amount of AuNPs aggregates.

The UV/visible spectroscopic titration experiment of the mono-functionalized AuNPs **77** with TrisDB24C8 **86** in different ratios (w/w= 1:1, 1:2.5, 1:4) showed similar results. For the mixing ratio 1:2.5 (w/w) of the mono-functionalized AuNPs **77** with TrisDB24C8 **86**, there was a sharp plasmonic absorption peak at ~700 nm corresponded to the AuNPs aggregation (Figure 3-19b). The intensity of the plasmonic absorption peak was not as strong as the supramolecular dimers BisDB24C8 \supset [**69**·HTFA·AuNP]₂ with the use of BisDB24C8 **82**. Such difference may be attributed to the interparticle distance of AuNPs in supramolecular trimers TrisDB24C8 \supset [**69**·HTFA·AuNP]₃ which was longer than that in supramolecular dimers BisDB24C8 \supset [**69**·HTFA·AuNP]₂ (see later section). While for other ratios of mixing the mono-functionalized AuNPs **77** with TrisDB24C8 **86** (w/w = 1:1 and 1:4), the plasmonic absorption was not observed clearly, which indicated the incorrect stoichiometric ratios of the components. The stoichiometric ratio of the components was important because there exists in excess or short of the tris-crown ether linker. With an excess of tris-crown ether linker, a mono-functionalized AuNP

can be interacted with only one tris-crown ether linker, resulting in the fact that plasmonic absorption was not observed. For the situation of insufficient tris-crown ether linker, the mono-functionalized AuNPs would be in excess so that the individual mono-functionalized AuNP absorption dominant in the UV/visible absorption.

The addition of base to the supramolecular nanostructures $\text{BisDB24C8} \supset [\mathbf{69}\cdot\text{HTFA}\cdot\text{AuNP}]_2$ and $\text{TrisDB24C8} \supset [\mathbf{69}\cdot\text{HTFA}\cdot\text{AuNP}]_3$ can disrupt the dimeric and trimeric self-assemblies, giving the UV/visible spectra simply as the sum of their separate components. These observations concluded the successful self-assembly between the mono-functionalized AuNPs **77** with the divalent (**82**) and trivalent (**86**) linkers to form supramolecular nanostructures $\text{BisDB24C8} \supset [\mathbf{69}\cdot\text{HTFA}\cdot\text{AuNP}]_2$ and $\text{TrisDB24C8} \supset [\mathbf{69}\cdot\text{HTFA}\cdot\text{AuNP}]_3$ respectively.

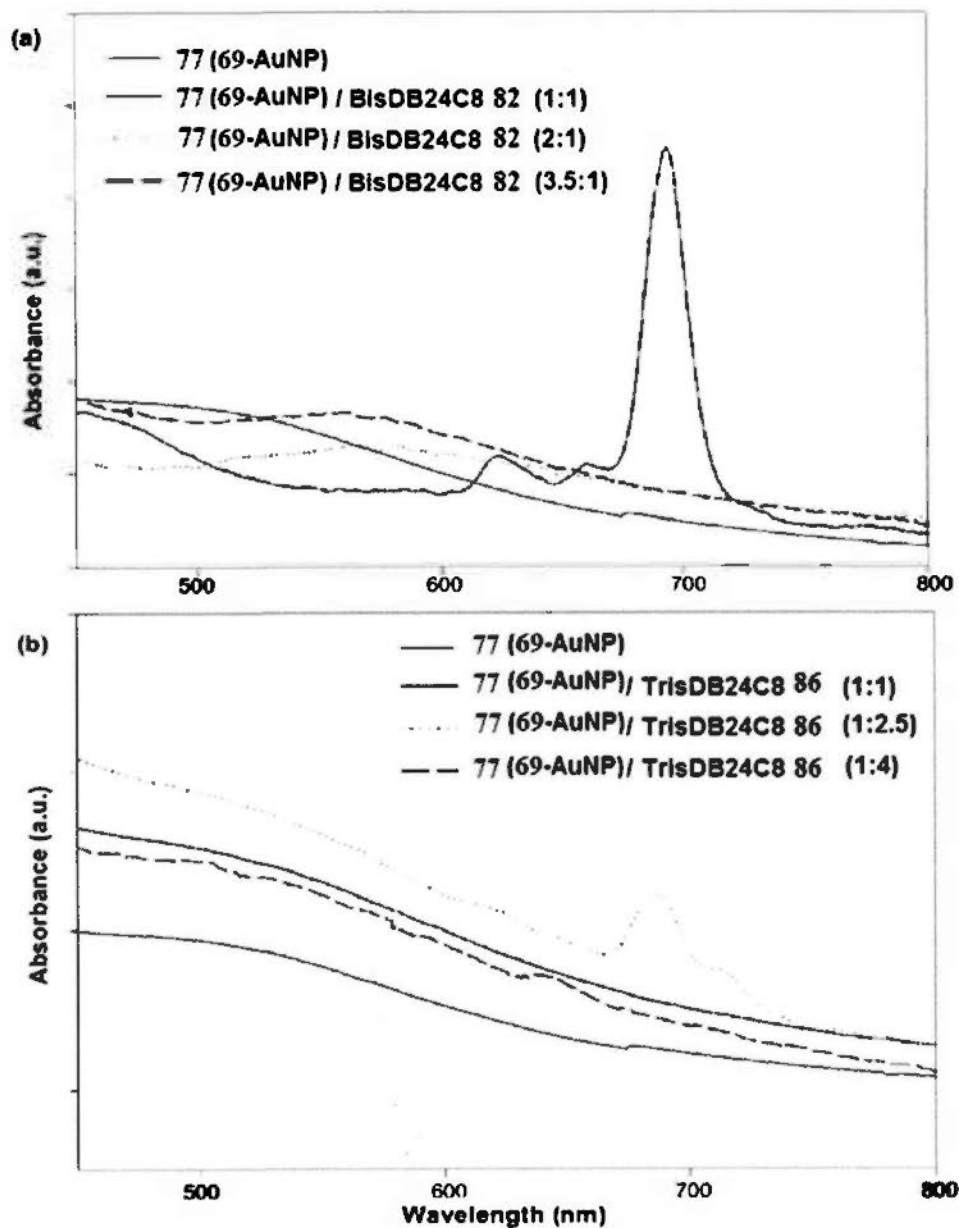


Figure 3-19. Staked UV/visible absorption spectra (CH_2Cl_2 , 298 K) of a) 77 (69-AuNP) titrated with different amounts of BisDB24C8 82 (w/w = 1:1, 2:1, 3.5:1) and b) 77 (69-AuNP) titrated with different amounts of TrisDB24C8 86 (w/w = 1:1, 1:2.5, 1:4).

The titrated solutions were analyzed by TEM. For solution of **77** (**69**-AuNP) titrated with BisDB24C8 **82** (w/w = 1:1), there were significant amounts of dimer pairs observed in the TEM (Figure 3-20a,b). The apparent interparticle spacing between the AuNP dimers ranges from 2.8 to 4.7 nm (See Section 3.8.5). For the solutions with other different titration ratios, the percentages of dimers over monomer were lower than that with the titration ratio of 1:1 (w/w). Moreover, there were no higher order supramolecular structures, such as trimers or tetramers, observed under TEM (Figure 3-21a). Hence, the obtained product should not contain multi-functionalized AuNPs, such as di-functionalized, tri-functionalized, etc, but contain mono-functionalized AuNPs **77** in near quantitative yield. Since the formation of supramolecular structures is concentration dependent, the observation of individual nanoparticles in the mixture can be due to the lowered binding affinity of the supramolecular species at low concentration during sample coatings.

For the solutions containing the supramolecular trimers, the nanoparticles **77** (**69**-AuNP) which were titrated with TrisDB24C8 **86** (w/w = 1:2.5), were analyzed by TEM. It possessed the sharpest red-shifted plasmonic absorption among all trimers containing solutions. There were dimers and trimers found in the solution (Figure 3-20c,d; blue circle for dimers; red circle for trimers). The apparent interparticle spacing between the AuNPs in trimers ranges from 1.5 to 5.1 nm (See

Section 3.8.5). For the solutions with other different titration ratios, the percentages of trimers were lower than that with the titration ratio of 1:2.5 (w/w). Moreover, there were no higher order supramolecular structures, such as tetramers, observed under TEM (Figure 3-21b).

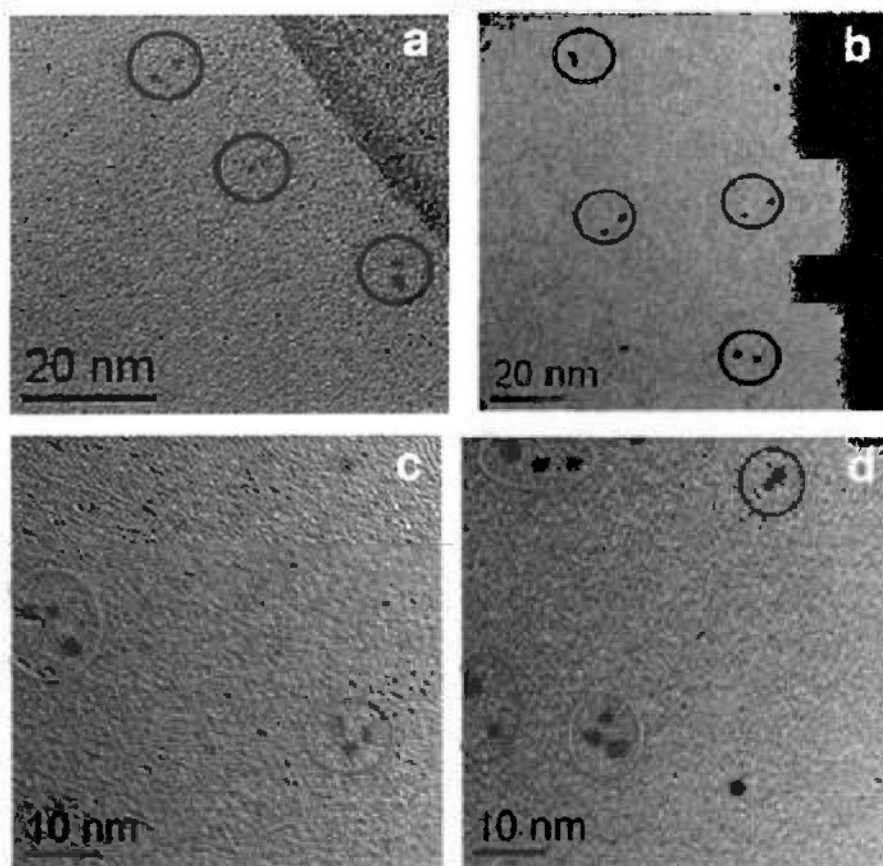


Figure 3-20. TEM images of a,b) the supramolecular dimers prepared by mixing 77 (69-AuNP) (~0.2 mg/mL) with BisDB24C8 82 in ratio 1:1 w/w, and c,d) the supramolecular trimers prepared by mixing 77 (69-AuNP) (~0.2 mg/mL) with TrisDB24C8 86 in ratio 1:2.5 w/w with blue circle indicated for dimers and red circle indicated for trimers.

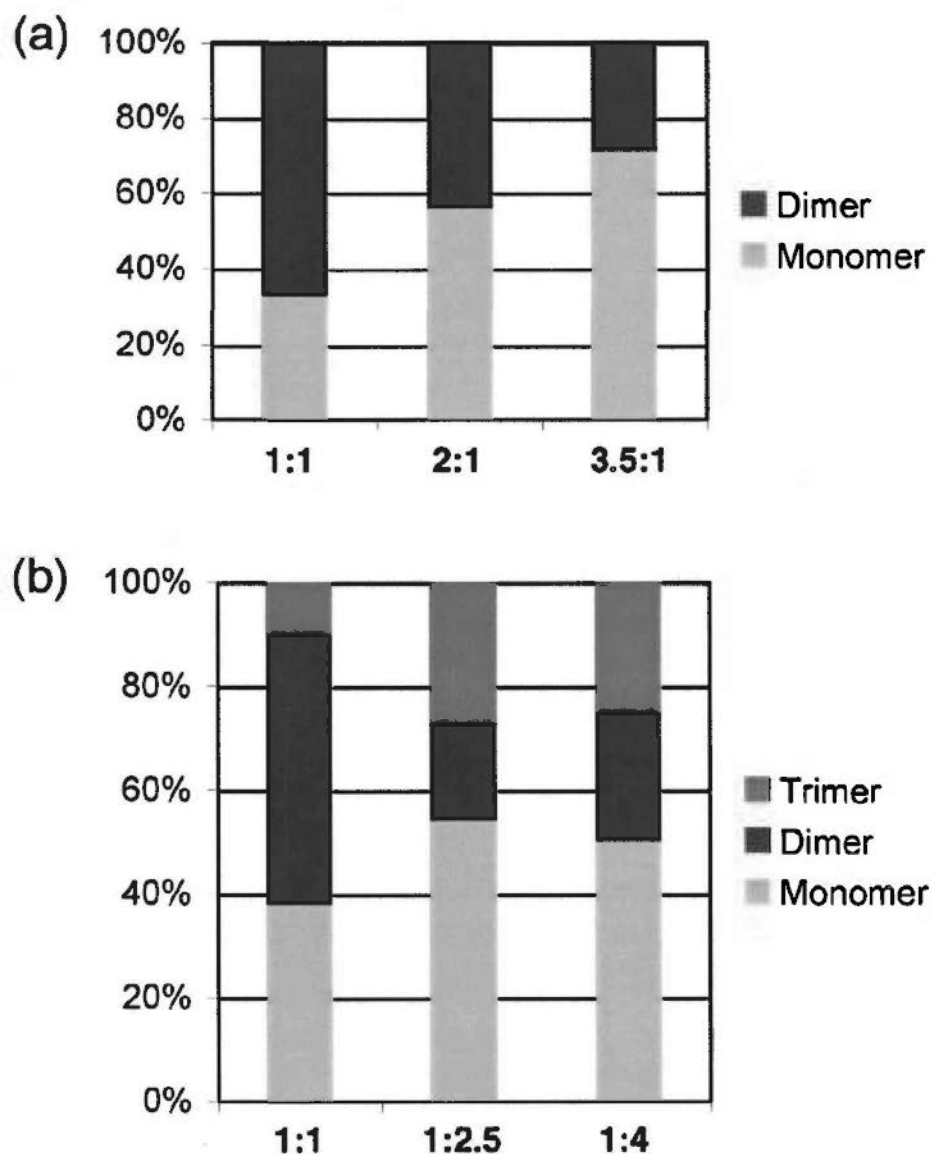


Figure 3-21. Statistical distributions in TEM analysis of a) 77 (69-AuNP) with BisDB24C8 82 with titration ratios of 1:1, 2:1 and 3.5:1; and b) 77 (69-AuNP) with TrisDB24C8 86 with titration ratios of 1:1, 1:2.5 and 1:4.

It was found that the trimers were mostly appeared as triangular shapes with a small amount of near-linear shapes. The formation of the novel near-linear shaped trimers was due to the adaptation of a folded TrisDB24C8 86 conformation in the

addition to the aliphatic attractive forces between the AuNPs' surfaces coated by numerous *n*-butyl groups (Figure 3-22).

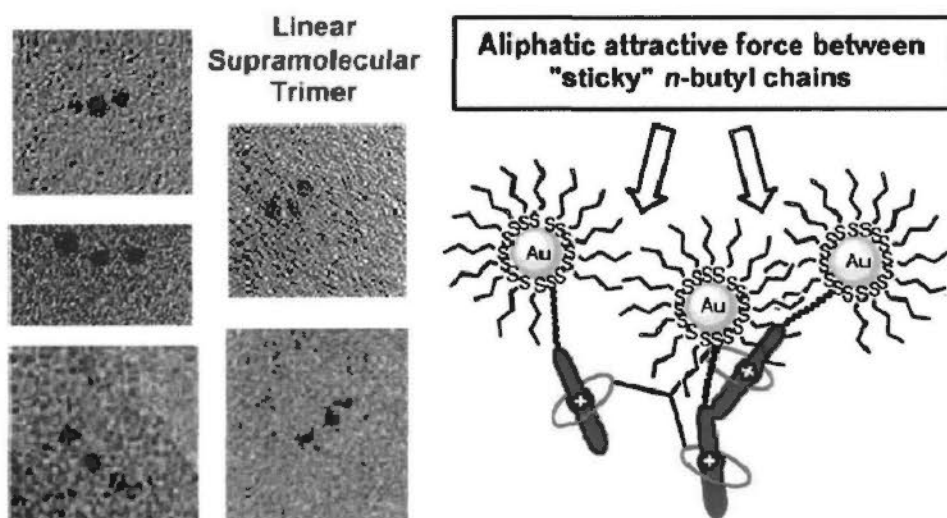


Figure 3-22. The near-linear shaped supramolecular trimers and the graphical representation of formation with the aliphatic attractive force between AuNPs' surfaces coated by the numerous of *n*-butyl groups.

3.8.5 Computational models of the AuNPs supramolecular dimers and trimers

Molecular models were constructed using Chem3D Ultra 8.0 with built-in MM2 simulations. AuNPs were omitted. The simulation pictures demonstrated the self-assemblies between the disulfide ligand and BisDB24C8 or TrisDB24C8 linkers.

There are two scenarios for the supramolecular AuNP dimers. Figure 3-23 reveals the supramolecular dimers where the disulfides (which are attached to AuNPs, but are omitted here) are positioned in opposite side from the linker with the disulfides distance 4.7 nm. Figure 3-24 shows the supramolecular dimers where the disulfides are positioned in same side from the linker with the disulfides distance 4.7

nm. Figure 3-25 shows the supramolecular dimers where the disulfides are positioned in same side from the linker with a distance of 2.8 nm.

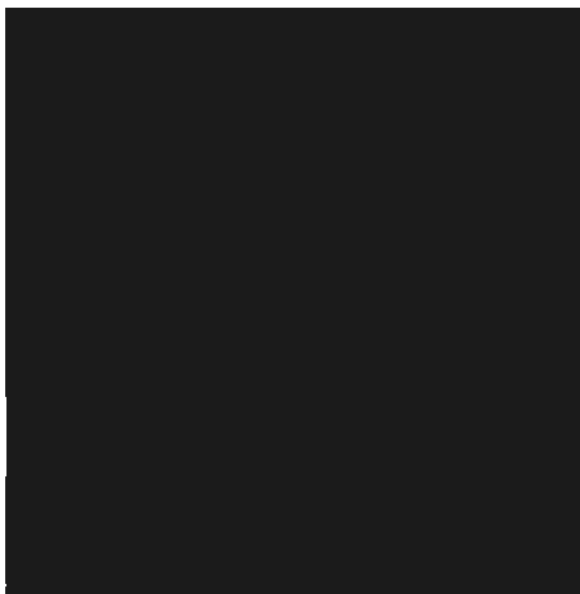


Figure 3-23. The supramolecular dimers BisDB24C8 \supset [69-HTFA·AuNP]₂ with a distance of 4.7 nm between the two disulfides. (Key: Carbon: gray; hydrogen: white; oxygen: red; nitrogen: blue; sulfur: yellow.)



Figure 3-24. The supramolecular dimers BisDB24C8 \supset [69-HTFA·AuNP]₂ with a distance of 3.5 nm between the two disulfides. (Key: Carbon: gray; hydrogen: white; oxygen: red; nitrogen: blue; sulfur: yellow.)

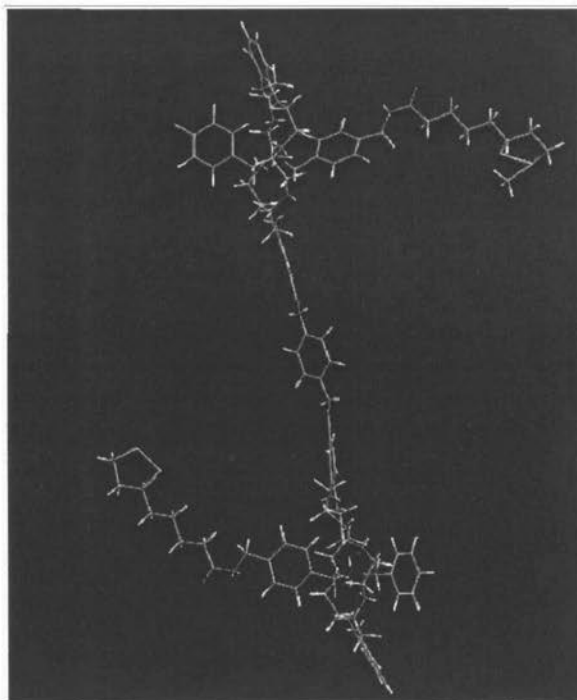


Figure 3-25. The supramolecular dimers BisDB24C8 \square [69•HTFA•AuNP]₂ with a distance of 2.8 nm between the two disulfides. (Key: Carbon: gray; hydrogen: white; oxygen: red; nitrogen: blue; sulfur: yellow.)

There are three scenarios for the supramolecular AuNPs trimers. Figure 3-26 shows the supramolecular trimers where the disulfides are in triangular shaped with the distance 2.8–5.1 nm between the two disulfides. Figure 3-27 shows the supramolecular trimers where the disulfides are in triangular shaped with the distance 2.8–3.6 nm between the two disulfides. Figure 3-28 shows the supramolecular trimers where the disulfides are in near-linear shaped with the distance 1.5–3.7 nm between the two disulfides.

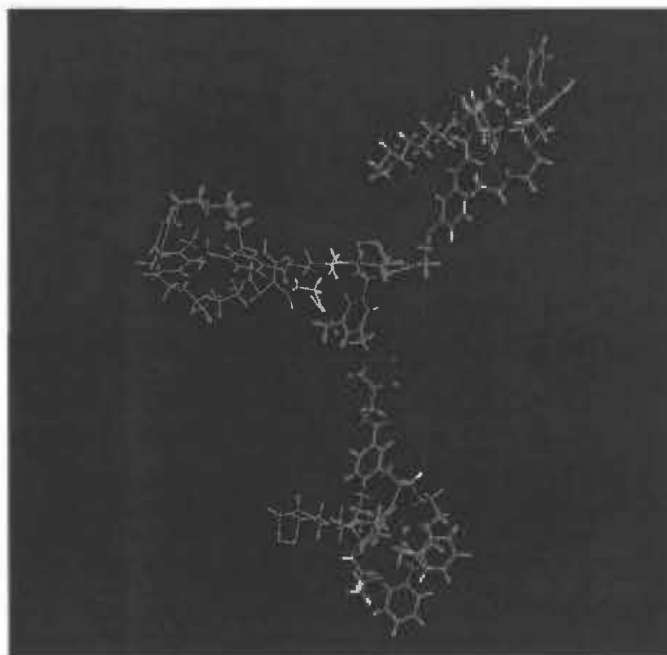


Figure 3-26. The supramolecular trimers $\text{TrisDB24C8} \supset [\text{69-HTFA} \cdot \text{AuNP}]_3$ with the distance 2.8–5.1 nm between the two disulfides. (Key: Carbon: gray; hydrogen: white; oxygen: red; nitrogen: blue; sulfur: yellow.)

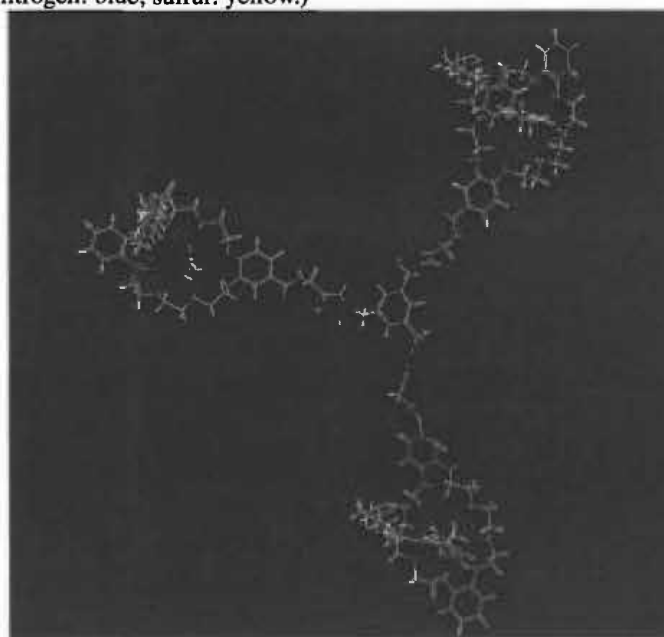


Figure 3-27. The supramolecular trimers $\text{TrisDB24C8} \supset [\text{69-HTFA} \cdot \text{AuNP}]_3$ with the distance 2.8–3.6 nm between the two disulfides. (Key: Carbon: gray; hydrogen: white; oxygen: red; nitrogen: blue; sulfur: yellow.)



Figure 3-28. The supramolecular trimers $\text{TrisDB24C8} \supset [\mathbf{69} \cdot \text{HTFA} \cdot \text{AuNP}]_3$ with the distance 1.5–3.7 nm between the two disulfides. (Key: Carbon: gray; hydrogen: white; oxygen: red; nitrogen: blue; sulfur: yellow.)

3.8.6 Control experiments

A control experiment has been performed without the use of solid-phase support polymer PS Wang resin **75**. The resulted AuNPs were randomly functionalized with more than one amine **69** functional group on each AuNP due to the uncontrolled place exchange reaction. After the addition of the trifluoroacetic acid, these randomly functionalized AuNPs **87** were treated with different amounts of BisDB24C8 **82** (w/w = 1:1, 2:1 and 4:1), 3-D networks of AuNPs were formed (Figure 3-29) and gave maximum plasmonic absorption bands at 620 nm and 700 nm (Figure 3-30).

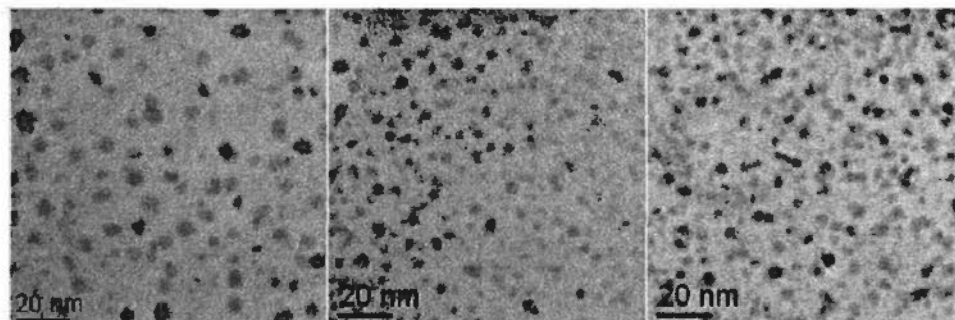


Figure 3-29. TEM images of randomly functionalized AuNPs **87** treated with different amounts of BisDB24C8 **82** with ratios a) 1:1, b) 2:1 and c) 4:1.

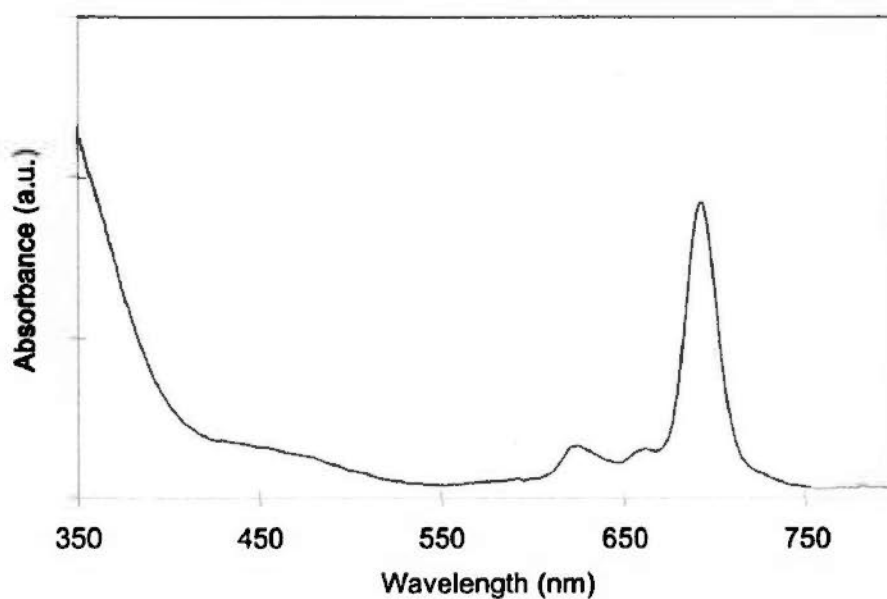


Figure 3-30. UV/visible absorption spectrum of randomly functionalized AuNPs treated with different amounts of BisDB24C8 **82** with ratios 1:1.

Another control experiment has been performed with mono-functionalized AuNPs **77** (**69**-AuNP) by treating with trifluoroacetic acid and DB24C8 instead of linkers **82** and **86**. The crown ether and the ammonium ligand on the AuNPs **77** self-assembled to form DB24C8 \supset [**69**·HTFA·AuNP]. Such mixture was analyzed by TEM and showed only segregated nanoparticles (Figure 3-31).

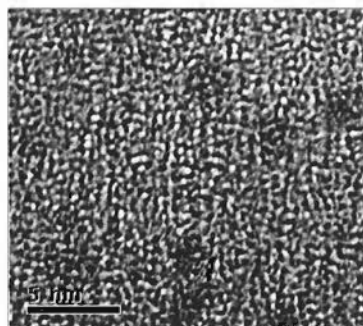


Figure 3-31. TEM image of DB24C8 \square [69·HTFA·AuNP].

3.9 Section conclusion

To conclude, novel amine mono-functionalized AuNPs **77** were synthesized and purified with supramolecular assisted method utilizing a crown ether-modified polystyrene Wang resin **76** and crown ether-modified superparamagnetic iron oxide nanoparticles **80**. The synthetic process was characterized by FT-IR, far-IR, XPS and visualized by color changes. The purification process was characterized by FT-IR, TEM and EDX. The purified mono-functionalized AuNPs **77** were characterized by TEM, FT-IR, XPS and UV/visible absorption spectroscopy. The supramolecular motifs with acid/base switchability have been found as satisfactory templates for the synthesis and purification of mono-functionalized AuNPs. Our approach enables us to obtain mono-functionalized AuNPs **77** with near quantitative yield with characterization through formation of novel supramolecular dimers and trimers. Such supramolecular nanostructures were observed under TEM and characterized with sharp plasmonic absorptions. Furthermore, the material system could be recycled and reused, so that the preparation and purification could be repeated numerous times instead of time-consuming chromatographic separation of products.

Chapter Four – Superficial Application of Discretely Functionalized AuNPs

4.1 Surface plasmon resonance characterization - General considerations

In this chapter, mechanoresponsive, acid/base-driven self-assembly/disassembly of discretely mono-functionalized AuNPs **77** on crown ether-modified gold thin film *via* pseudorotaxane chemistry³⁸ based on a novel lab-on-a-chip technique, is discussed.³² The aims of the experiment are (1) to simultaneously purify and characterize the mono-functionalized AuNPs **77** with SPR and (2) to study the different behaviors of mono-functionalized AuNPs with the randomly functionalized AuNPs in terms of the ON/OFF switchable capability of the pseudorotaxanes and their SPR signals. The mono-functionalized AuNPs should possess different SPR properties compared to the randomly functionalized AuNPs. This is because the number of ligands and the distance of agglomerates of them will render distinctive properties.^{2,16a-c} Since the discretely functionalized AuNPs contain only few and known number of recognition functional groups on the AuNPs, the discretely functionalized AuNPs are believed to provide more quantitative information for biosensing applications.^{29,55} Hence, our method which utilizes the mono-functionalized AuNPs with only one recognition functional group, can open up future applications for single molecule detection. The strategy of the experiment was to employ the SPR microfluidic device which fits on

top of a gold thin film to detect the surface plasmon polariton (SPP) absorption signals. The microfluidic device with the gold thin film experimental setup was equipped with prism settings for total internal reflection. SPP absorption signals originated from the gold thin film were observed by a charge-coupled device (CCD) camera (See Chapter 1).^{17a,e-f} Towards the applications utilizing AuNPs on the surface of gold thin film, SPR coupling with enhanced signal was expected to be observed. The acid/base-driven self-assembling and disassembling process of both the mono-functionalized AuNPs **77** and the randomly functionalized AuNPs **87** can be characterized through the changes in the SPP absorption signals in real-time. Moreover, the mono-functionalized AuNPs **77** can be purified and separated from the non-functionalized AuNPs **74** by such self-assembling and disassembling processes. Quantification study can also be studied to determine the amount of mono-functionalized AuNPs **77** obtained after the purification.

Such method for characterizing discretely functionalized AuNPs has several advantages over the conventional methods such as transmission electron microscopy (TEM), UV/visible absorption spectroscopy, and gel electrophoresis, etc. First, our method enables real-time monitoring of the self-assembling and disassembling processes of the AuNPs on the gold thin film, while all these conventional methods are difficult to be monitored in real-time. Second, additional linkers are required for

forming dimers, trimers, etc., for further UV/visible absorption spectroscopy and TEM analysis. Exact stoichiometry of the linker and AuNP is necessary to produce significant signals. Third, our mono-functionalized AuNPs **77** possess only one positive charge on the ammonium group, such small mass-to-charge ratio has negligible difference compared to the non-functional AuNPs **74**. Therefore, purification and characterization of the mono-functionalized AuNPs **77** from their crude mixture with an excess of non-functionalized AuNPs **74** cannot be performed by using gel electrophoresis. Fourth, isolation of the mono-functionalized AuNPs **77** after the characterization is inconvenient or not applicable for the conventional methods. That is, the AuNP dimers or trimers after the UV/visible spectroscopy and TEM analysis are difficult to be separated, whereas any sample coated on the copper grid for TEM analysis is also difficult to be recovered. Most importantly, the sensitivity of SPP absorption is much higher than the UV/visible absorption by at least 100-fold.³²

4.2 Device fabrication

The microfluidic device setup is shown in Figure 4-1a and Figure 4-1b. The device consists of a microfluidic chamber with a modified gold thin film (45 nm) on the glass surface. The gold thin film with dimension of 5 mm x 5 mm was coated on the glass surface by DC sputtering method.⁵⁶ Simplified procedure of the setup is shown in Figure 4-1c. A polydimethylsiloxane (PDMS) chamber was made by mixing the PDMS prepolymer and the curing agent (tridecafluoro-1,1,2,2-tetrahydrooctyl trichlorosilane) in a volume ratio of 10:1.⁵⁷ Then, the uncured PDMS was coated on a SU-8 2100 (a epoxy-based negative photoresist, 120 μm) master mould.⁵⁸ The mold with patterned PDMS was cured at 80 °C in the oven for 1 hour. The glass plate was then bonded to a polydimethylsiloxane (PDMS) chamber by exposing to oxygen plasma with 77 W reflected power, 90 mTorr chamber pressure, and an exposure time of 30 seconds. The as-fabricated PDMS chamber and the glass were compressed immediately together with a clamp after the plasma process. The PDMS-glass structure was put in the oven at 80 °C for 2 hours which can strengthen the PDMS-glass layer bond. Two fluidic ports were then inserted.

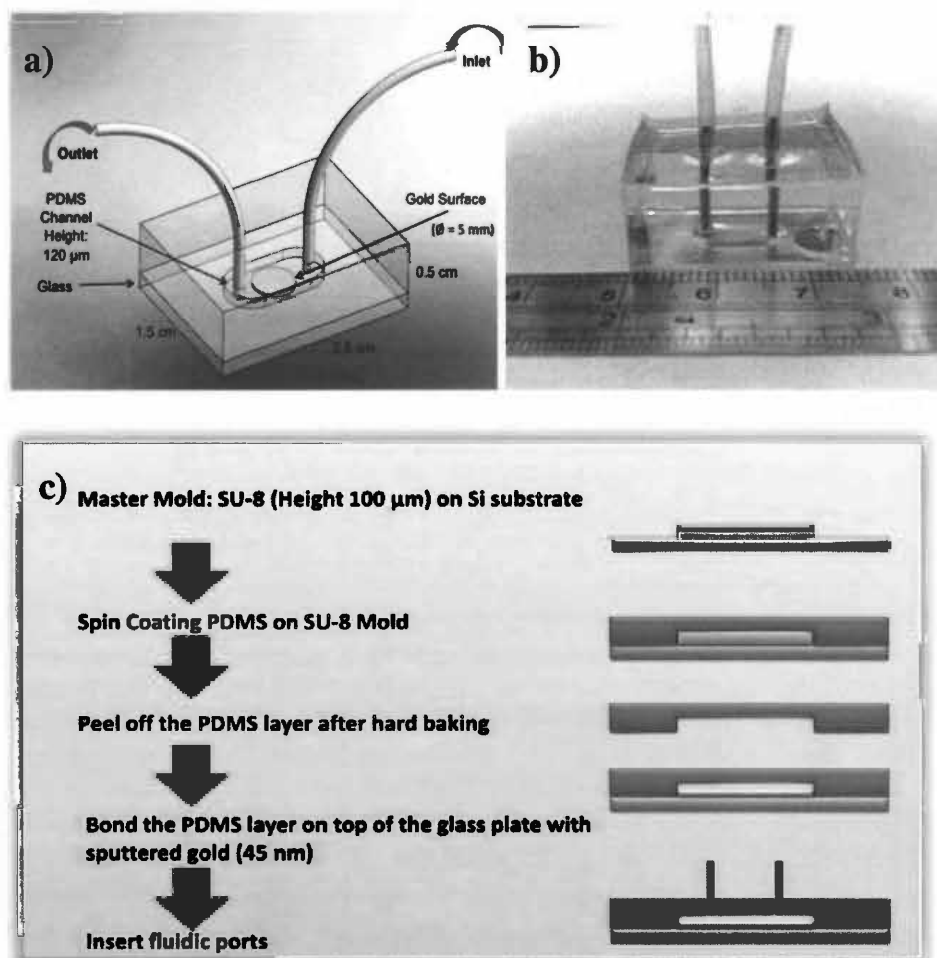


Figure 4-1. The PDMS-based microfluidic device with a gold thin layer platform illustrated by a) graphically representation and b) camera picture. The simplified procedure of preparation of the microfluidic device is shown in c).

4.3 General instrumental setup

The microfluidic device was put on a $25\ \text{mm}$ equilateral triangular prism coated with a layer of index matching oil to provide optical continuity between the two accessories. A helium–neon laser with a laser with a central wavelength of $632.8\ \text{nm}$ was used as the laser source in the experiment, the laser beam was expanded by

1.875 times by using two plano-convex lenses with focal lengths 16 mm and 30 mm respectively. The light intensity was controlled by placing a polarizer and a 10 nm slit between the lenses. A 2048 effective pixels one-dimensional linear array of CCD detector with personal computer and self-written programs were used to capture and process the signals (Figure 4-2a-c).

The signals received by the CCD was extremely sensitive to light, hence, the experiment was conducted in a dark room. While the light source traversed through several optical lenses, an optical split and equilateral triangular prism, the resulted light intensity had been attenuated. Moreover, there were electronic noises as received by the CCD because the raw signals received should contain noises and fluctuations. These noises and fluctuations were minimized with a three-step denoising process in self-written program operated in Microsoft® Windows® developed by our group. Firstly, background signal subtraction was performed to remove any spurious signals due to the optical interference effects. Secondly, 30 signal traces per second were obtained from the CCD arrays with the removal of the high frequency components. Thirdly, the data points were fitted to a three order curve to refine the resolution by a least square method. The SPR dip measurements with high resolution were found to be effective with this processing. The physical meaning of the changes in refractive index and hence, the pixel changes (+ or -)

equal to the angle shift in the resonance angle.^{17m}

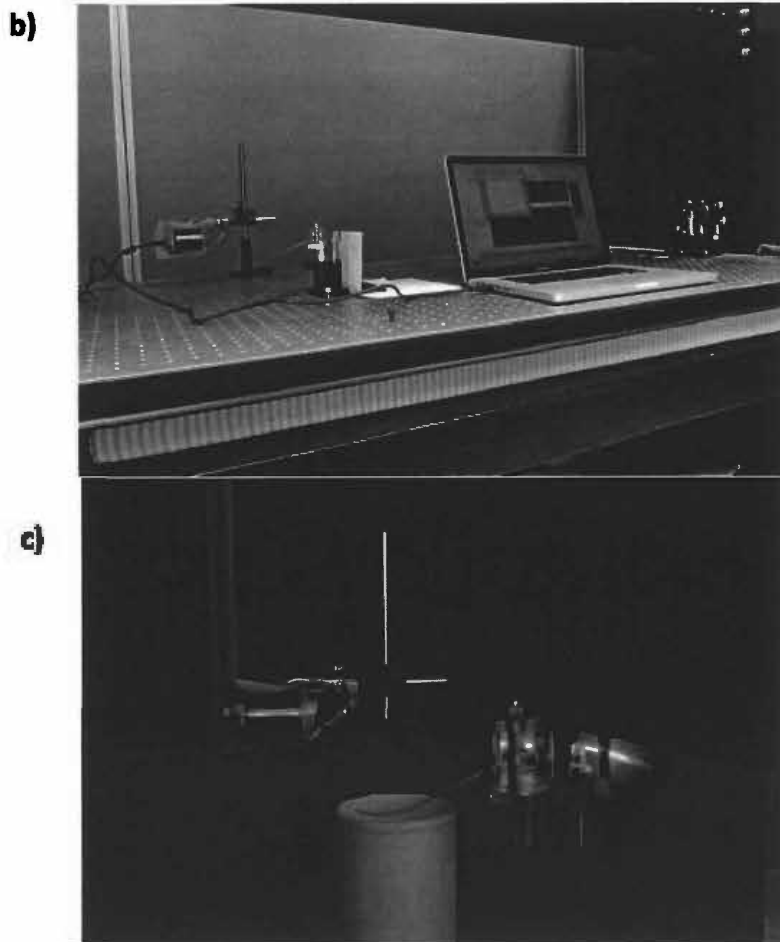
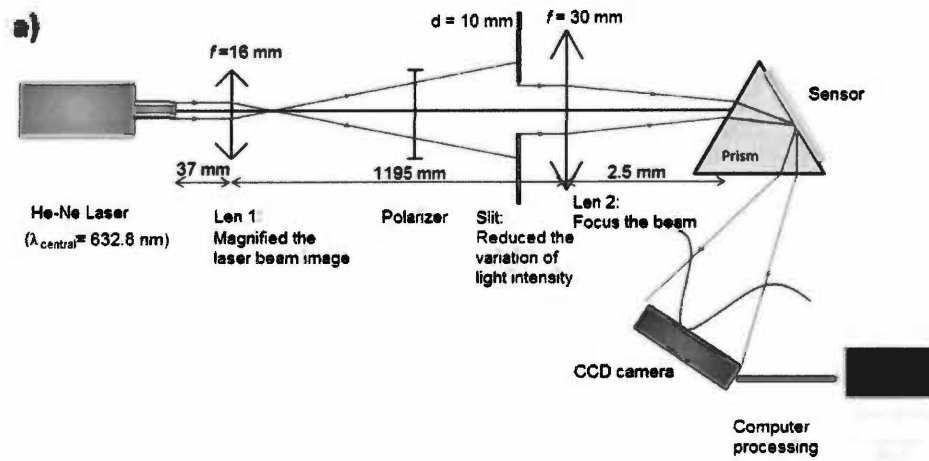
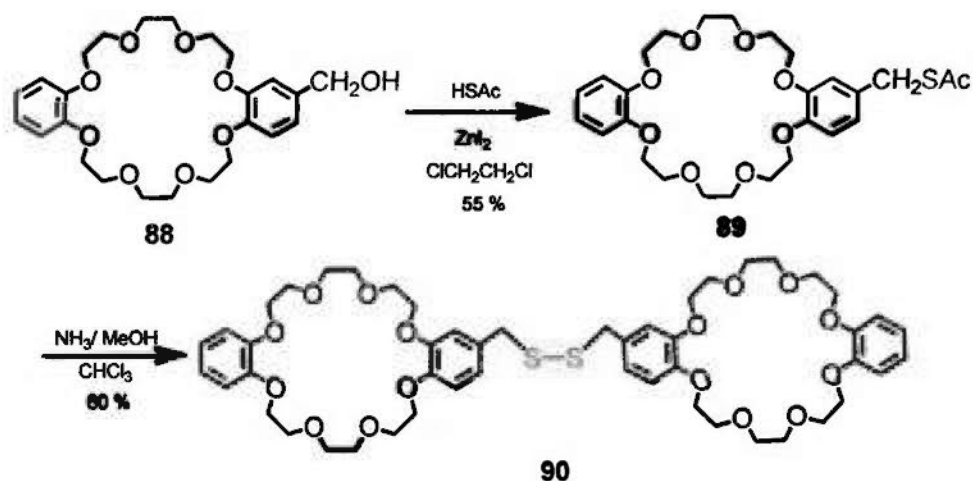


Figure 4-2. Experimental setup with microfluidic device in a) graphical representation; b) and c) camera pictures.

4.4 Synthesis and characterization of precursor

The gold thin film was modified by DB24C8, therefore, a DB24C8 with disulfides functionality was synthesized for the surface functionalization of the gold thin film.

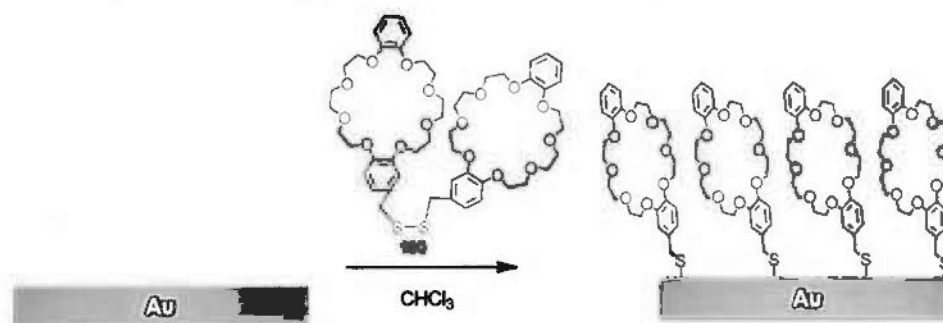


Scheme 31. The synthetic route of the disulphides (DB24C8CH₂S)₂ **100**.

To begin with, DB24C8CH₂OH **88**^{41c} was reacted with thioacetic acid in the presence of zinc iodide in 1,2-dichloroethane to afford DB24C8CH₂SAc **89** with 55 % yield (Scheme 31). The thioacetate was deprotected by the addition of ammonia in methanol and chloroform with stirring in air. Finally, the disulfides (DB24C8CH₂S)₂ **90** was obtained with 60 % yield. The obtained disulfides should be able to interact with the gold surface to form new Au–S bonds.

4.5 Self-assembling monolayer of crown ether on gold surface

The disulfides (DB24C8CH₂S)₂ **90** (2 mg in 10 mL chloroform) solution was injected into the sensor chamber and stored at room temperature for 12 hours to allow complete self-assembly of the crown ethers onto the gold surface (Scheme 32).



Scheme 32. Self-assembling monolayer of crown ether on gold surface by formation of Au–S bonds.

The whole modification process was shortened to around 100 minutes so that it can be easier to be monitored on the microfluidic device. The SPR dip location change showed that the crown ether had been self-assembled on the gold surface (Figure 4-3). For instance, the SPR dip location shifted to about -875 pixels upon the addition of the crown ether solution with a flow rate $600 \mu\text{Lmin}^{-1}$. It should be noticed that the SPR dip location shifted gradually for 1000 seconds instead of a sharp shift. It may be attributed to the dissociation reaction of the disulfide bonds for the formation of new Au–S bonds. Addition of a second batch of crown ether solution at 3000 second gradually shifted the SPR dip location in 500 seconds to the previous -875 pixels. However, upon the third and the fourth batch addition of the crown ether solution at 4800 and 5200 second, the SPR dip location shifted to -700

pixels, indicating that the crown ethers were self-assembled onto the gold surface. The sensitivity of the SPR dip shift decreases upon the surface modification since the distance between bare gold and the analytes will be separated by a mono-layer thin film of organic matter, and hence, the distance-dependent surface plasmon polaritons effect will be decreased. Therefore, further addition of crown ether solution did not give a more negative shift in SPR dip location, but a less negative shift at -700 pixels. Finally, pure chloroform was injected to remove any free crown ether in the solution in the device and the SPR dip location gave a permanent negative shift at -430 pixels from the baseline. Hence, the crown ether has been self-assembled on the surface of the gold thin film by the formation of Au-S bond.

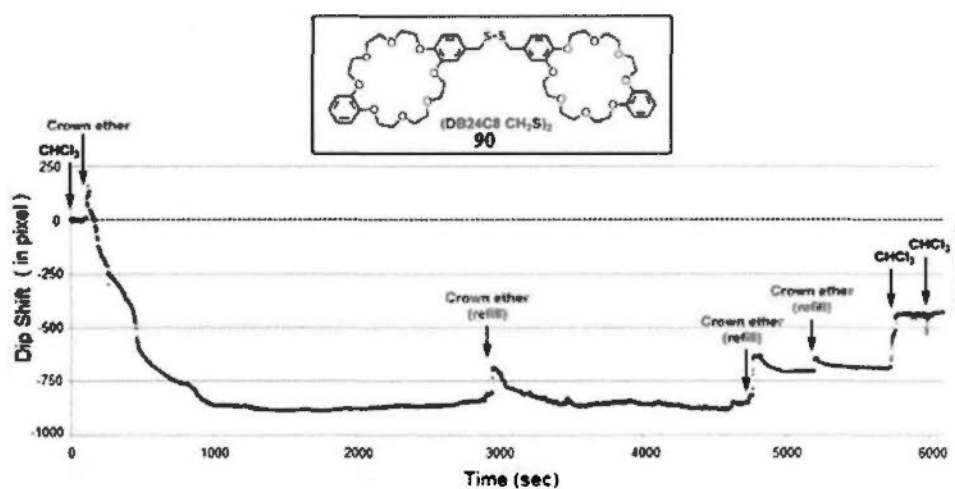


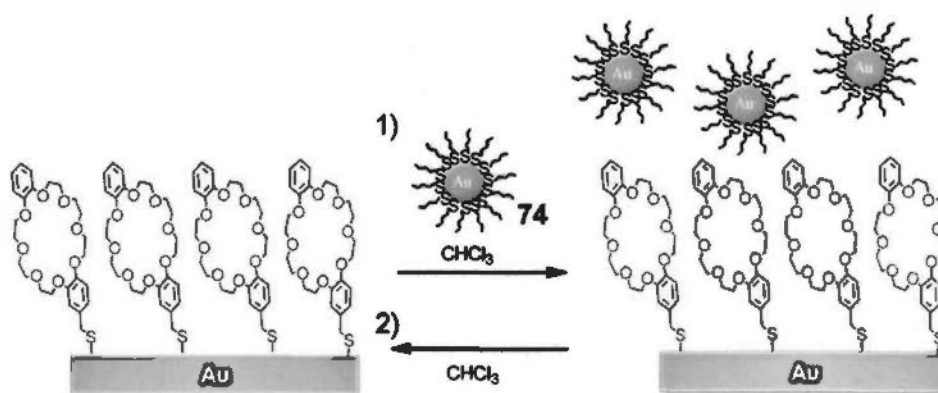
Figure 4-3. Modification of gold thin film by $(\text{DB24C8-CH}_2\text{S})_2$ **90**, which was characterized and monitored by SPR trace in real-time.

4.6 SPR characterization of the self-assembling and disassembling process

The SPR trace of the mono-functionalized, crude, randomly functionalized AuNPs during self-assembling and disassembling on the gold surface and the non-functionalized AuNPs were monitored carefully in real-time in order to achieve the aims of the experiments.

4.6.1 *n*-butanethiolate coated AuNPs

A control experiment was first performed with *n*-butanethiolate AuNPs **74** (Scheme 33). Since the *n*-butanethiolate AuNPs **74** was coated with *n*-butanethiolate without any functional groups that can be self-assembled with the crown ether, it is regarded as non-functionalized AuNPs. It was expected that such AuNPs would not be self-assembled on the gold surface and can be washed away by the addition of solvent. Hence, the SPR trace should return to its baseline as the dip shift due to the absence of AuNPs.



Scheme 33. The injection of non-functionalized AuNPs to the crown ether-coated gold surface and the washing process to remove the nanoparticles.

For instance, the non-functionalized AuNPs 74 was injected to the microfluidic device with a flow rate $600 \mu\text{Lmin}^{-1}$ (Figure 4-4), the dip shifted to an average -50 pixel over about 600 seconds with the three successive additions. When pure chloroform was injected at 800 second, the SPR dip returned back to the baseline, indicating that, expectedly, the non-functionalized AuNPs were not self-assembled onto the gold surface.

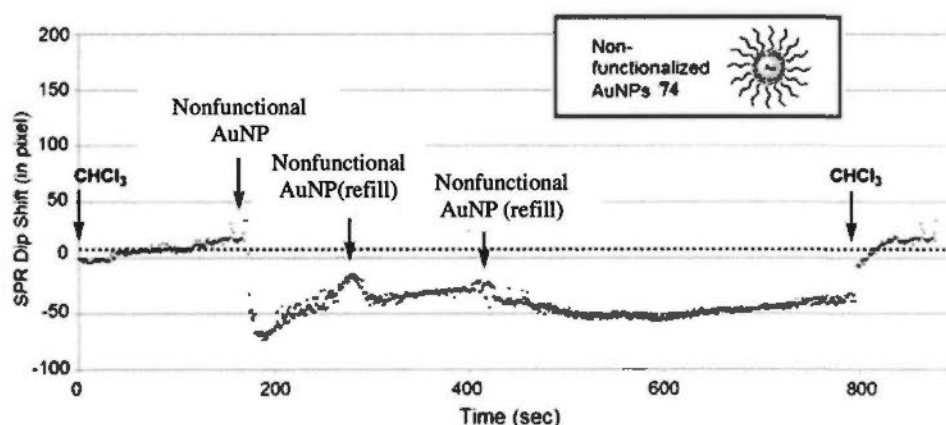
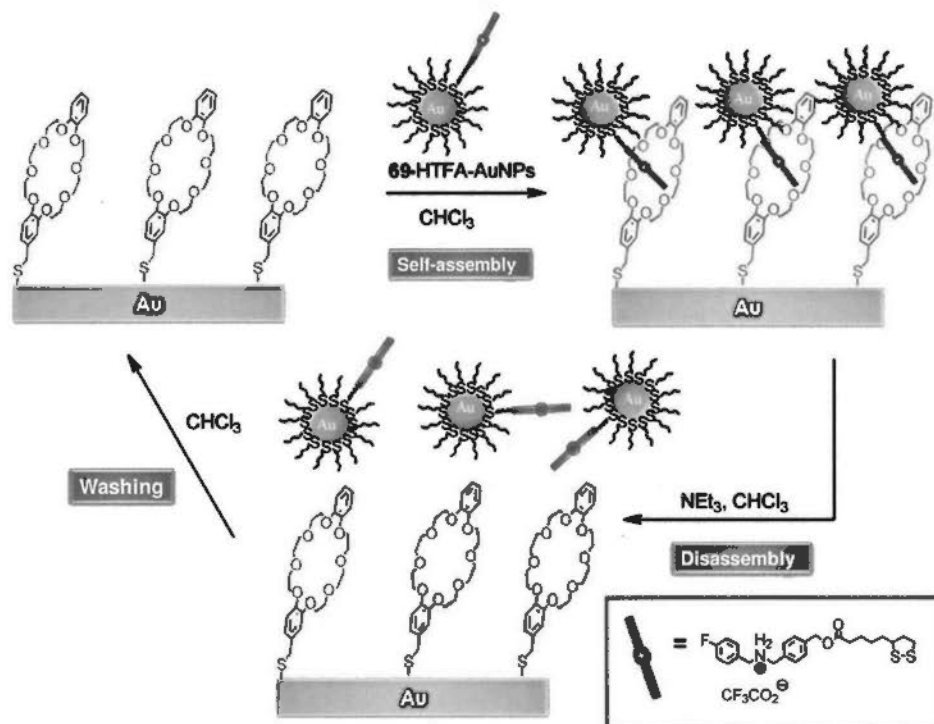


Figure 4-4. The SPR trace of non-functionalized AuNPs 74.

4.6.2 Purified discretely mono-functionalized AuNPs

The purified mono-functionalized AuNPs 77 were obtained from the supramolecular solid-phase site-isolation method after magnetic purification (See Chapter 3).⁴² It was expected that the secondary ammonium mono-functionalized AuNPs (69-HTFA·AuNPs) were self-assembled with the crown ether of the gold surface by forming pseudorotaxanes via multiple hydrogen bonds, such as $[\text{C}-\text{O}\cdots\text{H}-\text{N}^+]$ and $[\text{C}-\text{O}\cdots\text{H}-\text{C}-\text{N}^+]$, ion-dipole interactions and $\pi-\pi$ interactions, etc. The

pseudorotaxane formation can be switched ON or OFF by adding acid/base to the system so that the amine on AuNPs was protonated or the ammonium on AuNPs was deprotonated, respectively (Scheme 34).



Scheme 34. The self-assembling and disassembling processes of the mono-functionalized AuNPs 77.

The SPR dip shift was monitored carefully for the whole self-assembling and disassembling processes (Figure 4-5a). The SPR dip location was calibrated to zero as baseline for pure chloroform in the microfluidic device (Figure 4-5a, zone A). The amine group in mono-functionalized AuNPs was first protonated by trifluoroacetic acid to give ammonium mono-functionalized AuNPs in chloroform. At 150 second (Figure 4-5a, zone B), mono-functionalized AuNPs in chloroform was injected to the

device with a flow rate $600 \mu\text{Lmin}^{-1}$ at 300 second with sharp shift of -110 pixels. The system was settled for 600 seconds and then a steady signal at -40 pixels was observed. In order to maximize the amount of the mono-functionalized AuNPs that was self-assembled on the gold surface, another batch of the mono-functionalized AuNPs was injected with the same flow rate at 900 seconds to the device. Again, a sharp shift in dip location was finally steady at -70 pixels. The second injection gave a more negative pixel shift than the first injection, which indicated that more mono-functionalized AuNPs were self-assembled on the gold surface on the addition of free mono-functionalized AuNPs floating in the solution within the volume space of the device. Then, pure chloroform was injected to the device (Figure 4-5a, zone C) to wash away the free mono-functionalized AuNPs. The SPR dip shift was steady at -30 pixels for 400 seconds until the addition of base, which showed that the mono-functionalized AuNPs was self-assembled on the crown ether of the gold surface successfully. The pseudorotaxane structure was stable in the chloroform flow. Then, the injection of triethylamine base solution (11 % in chloroform) with a flow rate $600 \mu\text{Lmin}^{-1}$ continuously twice was performed so as to disassemble the mono-functionalized AuNPs (Figure 4-5a, zone D).^{39j,k} The dip location shifted to steady positive pixel values between $+60$ and $+70$ pixels. The deprotonated mono-functionalized AuNPs were disassembled from the gold surface. Finally, pure

chloroform was injected with the same flow rate to the device to wash away any free AuNPs left in addition to the base solution and excess salts (Figure 4-5a, zone E). The dip location was then returned to zero pixel (the baseline).

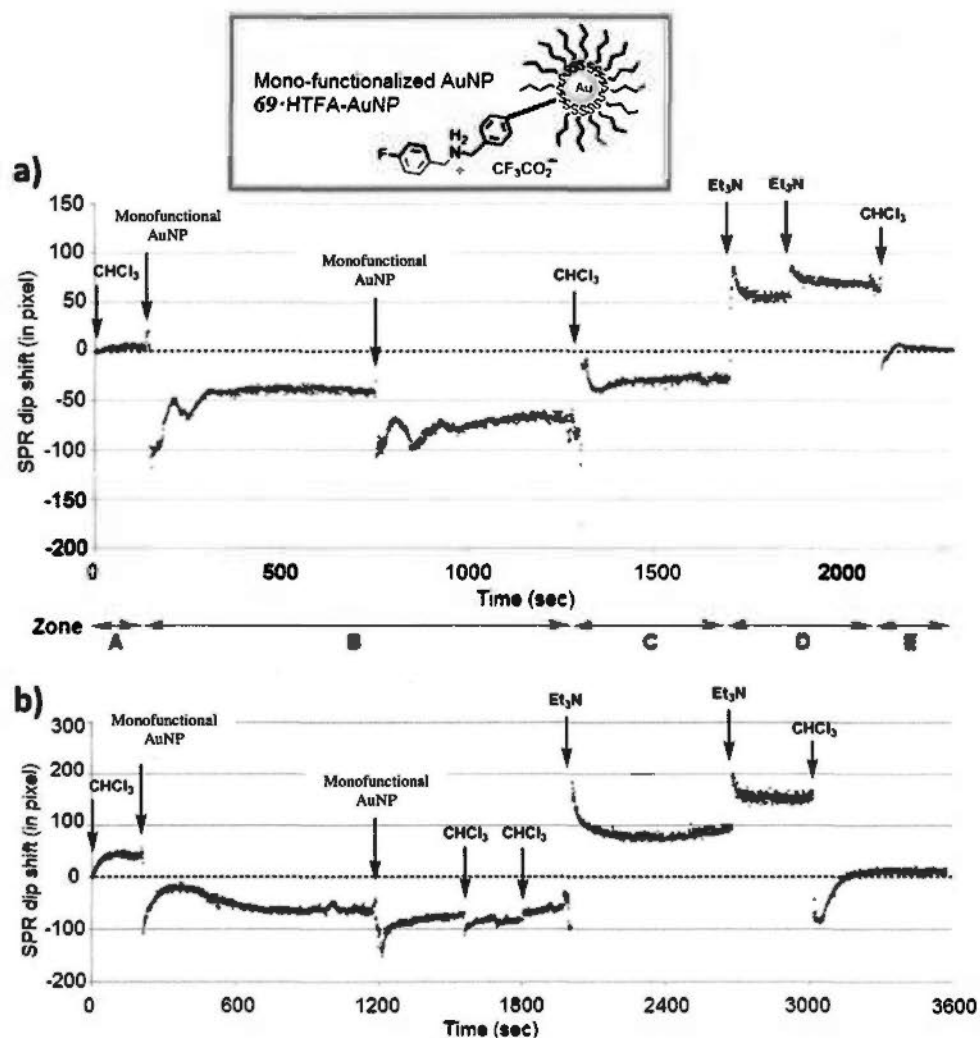


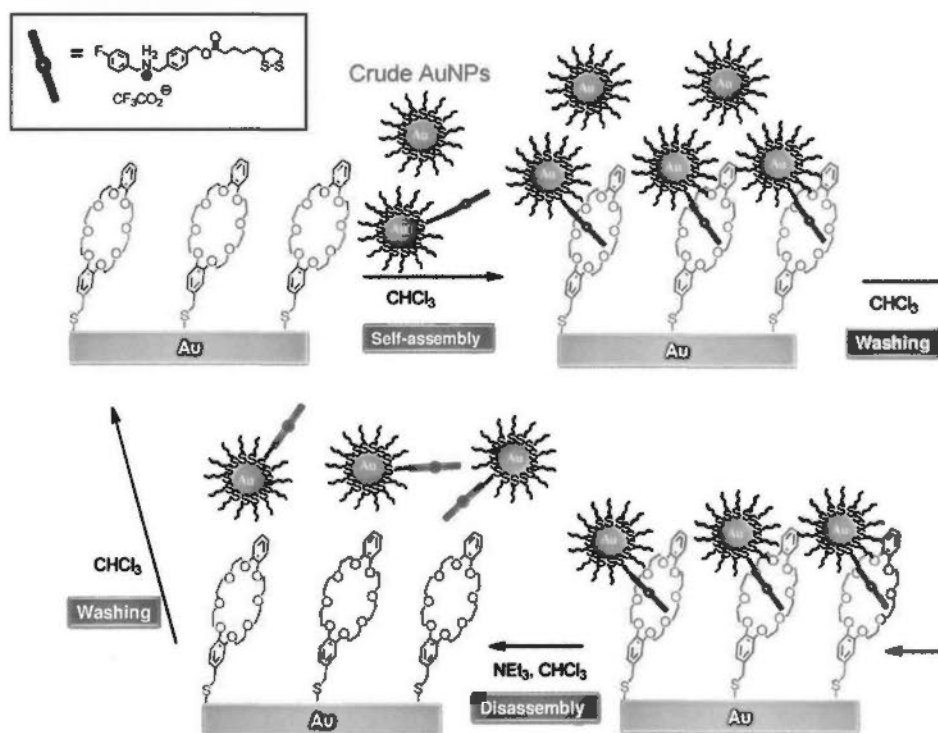
Figure 4-5. a) The real-time SPR trace of the self-assembling and disassembling processes of the mono-functionalized AuNPs on the crown ether-coated gold surface. Additional SPR trace of the processes was shown in b).

Hence, no AuNPs remained on the gold surface of the device. A complete acid/base-driven self-assembling and disassembling process of the

mono-functionalized AuNPs on the crown ether-coated gold surface was achieved. The SPR device can be reused for repeated experiments whereas similar results were achieved with a high reproducibility (Figure 4-5b).

4.6.3 Crude AuNPs from the synthetic process

In order to test the feasibility of purifying the mono-functionalized AuNPs, a significant amount of the interfering species (non-functionalized AuNPs **74**) is present as a crude mixture of the mono-functionalized AuNPs **77**. Therefore, the crude mixture of AuNPs obtained from the preparation of the mono-functionalized AuNPs **77** by supramolecular solid phase site isolation method in the presence of significant amounts of the non-functionalized AuNPs **74**, were tested for the purification analysis. The ratio of the mono-functionalized AuNPs **77** to the non-functionalized AuNPs **74** in the crude mixture was approximately 1.8:1 based on the calculation from the recovery of the mono-functionalized AuNPs (6.3 mg) starting from 10.0 mg non-functionalized AuNPs. Though it has been explored by us that the magnetic separation⁴² was efficient to give the mono-functionalized AuNPs, a novel SPR technique to simultaneously purify and characterized the mono-functionalized AuNPs was developed and compared to their efficiencies.



Scheme 35. The self-assembling and disassembling processes of the crude mixture of AuNPs.

For instance (Scheme 35), the crude mixture of AuNPs obtained from the synthesis of the mono-functionalized AuNPs was injected to the device with a flow rate $600 \mu\text{Lmin}^{-1}$ at 140 second (Figure 4-6, zone A). The SPR dip shift changed to -200 pixels, gradually from 140 second to 750 second (Figure 4-6, zone B). While the injection of the second batch of the AuNPs solution further changed the dip shift to -400 pixels, gradually from 750 second to 1350 second. It was noticed that the dip shift changed gradually which was similar to that in the case of non-functionalized AuNPs. Such phenomenon may be explained that the non-functionalized AuNPs did not consist of ammonium functional groups and hence, they would not be

self-assembled on the crown ether-coated gold surface, and they were just dispersed in the solution and slowly diffused to the gaps between crown ether or defects of the gold surface, resulting in a decrease in distance between AuNPs and gold surface. While the self-assembling process of the mono-functionalized AuNPs gave fast responses to give a steady SPR dip shift (see previous section) which showed that the formation of pseudorotaxane was highly favorable. Since the crude mixture of AuNPs consisted of both types of nanoparticles, the properties of the SPR dip shift were expected to combine with the properties of these nanoparticles, which gave an overall change in SPR dip shift gradually. The injection of pure chloroform to the device (Figure 4-6, zone C) to remove any excess mono-functionalized AuNPs and the free non-functionalized AuNPs gave a rapid dip shift to -110 pixels (Figure 4-6, zone C, blue arrow), which corresponded to the self-assembled mono-functionalized AuNPs. Hence, the injection of triethylamine solution (11 % in chloroform) would deprotonate the ammonium group on the AuNPs and also the mono-functionalized AuNPs would be disassembled (Figure 4-6, zone D).

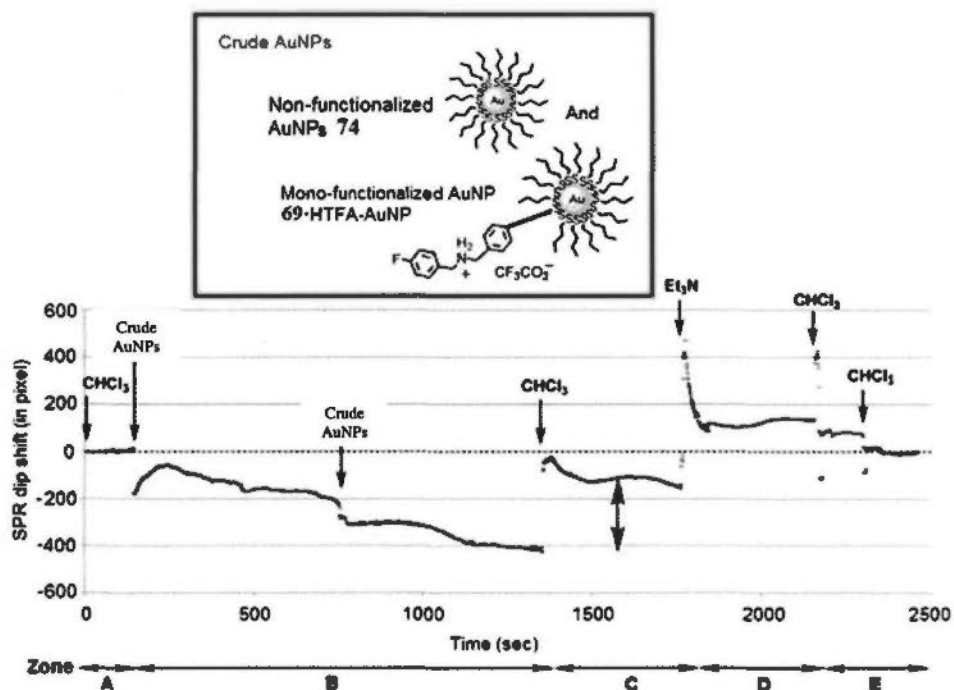


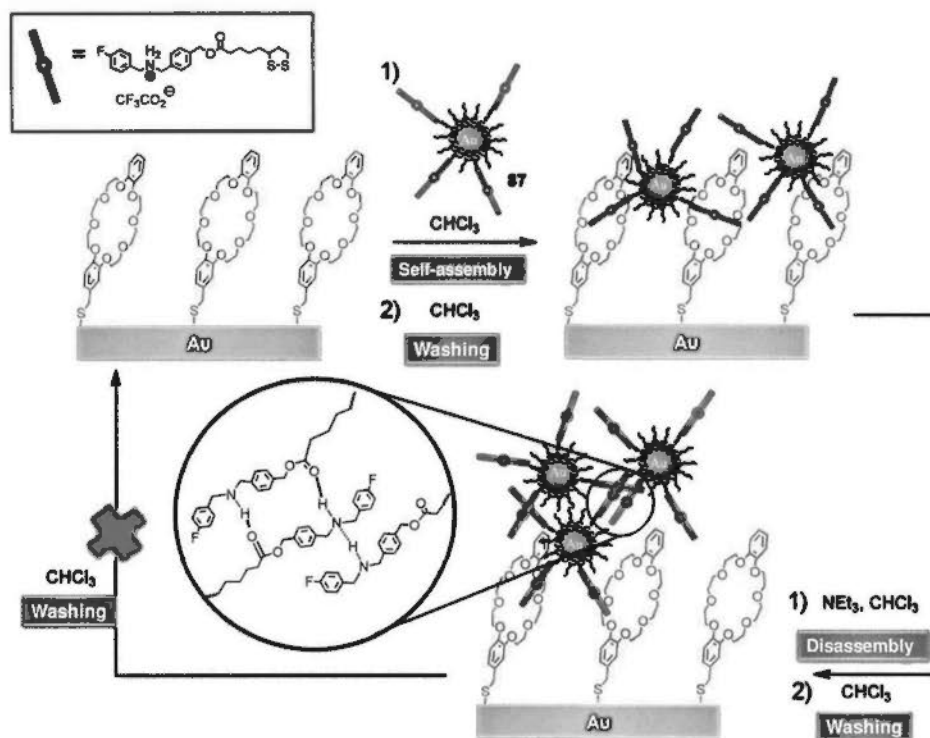
Figure 4-6. The real-time SPR trace of the self-assembling and disassembling processes of the mono-functionalized AuNPs on the crown ether-coated gold surface in the presence of the non-functionalized AuNPs (crude mixture).

Finally, the subsequent washing step for the device by injecting pure chloroform twice (Figure 4-6, zone E) gave a SPR dip shift at zero pixel (baseline), which indicated that all mono-functionalized AuNPs were washed away. The ON/OFF switching of the pseudorotaxane was also complete in this case which was the same as that with purified mono-functionalized AuNPs. The mono-functionalized AuNPs were obtained with excellent efficiency whereas a quantification study was performed and discussed in section 4.2.1.

4.6.4 Randomly functionalized AuNPs

Randomly functionalized AuNPs **87** with an uncertain number of amine ligand **69** on the surface of the AuNPs were synthesized from an uncontrolled ligand place exchange reaction in the absence of the solid phase support resin.⁴² The number of amine groups on each nanoparticle may vary from particles to particles. The study of the self-assembling and disassembling properties of the randomly functionalized AuNPs by SPR device was crucially important since most of the current applications are involved with randomly functionalized AuNPs (See section 1.6). It was expected that the SPR properties of the randomly functionalized AuNPs and mono-functionalized AuNPs are different due to different numbers and nature of the ligand on the AuNPs, leading to different applications. Moreover, the ligands on each randomly functionalized nanoparticles may interact strongly and multivalently with themselves to form an aggregated shell. Therefore, the interactions between a functionalized ligand with target molecules could be difficult to proceed. Moreover, the SPR signals of the resulting AuNP aggregates may not be quantitative to the target detection since randomly functionalized AuNPs usually formed a network of aggregates. These aggregates will perhaps contain any unbounded AuNPs by a trapping effect. The amount of target interacts with each randomly functionalized nanoparticle could be different and that the degree of network aggregation varies

from time-to-time for repeated measurements.



Scheme 36. The self-assembling and disassembling process of the randomly functionalized AuNPs 97.

Therefore, the self-assembling and disassembling processes of the randomly functionalized AuNPs were subjected to the SPR characterization (Scheme 36). The randomly functionalized AuNPs solution was injected to the device three times (Figure 4-7, zone B). The SPR dip location shifted to -130 , -170 and -180 pixels respectively. It was worth to point out that the dip shift was also sharp and fast responsive as the mono-functionalized AuNPs. Hence, the self-assembling process of the randomly amine-functionalized AuNPs was also a fast and efficient process. There were no gradual shifts in dip location, so the nanoparticles solution should not

consist of any non-functionalized AuNPs. The triple addition of the randomly functionalized AuNPs gave also more negative shifts each time. After the AuNPs were self-assembled onto crown ether-coated gold surface, the solution was more saturated with the free randomly functionalized AuNPs dispersed throughout the solution. Then, pure chloroform was injected to the device to remove any free randomly functionalized AuNPs (Figure 4-7, zone C). It indicated that the randomly functionalized AuNPs were successfully self-assembled onto the crown ether-coated gold surface. After that, a base (pure triethylamine) was injected (Figure 4-7, zone D) to the device, and the device was washed with pure chloroform four times to remove any free AuNPs, base and salts (Figure 4-7, zone E). It was quite surprising that there was residue permanent dip shift at -40 pixels (Figure 4-7, zone E, blue arrow). The disassembling process of the randomly functionalized AuNPs on the crown ether-coated gold surface was different from that of mono-functionalized AuNPs and their crude mixture with non-functionalized AuNPs. Hence, the result showed that partial randomly functionalized AuNPs were still assembled onto the gold surface.

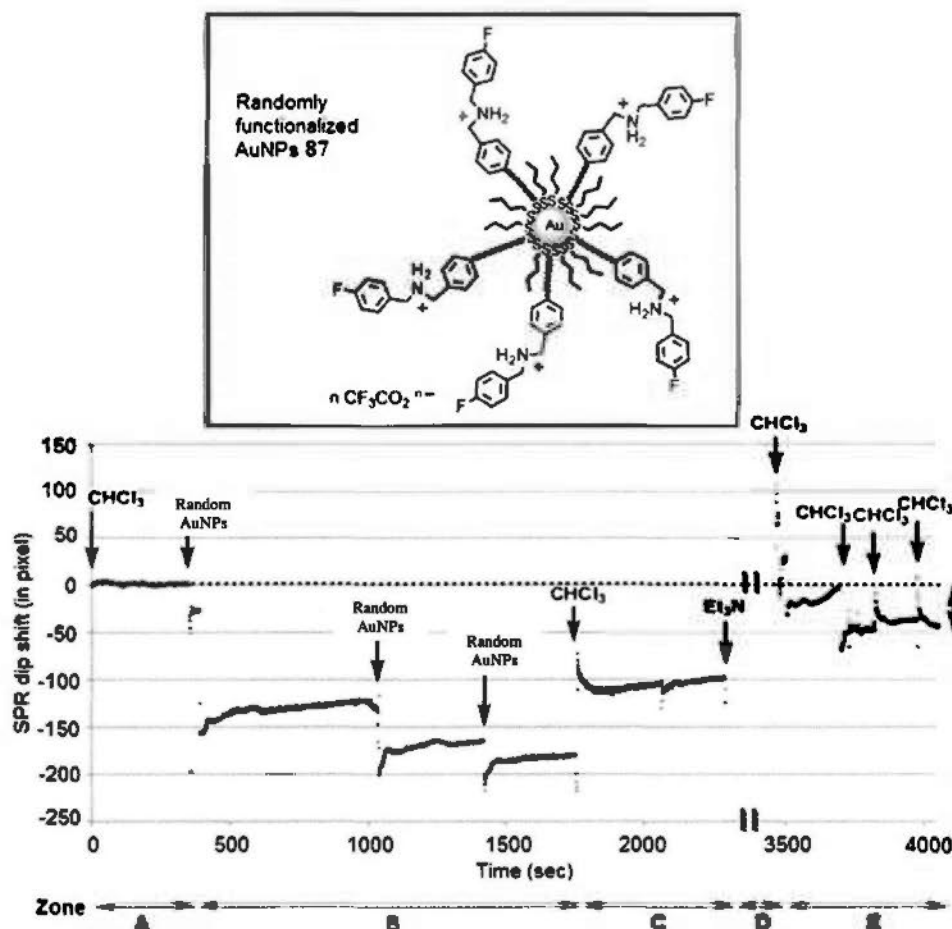


Figure 4-7. The real-time SPR trace of the self-assembling and disassembling processes of the randomly functionalized AuNPs 87 on the crown ether-coated gold surface.

It was reasonable that after the extensive washing process with chloroform and base treatment, there were smaller number of functional groups could be deprotonated and washed away. As proposed in the beginning of this section, a series of randomly functionalized AuNPs with a larger number of functional groups were still interacted to the crown ether-coated gold surface by multivalent binding mode with enhanced stability towards the base, such as multiple hydrogen bonds and π - π interactions.^{59a}

4.7 Atomic force microscopy

The morphologies of the crown ether-coated gold surface (Figure 4-8a), the crown ether-coated gold surface upon self-assembling of mono-functionalized AuNPs (Figure 4-8b) and randomly functionalized AuNPs (Figure 4-8c) were determined by atomic force microscopy (AFM). The crown ether coated-gold surface was relatively flat (Figure 4-8a) and the surface became rougher upon self assembling of the mono-functionalized AuNPs (Figure 4-8b). The spherical domains observed on such rough surface are believed to be the AuNPs. On the other hand, the crown ether-coated gold surface upon self-assembling of randomly functionalized AuNPs (Figure 4-7c) had a rough surface with more spherical domains, which were the AuNPs. Meanwhile, the randomly functionalized gold nanoparticles self-assembled the crown ether-coated gold surface after the base treatment (Figure 4-7, zone D and E) showed significant amount of spherical domains after washing with chloroform extensively. Such observation matched with the SPR dip shift result, and our hypothesis that a series of randomly functionalized AuNPs were still intact of the crown ether coated-gold surface with enhanced base stability.

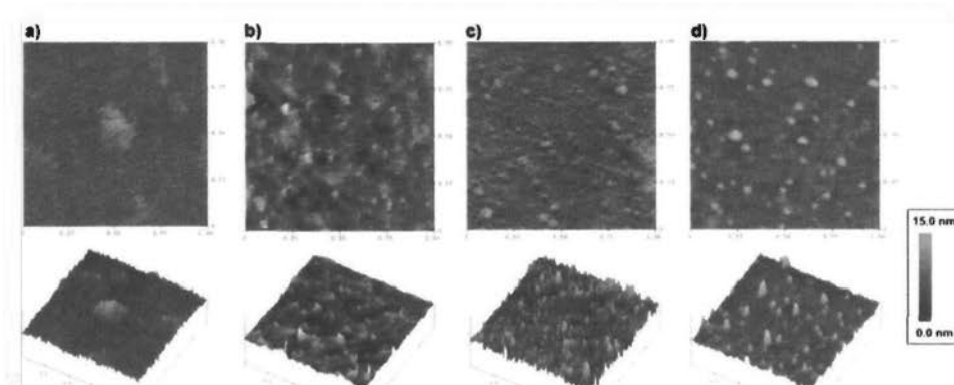


Figure 4-8. $1\ \mu\text{m} \times 1\ \mu\text{m}$ 2-D (above) and 3-D (below) atomic force microscopic images of a) crown ether-coated gold surface; b) crown ether-coated surface self-assembled with mono-functionalized AuNPs; c) crown ether-coated gold surface self-assembled with randomly functionalized AuNPs and d) crown ether-coated gold surface self-assembled with randomly functionalized AuNPs after washing with base and chloroform.

4.8 Purification of mono-functionalized AuNP from crude mixture

The mono-functionalized AuNPs were obtained from purification by the microfluidic device. Following the same procedure as in section 4.1.6.3 and started with 0.4 mg crude AuNPs with a concentration of 2.5 $\mu\text{g/mL}$, the final AuNP solutions obtained from the injection of base and chloroform were collected and dried in vacuum. Then, it was subjected to the ^1H NMR spectroscopic analysis.

4.8.1 Quantification study

Nitromethane was used as the internal standard to determine the yield of the mono-functionalized AuNPs obtained from the microfluidic device. For instance, known amount of the nitromethane (0.05 μL) was added to the CDCl_3 solution of the obtained mono-functionalized AuNPs and subjected to ^1H NMR spectroscopic analysis for about 1000 scans (Figure 4-9). The ratio of benzyl- CH_2 -⁴² at chemical shift δ 5.16 to the internal standard CH_3 - at the chemical shift at δ 4.33 was 0.1813 to 100. Hence, there was about 0.19 mg mono-functionalized AuNPs obtained, the percentage yield was about 48 % with relative error of 5 %.^{59b} Since the percentage yield of mono-functionalized AuNPs after magnetic separation, the purification efficacy after microfluidic purification was comparable.

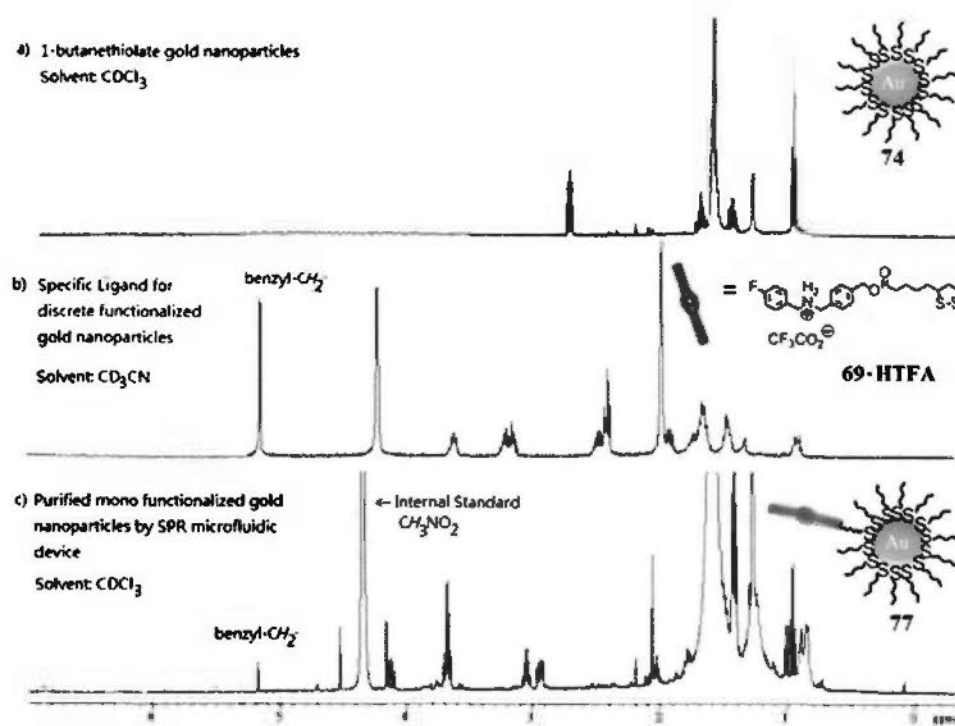


Figure 4-9. Stacked ^1H NMR of a) 1-butanethiolate (nonfunctional) AuNPs (2 nm); b) specific ligand for discrete functionalized AuNPs; and c) mono-functionalized AuNPs after purification by the SPR microfluidic device (Number of scan = 1567, relaxation delay (d1) = 1 sec).

4.9 Section conclusion

Chloroform-compatible microfluidic device for real-time surface plasmon resonance characterization was developed to monitor the self-assembling and disassembling processes of mono-functionalized AuNPs **77**, non-functionalized/mono-functionalized (crude) AuNPs, and the randomly functionalized AuNPs **87**. The SPR response trace of mono-functionalized AuNPs showed complete acid/base-driven ON/OFF switching of pseudorotaxane on the gold surface. The mono-functionalized AuNPs **77** can be simultaneously characterized by SPR dip shifts and isolated from the non-functionalized AuNPs **74** in the crude mixture solution with comparable efficacy to the magnetic separation. On the other hand, the randomly functionalized AuNPs showed incomplete disassembling from the gold surface upon base treatment. The residue randomly functionalized AuNPs should possess a higher number of functional groups on each nanoparticle, so that the multivalent binding was feasible with enhanced stability to base. The SPR response traces of mono-functionalized AuNPs and randomly functionalized AuNPs were different, which was an important finding towards applications. Since the mono-functionalized AuNPs showed complete ON/OFF switchable pseudorotaxane properties, the reusability, and quantification were expected to give better result than the commonly used randomly functionalized AuNPs for further applications.

Moreover, the characterization and purification processes could be repeated several times and using a larger area of gold plate, so that larger quantity of AuNPs can be synthesized and purified. Since each mono-functionalized AuNPs possess one specific functional group, so it can open up the future applications of single molecule detection. These mono-functionalized AuNPs would be eventually immobilized⁶⁰ with oligonucleotides for improved DNA sensing applications compared with the commonly used randomly functionalized AuNPs.

Chapter Five – Applications as Short Base-pairing DNA Sensors

5.1 General considerations

DNA sensors have been greatly investigated in recent years because these sensors can be used to detect some pathogenic and genetic diseases.⁶¹ Many sensors rely on the chemical post-modification on the target polynucleotides by adding fluorescent probes or other types of labeling moieties.⁶² These processes are somewhat time-consuming and costly. In recent advance in nanotechnology, sensors that are combined with polynucleotides, can be directly used for DNA detection without any chemical modification. AuNPs is a desirable and outstanding candidate for this application because it is relatively stable, non-aggregated compared to other nanoparticles (e.g., magnetic particles), size tunable (down to sub-nanometer), shape tunable (e.g., spheres, cube, rod, etc.), and size/shape/distance-dependent optical properties.^{1f,63} Most of the sensor applications employ the use of randomly functionalized AuNPs as the components for further DNA attachments.^{12a-c,55a,64} DNA primers are usually attached on the surface of AuNPs by a place exchange reaction of thiolate. After addition of the target DNAs, there exists a change of UV absorbance at the characteristic peaks of gold–DNA complexes at 260 nm, 520 nm and beyond, which correspond to the formation of the gold–DNA complexes and

hence, a decrease in the interparticle distance between AuNPs.^{12c,55a}

However, there exists particle-particle repulsions between bulky and negatively charged DNA, thereby affecting the “melting point” of the gold–DNA complexes in randomly functionalized AuNPs.^{12b} Such deviations may be different from batch-to-batch and depend on different lengths and sequences of DNA used. Calibration of such AuNP-based sensors would be required for individual experiments when different lengths and sequences of DNA are used.

It was also found that the probe density of the AuNPs alter the properties of gold–DNA complexes,^{12b} i.e., the “melting point” of the gold–DNA complexes decreased with the decrease in probe density. Such probe density change was achieved by adding some diluent strands onto the AuNPs via place exchange reaction, which was an average (by estimation) in all of the AuNPs present. It is unsure that all AuNPs possess the same or very close for the probe density and that the probe density would approximately go down to 33%.

Herein, we report the use of mono-functionalized AuNPs for the attachment of short single-strand DNA (10 base pairs) by simple and quantitative thiol-maleimide click reaction to afford the mono-functionalized AuNP-based DNA sensors.⁷² It is not necessary to synthesize additional mercaptoalkyloligonucleotide or to use a longer sequence of DNA, which is essential for the randomly functionalized AuNPs to have

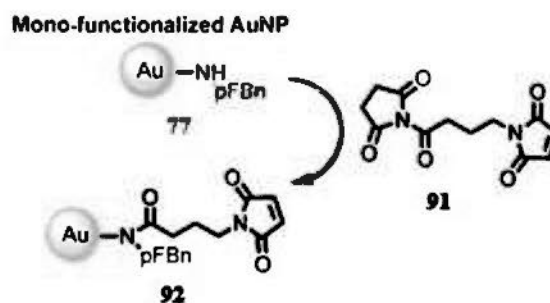
some spaces for effective agglomeration.^{12b} Hence, commercially available mercapto-oligonucleotide can be used. Moreover, a relatively short sequence of DNA (10 base pairs) was attached to the mono-functionalized AuNPs to provide minimal steric and electrostatic repulsions between AuNPs during DNA assemblies. We report, for the first time, the use of mono-functionalized oligonucleotide AuNPs as sensor for a polynucleotide related to Pathogenicity island of vancomycin-resistant *Enterococcus faecalis* at sub-nanomole concentrations. Tail-to-tail and head-to-head dsDNA–AuNP dimeric assemblies can be formed and characterized by UV/visible absorption spectroscopy, providing future nano-medicinal applications.^{32,65}

The dsDNA–AuNP complexes studied are dissolved in mixture of organic solvents (*N,N'*-dimethylformamide (DMF) and CHCl₃) with specific amounts of NaCl solution. The use of organic solvents for DNA assembly provides new approaches for novel structural gene delivery.⁶⁶ Moreover, dsDNA–AuNP sensors could be operated in alcoholic solvents.⁶⁷ Because of the DNA denaturing nature involving DMF, dsDNA–AuNP sensors that are compatible with DMF solvent, have not been reported yet. However, it was found that DNA assemblies of short sequences (21 base pairs) were basically intact even in 95% DMF solution, while longer sequences DNA were denatured.⁶⁸ The melting temperature study of the short sequences DNA has been done by the authors.⁶⁸ Such findings support that our target

double stranded DNA (10 base pairs) AuNPs would be stable in the organic solvent systems.

5.2 Synthesis of the mono-maleimide functionalized AuNPs

Mono-amine functionalized AuNPs **77** was simply reacted with *N*-succinimido 4-maleimidobutanoate **91** (Scheme 37). After purification with repeated vacuum drying, sonicating in and washing with acetonitrile, mono-maleimide functionalized AuNPs **92** was obtained which have been characterized by the appearance of maleimide IR absorption band at 1707 cm^{-1} (Figure 5-1).⁶⁹ Moreover, there are new amide C=O absorption peak at about 1651 cm^{-1} with the shift of the para-substituted aromatic C–H stretching from 804 cm^{-1} to 827 cm^{-1} .



Scheme 37. The synthesis of mono-maleimide functionalized AuNPs.

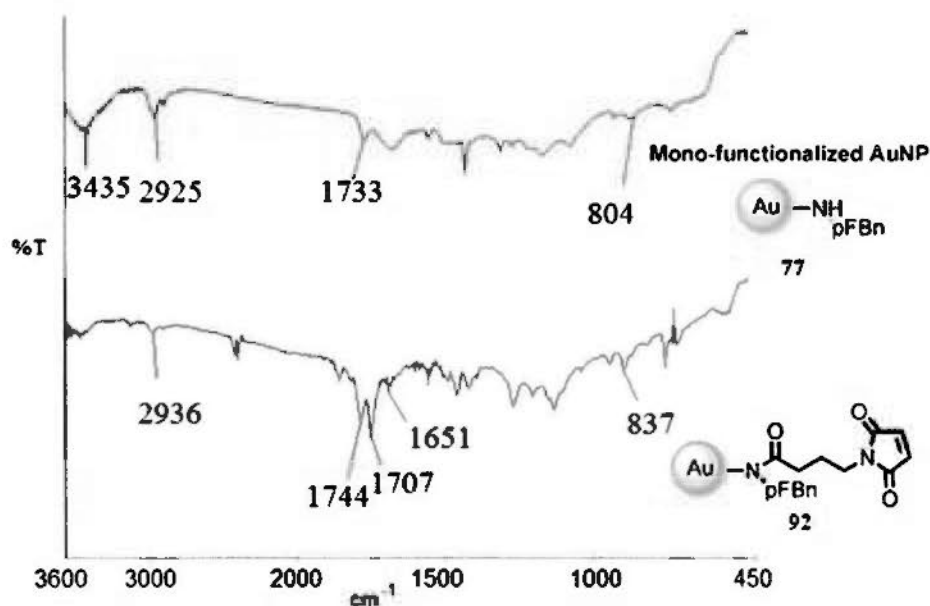
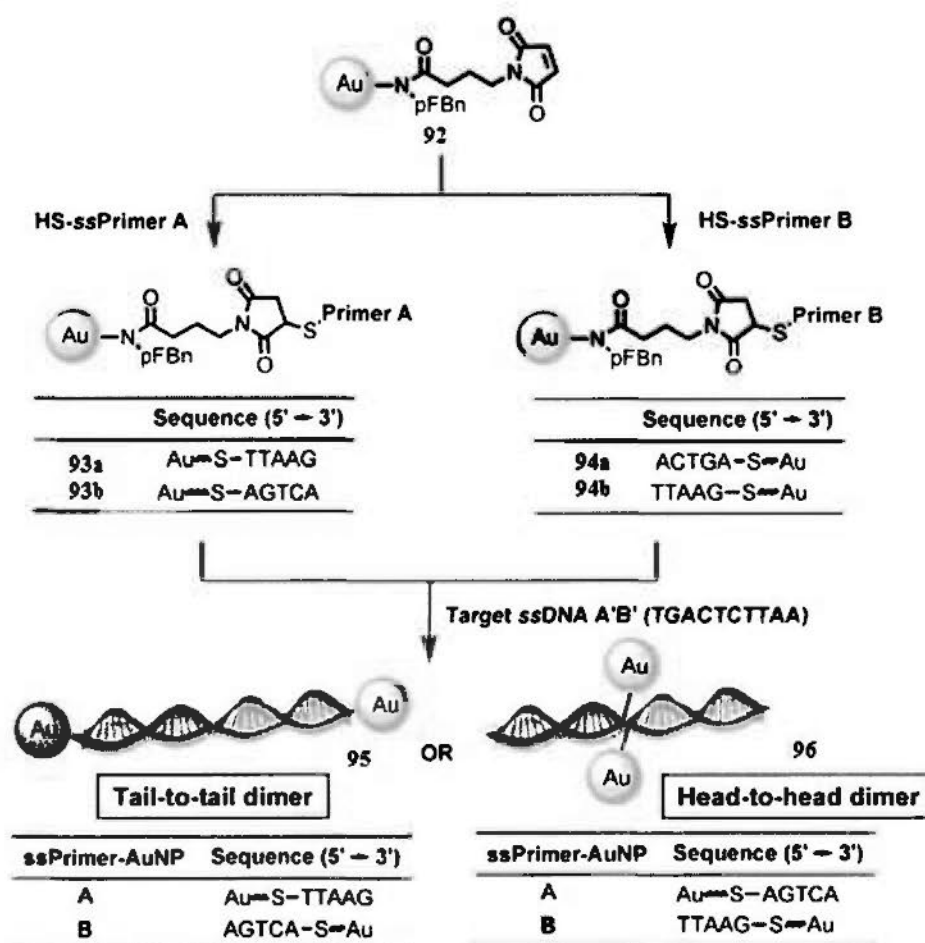


Figure 5-1. The FT-IR spectrum of the mono-functionalized AuNPs 77 and mono-maleimide functionalized AuNPs 92.

5.3 Synthesis of the mono-ssPrimer functionalized AuNPs and dsDNA-AuNP dimers

Thiolate primers (type A and type B) that were complementary to the target DNA A'B' (5'→3', TGA₂CTTAA), were attached independently to the mono-maleimide functionalized AuNPs by thiol-maleimide click reaction (Scheme 38) to give mono-ssPrimerA functionalized AuNPs 93a and 93b and mono-ssPrimerB functionalized AuNPs 94a and 94b. To achieve a tail-to-tail dimeric AuNP nanostructure, primers A and B are HS-TTAAG and AGTCA-SH (5' to 3'), respectively. On the other hand, primers A and B are TTAAG-SH and HS-AGTCA (5' to 3') to achieve a head-to-head dimeric AuNP nanostructure. Thiol-maleimide click reaction was used since the reaction condition was mild and the reaction yield was

quantitative.⁷⁰ The target DNA A'B' was then added to a pair of mono-ssPrimerA and mono-ssPrimerB functionalized AuNPs for DNA hybridization, which will lead to tail-to-tail and head-to-head alignments of dsDNA–AuNP dimers 95 and 96 respectively.



Scheme 38. The formation of dsDNA–AuNP dimers with head-to-head and tail-to-tail alignments, utilizing mono-functionalized AuNPs.

The success of the thiol-maleimide click reaction has been characterized by the disappearance of maleimide IR absorption band at 1707 cm^{-1} and the appearance of DNA symmetric PO_2^- at 1094 cm^{-1} (head-to-head) and 1097 cm^{-1} (tail-to-tail) (Figure 5-2).^{71a-b} Detailed IR assignments were tabulated in Table 5-1.

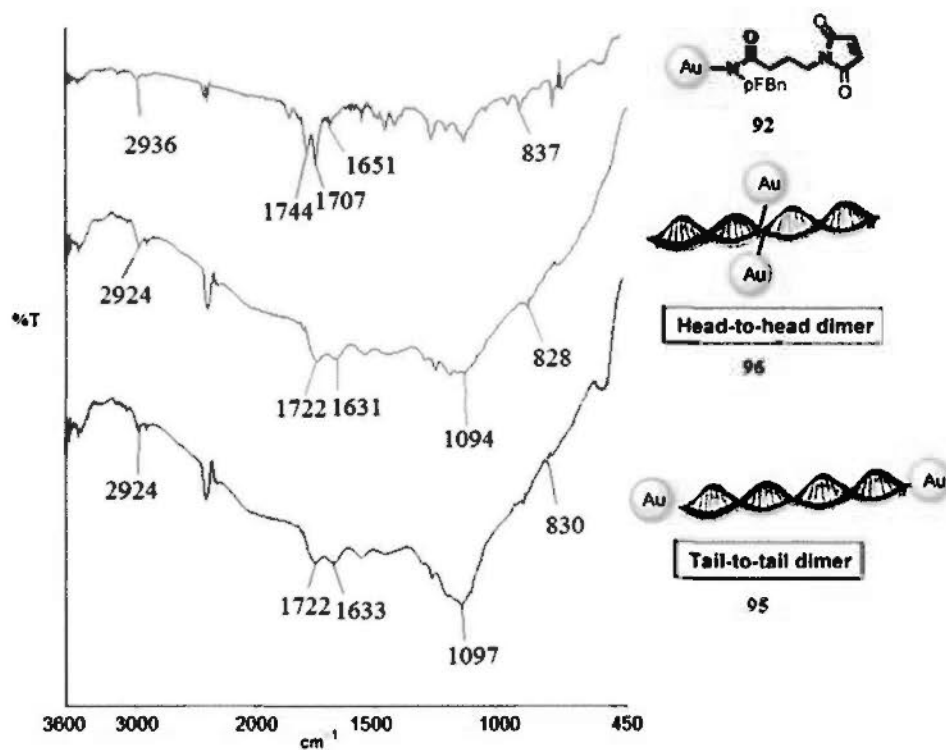


Figure 5-2. FT-IR spectra of mono-maleimide functionalized AuNPs 92, dsDNA-AuNP dimers with head-to-head alignments 96 and with tail-to-tail alignments 95.

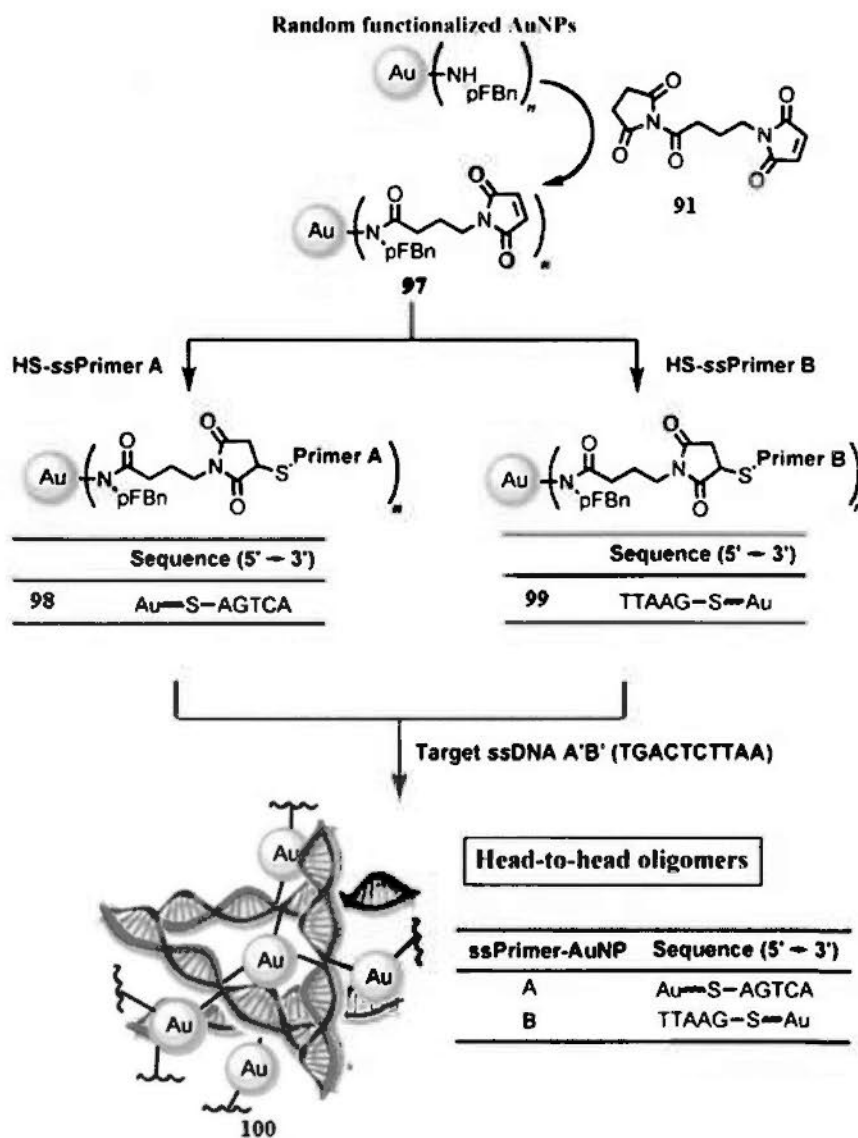
Table 5-1. The FT-IR absorption peaks assignments of mono-maleimide functionalized AuNPs **92**, *ds*DNA–AuNP dimers with head-to-head alignments **96** and with tail-to-tail alignments **95**.

	IR stretching frequency	Assignments
Mono-maleimido functionalized AuNP 92	2936 cm ⁻¹	Alkane C–H stretching
	1744 cm ⁻¹	Ester C=O stretching
	1707 cm ⁻¹	Asymmetric maleimide C=O stretching
	1651 cm ⁻¹	Amide C=O stretching
	837 cm ⁻¹	Para-substituted aromatics C–H
<i>ds</i> DNA–AuNP (head-to-head dimer) 96	2924 cm ⁻¹	Alkane C–H stretching
	1722 cm ⁻¹	Ester C=O stretching
	1631 cm ⁻¹	Amide C=O stretching
	1094 cm ⁻¹ (broad)	Symmetric PO ₂ ⁻ stretching (DNA)
	828 cm ⁻¹	Para-substituted aromatics C–H
<i>ds</i> DNA–AuNP (tail-to tail dimer) 95	2924 cm ⁻¹	Alkane C–H stretching
	1722 cm ⁻¹	Ester C=O stretching
	1633 cm ⁻¹	Amide C=O stretching
	1097 cm ⁻¹ (broad)	Symmetric PO ₂ ⁻ stretching (DNA)
	830 cm ⁻¹	Para-substituted aromatics C–H

5.4 Synthesis of random-ssPrimer functionalized AuNPs and *ds*DNA–AuNP random structures

Random-amine functionalized AuNPs was reacted with *N*-succinimido 4-maleimidobutanoate **91**, the obtained random-maleimide functionalized AuNPs **97** after purification was subjected to thiol-maleimide click reaction with two different thiolate primers (Scheme 39) to give random-ssPrimerA and random-ssPrimerB functionalized AuNPs **98** and **99** respectively. Then the target DNA was added to undergo hybridization, which will lead to *ds*DNA–AuNP

oligomers with head-to-head alignments 100.



Scheme 39. The formation of *dsDNA*-AuNP oligomers with head-to-head alignments, utilizing random-functionalized AuNPs.

5.5 Melting temperature analysis

The *dsDNA* will dissociate into its *ssDNA* upon increasing in temperature of the system. Upon dissociation, the absorption peaks in 260 nm will increase due to hyperchromic effect. The melting temperature of the *dsDNA* referred to the maximum point of the first derivative of the melting temperature curve, which is the temperature at which half of the DNA is in random coil and half of the DNA is in double-helical form.^{71c} Noticeably, DMF has a UV cut-off wavelength at 268 nm so that the typical DNA melting characteristic peak at 260 nm would not be feasible for monitoring the *dsDNA* assembly and disassembly. Herein, the absorbance change at 521 nm was monitored to evaluate the properties of the *dsDNA*-AuNP complexes. The concentration of the primers and AuNPs used for UV/visible absorption spectroscopic measurements are denoted in Table 5-2.

Table 5-2. Concentration of primer and AuNPs for UV/visible absorption spectroscopic and transmission electron microscopic measurements. *Randomly functionalized AuNPs are used.

Entry	[Primer A] = [Primer B] = [Target A'B'] (μM)	[AuNP] (mg/mL)
1-6	0.3989	0.0614
7-12	0.3991	0.0614
(13-15)*	1.9515	0.0601

Upon addition of the target *ssDNA* A'B' to the mono-*ssPrimer* functionalized AuNPs, the absorbance of AuNP at 521 nm would be disappeared, indicating that new *dsDNA*-AuNP nanostructures were formed. Upon the melting temperature

analysis, the increase of temperature of the *dsDNA*-AuNP would increase the relative absorbance at 521 nm, indicating that the AuNPs were dissociated into its monomeric state. Melting curves were plotted wherein the melting temperatures were determined according to the first derivatives of the curves (Table 5-3 and Figure 5-3). The *dsDNA*-AuNP complexes possess two structural alignments: tail-to-tail and head-to-head. For tail-to-tail alignment, two AuNPs were expected to align at the each ends connected with the target *dsDNA* strand. For head-to-head alignment, two AuNPs were expected to align closely at the middle of the target *dsDNA* strand. However, red shift of characteristic absorption wavelength from 520 nm to 650 nm was not observed in both cases. It may be attributed that the formation of AuNP dimers having small agglomeration and the interparticle distance are longer than the average size of nanoparticles, whereas such shifts are too weak to be detected.^{12d, 29}

By comparing the melting temperature results (Table 5-2), the head-to-head alignments possess similar melting temperatures than that of the tail-to-tail alignments with the same conditions. It is an exceptional finding when randomly functionalized AuNPs were used. It is believed that they possess enhanced steric and electrostatic repulsions between DNAs in the randomly functionalized AuNPs in close proximity. This effect can be minimized by using mono-functionalized AuNP.

Table 5-3. a) Primer sequences of different entries; b) Melting temperature of *dsDNA*-AuNP nanostructures by observing the absorbance change at 521 nm. *Randomly functionalized AuNPs are used. (Errors < 3%)

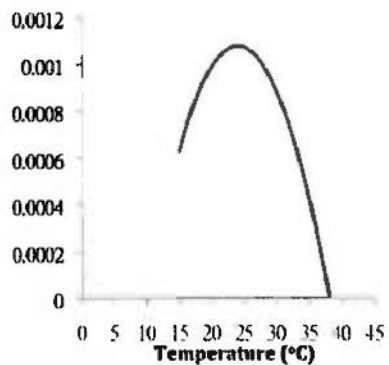
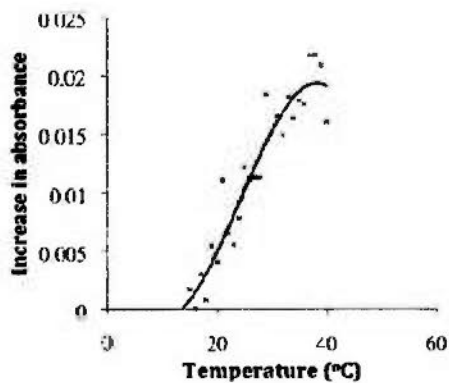
a)

Entry	<i>ss</i> Primer A (5'→3')	<i>ss</i> Primer B (5'→3')	<i>ss</i> Target A'B' (5'→3')	<i>dsDNA</i> -AuNP alignment
1-6	HS-TTAAG	AGTCA-SH	TGACTCTTAA	Tail-to-tail
7-12	TTAAG-SH	HS-AGTCA	TGACTCTTAA	Head-to-head
(13-15)*	TTAAG-SH	HS-AGTCA	TGACTCTTAA	Head-to-head

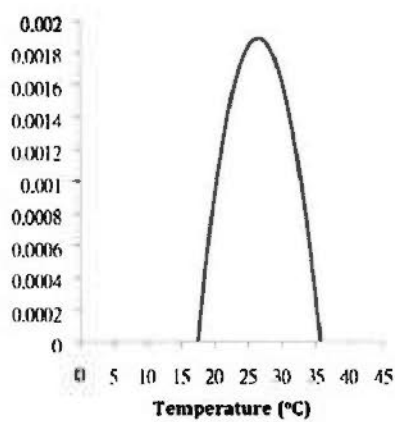
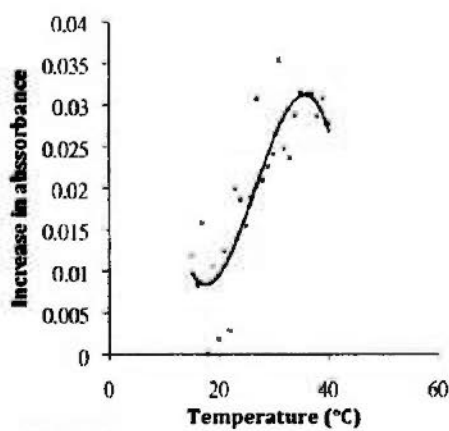
b)

Entry	Melting temperature (°C)	Solvent ratio (DMF/CHCl ₃ /H ₂ O)	[NaCl] (μM)	<i>dsDNA</i> -AuNP alignment
1	24.1	1 : 1 : 0.03	1 μM	Tail-to-tail
2	26.6	1 : 1 : 0.03	5 μM	Tail-to-tail
3	29.3	1 : 1 : 0.03	10 μM	Tail-to-tail
4	24.9	1 : 2 : 0.03	1 μM	Tail-to-tail
5	27.8	1 : 2 : 0.03	5 μM	Tail-to-tail
6	30.0	1 : 2 : 0.03	10 μM	Tail-to-tail
7	23.8	1 : 1 : 0.03	1 μM	Head-to-head
8	26.5	1 : 1 : 0.03	5 μM	Head-to-head
9	29.0	1 : 1 : 0.03	10 μM	Head-to-head
10	25.2	1 : 2 : 0.03	1 μM	Head-to-head
11	27.0	1 : 2 : 0.03	5 μM	Head-to-head
12	30.3	1 : 2 : 0.03	10 μM	Head-to-head
13*	27.1	1 : 1 : 0.03	1 μM	Head-to-head
14*	28.6	1 : 1 : 0.03	5 μM	Head-to-head
15*	31.7	1 : 1 : 0.03	10 μM	Head-to-head

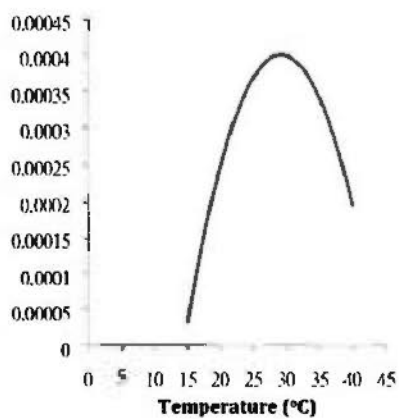
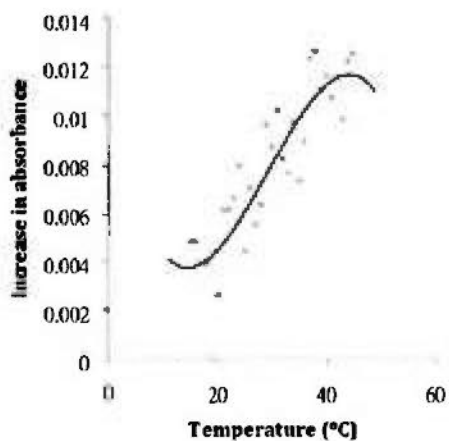
Entry 1



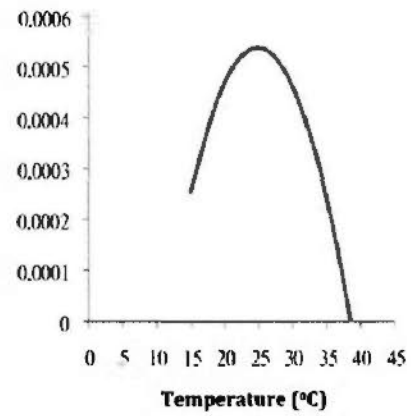
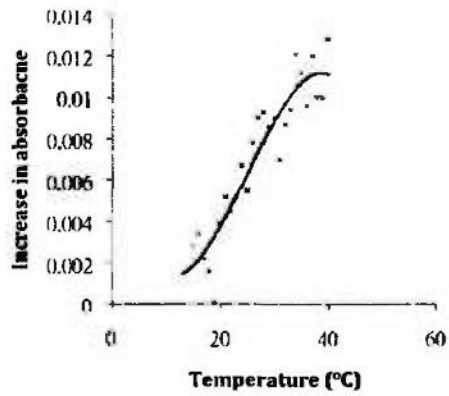
Entry 2



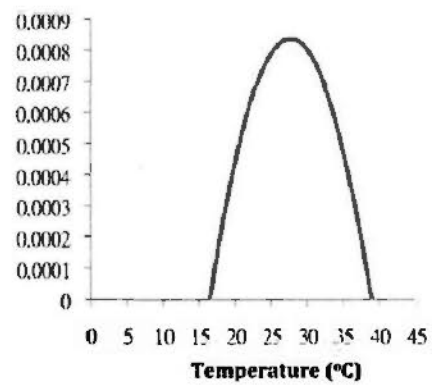
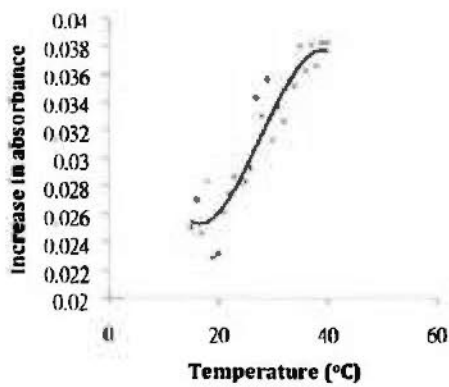
Entry 3



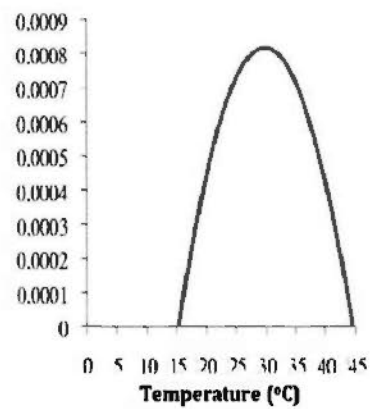
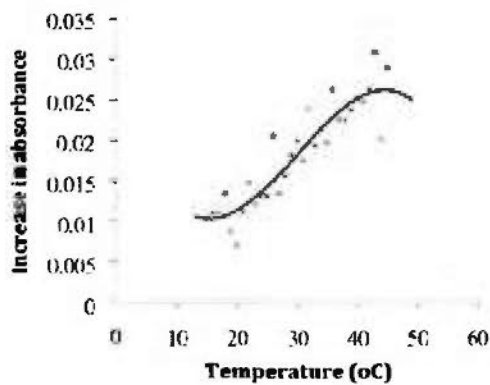
Entry 4



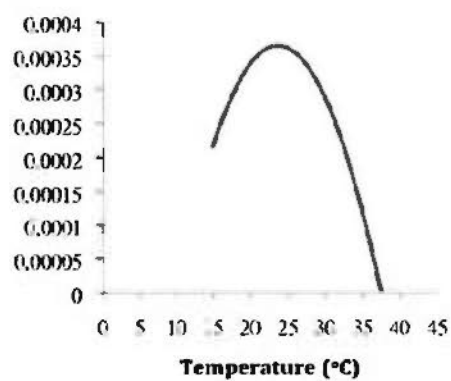
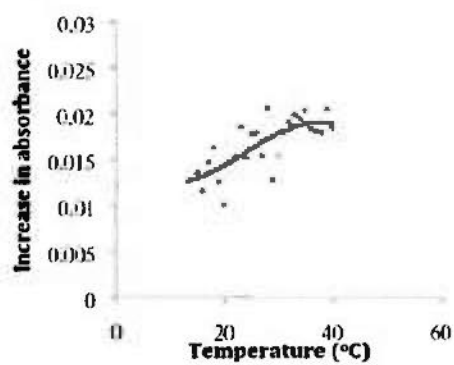
Entry 5



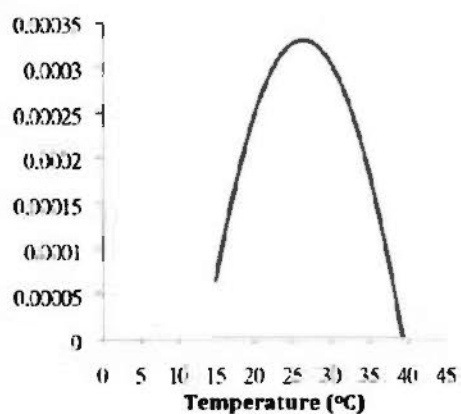
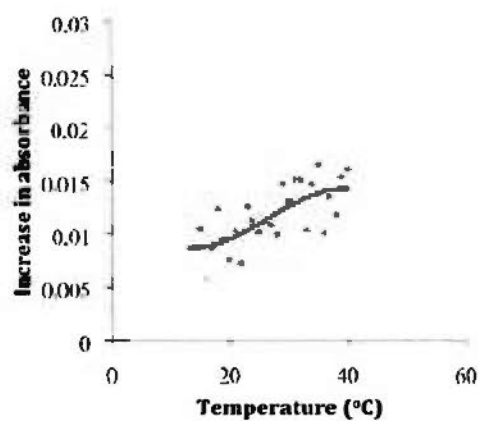
Entry 6



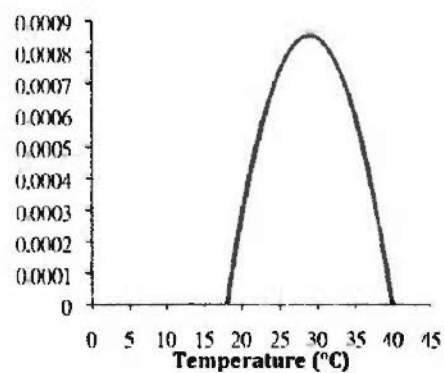
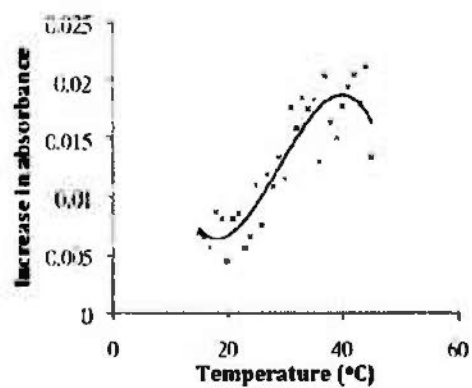
Entry 7



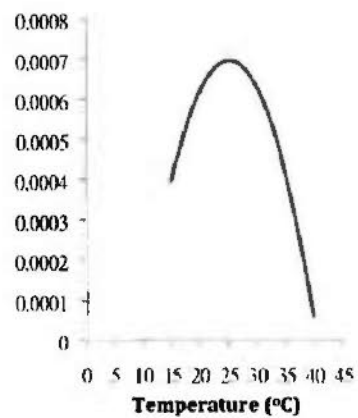
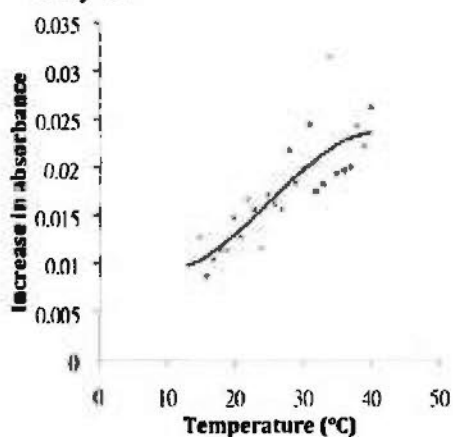
Entry 8



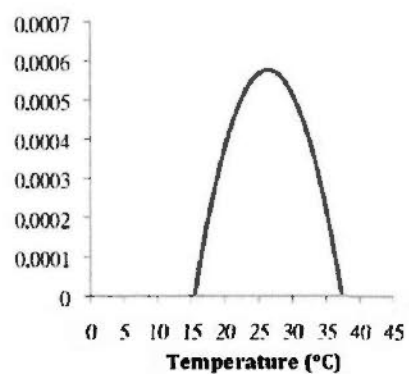
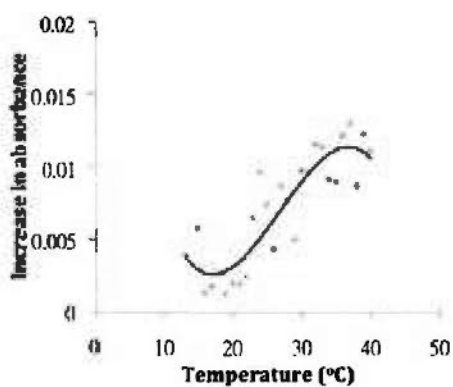
Entry 9



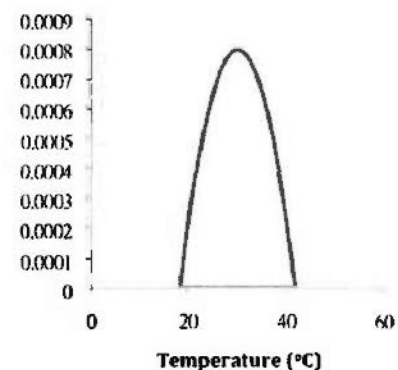
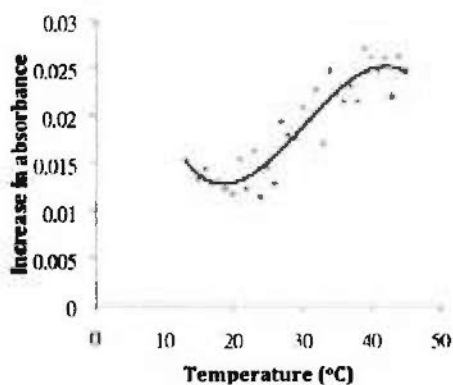
Entry 10



Entry 11



Entry 12



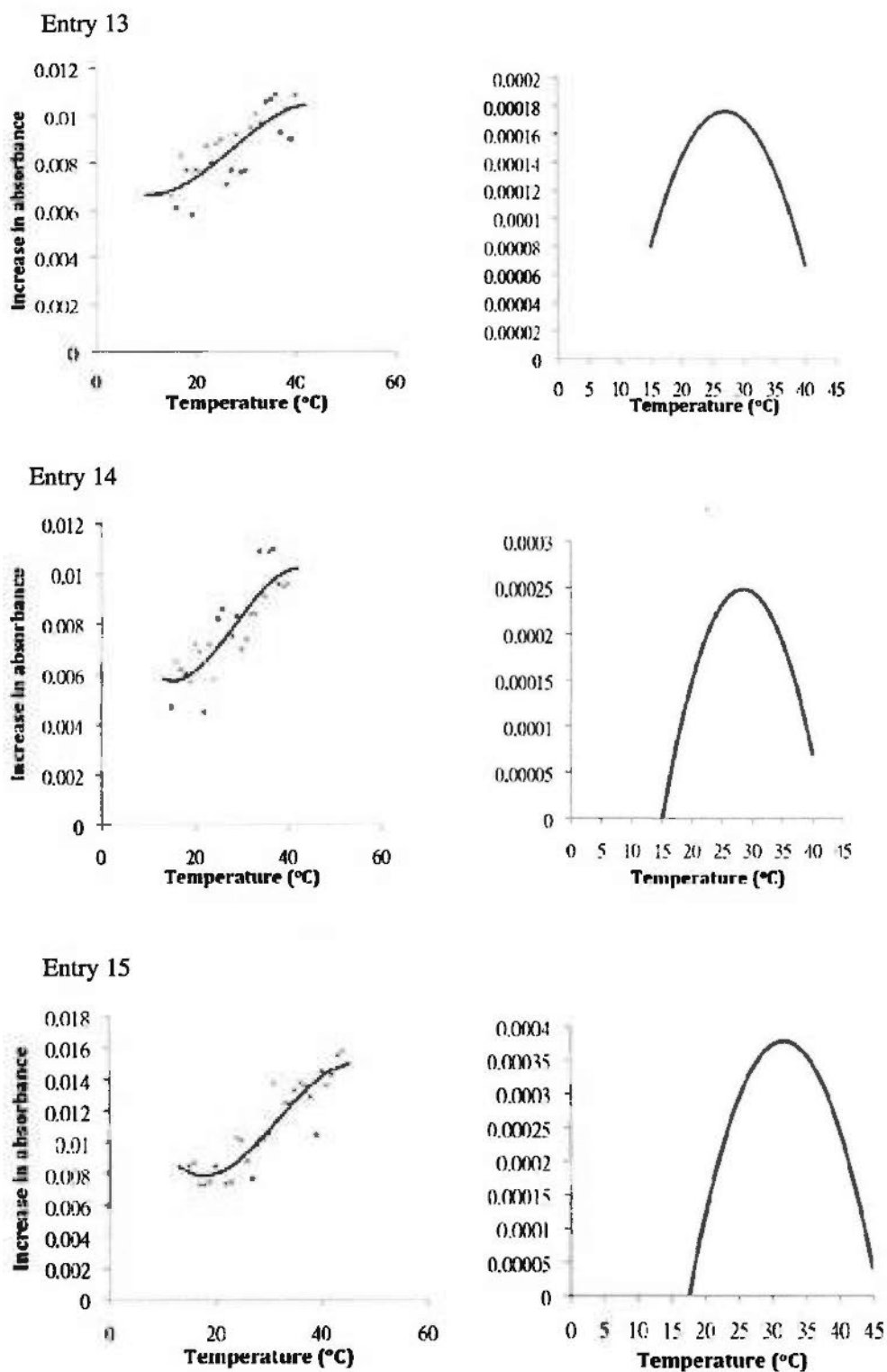


Figure 5-3. The relative increase in absorbance at 521 nm and the first derivative against temperature of different entries.

Salts are essential for DNA assembly for charge balance in the *dsDNA* structures, especially in the presence of organic solvents. The salt effect on the formation of *dsDNA*-AuNP nanostructures was studied (Figure 5-4). Three different concentrations of sodium chloride solution (1, 5, and 10 μM) were added to the mixtures. It was found that the melting temperature (Table 5-3) of the *dsDNA*-AuNP complexes increases with increasing salt concentrations for both tail-to-tail and head-to-head alignments.

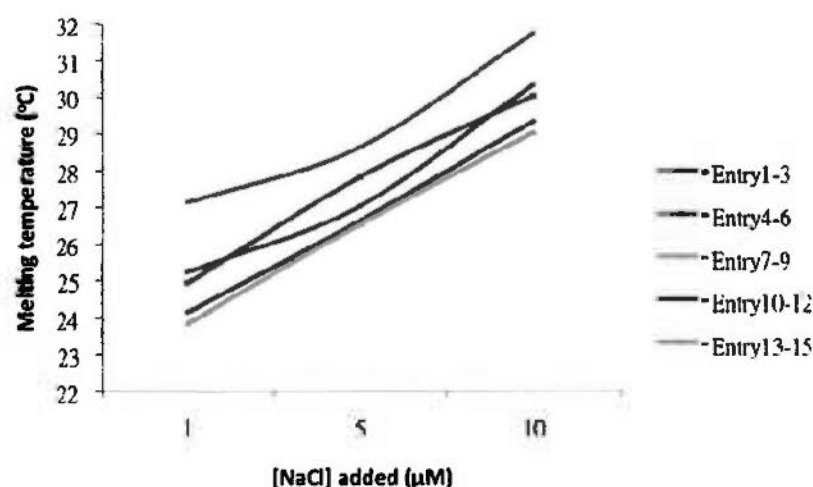


Figure 5-4. Relationship between salt concentration and melting temperature of *dsDNA*-AuNP nanostructures.

Solvent effect on forming the *dsDNA*-AuNP complexes is also studied by increasing the ratio of CHCl_3 to DMF. Since the target DNA consists of 10 base pairs, such short DNA increases the hydrophobicity and hence reduces the free energy in the annealing process. Moreover, the mono-*ssPrimer* functionalized AuNPs are more

soluble in CHCl_3 than in DMF. Therefore, addition of CHCl_3 should also increase the stability of the *dsDNA*-AuNP nanostructures. As a result, the melting temperatures of *dsDNA*-AuNP nanostructures increase with increasing CHCl_3 ratio.

The melting temperature difference of *dsDNA* between the mono-functionalized AuNPs (entry 7-9) and the randomly functionalized AuNPs (entry 13-15) is compared. The melting temperatures using the randomly functionalized AuNPs for *dsDNA* assembly are higher than those of the mono-functionalized AuNPs by 1.9-3.3 °C with the same conditions. That is, the melting temperature increases with increasing probe density. Therefore, the probe density was tunable not only by diluents stranded place exchange reaction, but also by controlling the functional ligand density of the particle's surface.

5.6 TEM characterization of *dsDNA*-AuNP structures

The *dsDNA*-AuNP solutions were analyzed by TEM with nearly the same AuNP concentrations (Table 5-2). The TEM images of solutions of entries 3 and 6, which contain the tail-to-tail dimeric species, reveal significant amounts of AuNP dimer pairs (Figure 5-5, pairing of dark dots). Similarly, significant amounts of AuNP dimer pairs are also observed in their TEM images for the solutions of entries 9 and 12 from which they contain head-to-head dimeric species. In contrast, the TEM image

of the solution of entry 15 reveals agglomerated AuNP nanostructures. This observation demonstrates that the randomly functionalized AuNPs involve the formation of a network of AuNPs while the mono-functionalized AuNPs form discrete nanostructures.

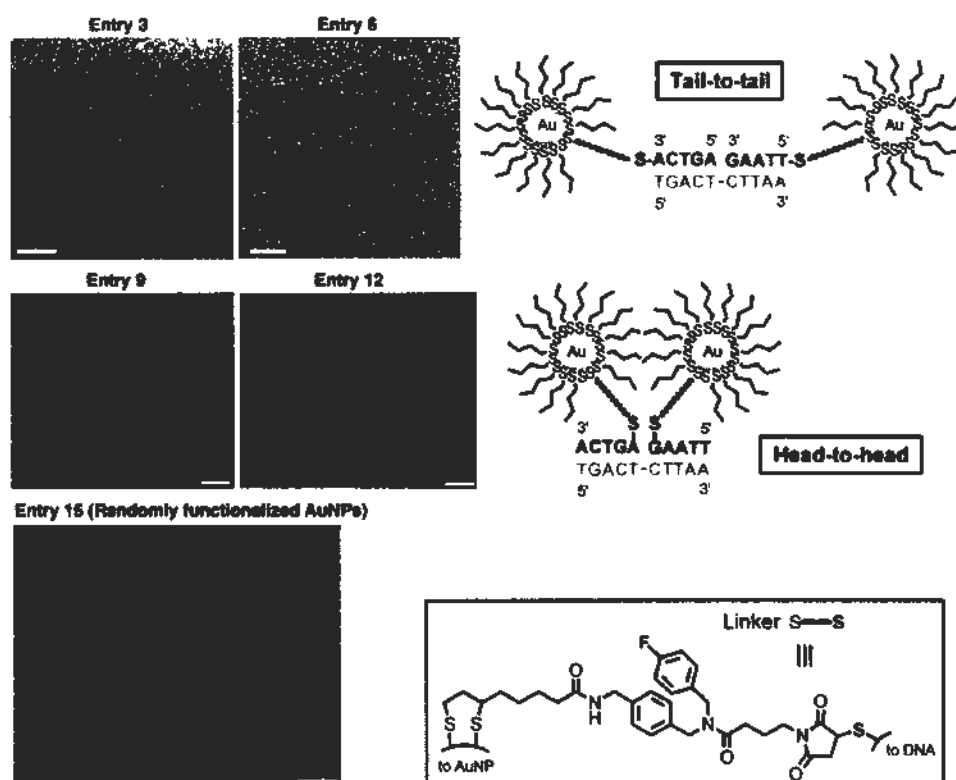


Figure 5-5. Transmission electron microscopic images of entries 3 and 6 (*dsDNA*-AuNP, tail-to-tail alignment); entries 9 and 12 (*dsDNA*-AuNP, head-to-head alignment); and entry 15 (*dsDNA*-randomly functionalized AuNP, head-to-head alignment). The scale bar (white) represents 20 nm.

5.7 Section conclusion

In conclusion, short *ssDNA* sensors that involve mono-functionalized AuNPs are first reported. By way of an example, the hybridization and the detection of a 10 base-pair oligonucleotide which relates to Pathogenicity island of vancomycin-resistant *Enterococcus faecalis*, have been demonstrated in organic solvent mixtures at sub-nanomole concentrations. It was found that the melting temperature of the *dsDNA*–AuNP complexes increases with increasing salt concentrations as well as the chloroform in the solvent ratio, demonstrated in both tail-to-tail and head-to-head alignments. Transmission electron microscopic images of the *dsDNA*–AuNP complexes with mono-functionalized AuNPs reveal significant amounts of dimeric AuNP species while that of randomly functionalized AuNPs reveal an agglomerated AuNP nanostructures. This randomly agglomerated nanostructure may result in cross binding of non-hybridized DNA and AuNP trapping within the network, leading to inaccurate shifts of UV/visible absorption signals. While our mono-functionalized AuNPs which provide one to one DNA annealing to AuNP, the spectroscopic signals are revealed from the formation of discrete *dsDNA*–AuNP dimeric complexes. This approach based on the formation of less-steric head-to-head alignment may provide a more quantitative sensing property, providing a great potential in future applications in nanomedicine and sensor development.

Chapter Six – Conclusion and Outlook

Novel discretely mono-functionalized AuNPs were synthesized by supramolecular solid-phase chemistry, which was then purified by crown ether-coated iron oxide *via* magnetic separation with high efficiency. The synthetic strategy provided a mild condition of reaction with improved yield when compared with the traditional covalent synthesis. Moreover, the intermediates of resin structures and nanostructures were first characterized step-by-step in the syntheses, by FT-IR and XPS. The novel supramolecular dimers and trimers with discretely mono-functionalized AuNPs were also reported with significant changes of SPR dip shifts.

The discretely mono-functionalized AuNPs were expected to possess different physical and chemical properties compared to the commonly used randomly functionalized AuNPs. Moreover, the discretely mono-functionalized AuNPs should provide more quantitative results in several sensing applications since they enabled single molecule detection rather than unknown, on an average number of targets detection. Such hypothesis was supported by (1) the simultaneously purification and SPR characterization of mono-functionalized AuNPs and randomly functionalized AuNPs by a SPR microfluidic device; (2) the differences of melting temperature of *ds*DNA–AuNP complexes formed by mono-functionalized AuNPs and randomly

functionalized AuNPs.

The mono-functionalized AuNPs were found to possess complete ON/OFF switching properties of pseudorotaxane structures while the randomly functionalized AuNPs were found to possess incomplete ON/OFF switching properties. Such difference in chemical properties affected the reaction involving the AuNPs so as to their sensor applications in giving a more sensitive and quantitative results. For instance, there may be a residual signal of target with the randomly functionalized AuNPs when the AuNPs pseudorotaxane was in the OFF state.

The melting temperatures of 10 base pairs *dsDNA*–AuNP complexes formed by mono-functionalized AuNPs were also found to be lower than that of the randomly functionalized AuNPs. Such difference in physical properties of the complexes would also affect the quantitative result of sensor applications. For instance, the multiple DNA chains of randomly functionalized AuNPs increased the stability of the *dsDNA*–AuNP complexes. Hence, the melting temperature of the complexes did not reflect the real, discrete double-stranded DNA melting temperature.

The mono-functionalized AuNPs were effectively synthesized and characterized as well as to give a more sensitive and quantitative result in terms of DNA sensing applications. This research would open up the future of single molecule detection.

Chapter Seven – Experimental Procedures

7.1 General Information

For experiments related to Chapter 3

General consideration

All chemicals were purchased from Aldrich or Acros and used without further purification. All solvents were dried, distilled and stored with molecular sieves (4 Å). Tetrahydrofuran (THF) was dried with Na-benzophenone; CH₂Cl₂ was dried with NaH and *N,N'*-dimethylformamide (DMF) was dried with CaH₂. Polystyrene Wang resin (PS resin) which was purchased from Aldrich, composed of a 1% 1,4-divinylbenzene (DVB) cross-linked 4-benzyloxybenzyl alcohol, polymer-bound resin with particle size of 100–200 mesh and a hydroxyl group density of 1.0–1.5 mmol/g. All reactions were performed under high purity nitrogen. Thin layer chromatography (TLC) was performed on silica gel 60 F254 (Merck). Column chromatography was performed on silica gel 60F (Merck 9385, 0.040–0.063 mm). Neodymium-iron-boron (NIB) magnets were used.

Characterization

All nuclear magnetic resonance (NMR) spectra were recorded on either a Bruker DPX 300 (¹H: 300 MHz; ¹³C: 76 MHz) or Bruker Advance 400 (¹H: 400 MHz; ¹³C: 101 MHz) spectrometer at 298 K and CDCl₃ was used as the solvent unless

otherwise stated. The residual proton resonance signals of the non-deuterated solvents were used as reference calibration. Chemical shifts are reported as parts per million (ppm) for both ^1H and ^{13}C NMR spectroscopies. Electrospray ionization (ESI) mass spectra were measured on a Thermo Finnigan MAT95XL mass spectrometer with $\text{CH}_2\text{Cl}_2/\text{MeOH}$ (1:1) as the mobile phase. The reported molecular mass (m/z) values correspond to the most abundant monoisotopic masses. Melting points were measured on an Electrothermal 9100 digital melting point apparatus and are uncorrected. Thermogravimetric analysis (TGA) were performed on a TA Instruments Hi-Res TGA 2950 Thermogravimetric Analyzer from 30 to 800 °C (heating rate = 50 °C/min). FTIR spectra were recorded using a Perkin Elmer Spectrum I while far-IR spectra were recorded using a Nicolet-Nexus 670 FTIR ESP. Prior to recording the FTIR spectra, solid samples were grounded with analytical grade KBr (10:1 KBr:sample) and that powder was pressed with pressure to produce a pellet for IR measurement. For recording the far-IR spectra, the sample chamber of the instrument was flashed with anhydrous N_2 for 4 h. Solid samples were grounded into fine powder followed by the addition of a few drops of analytical paraffin oil. The powder/oil mixture was then subjected to further grinding. Subsequently, the mixture was placed on a polystyrene pellet for IR measurement. UV/Visible absorption spectra were obtained using a Cary 5G UV-Vis-NIR spectrophotometer.

High-resolution transmission electron microscopic (TEM) images were obtained under a FEI TecnaiF20 Field Emission Transmission Electron Microscope. A drop of the sample solution with a concentration approximately 0.2 mg/mL was added to a carbon-coated copper grid for TEM analysis. X-ray powder diffraction patterns (XRD) of the products were obtained on a Japan Rigaku DMax- γ A rotation anode X-ray diffractometer equipped with graphite monochromatized Cu K α radiation ($\lambda = 1.54178 \text{ \AA}$).

For experiments related to Chapter 4

General methods

25 mm \times 25 mm \times 1 mm N-BAF10 glass and 25 mm equilateral prism with a refractive index of 1.67003 were purchased from TEMTO Technology Co. Ltd. Polydimethylsiloxane (PDMS) was prepared by SYLGARD 184 silicone elastomer kit from Dow Corning. KDS Gemini 88 dual rate syringe pump was used. Monofunctional (secondary amine) AuNPs, nonfunctional (*n*-butanethiolate) AuNPs, and their crude mixtures were prepared according to the Chapter 3. All chemicals were purchased from Aldrich or Acros and used without further purification. Thin layer chromatography (TLC) was performed on silica gel 60 F254 (Merck). Column chromatography was performed on silica gel 60F (Merck 9385, 0.040–0.063 mm).

Characterization

All nuclear magnetic resonance (NMR) spectra were recorded on Bruker Avance 400 (^1H : 400 MHz; ^{13}C : 101 MHz) spectrometer at 298 K and CDCl_3 was used as the solvent. The residual proton resonance signals of the non-deuterated solvents were used as reference calibration. Chemical shifts δ are reported as parts per million (ppm) for both ^1H and ^{13}C NMR spectroscopies. Electrospray ionization (ESI) mass spectra were measured on a Thermo Finnigan MAT95XL mass spectrometer with $\text{CH}_2\text{Cl}_2/\text{MeOH}$ (1:1) as the mobile phase. The reported molecular mass (m/z) values correspond to the most abundant monoisotopic masses. Melting points were measured on an Electrothermal 9100 digital melting point apparatus and are uncorrected. Atomic force microscopy (AFM) spectra were measured with scan size $5.000 \times 5.000 \mu\text{m}$ and a scan rate of 1.001 Hz.

*For experiments related to Chapter 5**General Consideration*

Chemicals were purchased from Aldrich unless otherwise specified. *N,N'*-Dimethylformamide (DMF) was distilled and dried with 4 Å molecular sieves. Analytical grade chloroform (CHCl_3) was used without further purification. Custom DNA primers with HPLC purification were purchased from Invitrogen.

Characterization

Temperature-controlled UV/visible measurements were performed with a Beckman DU-7500 photo-diode array spectrophotometer. High-resolution transmission electron microscopic (HR-TEM) images were obtained with a FEI TecnaiF20 Field Emission Transmission Electron Microscope. Deionized water was obtained from a Barnstead RO pure system. FTIR spectra were recorded using a Perkin Elmer Spectrum I. Prior to the recording of FTIR spectra, solid samples were grounded with analytical grade KBr (10:1 KBr:sample) and that powder was pressed with pressure to produce a pellet for IR measurement.

7.2 Experimental Procedures

For experiments related to Chapter 3

Amine 69. To a solution of compound **73** (2.98 g, 5.58 mmol) and phenol (8.40 g, 89.3 mmol) in CH₂Cl₂ (10 mL) at ambient temperature, trimethylsilyl chloride (TMSCl, 3.90 mL, 30.7 mmol) in CH₂Cl₂ (10 mL) was added dropwise. The reaction mixture was then stirred for 4 h. Subsequently, the reaction mixture was quenched with 2 M NaOH and extracted with CHCl₃. The organic extract was washed with saturated NaCl, dried (anhydrous MgSO₄) and filtered. The filtrate was concentrated under reduced pressure to give a residue. The residue was purified by column chromatography using hexane/EtOAc (2:1 gradient to 1:2) as the eluent to give an oil (2.40 g, 98%). ¹H NMR (CD₃CN, 400 MHz) δ 1.35–1.46 (m, 2H), 1.53–1.71 (m, 4H), 1.79–1.88 (m, 1H), 2.31–2.42 (m, 3H), 3.03–3.17 (m, 2H), 3.53 (quin, *J* = 3.2 Hz, 1H), 3.70 (s, 2H), 3.72 (s, 2H), 5.07 (s, 2H), 7.02–7.07 (m, 2H), 7.30–7.36 (m, 6H); ¹³C NMR (CD₃CN, 101 MHz) δ 25.4, 29.3, 34.6, 35.2, 39.2, 41.0, 52.8, 53.2, 57.3, 66.5, 115.6, 115.8, 129.0, 130.7, 130.8, 136.0, 137.9, 138.0, 141.9, 161.4, 163.8, 173.9; MS(HR-ESI) calcd for C₂₃H₂₉FNO₂S₂ *m/z* = 434.1618 (Theory); Found *m/z* = 434.1632 ([M+H]⁺, 100%).

Ammonium 69·HPF₆. Compound **69** (2.40 g, 5.47 mmol) was dissolved in CH₂Cl₂ (10 mL) with vigorous stirring. Hexafluorophosphoric acid (60% in water, 1.13 mL,

8.21 mmol) was added dropwise into the solution. After 10 min, water was added to dilute the reaction mixture. The reaction mixture was then extracted with CH_2Cl_2 twice, the combined organic layers were dried with anhydrous Na_2SO_4 . After the filtration of the solids, the filtrate was evaporated under reduced pressure to give a pale yellow solid (2.50 g, 79%). M.p. 141.9–142.9 °C. ^1H NMR (CD_3CN , 400 MHz) δ 1.38–1.46 (m, 2H), 1.56–1.73 (m, 4H), 1.85–1.91 (m, 1H), 2.35–2.45 (m, 3H), 3.09–3.18 (m, 2H), 3.58 (quin, $J = 3.2$ Hz, 1H), 4.18 (s, 2H), 4.18 (s, 2H), 5.11 (s, 2H), 7.16–7.20 (m, 2H), 7.41–7.53 (m, 6H); ^{13}C NMR (CD_3CN , 101 MHz) δ 25.4, 29.4, 34.5, 35.3, 39.3, 41.1, 51.6, 52.0, 57.4, 66.1, 116.7, 116.9, 128.0, 129.4, 131.4, 131.5, 131.6, 133.6, 133.7, 139.2, 163.0, 165.5, 174.1; MS(HR-ESI) calcd for $\text{C}_{23}\text{H}_{29}\text{FNO}_2\text{S}_2$ $m/z = 434.1618$; Found $m/z = 434.1616$ ($[\text{M}-\text{PF}_6]^+$, 100%).

Boc-protected amine 73. To a solution of (\pm)-thioctic acid (**72**, 1.62 g, 7.87 mmol) in NEt_3 (1.10 mL, 7.86 mmol) and THF (10 mL) at -3 °C, isobutyl chloroformate (IBCF, 1.02 mL 7.86 mmol) was added to give a pale yellow solution. After 30 min, the *t*-butyloxycarbonyl (Boc)-protected compound **71**^{39j} (3.21 g, 7.86 mmol) and catalytic amount of 4-dimethylaminopyridine (DMAP) were added to the mixture. The reaction mixture was stirred for 4 h at ambient temperature. Subsequently, the excess solvents were evaporated *in vacuo* and the residue was dissolved in CHCl_3 . The solution was washed with saturated NaHCO_3 , H_2O , 2 M HCl and saturated NaCl

and finally taken up with CHCl_3 . The organic layer was dried (anhydrous MgSO_4) and filtered. The filtrate was concentrated under reduced pressure to give a residue. The residue was purified by column chromatography using hexane/EtOAc (8:1 gradient to 4:1) as the eluent to give an oil (2.98 g, 71%). ^1H NMR (CDCl_3 , 300 MHz) δ 1.43–1.48 (m, 11H), 1.65–1.67 (m, 4H), 1.85–1.87 (m, 1H), 2.33–2.40 (m, 3H), 3.08–3.11 (m, 2H), 3.53 (quin, $J = 3.2$ Hz, 1H), 4.21–4.33 (bs, 2H), 4.33–4.47 (bs, 2H), 5.09 (s, 2H), 6.95–7.00 (m, 2H), 7.05–7.25 (bs, 4H), 7.30 (d, $J = 7.8$ Hz, 2H); ^{13}C NMR (CDCl_3 , 76 MHz) δ 25.1, 28.8, 29.1, 34.4, 35.0, 38.9, 40.6, 48.8, 49.2, 56.7, 66.3, 80.6, 115.6, 115.9, 128.0, 128.5, 128.9, 129.5, 130.0, 134.1, 135.1, 138.4, 156.2, 160.8, 164.1, 173.6; MS (HR-ESI) calcd for $\text{C}_{28}\text{H}_{36}\text{FNO}_4\text{S}_2\text{Na}$ $m/z = 556.1962$; Found $m/z = 556.1960$ ($[\text{M}+\text{Na}]^+$, 100%).

PS-DB24C8 76. To a mixture of DB24C8- CO_2H $70^{4\text{ta-c}}$ (0.74 g, 1.51 mmol) in DMF (5 mL) and NEt_3 (0.21 mL, 1.50 mmol) at -3 °C was added IBCF (0.20 mL, 1.54 mmol) to give a pale yellow solution. After 30 min, PS Wang resin **75** (2.13 g, preswollen in DMF (10 mL) for 1 h) and a catalytic amount of DMAP were added to give a pale brown solution with the dispersion of resin. The reaction was stirred overnight at ambient temperature. The resulting solution was filtered and washed with CH_2Cl_2 several times. The filtered resin was obtained as the PS-DB24C8 **76**. Furthermore, the excess solvents of the filtrate were evaporated. The resulting solid

was redissolved in CHCl_3 , and the solution was washed with saturated NaHCO_3 , water, and 2 M HCl. The pH of the solution was carefully adjusted to 4. The organic layer was washed with saturated NaCl, dried (anhydrous MgSO_4), and filtered. Then, the filtrate was evaporated to dryness under reduced pressure to give a white solid. The remaining amount of the DB24C8- CO_2H **70** as in the filtrate was determined by ^1H NMR with the addition of known amount of MeNO_2 (5.4 μL) as an internal standard. By comparing the integration ratio between the methyl hydrogen signal from the internal standard and the ethylene glycol hydrogen signal from the crown ether, the yield of the reaction was found to be 77%. The PS-DB24C8 **76** was characterized by the presence of the significant C=O absorption band at 1741 cm^{-1} in the FT-IR spectrum (KBr, solid). A control experiment was done with the same procedure, but the solvent was changed to CH_2Cl_2 , from which no reaction occurred, that is, 100% of the DB24C8- CO_2H **70** was present in the filtrate.

PS-DB24C8 \supset $[\mathbf{69}\cdot\text{HPF}_6]_n$. All the resin PS-DB24C8 **76** prepared from the previous step was swelled in CH_2Cl_2 (10.3 mL) and MeCN (1.7 mL) with gentle mechanical shaking. Compound $\mathbf{69}\cdot\text{HPF}_6$ (0.48 g, 0.82 mmol) was added to the resin suspension at $40\text{ }^\circ\text{C}$ for 1 h and at ambient temperature for 2 h. Subsequently, the resin was filtered and washed with CH_2Cl_2 (10 mL): FTIR (KBr, solid) $\nu = 3231$ and 3252 cm^{-1} [N^+H_2], 1735 cm^{-1} [C=O].

PS-DB24C8 \square **[69-HPF₆-AuNP]_n**. *n*-Butanethiolate-coated AuNPs (10.0 mg), as prepared from the modified literature procedure, were added to a solution of **PS-DB24C8** \square **[69-HPF₆]_n** in CH₂Cl₂ (10.3 mL) and MeCN (1.7 mL). The mixture was shaken gently at 40 °C for 4 h and at ambient temperature for 24 h. The resulting resin was then filtered and washed with CH₂Cl₂ (10 mL): FTIR (KBr, solid) $\nu = 233$ cm⁻¹ [N⁺H₂], 1737 cm⁻¹ [C=O]; far-IR (suspension in paraffin oil) $\nu = 249$ cm⁻¹ [Au-S].

69-AuNP 77. The resin **PS-DB24C8** \square **[69-HPF₆-AuNP]_n** was suspended in CH₂Cl₂ (10.3 mL) and MeCN (1.7 mL). NEt₃ (0.23 mL) was added to the suspension with gentle mechanical shaking for 40 min at ambient temperature. The resin was then filtered and washed with CH₂Cl₂ (10 mL). The filtrate was evaporated *in vacuo*, and the residue was washed with cold EtOH. Finally, the resulting solid was dissolved in CH₂Cl₂. Purification was facilitated with **SPIO-DB24C8 80**: First, a solution of **SPIO-DB24C8 80** (1.0 g) in CH₂Cl₂ (3 mL) was sonicated for 10 min. The crude **69-AuNP** products in CH₂Cl₂ were mixed with the **SPIO-DB24C8 80** solution. H-TFA (0.15 mL, 1.95 mmol) was added to the mixture and shaken mechanically for 15 min. A magnet was placed near the reaction flask to magnetically attract all of the magnetic particles. The supernatant was discarded and placed aside, while the magnetic particles were washed with CH₂Cl₂ under the

application of magnetic field. A solution of Et₃N (0.28 mL, 2.00 mmol) in CH₂Cl₂ (5 mL) was added to the resulting magnetic particles. The solution was then mechanically shaken for 15 min. A magnet was placed near the reaction flask to magnetically attract all the magnetic particles, and then the supernatant was collected, washed with H₂O, and dried *in vacuo* to give the purified **69-AuNPs** (6.3 mg): FTIR (KBr, solid) $\nu = 1733\text{ cm}^{-1}$ [C=O], 804 cm^{-1} [*para*-substituted aromatic C–H]; far-IR (suspension in paraffin oil) $\nu = 249\text{ cm}^{-1}$ [Au–S]; UV/visible (CH₂Cl₂, L mg⁻¹ cm⁻¹) $\epsilon = 2.00, 0.84, \lambda_{\text{max}} = 265.5\text{ and }525\text{ nm}$. Conversion yields: 3.0 mg of **69-AuNP** per gram of PS Wang resin **75** (–OH density = 1.0–1.5 mmol/g) and 2.3 mg of **69-AuNP** per gram of PS–DB24C8 **76** (–DB24C8 density ~ 1.0 mmol/g).

SPIO 78. The superparamagnetic iron oxide (SPIO, Fe₃O₄) particles were prepared through a solvothermal reaction. Briefly, FeCl₃·6H₂O (0.54 g), sodium acrylate (1.5 g) and NaOAc (1.5 g) were dissolved in ethylene glycol (20 mL) under magnetic stirring. The obtained homogeneous yellow solution was transferred to a Teflon-lined stainless-steel autoclave and sealed to heat at 200 °C. After the reaction for 10 h, the autoclave was cooled to room temperature. The obtained magnetite particles were washed with EtOH and doubly deionized water for several times, and finally dispersed in EtOH (25 mL).

SPIO-NH₂ 79. In a typical process, the as-prepared Fe₃O₄ / EtOH solution (2 mL)

was mixed with H₂O (3 mL), NH₄OH (1 mL) and EtOH (20 mL). The mixture was homogenized by ultrasonication. After 30 min, tetraethylorthosilicate (TEOS, 0.1 mL) in EtOH (6 mL) was injected into the solution within 30 min. After the reaction was performed for 1 h, the products were collected by the help of a magnet, washed with EtOH and H₂O several times. Then, the products (0.1 g) were re-dispersed in EtOH (50 mL) by ultrasonication. Subsequently, aminopropyltriethoxysilane (APTES, 2 mL) solution was introduced into the solution and stirred for 48 h to complete the grafting experiment. The products were collected by the help of a magnet, washed with EtOH and H₂O several times. Finally, the product was dried in vacuum for 12 h to obtain the SPIO-NH₂ microspheres. FTIR (KBr, solid) $\nu = 1092 \text{ cm}^{-1}$ [Si-O], 588 cm^{-1} [Fe-O].

SPIO-DB24C8 80. A solution of DB24C8-CO₂H **70** (1.42 g, 2.88 mmol) in CH₂Cl₂ (5 mL) was shaken with a mechanical shaker at -3 °C under N₂. NEt₃ (0.40 mL, 2.88 mmol) was added to the solution. After 15 min, IBCF (0.37 mL, 2.85 mmol) was added to the solution. After 30 min, a sonicated (30 min) solution of SPIO-NH₂ **79** microspheres (0.97 g) and catalytic amount of DMAP in CH₂Cl₂ (5 mL) were added. The reaction mixture was stirred for 24 h at ambient temperature. A magnet was placed near the reaction flask to magnetically attract all the magnetic particles. The supernatant was discarded and the magnetic particles were washed with CH₂Cl₂

under the application of magnetic field. The magnetic particles were further treated with dilute acetic acid to consume any free amine moiety on the SPIO-DB24C8 **80** particles. A magnet was placed near the reaction flask to magnetically attract all the particles. The supernatant was discarded and the magnetic particles were washed with CH₂Cl₂ under the application of magnetic field. The pale brown solid SPIO-DB24C8 **80** obtained was dried in vacuum. The discarded solution which contains DB24C8-CO₂H **70** was concentrated under reduced pressure and then subjected for ¹H NMR analysis with an internal standard (MeNO₂). The amount of the residue DB24C8-CO₂H **70** was determined in order to calculate the amount of DB24C8-CO₂H **70** that was reacted with the SPIO-NH₂ **79**. FTIR (KBr, solid) $\nu = 1629\text{ cm}^{-1}$ [amide N-H], 1093 cm^{-1} [Si-O], 586 cm^{-1} [Fe-O].

BisDB24C8 82. To a mixture of DB24C8-CO₂H **70** (0.40 g, 0.81 mmol), hydroquinone (**81**, 0.045 g, 0.41 mmol) and catalytic amount of DMAP in CH₂Cl₂ (5 mL) and THF (2.5 mL) at 0 °C, dicyclohexyl carbodiimide (DCC, 0.32 g, 1.54 mmol) was added. The mixture was stirred for 24 h at ambient temperature. A precipitate was formed. Subsequently, the precipitate was filtered off and then the filtrate was concentrated under reduced pressure to give a residue. The residue was purified by column chromatography using EtOAc/EtOH (3:1) as the eluent to give the product as a white solid (0.18 g, 42%). M.p. 101.9–102.8 °C. ¹H NMR (CDCl₃, 400 MHz) δ

3.84–3.86 (m, 16H), 3.93 (m, 16H), 4.15–4.20 (m, 16H), 6.79–6.95 (m, 14H), 7.61 (s, 2H), 7.80 (d, $J = 8$ Hz, 2H); ^{13}C NMR (CDCl_3 , 101 MHz) δ 69.4, 69.47, 69.59, 69.74, 69.88, 70.06, 71.39, 71.55, 112.15, 114.14, 114.75, 116.16, 121.58, 121.61, 122.28, 122.63, 124.81, 144.22, 148.42, 148.96, 153.46, 165.52; MS(HR-ESI): calcd for $\text{C}_{31}\text{H}_{36}\text{O}_{11}\text{Na}$ $m/z = 607.1550$ (Theory); Found $m/z = 607.2178$ ($[\text{M}+\text{Na}+\text{Cs}]^{2+}$, 100%).

DB24C8-Act 84. To a mixture of DB24C8-CO₂H **70** (2.01 g, 4.07 mmol) and propargyl alcohol (**83**, 1.70 mL, 29.2 mmol) in CH_2Cl_2 (20 mL) at 0 °C, 1-ethyl-3-(3-dimethylaminopropyl) carbodiimide methiodide (EDCI, 2.67 g, 8.98 mmol) and a catalytic amount of DMAP were added and stirred for overnight. After that, the excess solvent was evaporated *in vacuo* to give a residue. The residue was purified by column chromatography using EtOAc as the eluent to give a pale brown solid (1.34 g, 62%). M.p. 97.9–98.4 °C. ^1H NMR (CDCl_3 , 400 MHz) δ 2.50–2.51 (t, $J = 2.4$ Hz, 1H), 3.83 (s, 4H), 3.83 (s, 4H), 3.90–3.94 (m, 8H), 4.13–4.15 (t, $J = 4.0$ Hz, 4H), 4.17–4.19 (t, $J = 4.0$ Hz, 4H), 4.87–4.88 (d, $J = 2.4$ Hz, 2H), 6.83–6.89 (m, 5H), 7.52 (s, 1H), 7.67 (d, $J = 8.6$ Hz, 1H); ^{13}C NMR (CDCl_3 , 101 MHz) δ 52.4, 69.4, 69.5, 69.6, 69.7, 69.8, 70.0, 71.4, 71.5, 71.6, 75.0, 78.0, 112.0, 114.0, 114.4, 121.5, 122.0, 124.4, 148.4, 149.0, 153.3, 165.6; MS(HR-ESI) calcd for $\text{C}_{28}\text{H}_{34}\text{O}_{10}\text{Na}$ $m/z = 553.2044$; Found $m/z = 553.2055$ ($[\text{M}+\text{Na}]^+$, 100%).

TrisDB24C8 86. To a mixture of DB24C8-Act **84** (1.22 g, 2.31 mmol), diisopropylethylamine (DIPEA, 0.81 mL, 4.65 mmol) and 1,3,5-tris(azidomethyl)-benzene (**85**, 0.17 g, 0.71 mmol) in MeCN (20 mL), CuI (0.10 g, 0.53 mmol) was added to give a bright yellow mixture. The solution became pale yellow after the stirring for overnight and became pale brown after the stirring for a week. A solid precipitate was formed. The solid was filtered and washed with MeCN. Then, the solid was dissolved in chloroform and washed with saturated NH₄Cl, 2 M HCl, saturated NaHCO₃ and then 2 M HCl, saturated NaCl. The organic layer was dried with anhydrous MgSO₄. After filtration, the filtrate was concentrated to give a pale brown solid (1.12 g, 85%). M.p. 50.0–50.8 °C. ¹H NMR (CDCl₃, 400 MHz) δ 3.81 (s, 12H), 3.82 (s, 12H), 3.89–3.93 (m, 24H), 4.12–4.17 (m, 24H), 5.40 (s, 6H), 5.44 (s, 6H), 6.81–6.89 (m, 15H), 7.13 (s, 3H), 7.48–7.49 (d, *J* = 8.4 Hz, 3H), 7.61–7.63 (m, 6H); ¹³C NMR (CDCl₃, 101 MHz) δ 53.5, 57.9, 69.4, 69.5, 69.6, 69.7, 69.8, 70.0, 71.4, 71.5, 71.6, 112.0, 114.1, 114.4, 121.5, 122.3, 124.3, 127.8, 136.9, 143.9, 148.4, 149.0, 153.3, 166.3; MS(HR-ESI) calcd for C₉₃H₁₁₁N₉O₃₀Na *m/z* = 1856.7329; Found *m/z* = 1856.7249 ([M+Na]⁺, 100%).

Randomly functionalized AuNPs 87. The synthetic route of the randomly functionalized AuNPs **87** followed the same procedure of synthesis of **69-AuNPs** without the solid phase support resin. The AuNPs were randomly functionalized with

more than one amine **69** functional groups on each AuNP due to the uncontrolled place exchange reaction.

General procedures for the self-assembly of supramolecular dimers and trimers.

The purified **69**-AuNPs were mixed with different ratios (w/w) of BisDB24C8 **82** and TrisDB24C8 **86** in a CH₂Cl₂/H-TFA (22:1) solution to form the BisDB24C8 \supset [**69**-HTFA·AuNP]₂ and TrisDB24C8 \supset [**69**-HTFA·AuNP]₃, respectively. The concentration of the **69**-AuNP was 0.2 ± 0.05 mg/mL in CH₂Cl₂/H-TFA (22:1). Aliquots of these solutions were used directly for TEM and UV/visible spectroscopic measurements.

For experiments related to Chapter 4

SU-8 mold. The experimental procedure SU-8 molding can be found in http://engineering.tufts.edu/microfab/index_files/SOP/SU-8%20Processing.pdf.

PDMS molding. The simplified experimental procedures of PDMS molding have been discussed in the Chapter 4. A more detail experimental procedure can be found in http://engineering.tufts.edu/microfab/index_files/SOP/PDMS%20on%20SU8%20Mold%20SOP.pdf.

Mono-functionalized AuNPs (**69**-AuNPs), nonfunctional (*n*-butanethiolate) AuNPs **74**, and their crude mixtures were prepared according to Chapter 3.

Randomly functionalized AuNPs 87. *n*-Butanethiolate-coated (nonfunctional)

AuNPs (10.0 mg) were added to the secondary amine ligand compound **69** (0.36 g, 0.82 mmol) in CH₂Cl₂ (10.3 mL) and MeCN (1.7 mL) with gentle shaking at 40 °C for 4 h and then at ambient temperature for 24 h. The mixture was then vacuum dried and washed by cold ethanol several times with vigorous shaking to remove any unreacted ligand compound. Subsequently, CHCl₃ (10 mL) was added to dissolve the AuNPs. The AuNP solution was then centrifuged (4400 rpm, 20 s) whereas the soluble AuNPs layer was collected and then vacuum dried to afford the randomly functionalized AuNPs.

DB24C8-CH₂SAc 89. DB24C8-CH₂OH **88**^{41d} (1.20 g, 2.49 mmol) was dissolved in ClCH₂CH₂Cl (10 mL) and stirred under N₂. ZnI₂ (0.91 g, 2.85 mmol) was added to the solution. Thioacetic acid (AcSH) (0.9 mL, 12.59 mmol) was added to the solution and stirred overnight at room temperature under N₂. Water was added and the product was extracted with chloroform twice. The product was then purified by flash column chromatography using hexane/ethyl acetate (1:2 v/v) gradient to 1:4 v/v as the eluent to give an off-white solid (0.73 g, 55%). Mp 68.2–69.5 °C; ¹H NMR (400 MHz, CDCl₃, δ): 2.33 (s, 3 H), 3.82–3.83 (m, 8 H), 3.88–3.92 (m, 8 H), 4.04 (s, 2 H), 4.10–4.15 (m, 8 H), 6.75–6.81 (m, 3 H), 6.85–6.90 (m, 4 H); ¹³C NMR (101 MHz, CDCl₃, δ): 30.5, 33.4, 69.5, 69.6, 70.0, 70.0, 71.4, 113.9, 114.0, 114.1, 114.5, 121.5, 121.7, 130.7, 148.2, 149.0, 149.0; MS(HR-ESI) calcd for C₂₇H₃₆O₉SNa *m/z* =

559.1972; Found $m/z = 559.1980$ ($[M + Na]^+$, 100%).

(DB24C8CH₂S)₂ **90**. Minimum amount of chloroform was added to dissolve DB24C8-CH₂SAc **89** (0.10 g, 0.19 mmol) with stirring. Ammonia in methanol (2 M, 15 mL, 901 mmol) was then added to the solution. After three days reaction in air, water was added and the product was extracted with chloroform twice. The excess of solvent of the organic layer was evaporated *in vacuo* to give an off-white solid (0.11 g, 60%). Mp 109.3–109.7 °C; ¹H NMR (400 MHz, CDCl₃, δ): 3.54 (s, 4 H), 3.79–3.80 (m, 16 H), 3.88–3.89 (m, 16 H), 4.09–4.12 (m, 16 H), 6.73–6.78 (m, 6 H), 6.83–6.88 (m, 8 H); ¹³C NMR (101 MHz, CDCl₃, δ): 43.1, 69.3, 69.4, 69.8, 69.8, 71.2, 113.6, 114.0, 114.9, 130.3, 148.3, 148.7, 148.8; MS(HR-ESI) calcd for C₅₀H₆₆O₁₆S₂Na $m/z = 1009.3684$; Found $m/z = 1009.3671$ ($[M + Na]^+$, 100%).

General preparation procedure of AuNPs samples for SPR analysis

AuNPs were dissolved in CHCl₃ (3 mL) and washed with deionized water. The CHCl₃ layer was vacuum dried for 24 h. The AuNPs were made up to 2.5 mgmL⁻¹ in CHCl₃. Four drops of 11% trifluoroacetic acid in CHCl₃ were added to the solution. The solution was gently shaken until all AuNPs were dissolved. AuNP solutions were injected to the microfluidic device via a syringe pump with flow rate of 600 mL min⁻¹ for 150 s and the solution was then left for 300 to 500 seconds for SPR measurements at ambient temperature.

For experiments related to Chapter 5**Mono-maleimide functionalized AuNPs 92.** Mono-amine functionalized AuNPs 77

(0.7 mg) was dissolved in CHCl_3 (1 mL) followed by addition of *N*-succinimido 4-maleimidobutanoate 91 (0.7 mg). The reaction was vigorously shaken overnight in a water bath. The solvent was then evaporated *in vacuo*, followed by an addition of an excess of MeCN and sonicated for 30 seconds. Excess of solvent was discarded and the washing process was repeated three times. Then, the mixture was evaporated to dryness. CHCl_3 (1.40 mL) and DMF (1.40 mL) were added to re-dissolve the AuNPs to obtain the series of 1:1 CHCl_3 /DMF solvent ratio. CHCl_3 (1.87 mL) and DMF (0.93 mL) were added to re-dissolve the AuNPs to obtain the series of 2:1 CHCl_3 /DMF solvent ratio. FT-IR (KBr, solid) $\nu = 2936 \text{ cm}^{-1}$ [Alkane C-H], 1744 cm^{-1} [Ester C=O], 1707 cm^{-1} [Asymmetric maleimide C=O], 1651 cm^{-1} [Amide C=O], 837 cm^{-1} [Para-substituted aromatics C-H].

Mono-ssPrimer functionalized AuNPs (93a,b-94a,b). *ssPrimerA-SH* and *ssPrimerB-SH* were dissolved in DMF/ H_2O (91:9). To 200 μL of the above AuNP solution was added 0.32 nmoles *ssPrimer A-SH* and 0.32 nmoles *ssPrimer B-SH* (Chapter 5, Table 5-3a) by extraction from primers bulk solutions. Two drops of 1% Et_3N in CHCl_3 was added. Then, 300 μL CHCl_3 and 300 μL DMF were added to the solution. Then, 10 μL of three different concentrations (1, 5, and 10 μM) of NaCl

solution were added to the three batches of solution, which were then vigorously shaken overnight.

dsDNA–AuNP dimers (95-96). To prepare the *dsDNA–AuNP* dimers, target DNA with sequence TGACTCTTAA (0.32 nmoles) was added to the reaction mixture of mono-ssPrimer functionalized AuNPs (with type A and B) and was vigorously shaken overnight. Tail-to-tail dimer **95**, FT-IR (KBr, solid) $\nu = 2924\text{ cm}^{-1}$ [alkane C–H], 1722 cm^{-1} [ester C=O], 1631 cm^{-1} [amide C=O], 1094 cm^{-1} (broad) [symmetric PO_2^- stretching (DNA)], 828 cm^{-1} [para-substituted aromatics C–H]. Head-to-head dimer **96**, FT-IR (KBr, solid) $\nu = 2924\text{ cm}^{-1}$ [alkane C–H], 1722 cm^{-1} [ester C=O], 1633 cm^{-1} [amide C=O], 1097 cm^{-1} (broad) [symmetric PO_2^- stretching (DNA)], 830 cm^{-1} [para-substituted aromatics C–H].

Random-maleimide functionalized AuNPs 97. Random-amine functionalized AuNPs (0.7 mg) was dissolved in CHCl_3 (1 mL) followed by addition of *N*-succinimido 4-maleimidobutanoate (3.5 mg). The reaction was vigorously shaken overnight in a water bath. The solvent was then evaporated *in vacuo*, followed by an addition of an excess of MeCN and sonicated for 30 seconds. Excess of solvent was discarded and the washing process was repeated three times. Then, the mixture was evaporated to dryness. CHCl_3 (1.40 mL) and DMF (1.40 mL) were added to re-dissolve the AuNPs to obtain a 1:1 CHCl_3 :DMF ratio.

Random-ssPrimer functionalized AuNPs (98-99). *ssPrimerA-SH* and *ssPrimerB-SH* were dissolved in DMF/H₂O (91:9). To 200 μ L of the above AuNP solution was added 1.6 nmoles *ssPrimer A-SH* and 1.6 nmoles *ssPrimer B-SH* (Chapter 5, Table 5-3a) by extraction from primers bulk solutions. Two drops of 1% Et₃N in CHCl₃ was added. Then, 300 μ L CHCl₃ and 300 μ L DMF were added to the solution. Then, 10 μ L of three different concentrations (1, 5, and 10 μ M) of NaCl solution were added to the three batches of solution, which were then vigorously shaken overnight.

***dsDNA*-AuNPs random structures 100.** To prepare the random *dsDNA*-functionalized AuNPs, target DNA with sequence TGACTCTTAA (1.6 nmoles) was added to the reaction mixture of random-*ssPrimer* functionalized AuNPs (with type A and B) and was vigorously shaken overnight.

General procedure for UV/visible absorption spectroscopy measurement

UV/visible absorption spectroscopy was performed at 15 °C. Solutions of mono-maleimide functionalized AuNPs were further diluted with CHCl₃ (300 μ L) and DMF (300 μ L). The concentrations of primers and AuNPs used for UV/visible absorption spectroscopic measurements are denoted in Table 5-2 of Chapter 5.

General procedure for melting temperature measurement

Solutions of mono- and random-*dsDNA* functionalized AuNPs were transferred to a

quartz cuvette for UV/visible absorption spectroscopic measurements. The temperature of the cuvette was increased from 15 to 40 °C (for 1 and 5 μM NaCl series) and from 15 to 45 °C (for 10 μM NaCl series) with 1.0 °C increases per minute. The normalized increases in absorbance of 521 nm (corresponded to monomer of AuNPs) were analyzed whereas their first derivatives were evaluated to obtain the melting temperature of the *ds*DNA–AuNP dimer nanostructures.

General procedure for transmission electron spectroscopy analysis

Based on the sample concentrations list in Table 5-2 of Chapter 5, a drop of sample solution was drop-casted on a carbon-coated copper grid for TEM analysis.

References:

1. For reviews of gold nanoparticles: a) Eustis, S.; El-Sayed, M. A. *Chem. Soc. Rev.* **2006**, *35*, 209-217; b) Descalzo, A. B.; Martínez-Máñez, R.; Sancenón, F.; Hoffmann, K.; Rurack, K. *Angew. Chem., Int. Ed.* **2006**, *45*, 5924-5948; c) Funston, A. M.; Mulvaney, P.; Murray, R. W. *Langmuir* **2009**, *25*, 13840-13851; d) Drechsler, U.; Erdogan, B.; Rotello, V. M. *Chem. Eur. J.* **2004**, *10*, 5570-5579; e) Shenhar, R.; Rotello, V. M. *Acc. Chem. Res.* **2003**, *36*, 549-561; f) Wilson, R. *Chem. Soc. Rev.* **2008**, *37*, 2028-2045; g) Daniel, M.-C.; Astruc, D. *Chem. Rev.* **2003**, *104*, 293-346.
2. Ozin, G. A.; Arsenault, A. C.; Cademartiri, L. *Nanochemistry A Chemical Approach to Nanomaterials*, RSC Publishing, U.K., 2009.
3. a) Sau, T. K.; Pal, A.; Jana, N. R.; Wang, Z. L.; Pal, T. *Size J. Nanopart. Res.* **2001**, *3*, 257-261; b) Meltzer, S.; Resch, R.; Koel, B. E.; Thompson, M. E.; Madhukar, A.; Requicha, A. A. G.; Will, P. *Langmuir* **2001**, *17*, 1713-1718; c) Mallick, K.; Wang, Z. L.; Pal, T. *J. Photochem. Photobiol.* **2001**, *140*, 75-80; d) Kimling, J.; Maier, M.; Okenve, B.; Kotaidis, V.; Ballot, H.; Plech, A. *J. Phys. Chem. B* **2006**, *110*, 15700-15707; e) Niidome, Y.; Hori, A.; Sato, T. *Chem. Lett.* **2000**, 310-311.
4. a) Reed, J. A.; Cook, A.; Halaas, D. J.; Parazolli, P.; Robinson, A.; Matula, T. J.; Griezer, F. *Ultrason. Sonochem.* **2003**, *10*, 285-289; b) Okitsu, K.; Yue, A.; Tanabe, S.; Matsumoto, H.; Yobiko, Y. *Langmuir* **2001**, *17*, 7717-7720
5. Shimizu, T.; Teranishi, T.; Hasegawa, S.; Miyake, M. *J. Phys. Chem. B* **2003**, *107*, 2719-2724.
6. a) Turkevitch, J.; Stevenson, P. C.; Hillier, J. *Discuss. Faraday Soc.* **1951**, *11*, 55-75; b) Frens, G. *Nature: Phys. Sci.* **1973**, *241*, 20-22; c) Ojea-Jime'nez, I.; Romero, F. M.; Bastu's, N. G.; Puentes, V. *J. Phys. Chem. C*, **2010**, *114*,

References

- 1800-1804; d) Polte, J.; Ahner, T. T.; Delissen, F.; Sokolov, S.; Emmerling, F.; Thunemann, A. F.; Kraehnert, R. *J. Am. Chem. Soc.* **2010**, *132*, 1296-1301.
7. a) Brust, M.; Walker, M.; Bethell, D.; Schiffrin, D. J.; Whyman, R. J. *J. Chem. Soc., Chem. Commun.* **1994**, 801-802. b) Brust, M.; Fink, J.; Bethell, D.; Schiffrin, D. J.; Kiely, C. J. *J. Chem. Soc., Chem. Commun.* **1995**, 1655-1656; c) Zhu, M.; Lanni, E.; Garg, N.; Bier, M. E.; Jin, R. *J. Am. Chem. Soc.* **2008**, *130*, 1138-1139; d) Goulet, P. J. G.; Lennox, R. B. *J. Am. Chem. Soc.* **2010**, *132*, 9582-9584; e) Gutierrez-Wing, C.; Ascencio, J. A.; Pe' rez-Alvarez, M.; Marin-Almazo, M.; Jose'-Yacama'n, M. *J. Cluster Sci.* **1998**, *9*, 529-545. f) Hostetler, M. J.; Wingate, J. E.; Zhong, C. J.; Harris, J. E.; Vachet, R. W.; Clark, M. R.; Londono, J. D.; Green, S. J.; Stokes, J. J.; Wignall, G. D.; Gl' ish, G. L.; Porter, M. D.; Evans, N. D.; Murray, R. W. *Langmuir* **1998**, *14*, 17-30
8. Martin, M. N.; Basham, J. I.; Chando, P.; Eah, S. K. *Langmuir* **2010**, *26*, 7410-7417.
9. a) Murphy, C. J.; San, T. K.; Gole, A. M.; Orendorff, C. J.; Gao, J. X.; Gou, L.; Hunyadi, S. E.; Li, T. *J. Phys. Chem. B* **2005**, *109*, 13857-13870; b) Jana, N. R.; Gearheart, L.; Murphy, C. J. *Chem. Mater.* **2001**, *13*, 2313-2322; c) Sau, T. K.; Pal, A.; Jana, N. R.; Wang, Z. L.; Pal, T. *J. Nanopart. Res.* **2001**, *3*, 257-261; d) Meltzer, S.; Resch, R.; Koel, B. E.; Thompson, M. E.; Madhukar, A.; Requicha, A. A. G.; Will, P. *Langmuir* **2001**, *17*, 1713-1718.
10. a) Scott, R. W. J.; Wilson, O. M.; Crooks, R. M. *J. Phys. Chem. B* **2005**, *109*, 692-704; b) Boisselier, E.; Diallo, A. K.; Salmon, L.; Ornelas, C.; Ruiz, J.; Astruc, D. *J. Am. Chem. Soc.* **2010**, *132*, 2729-2742.
11. a) Templeton, A. C.; Hostetler, M. J.; Kraft, C. T.; Murray, R. W. *J. Am. Chem. Soc.* **1998**, *120*, 1906-1911; b) Ruiz, J.; Astruc, D. *J. Am. Chem. Soc.* **2002**, *124*,

References

- 1782-1789; c) Labande, A.; Astruc, D. *Chem. Comm.* **2000**, 1007-100; d) Hostetler, M. J.; Templeton, A. C.; Murray, R. W. *Langmuir* **1999**, *15*, 3782-3789
12. a) Elghanian, R.; Storhoff, J. J.; Mucic, R. C.; Letsinger, R. L.; Mirkin, C. A. *Science* **1997**, *277*, 1078-1081; b) Jin, R. C.; Wu, G. S.; Li, Z.; Mirkin, C. A.; Schatz, G. C. *J. Am. Chem. Soc.* **2003**, *125*, 1643-1654; c) Mirkin, C. A.; Letsinger, R. L.; Mucic, R. C.; Storhoff, J. J. *Nature* **1996**, *382*, 607; d) Mucic, R. C.; Storhoff, J. J.; Mirkin, C. A.; Letsinger, R. L. *J. Am. Chem. Soc.* **1998**, *120*, 12674; e) Stakenborg, T.; Peeters, S.; Reekmans, G.; Laureyn, W.; Jans, H.; Borghs, G.; Imberechts, H. *J. Nanopart. Res.* **2008**, *10*, 143-152
13. a) Li, G.; Lauer, M.; Schulz, A.; Boettcher, C.; Li, F.; Fuhrhop, J.-H. *Langmuir* **2003**, *19*, 6483-6491. b) Cheng, W.; Dong, S.; Wang, E. *Angew. Chem., Int. Ed.* **2003**, *42*, 449-452.
14. a) Daniel, M. C.; Ruiz, J.; Nlate, S.; Blais, J. C.; Astruc, D. *J. Am. Chem. Soc.* **2003**, *125*, 2617-2628; b) DeVries, G. A.; Brunnbauer, M.; Hu, Y.; Jackson, A. M.; Long, B.; Neltner, B. T.; Uzun, O.; Wunsch, B. H.; Stellacci, F. *Science* **2007**, *315*, 358-361.
15. a) Templeton, A. C.; Wuelfing, M. P.; Murray, R. W. *Acc. Chem. Res.* **2000**, *33*, 27-36; b) Buining, P. A.; Humbel, B. M.; Philipse, A. P.; Verkleij, A. J. *Langmuir* **1997**, *13*, 3921-3926; c) Hostetler, M. J.; Green, S. J.; Stokes, J. J.; Murray, R. W. *J. Am. Chem. Soc.* **1996**, *118*, 4212-4213; d) Templeton, A. C.; Hostetler, M. J.; Warmoth, E. K.; Chen, S.; Hartshorn, C. M.; Krishnamurthy, V. M.; Forbes, M. D. E.; Murray, R. W. *J. Am. Chem. Soc.* **1998**, *120*, 4845-4849; d) Itoh, H.; Tahara, A.; Naka, K.; Chujo, Y. *Langmuir* **2004**, *20*, 1972-1976.
16. a) Yang, Y. Y.; Chen, S. W. *Nano Lett.* **2003**, *3*, 75-79; b) Mulvaney, P. *Langmuir* **1996**, *12*, 788-800; c) Kneipp, K.; Kneipp, H.; Itzkan, I.; Dasari, R. R.; Feld, M. S.;

References

- Dresselhaus, M. S. *Top. Appl. Phys.* **2002**, *82*, 227-247; d) Alvarez, M. M.; Khoury, J. T.; Schaaff, T. G.; Shafiqullin, M. N.; Vezmar, I.; Whetten, R. L. *J. Phys. Chem. B* **1997**, *101*, 3706-3712; e) Logunov, S. L.; Ahmadi, T. S.; El-Sayed, M. A.; Khoury, J. T.; Whetten, R. L. *J. Phys. Chem. B* **1997**, *101*, 3713-3719; f) Schaaf, T. G.; Shafiqullin, M. N.; Khoury, J. T.; Vezmar, I.; Whetten, R. L.; Cullen, W. G.; First, P. N.; Gutierrez-Wing, C.; Ascencio, J.; Jose-Yacamun, M. *J. Phys. Chem. B* **1997**, *101*, 7885-7891; f) Melinger, J. S.; Kleiman, V. D.; McMorrow, D.; Gröhn, F.; Bauer, B. J.; Amis, E. *J. Phys. Chem. A* **2003**, *107*, 3424-3431; g) Souza, G. R.; Yonel-Gumruk, E.; Fan, D.; Easley, J.; Rangel, R.; Guzman-Rojas, L.; Miller, J. H.; Arap, W.; Pasqualini, R. *Plos One* **2008**, *3*, e2242; h) Shipway, A. N.; Lahav, M.; Gabai, R.; Willner, I. *Langmuir* **2000**, *16*, 8789-8795; i) Weisbecker, C. S.; Merritt, M. V.; Whitesides, G. M. *Langmuir* **1996**, *12*, 3763-3772.
17. a) Papanikolaou, N. *Phys. Rev. B* **2007**, *75*, 235426; b) Dionne, J. A.; Sweatlock, L. A.; Atwater, H. A.; Polman, A. *Phys. Rev. B* **2005**, *72*, 075405; c) Inagaki, T.; Motosuga, M.; Arakawa, E. T.; Goudonnet, J. P. *Phys. Rev. B* **1985**, *31*, 2548-2550; d) Pitarke, J. M.; Silkin, V. M.; Chulkov, E. V.; Echenique, P. M. *Rep. Prog. Phys.* **2007**, *70*, 1-87; e) Mock, J. J.; Hill, R. T.; Degiron, A.; Zauscher, S.; Chilkoti, A.; Smith, D. R. *Nano Lett.* **2008**, *8*, 2245-2252; f) Wang, K.; Schonbrun, E.; Crozier, K. B. *Nano Lett.* **2009**, *9*, 2623-2629; g) Ho, H. P.; Law, W. C.; Wu, S. Y.; Lin, C. L.; Kong, S. K. *Biosens. Bioelectron.* **2005**, *20*, 2177-2180; h) Yu, X. L.; Wang, D. X.; Yan, Z. B. *Sens. Actuat. B-Chem.* **2003**, *91*, 285-290; i) Lyon, L. A.; Musick, M. D.; Smith, P. C.; Reiss, B. D.; Pena, D. J.; Natan, M. J. *Sens. Actuat. B-Chem.* **1999**, *54*, 118-12; j) He, L.; Musick, M. D.; Nicewarner, S. R.; Salinas, F. G.; Benkovic, S. J.; Natan, M. J.; Keating, C. D. *J. Am. Chem. Soc.*

References

- 2000, 122, 9071-9077; k) Maitani, M. M.; Ohlberg, D. A. A.; Li, Z. Y.; Allara, D. L.; Stewart, D. R.; Williams, R. S. *J. Am. Chem. Soc.* **2009**, 131, 6310-6311; l) Gifford, L. K.; Sendroiu, I. E.; Corn, R. M.; Luptak, A. *J. Am. Chem. Soc.* **2010**, 132, 9265-9267; m) Kabashin, A. V.; Patskovsky, S.; Grigorenko, A. N. *Opt. Express* **2009**, 17, 21191-21204; n) Wong, C. L.; Ho, H. P.; Suen, Y. K.; Kong, S. K.; Chen, Q. L.; Yuan, W.; Wu, S. Y. *Biosens. Bioelectron.* **2008**, 24, 606-612; o) Yeung, C. L.; Iqbal, P.; Allan, M.; Lashkor, M.; Preece, J. A.; Mendes, P. M. *Adv. Funct. Mater.* **2010**, 20, 2657-2663; p) Homola, J. *Chem. Rev.* **2008**, 108, 462-493.
18. a) Badia, A.; Cuccia, L.; Demers, L.; Morin, F.; Lennox, R. B. *J. Am. Chem. Soc.* **1997**, 119, 2682-2692; b) Ulman, A. *Chem. Rev.* **1996**, 96, 1533-1554; c) Mahmoud, K. A.; Male, K. B.; Hrapovic, S.; Luong, J. H. T. *ACS Appl. Mater. Inter.* **2009**, 1, 1383-1386; d) Serna, R.; Dreyfus, R. W.; Solis, J.; Afonso, C. N.; Allwood, D. A.; Dyer, P. E.; Petford-Long, A. K. *Appl. Surf. Sci.* **1998**, 127, 383-387; e) Giersig, M.; Mulvaney, *Langmuir* **1993**, 9, 3408-3413; f) Terrill, R. H.; Postlethwaite, T. A.; Chen, C.-H.; Poon, C.-D.; Terzis, A.; Chen, A.; Hutchison, J. E.; Clark, M. R.; Wignall, G.; Londono, J. D.; Superfine, R.; Falvo, M.; Johnson, C. S., Jr.; Samulski, E. T.; Murray, R. W. *J. Am. Chem. Soc.* **1995**, 117, 12537-12548.
19. a) Haruta, M.; Ueda, A.; Tsubota, S.; Torres Sanchez, R. M. *Catal. Today* **1996**, 29, 443-447; b) Schubert, M. M.; Hacjenberg, S.; van Vee, A. C.; Muhler, M.; Plzak, V.; Behm, R. *J. Catal.* **2001**, 197, 113-122; c) Sakurai, H.; Haruta, M. *Catal. Today* **1996**, 29, 361-365; d) Pasquato, L.; Rancan, F.; Scrimin, P.; Mancin, F.; Frigeri, C. *Chem. Commun.* **2000**, 2253-2254; e) Bartz, M.; Küther, J.; Seshadri, R.; Tremel, W. *Angew. Chem., Int. Ed.* **1998**, 37, 2466-2468.

20. a) Hirsch, L. R.; Jackson, J. B.; Lee, A.; Halas, N. J.; West, J. *Anal. Chem.* **2003**, *75*, 2377-2381; b) Pavlov, V.; Xiao, Y.; Shlyahovsky, B.; Willner, I. *J. Am. Chem. Soc.* **2004**, *126*, 11768-11769; c) Huang, C. C.; Huang, Y. F.; Cao, Z. H.; Tan, W. H.; Chang, H. T. *Anal. Chem.* **2005**, *77*, 5735-5741; d) Wang, Z. X.; Levy, R.; Fernig, D. G.; Brust, M. *J. Am. Chem. Soc.* **2006**, *128*, 2214-2215; e) Qi, W. J.; Wu, D.; Ling, J.; Huang, C. Z. *Chem. Comm.* **2010**, *46*, 4893-4895; f) Li, W. Y.; Camargo, P. H. C.; Au, L.; Zhang, Q.; Rycenga, M.; Xia, Y. N. *Angew. Chem. Int. Ed.* **2010**, *49*, 164-168; g) Kaminker, R.; Lahav, M.; Motiei, L.; Vartanian, M.; Popovitz-Biro, R.; Iron, M. A.; van der Boom, M. E. *Angew. Chem. Int. Ed.* **2010**, *49*, 1218-1221; h) Jin, R. C. *Angew. Chem. Int. Ed.* **2010**, *49*, 2826-2829.
21. a) Kim, Y. J.; Johnson, R. C.; Hupp, J. T. *Nano Lett.* **2001**, *1*, 165-167; b) Lin, S. Y.; Liu, S. W.; Lin, C. M.; Chen, C. H. *Anal. Chem.* **2002**, *74*, 330-335.
22. a) Leggett, R.; Lee-Smith, E. E.; Jickells, S. M.; Russell, D. A. *Angew. Chem., Int. Ed.* **2007**, *46*, 4100-4103; b) Schnetz, B.; Margot, P. *Forensic Sci. Int.* **2001**, *118*, 21-28; c) Becue, A.; Champod, C.; Margot, P. *Forensic Sci. Int.* **2007**, *168*, 169-176.
23. a) Han, G.; Ghosh, P.; De, M.; Rotello, V. M. *Nanobiotechnol.* **2007**, *3*, 40-45; b) Brown, S. D.; Nativo, P.; Smith, J. A.; Stirling, D.; Edwards, P. R.; Venugopal, B.; Flint, D. J.; Plumb, J. A.; Graham, D.; Wheate, N. J. *J. Am. Chem. Soc.* **2010**, *132*, 4678-4684; c) Guo, S. T.; Huang, Y. Y.; Jiang, Q. A.; Sun, Y.; Deng, L. D.; Liang, Z. C.; Du, Q. A.; Xing, J. F.; Zhao, Y. L.; Wang, P. C.; Dong, A. J.; Liang, X. J. *ACS Nano* **2010**, *4*, 5505-5511.
24. a) Huo, Q.; Worden, J. G. *J. Nanopart. Res.* **2007**, *9*, 1013-1025; b) Shaffer, A. W.; Worden, J. G.; Huo, Q. *Langmuir* **2004**, *20*, 8343-8351.
25. a) Sung, K. M.; Mosley, D. W.; Peelle, B. R.; Zhang, S. G.; Jacobson, J. M. *J. Am.*

References

- Chem. Soc.* **2004**, *126*, 5064-5065; b) Worden, J. G.; Shaffer, A. W.; Huo, Q. *Chem. Comm.* **2004**, 518-519; c) Worden, J. G.; Dai, Q.; Shaffer, A. W.; Huo, Q. *Chem. Mater.* **2004**, *16*, 3746-3755.
26. Liu, X.; Worden, J. G.; Dai, Q.; Zou, J.; Wang, J.; Huo, Q. *Small* **2006**, *2*, 1126-1129.
27. a) Wilson, R.; Chen, Y.; Aveyard, J. *Chem. Comm.* **2004**, 1156-1157; b) Kruger, C.; Agarwal, S.; Greiner, A. *J. Am. Chem. Soc.* **2008**, *130*, 2710-2711.
28. a) Claridge, S. A.; Liang, H. Y. W.; Basu, S. R.; Frechet, J. M. J.; Alivisatos, A. P. *Nano Lett.* **2008**, *8*, 1202-1206; b) Zheng, J. W.; Constantinou, P. E.; Micheel, C.; Alivisatos, A. P.; Kiehl, R. A.; Seeman, N. C. *Nano Lett.* **2006**, *6*, 1502-1504; c) Aldaye, F. A.; Sleiman, H. F. *J. Am. Chem. Soc.* **2007**, *129*, 4130-4131; d) Olson, M. A.; Coskun, A.; Klajn, R.; Fang, L.; Dey, S. K.; Browne, K. P.; Grzybowski, B. A.; Stoddart, J. F. *Nano. Lett.* **2009**, *9*, 3185-3190; e) Mullen, D. G.; Borgmeier, E. L.; Desai, A. M.; van Dongen, M. A.; Barash, M.; Cheng, X. M.; Baker, J. R.; Holl, M. M. B. *Chem. Eur. J.* **2010**, *16*, 10675-10678.
29. Huo, F. W.; Lytton-Jean, A. K. R.; Mirkin, C. A. *Adv. Mater.* **2006**, *18*, 2304-2306.
30. Jackson, A. M.; Myerson, J. W.; Stellacci, F. *Nat. Mater.* **2004**, *3*, 330-336.
31. Dai, Q.; Worden, J. G.; Trullinger, J.; Huo, Q. *J. Am. Chem. Soc.* **2005**, *127*, 8008-8009.
32. Chak, C. P.; Chau, L. H.; Wu, S. Y.; Ho, H. P.; Li, W. J.; Mendes, P. M.; Leung, K. C. F. *J. Mater. Chem.* **2011**, *21*, in press.
33. a) Chen, G.; Wang, Y.; Tan, L. H.; Yang, M. X.; Tan, L. S.; Chen, Y.; Chen, H. Y. *J Am Chem Soc* **2009**, *131*, 4218-4219; b) Brousseau, L. C.; Novak, J. P.; Marinakos, S. M.; Feldheim, D. L. *Adv Mater* **1999**, *11*, 447-449.

34. Chen, J. I. L.; Chen, Y.; Ginger, D. S. *J. Am. Chem. Soc.* **2010**, *132*, 9600-9601.
35. Maitani, M. M.; Ohlberg, D. A. A.; Li, Z. Y.; Allara, D. L.; Stewart, D. R.; Williams, R. S. *J. Am. Chem. Soc.* **2009**, *131*, 6310-6311.
36. a) Aldaye, F. A.; Sleiman, H. F. *Angew. Chem. Int. Ed.* **2006**, *45*, 2204-2209; b) Nykypanchuk, D.; Maye, M. M.; Van Der Lelie, D.; Gang, O. *Nature* **2008**, *451*, 549-552.
37. Feldheim, D. L.; Keating, C. D. *Chem. Soc. Rev.* **1998**, *27*, 1-12.
38. a) Steed, J. W.; Atwood, J. L. *Supramolecular Chemistry*, John Wiley & Sons Limited, U.K., 2000 ; b) Klajn, R.; Stoddart, J. F.; Grzybowski, B. A. *Chem. Soc. Rev.* **2010**, *39*, 2203-2237.
39. a) Browne, W. R.; Feringa, B. L. *Nat. Nanotechnol.* **2006**, *1*, 25-35; b) Kay, E. R.; Leigh, D. A.; Zerbetto, F. *Angew. Chem., Int. Ed.* **2007**, *46*, 72-191; c) Sauvage, J. P. *Molecular machines and motors*, Springer, Berlin, 2001. d) Saha, S.; Leung, K. C.-F.; Nguyen, T. D.; Stoddart, J. F.; Zink, J. I. *Adv. Funct. Mater.* **2007**, *17*, 685-693; e) Philp, D.; Stoddart, J. F. *Angew. Chem. Int. Ed.* **1996**, *35*, 1155-1196; f) Leung, K. C. F.; Chak, C. P.; Lo, C. M.; Wong, W. Y.; Xuan, S. H.; Cheng, C. H. K. *Chem. Asian J.* **2009**, *4*, 364-381; g) Kolchinski, A. G.; Busch, D. H.; Alcock, N. W. *J. Chem. Soc., Chem. Commun.* **1995**, 1289-1291; h) Ashton, P. R.; Campbell, P. J.; Chrystal, E. J. T.; Glink, P. T.; Menzer, S.; Philp, D.; Spencer, N.; Stoddart, J. F.; Tasker, P. A.; Williams, D. J. *Angew. Chem., Int. Ed.* **1995**, *34*, 1865-1869; i) Badjic, J. D.; Ronconi, C. M.; Stoddart, J. F.; Balzani, V.; Silvi, S.; Credi, A. *J. Am. Chem. Soc.* **2006**, *128*, 1489-1499; j) Leung, K. C.-F.; Nguyen, T. D.; Stoddart, J. F.; Zink, J. I. *Chem. Mater.* **2006**, *18*, 5919-5928; k) Nguyen, T. D.; Leung, K. C. F.; Liong, M.; Pentecost, C. D.; Stoddart, J. F.; Zink, J. I. *Org. Lett.* **2006**, *8*, 3363-3366.

40. The association constants (K_a) for the 1:1 [DB24C8 \supset Dibenzylamine] pseudorotaxane formation are approximately $10^5 - 10^6$ in CH_2Cl_2 and $10^2 - 10^3$ in MeCN, which were measured using the isothermal titration calorimetry at 298 K. See: South, C. R.; Higley, M. N.; Leung, K. C.-F.; Lanari, D.; Nelson, A.; Grubbs, R. H.; Stoddart, J. F.; Weck, M. *Chem. Eur. J.* **2006**, *12*, 3789–3797.
41. a) Yamaguchi, N.; Hamilton, L. M.; Gibson, H. W. *Angew. Chem., Int. Ed.* **1998**, *37*, 3275-3279; b) Tokunaga, Y.; Seo, T. *Chem. Comm.* **2002**, 970-971; c) Jones, J. W.; Bryant, W. S.; Bosman, A. W.; Janssen, R. A. J.; Meijer, E. W.; Gibson, H. W. *J. Org. Chem.* **2003**, *68*, 2385-2389; d) Diederich, F.; Echegoyen, L.; Gomez-Lopez, M.; Kessinger, R.; Stoddart, J. F. *J. Chem. Soc. Perk. Trans. 2* **1999**, *8*, 1577-1586.
42. Chak, C. P.; Xuan, S. H.; Mendes, P. M.; Yu, J. C.; Cheng, C. H. K.; Leung, K. C. F. *ACS Nano* **2009**, *3*, 2129-2138.
43. Sellers, H.; Ulman, A.; Shnidman, Y.; Eilers, J. E. *J. Am. Chem. Soc.* **1993**, *115*, 9389-9401.
44. a) Fields, G. B. *Solid-phase peptide synthesis*, Academic Press, San Diego, 1997; b) Santini, R.; Griffith, M. C.; Qi, M. *Tetrahedron Lett.* **1998**, *39*, 8951-8954; c) Bennett, W.D.; Christensen, J. W.; Hamaker, L. K.; Peterson, M. L.; Rhodes, M. R.; Saneii, H. H. *Advanced Chemtech Handbook of Combinatorial & Solid Phase Organic Chemistry: A Comprehensive Guide to Principles, Products & Protocols*, Advanced ChemTech, Inc, Louisville, KY, 1998.
45. South, C. R.; Leung, K. C.-F.; Lanari, D.; Stoddart, J. F.; Weck, M. Noncovalent Side-Chain Functionalization of Terpolymers. *Macromolecules* **2006**, *39*, 3738–3744.
46. Coates, J.; Meyers, R. A., *Interpretation of Infrared Spectra, A Practical*

- Approach. In Encyclopedia of Analytical Chemistry*; John Wiley & Sons, Chichester, U.K., 2000.
47. Lin, S.Y.; Tsai, Y.T.; Chen, C.C.; Lin, C.M.; Chen, C.H. T. *J. Phys.Chem. B* **2004**, *108*, 2134–2139.
48. a) Kluth, G. J.; Carraro, C.; Maboudian, R. *Phys. Rev. B* **1999**, *59*, R10449–R10452; b) Mock, J. J.; Hill, R. T.; Degiron, A.; Zauscher, S.; Chilkoti, A.; Smith, D. R. *Nano Lett.* **2008**, *8*, 2245–2252.
49. Laurent, S.; Forge, D.; Port, M.; Roch, A.; Robic, C.; Elst, L. V.; Muller, R. N. *Chem. Rev.* **2008**, *108*, 2064–2110.
50. Wang, H. H.; Wang, Y. X. J.; Leung, K. C. F.; Au, D. W. T.; Xuan, S. H.; Chak, C. P.; Lee, S. K. M.; Sheng, H.; Zhang, G.; Qin, L.; Griffith, J. E.; Ahuja, A. T. *Chem. Eur. J.* **2009**, *15*, 12417-12425.
51. Leung, K. C. F.; Wang, Y. X. J.; Wang, H. H.; Xuan, S. H.; Chak, C. P.; Cheng, C. H. K. *IEEE Trans. Nanobiosci.* **2009**, *8*, 192-198.
52. Xuan, S. H.; Wang, Y. X. J.; Yu, J. C.; Leung, K. C. F. *Chem. Mater.* **2009**, *21*, 5079-5087.
53. Jiang, P.; Xie, S.-S.; Yao, J.-N.; Pang, S.-J.; Gao, H. J. *J. Phys. D: Appl. Phys.* **2001**, *34*, 2255–2259.
54. a) Wu, P.; Feldman, A. K.; Nugent, A. K.; Hawker, C. J.; Scheel, A.; Voit, B.; Pyun, J.; Fréchet, J. M. J.; Sharpless, K. B.; Fokin, V. V. *Angew. Chem., Int. Ed.* **2004**, *43*, 3928–3932; b) Aprahamian, I.; Miljanic, O. S.; Dichtel, W. R.; Isoda, K.; Yasuda, T.; Kato, T.; Stoddart, J. F. *Bull. Chem. Soc. Jpn.* **2007**, *80*, 1856–1869.
55. a) Alivisatos, A. P.; Johnsson, K. P.; Peng, X. G.; Wilson, T. E.; Loweth, C. J.; Bruchez, M. P.; Schultz, P. G. *Nature* **1996**, *382*, 609-611; b) Zanchet, D.; Micheel, C. M.; Parak, W. J.; Gerion, D.; Alivisatos, A. P. *Nano. Lett.* **2001**, *1*,

- 32-35; c) Claridge, S. A.; Goh, S. L.; Frechet, J. M. J.; Williams, S. C.; Micheel, C. M.; Alivisatos, A. P. *Chem. Mater.* **2005**, *17*, 1628-1635; d) Aldaye, F. A.; Sleiman, H. F. *J. Am. Chem. Soc.* **2007**, *129*, 4130-4131; e) Claridge, S. A.; Liang, H. Y. W.; Basu, S. R.; Frechet, J. M. J.; Alivisatos, A. P. *Nano. Lett.* **2008**, *8*, 1202-1206.
56. Sigmund, P. *Nucl. Instr. Meth. Phys. Rev. B* **1987**, *27*, 1-20.
57. Duffy, D. C.; McDonald, J. C.; Schueller, O. J. A.; Whitesides, G. M. *Anal. Chem.* **1998**, *70*, 4974-4984.
58. a) van Kan, J. A.; Rajta, I.; Ansari, K.; Bettiol, A. A.; Watt, F. *Microsyst. Technol.* **2002**, *8*, 383-386; b) Liu, J.; Cai, B.; Zhu, J.; Ding, G.; Zhao, X.; Yang, C.; Chen, D. *Microsyst. Technol.*, **2004**, *10*, 265-268; c) Shirtcliffe, N. J.; Aqil, S.; Evans, C.; McHale, G.; Newton, M. I.; Perry, C. C.; Roach, P. *J. Micromech. Microeng.* **2004**, *14*, 1384-1389.
59. a) Badjic, J. D.; Nelson, A.; Cantrill, S. J.; Turnbull, W. B.; Stoddart, J. F. *Acc. Chem. Res.* **2005**, *38*, 723-732; b) Cox, R. H.; Leyden, D. E.; Elving, P. J.; Bursey, M. M.; Kolthoff, I. M. *Treatise on Analytical Chemistry*, 2nd Edition, Wiley, U.S.A., 1983, 127-136.
60. Leung, K. C. F.; Ho, H. P.; Kwan, Y. W.; Kong, S. K. *Expert Rev. Mol. Diagn.* **2010**, *10*, 863-867.
61. a) Razin, S. *Mol. Cell. Probes*, **1994**, *8*, 497-511; b) Hacia, J. G.; Brody, L. C.; Chee, M. S.; Fodor, S. P. A.; Collins, F. S. *Nat. Genet.*, **1996**, *14*, 441-447.
62. a) Taton, T. A.; Mucic, R. C.; Mirkin, C.A.; Letsinger, R. L. *J. Am. Chem. Soc.* **2000**, *122*, 6305-6306; b) Shipway, A.N.; Willner, I. *Chem. Commun.* **2001**, *20*, 2035-2045; c) Reichert, J.; Csaki, A.; Kohler, J. M.; Fritzsche, W. *Anal. Chem.* **2000**, *72*, 6025-6029; d) Niemeyer, C. M.; Ceyhan, B.; Gao, S.; Chi, L.; Peschel,

- S.; Simon, U. *Colloid Polym. Sci.* **2001**, *279*, 68–72; e) Souza, G. R.; Miller, J. H. *J. Am. Chem. Soc.* **2001**, *123*, 6734–6735.
63. a) Jin, C. *Angew. Chem., Int. Ed.* **2010**, *49*, 2826–2829; b) Li, D.; Song, S.; Fan, C. *Acc. Chem. Res.* **2010**, *43*, 631–641.
64. a) Storhoff, J. J.; Elghanian, R.; Mucic, R. C.; Mirkin, C. A.; Letsinger, R. L. *J. Am. Chem. Soc.* **1998**, *120*, 1959–1964; b) Kim, J. Y.; Lee, J. S. *Nano Lett.* **2009**, *9*, 4564–4569.
65. a) Shankar, N.; Baghdayan, A. S.; Gilmore, M. S. *Nature* **2002**, *417*, 746–750; b) Yang, C.; Wang, Y.; Marty, J. L.; Yang, X. *Biosens. Bioelectron.* **2011**, *26*, 2724–2727; c) Huang, C.; Stakenborg, T.; Cheng, Y.; Colle, F.; Steylaerts, T.; Jans, K.; Dorpe, P. V.; Lagae, L. *Biosens. Bioelectron.* **2011**, *26*, 3121–3126; d) Wang, W.; Wu, W. Y.; Zhong, X.; Wang, W.; Miao, Q.; Zhu, J. J. *Biosens. Bioelectron.* **2011**, *26*, 3110–3114.
66. a) Luu, Y. K.; Kim, K.; Hsiao, B. S.; Chu, B.; Hadjiargyrou, M. *J. Control. Release* **2003**, *89*, 341–353; b) Liang, D. H.; Luu, Y. K.; Kim, K.; Hsiao, B. S.; Hadjiargyrou, M.; Chu, B. *Nucleic Acids Res.* **2005**, *33*, 170e.
67. Smith, B. D.; Liu, J. *J. Am. Chem. Soc.* **2010**, *132*, 6300–6301.
68. Ke, F.; Luu, Y. K.; Hadjiargyrou, M.; Liang, D. *PLoS ONE* **2010**, *5*, e13308.
69. Xiao, S. J.; Brunner, S.; Wieland, M. *J. Phy. Chem.* **2004**, *108*, 16508–16517.
70. a) Song, H. Y.; Ngai, M. H.; Song, Z. Y.; MacAry, P. A.; Hobley, J.; Lear, M. J. *Org. Biomol. Chem.* **2009**, *7*, 3400–3406; b) Pounder, R. J.; Stanford, M. J.; Brooks, P.; Richards, S. P.; Dove, A. P. *Chem. Commun.* **2008**, 5158–5160.
71. a) Hud, N.V.; Mailanovich, F. P.; Balhorn, R. *Biochemistry* **1994**, *33*, 7528–7535; b) Brewer, S. H.; Anthireya, S. J.; Lappi, S. E.; Drapcho, D. L.; Franzen, S. *Langmuir* **2002**, *18*, 4460–4464; c) SantaLucia, J. *Proc. Natl. Acad. Sci. USA*, **1998**,

References

- 95, 1460-1465.
72. Chak, C. P.; Lai, J. M. Y.; Sham, K. W. Y.; Cheng, C. H. K.; Leung, K. C. F., ,
RSC Adv., in press.

Appendix

List of NMR Spectra and Mass spectra

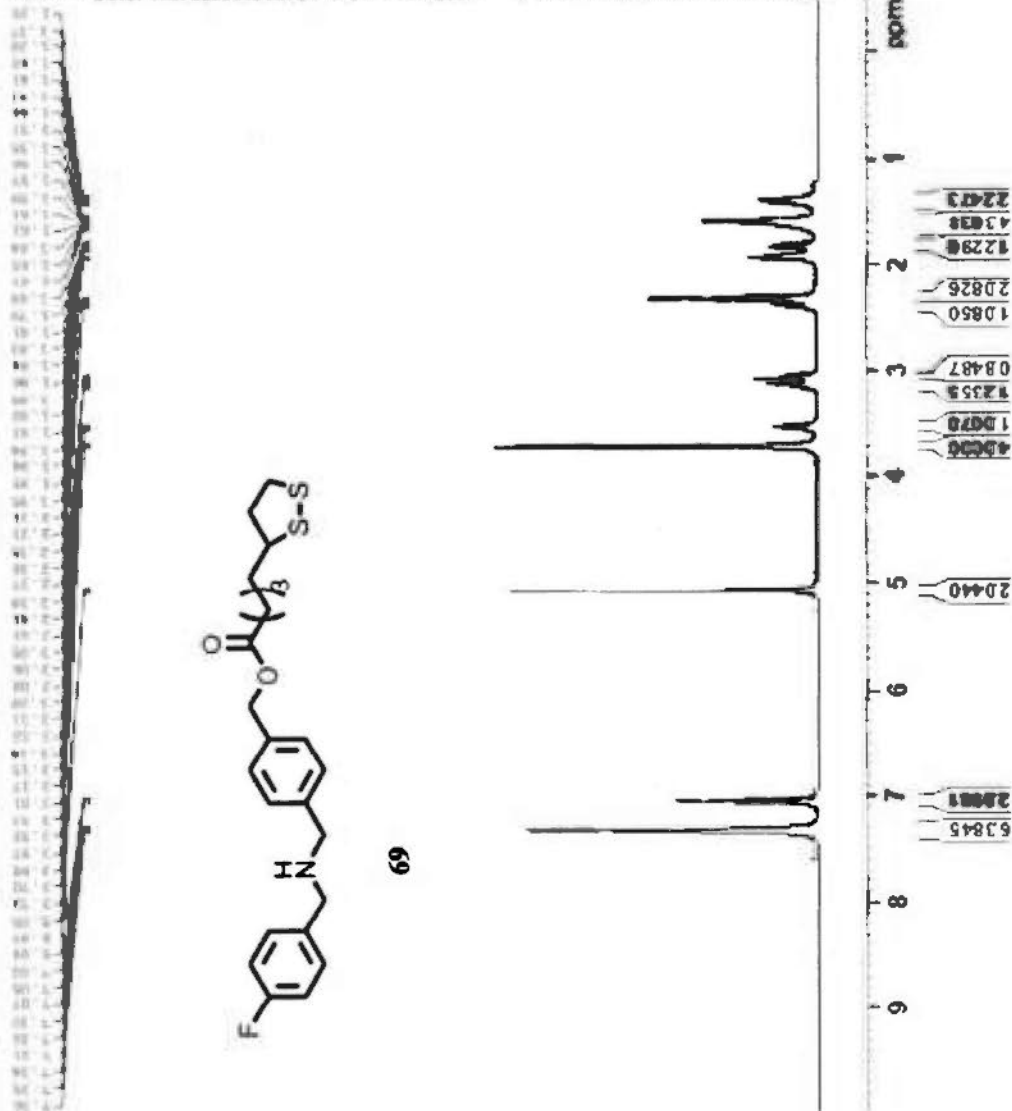
1. ^1H NMR spectrum of 69	A2
2. ^{13}C NMR spectrum of 69	A3
3. Mass spectrum of 69	A4
4. ^1H NMR spectrum of 69 ·HPF ₆	A5
5. ^{13}C NMR spectrum of 69 ·HPF ₆	A6
6. Mass spectrum of 69 ·HPF ₆	A7
7. 2D NMR spectrum of 68 ⊃ 69 ·HPF ₆	A8
8. ^1H NMR spectrum of 73	A9
9. ^{13}C NMR spectrum of 73	A10
10. Mass spectrum of 73	A11
11. ^1H NMR spectrum of 82	A12
12. ^{13}C NMR spectrum of 82	A13
13. Mass spectrum of 82	A14
14. ^1H NMR spectrum of 84	A15
15. ^{13}C NMR spectrum of 84	A16
16. Mass spectrum of 84	A17
17. ^1H NMR spectrum of 86	A18

18. ^{13}C NMR spectrum of 86	A19
19. Mass spectrum of 86	A20
20. ^1H NMR spectrum of 89	A21
21. ^{13}C NMR spectrum of 89	A22
22. Mass spectrum of 89	A23
23. ^1H NMR spectrum of 90	A24
24. ^{13}C NMR spectrum of 90	A25
25. Mass spectrum of 90	A26

¹H NMR Spectrum of Compound 69

NAME Thioestermonamine
 EXPNO 1
 PROCNO 1
 Date_ 20080514
 Time 21.29
 INSTRUM spect
 PROBHD 5 mm PNU1 13C
 PULPROG zg30
 TD 65536
 SOLVENT CD3CN
 NS 16
 DS 0
 SWH 10000.000 Hz
 FIDRES 0.152588 Hz
 AQ 3.2768500 sec
 RG 144
 DW 50.000 usec
 DE 6.50 usec
 TE 301.6 K
 D1 1.00000000 sec
 TDO 1

----- CHANNEL f1 -----
 NUC1 1H
 P1 5.00 usec
 PL1 0.00 dB
 PL1W 8.31434441 W
 SFO1 400.1316005 MHz
 SI 65536
 SF 400.1300076 MHz
 WDM EM
 SSB 0
 LB 0.30 Hz
 GB 0
 FC 1.00



¹³C NMR Spectrum of Compound 69

NAME Thioestermonoamine [C13]

EXPNO 1

PROCNO 1

Date_ 20080514

Time_ 21.34

INSTRUM spect

PROBHD 5 mm PADUL 13C

PULPROG zgpg

TD 131072

SOLVENT CD3CN

NS 1101

DS 0

SWH 29761.904 Hz

FIDRES 0.227065 Hz

AQ 2.2020595 sec

RG 303

DW 16.800 usec

DE 6.50 usec

TE 301.1 K

D1 1.0000000 sec

D11 0.0300000 sec

TDO 1

===== CHANNEL f1 =====

NUC1 13C

P1 5.00 usec

PL1 -0.60 dB

PL1W 41.24164963 W

SFO1 100.6208180 MHz

===== CHANNEL f2 =====

CPDPRG2 waltz16

NUC2 1H

PCPD2 90.00 usec

PL2 0.00 dB

PL12 16.10 dB

PL2W 8.31434441 W

PL12W 0.20409293 W

SFO2 400.1320007 MHz

SI 131072

SF 100.6126781 MHz

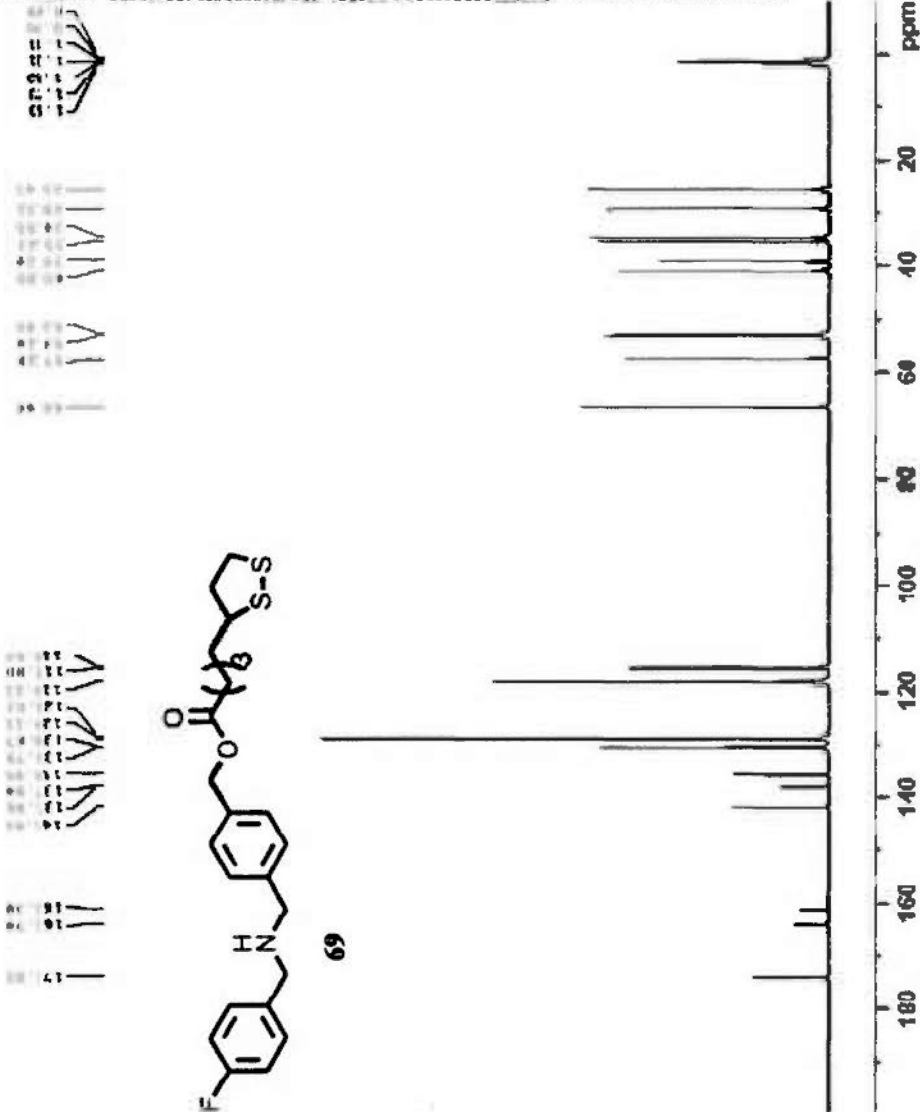
WDW EM

SSB 0

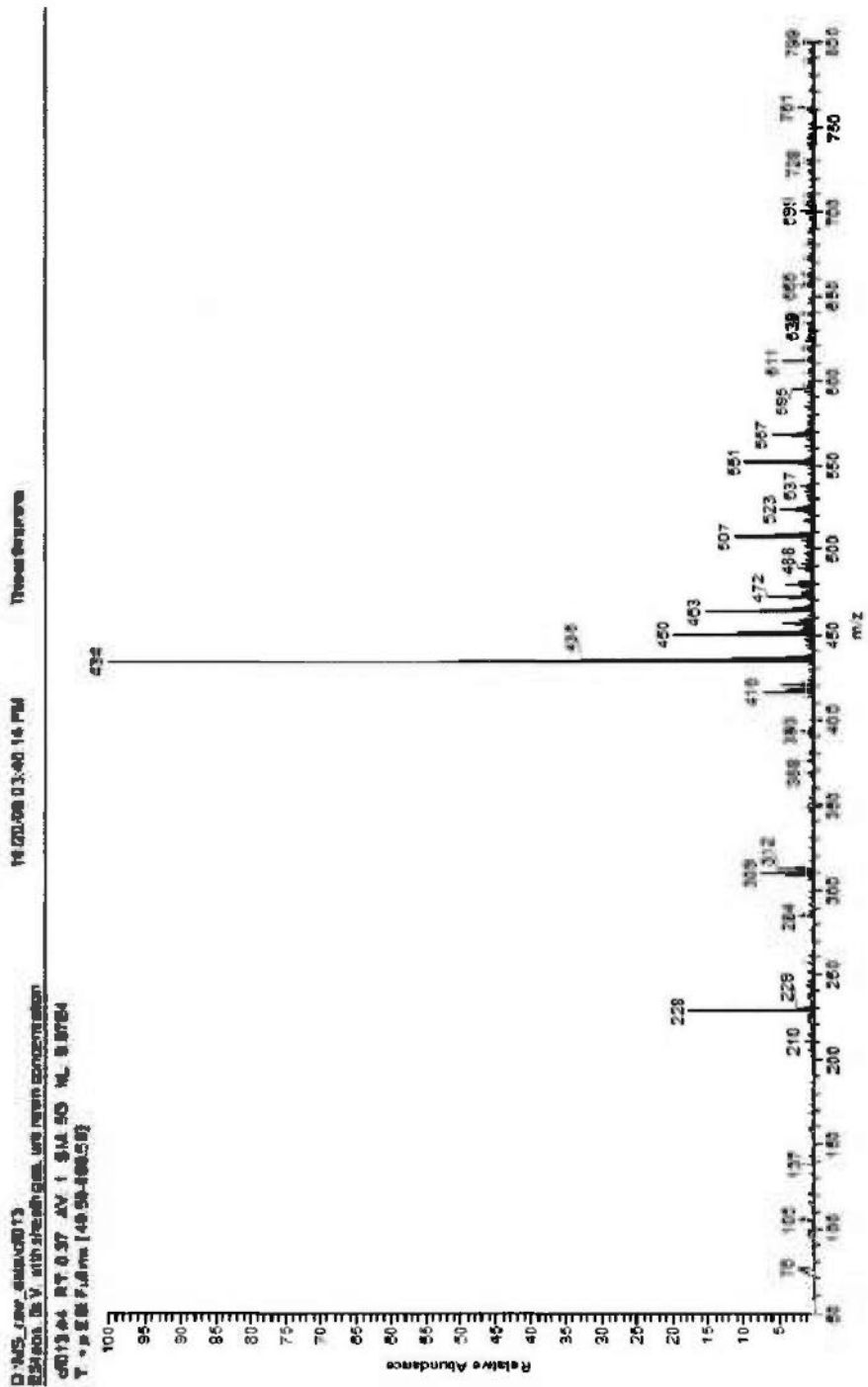
LB 3.00 Hz

GB 0

PC 1.40



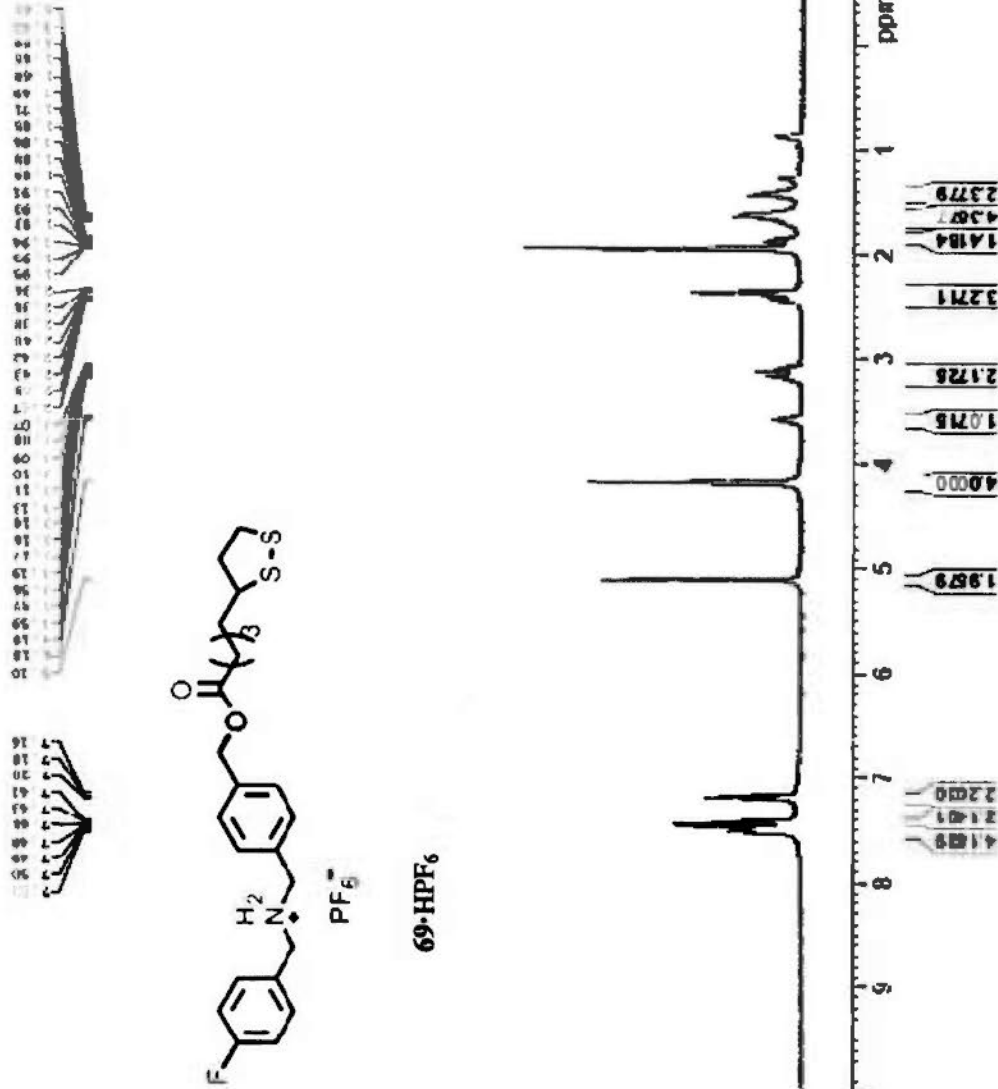
Mass Spectrum of Compound 69



¹H NMR spectrum of 69-HPF₆

NAME ThioestermonoaminePF6-
 EXPNO 1
 PROCNO 1
 Date 20080526
 Time 15.15
 INSTRUM spect
 PROBHD 5 mm PADUL 13C
 PULPROG zg30
 TD 65536
 CD3CN
 SOLVENT 16
 DS 0
 SWH 10000.000 Hz
 FIDRES 0.152588 Hz
 AQ 3.2768500 sec
 RG 203
 DW 50.000 usec
 DE 6.50 usec
 TE 296.2 K
 D1 1.00000000 sec
 TD0 1

----- CHANNEL f1 -----
 NUC1 1H
 P1 5.00 usec
 PL1 0.00 dB
 PL1W 8.31434441 W
 SF01 400.1316005 MHz
 SI 65536
 SF 400.1300072 MHz
 WDW EM
 SSB 0
 LB 0.30 Hz
 GB 0
 PC 1.00

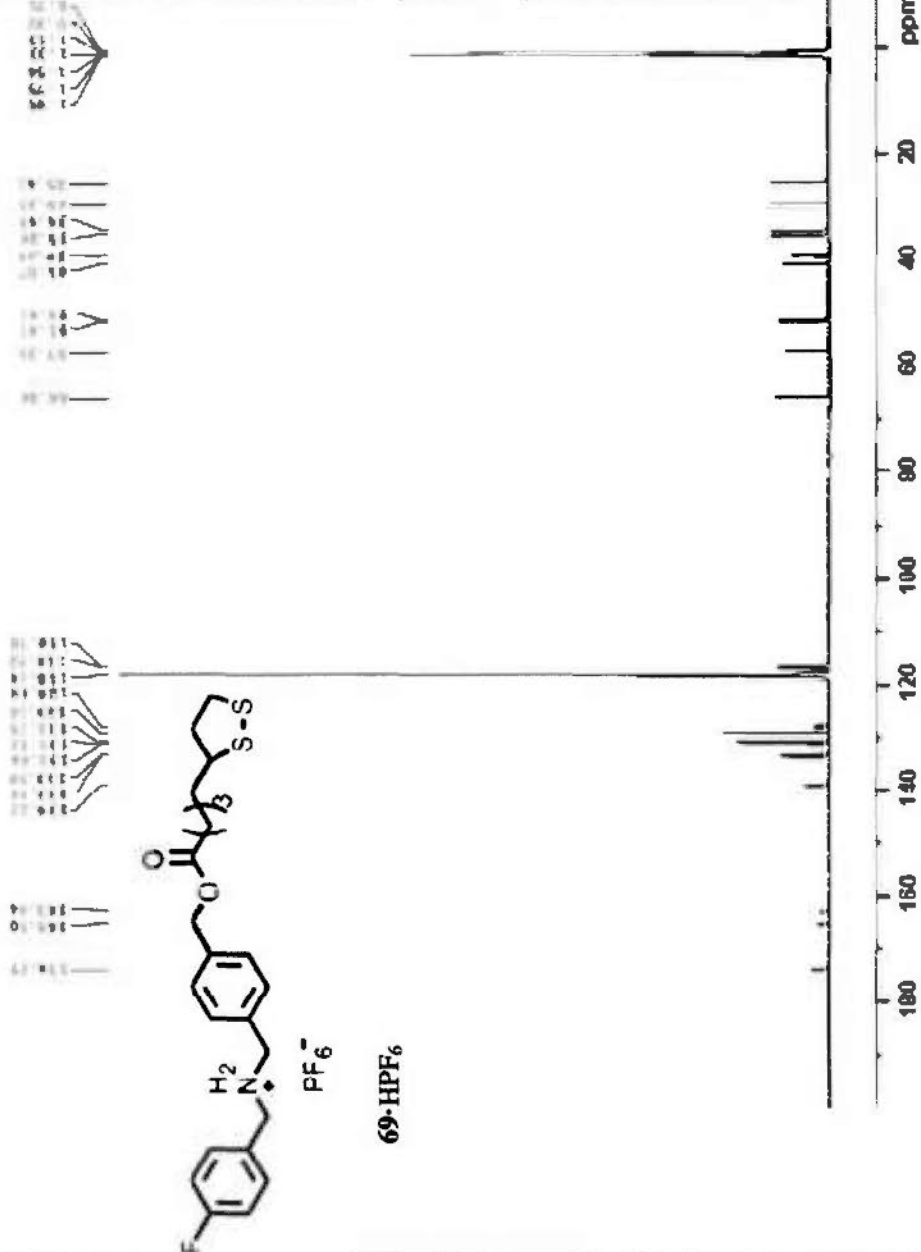


¹³C NMR spectrum of 69-HPF₆

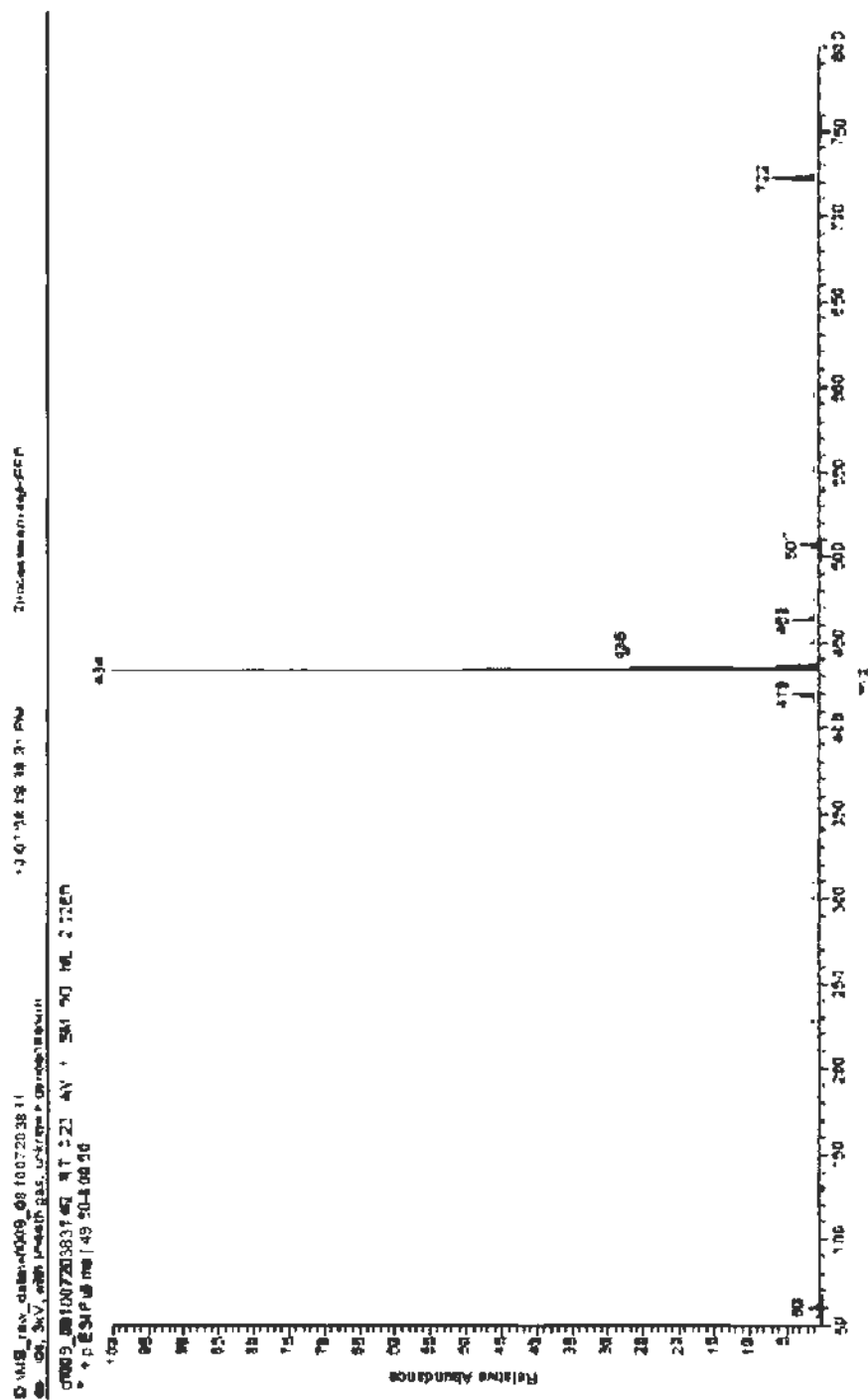
NAME ThioestermonoaminePF6 [C]
 EXPNO 1
 PROCNO 1
 Date_ 20080527
 Time 14.38
 INSTRUM spect
 PROBHD 5 mm PADUL 13C
 PULPROG zgpg
 TD 131072
 SOLVENT CD3CN
 NS 3142
 DS 0
 SWH 29761.904 Hz
 FIDRES 0.227065 Hz
 AQ 2.2020595 sec
 RG 203
 DW 16.800 usec
 DE 6.50 usec
 TE 298.9 K
 D1 1.00000000 sec
 D11 0.03000000 sec
 TDO 1

CHANNEL F1
 NUC1 13C
 P1 5.00 usec
 PL1 -0.60 dB
 PL1W 41.24164963 W
 SFO1 100.6208180 MHz

CHANNEL F2
 CPDPRG2 waltz16
 NUC2 1H
 PCPD2 90.00 usec
 PL2 0.00 dB
 PL12 16.10 dB
 PL2W 8.31434441 W
 PL12W 0.20409293 W
 SFO2 400.1320007 MHz
 SI 131072
 SF 100.6125682 MHz
 MDW EM
 SSB 0
 LB 3.00 Hz
 GB 0
 PC 1.40

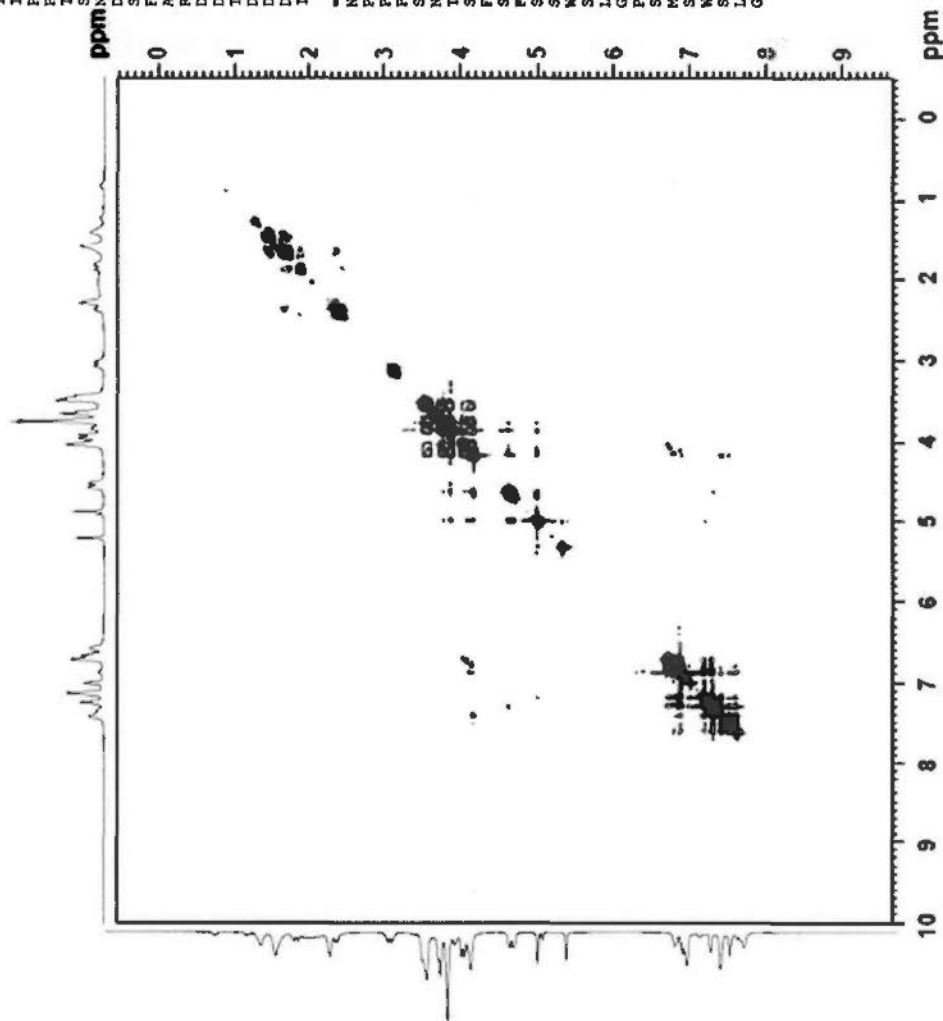


Mass spectrum of 69•HPF₆



2D NMR spectrum of 68 \rightarrow 69-HPF₆

NAME pong-ThioestermonaminePF₆-DM24C8O2Me-
 EXPNO 3
 PROCNO 1
 Date_ 20080812
 Time_ 21.08
 INSTRUM spect
 PROBDI 5 mm PABBI 1H/
 PULPROG zgpg30
 TD 2048
 SOLVENT CDCl₂
 NS 16
 DS 4
 SWH 4084.967 Hz
 FIDRES 1.994613 Hz
 AQ 0.2507252 sec
 RG 203
 DW 122.400 usec
 DE 6.50 usec
 TE 294.6 K
 D0 0.00011336 sec
 D1 2.00000000 sec
 D8 0.30000001 sec
 D9 0.00024480 sec
 IN0 0.00024480 sec
 CHANNEL f1
 NUC1 1H
 P1 7.10 usec
 PL1 -2.00 dB
 PL1W 13.1734718 W
 SFO1 400.1318413 MHz
 NDO 1
 ID 75
 SFO1 400.1318 MHz
 FIDRES 54.466232 Hz
 SW 10.209 ppm
 States-TPEI
 SI 1024
 SF 400.1300087 MHz
 WDW QSINE
 SSB 2
 LB 0.00 Hz
 GB 0
 PC 1.00
 SI 1024
 MC2
 SF 400.1300084 MHz
 WDW QSINE
 SSB 2
 LB 0.00 Hz
 GB 0

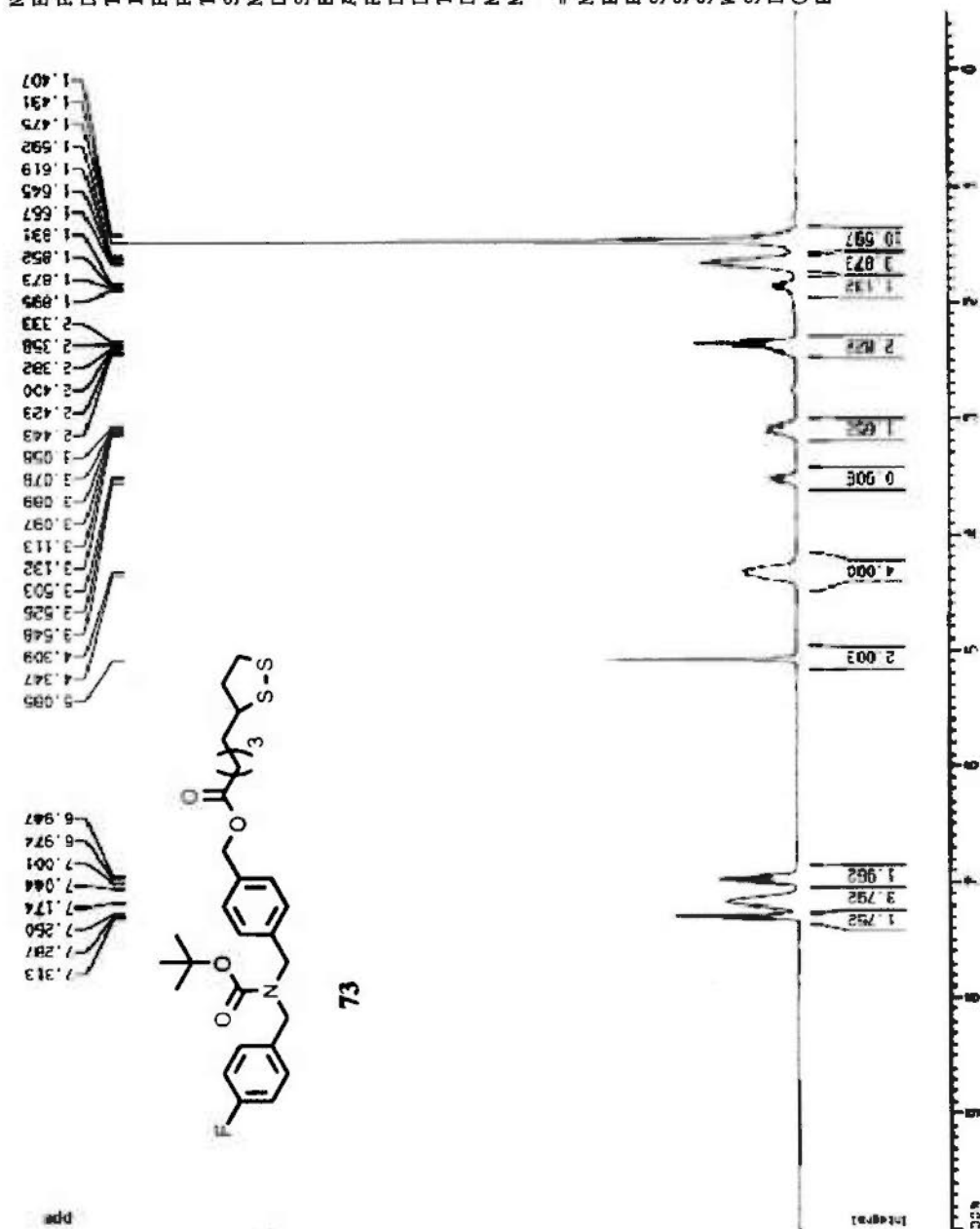


¹H NMR spectrum of 73

thioestermono-21-4-08

NAME 1
 EXPNO 1
 PROCNO 1
 Date_ 20080421
 Time 12.11
 INSTRUM dpx300
 PROBHD 5 mm BBO BB-1H
 PULPROG zg
 TD 32768
 SOLVENT CDC13
 NS 16
 DS 0
 SWH 8992.806 Hz
 FIDRES 0.274439 Hz
 AQ 1.8219508 sec
 RG 20.2
 DW 55.600 usec
 DE 79.43 usec
 TE 296.2 K
 D1 1.00000000 sec
 MCREST 0.00000000 sec
 MCWRK 0.01500000 sec

===== CHANNEL f1 =====
 NUC1 1H
 P1 5.00 usec
 PL1 -2.00 dB
 SF01 300.1312000 MHz
 SI 32768
 SE 300.1300057 MHz
 WDW EM
 SSB 0
 LB 0.30 Hz
 GB 0
 PC 1.00



¹³C NMR spectrum of 73

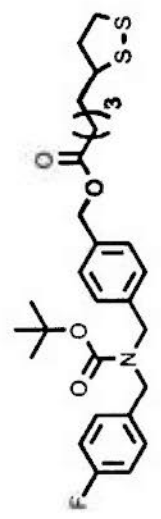
NAME thloestermono[c]-21-4-08
 EXPNO 1
 PROCNO 1
 Date_ 20080421
 Time 13.41
 INSTRUM dpx300
 PROBHID 5 mm BBO BB-1H
 PULPROG zgpg
 TD 65536
 SOLVENT CDCl3
 NS 2068
 DS 0
 SWH 22675.736 Hz
 FIDRES 0.346004 Hz
 AQ 1.445188 sec
 RG 8192
 DW 22.050 usec
 DE 6.00 usec
 TE 296.2 K
 D1 1.00000000 sec
 d11 0.03000000 sec
 MCREST 0.00000000 sec
 MCHRK 0.01500000 sec

===== CHANNEL f1 =====
 NUC1 13C
 P1 3.00 usec
 PL1 -6.00 dB
 SF01 75.4745111 MHz

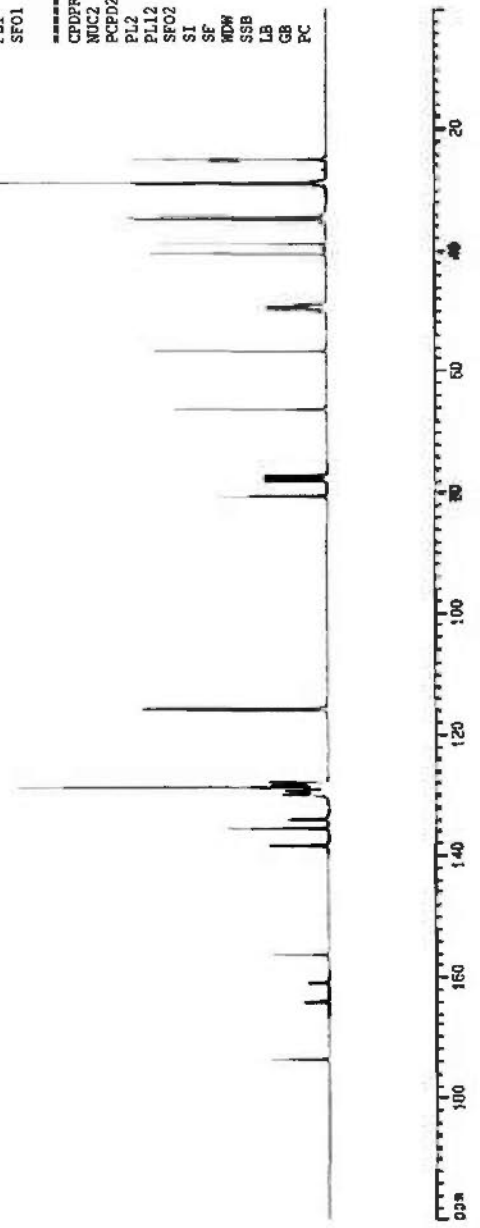
===== CHANNEL f2 =====
 CPDPRG2 waltz16
 NUC2 1H
 PCPD2 100.00 usec
 PL2 120.00 dB
 PL12 19.00 dB
 SF02 300.1315007 MHz
 SI 65536
 SF 75.4677198 MHz
 MDW EM
 SSB 0
 LB 3.00 Hz
 GB 0
 PC 1.40

85.648
 78.036
 77.812
 77.611
 77.187
 66.262
 56.702
 48.418
 48.194
 48.753
 48.603
 38.876
 34.972
 34.442
 29.127
 28.830
 25.052

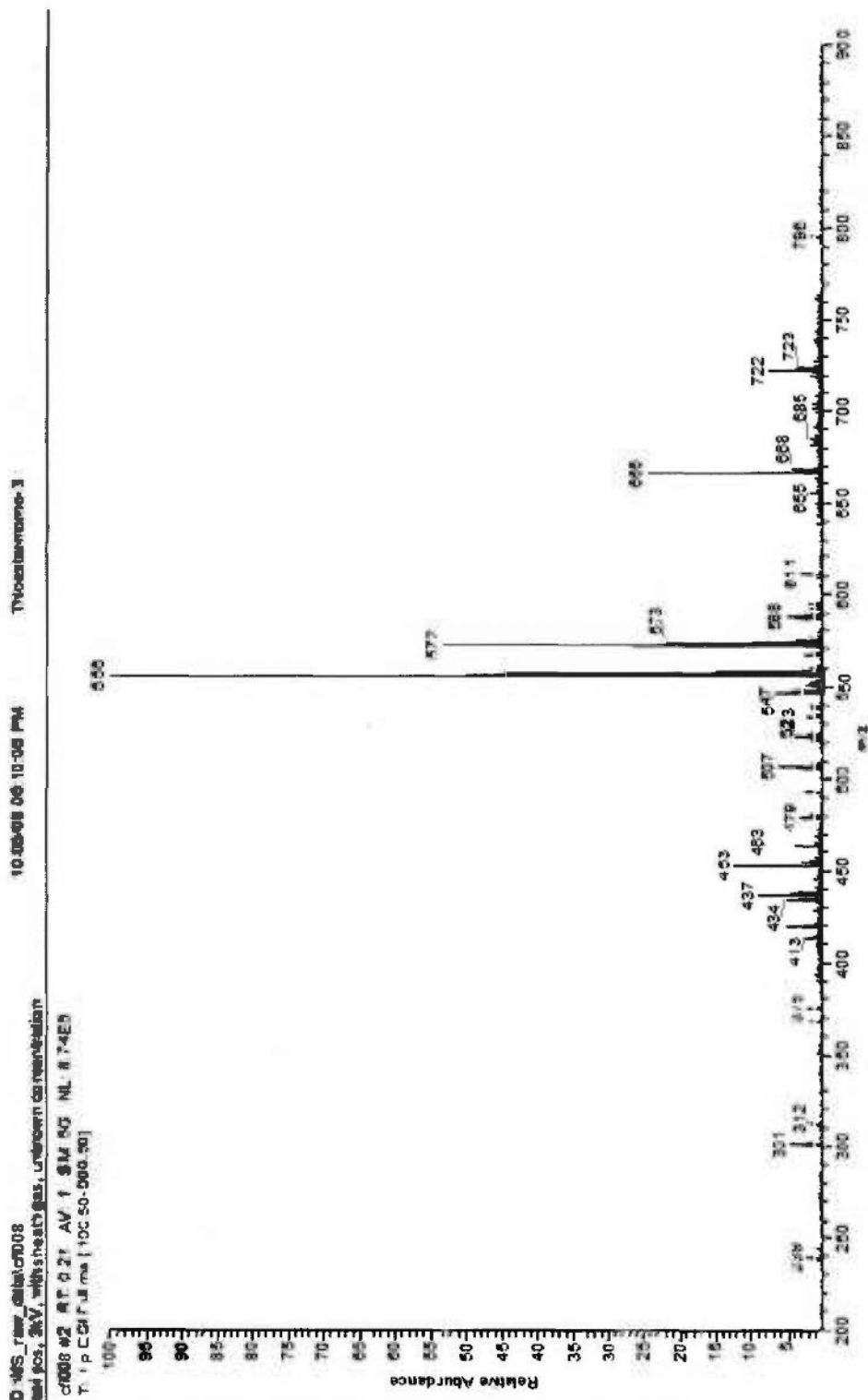
173.843
 164.060
 160.811
 156.227
 138.357
 135.514
 134.067
 129.996
 129.500
 128.905
 128.522
 128.018
 115.991
 115.608



73



Mass spectrum of 73



¹H NMR spectrum of 82

NAME pong-BisDB24C8-22-7-2011

EXPNO 1

PROCNO 1

Date_ 20110722

Time 14.16

INSTRUM spect

PROBHD 5 mm PABBO BE

PULPROG zg30

TD 65536

SOLVENT CDCl3

NS 16

DS 2

SWH 8223.685 Hz

FIDRES 0.125483 Hz

AQ 3.9846387 sec

RG 80.6

DW 60.800 usec

DE 6.50 usec

TE 298.0 K

DI 1.00000000 sec

TD0 1

===== CHANNEL f1 =====

NUC1 1H

P1 14.00 usec

PL1 -1.00 dB

PL1W 13.56617069 W

SFO1 400.1924713 MHz

SI 32768

SF 400.1900148 MHz

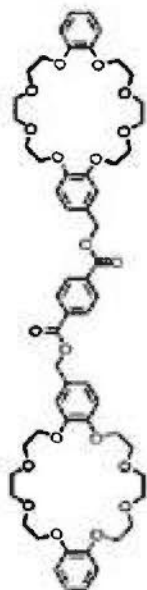
WDW EM

SSB 0

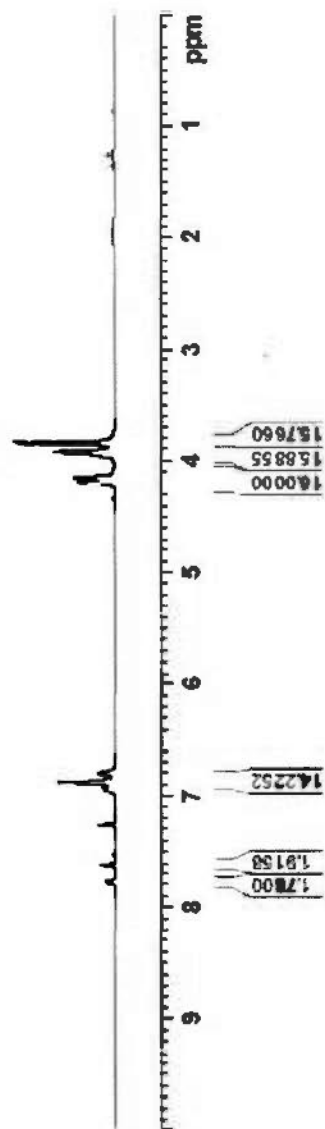
LB 0.30 Hz

GB 0

PC 1.00



82

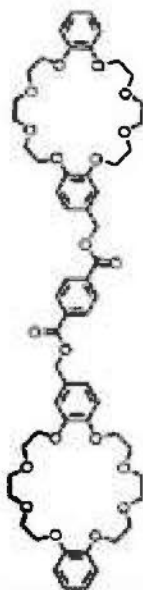
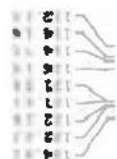


¹³C NMR spectrum of 82

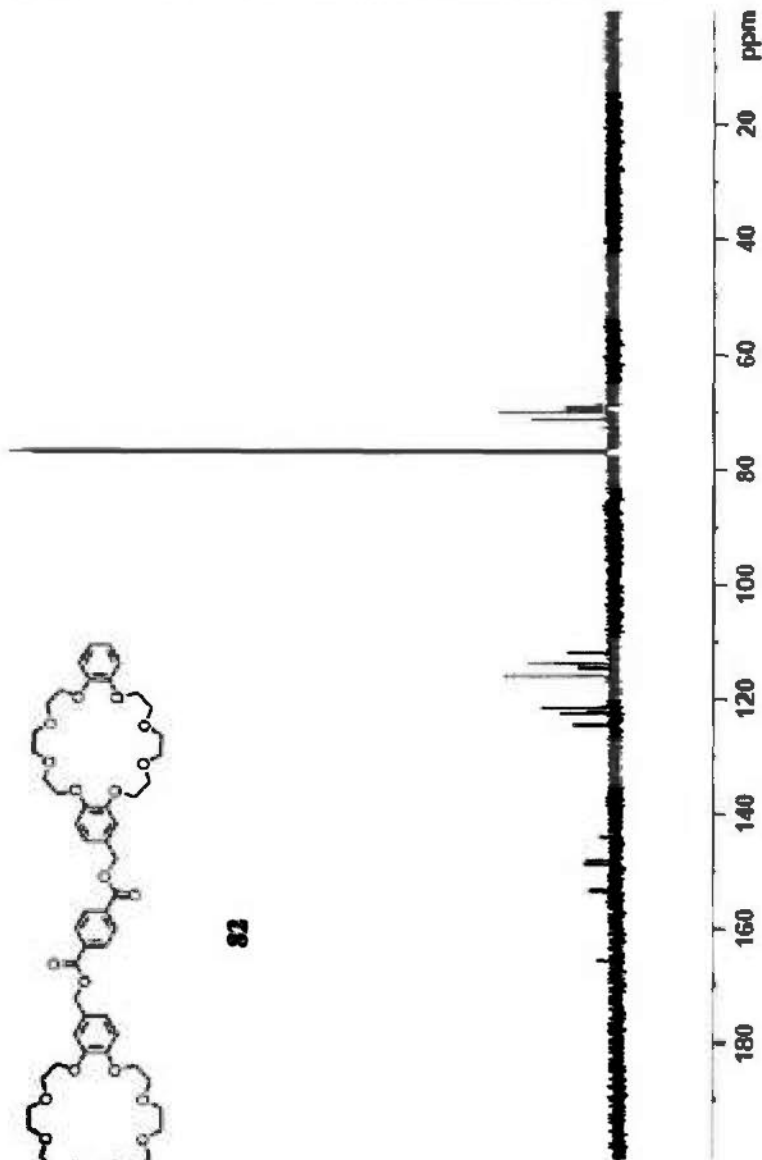
pong-BisDB24CB[C]-22-07-11

NAME 1
 EXPNO 1
 PROCNO 1
 Date_ 20110722
 Time 14.29
 INSTRUM spect
 PROBHD 5 mm PABBO BB-
 PULPROG zgpg30
 TD 65536
 SOLVENT CDCl3
 NS 510
 DS 4
 SWH 24038.461 Hz
 FIDRES 0.366798 Hz
 AQ 1.3631988 sec
 RG 2050
 DM 20.800 usec
 DE 6.50 usec
 TE 298.8 K
 D1 2.0000000 sec
 D11 0.03000000 sec
 TDO 1

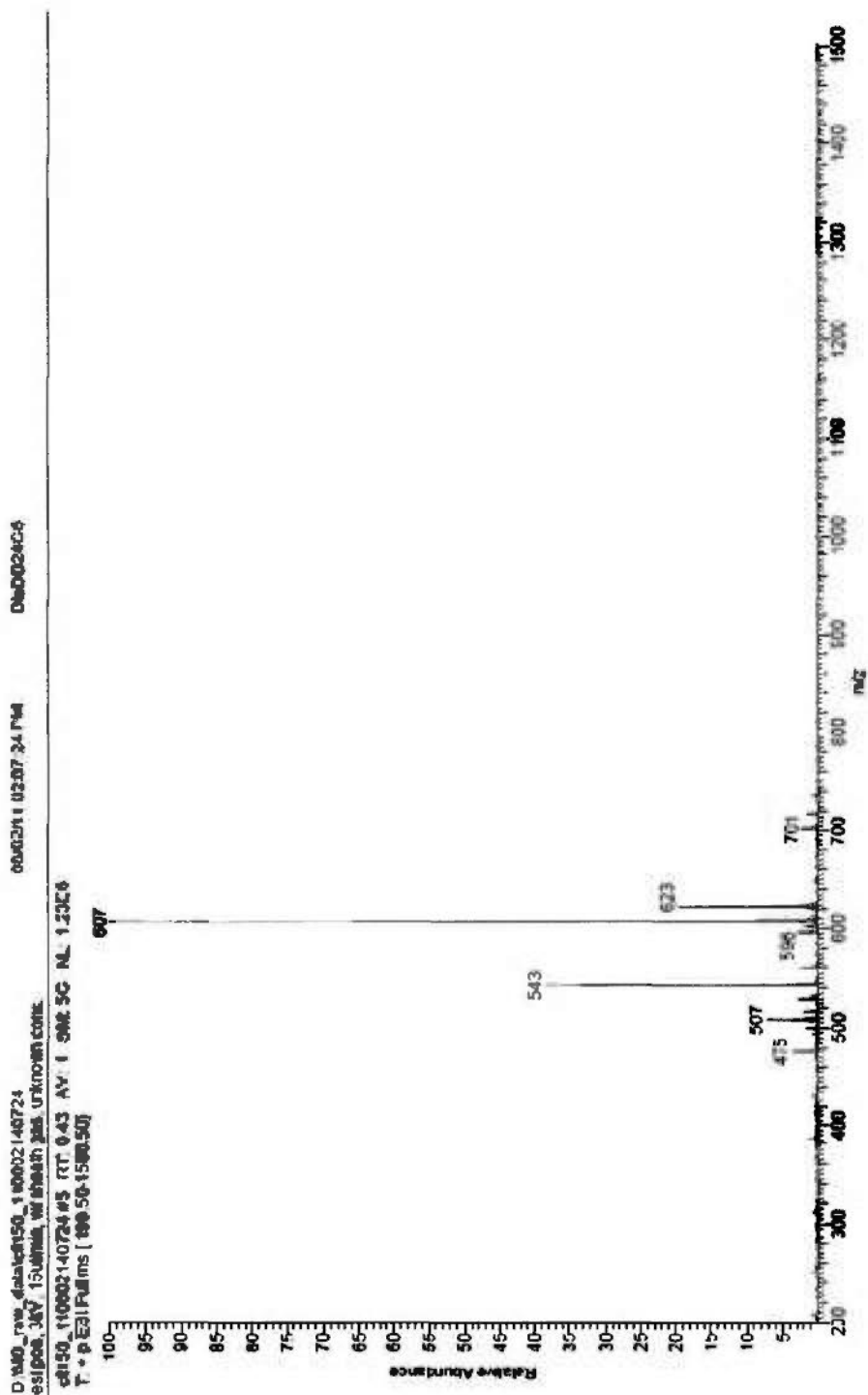
===== CHANNEL f1 =====
 NUC1 13C
 P1 9.90 usec
 PL1 -2.00 dB
 PL1W 55.33689499 W
 SF01 100.6379183 MHz
 ===== CHANNEL f2 =====
 CPDPRG2 waltz16
 NUC2 1H
 EPC02 90.00 usec
 PL2 -1.00 dB
 PL12 15.16 dB
 PL13 18.62 dB
 PL2W 13.56617069 W
 PL12W 0.32844096 W
 PL13W 0.14806664 W
 SF02 400.1916008 MHz
 SI 32768
 SF 100.6278449 MHz
 KDW EM
 SSB 0
 LB 1.00 Hz
 GB 0
 PC 1.40



82



Mass spectrum of 82

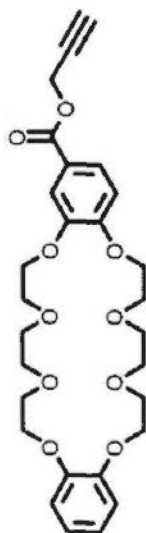


¹H NMR spectrum of 84

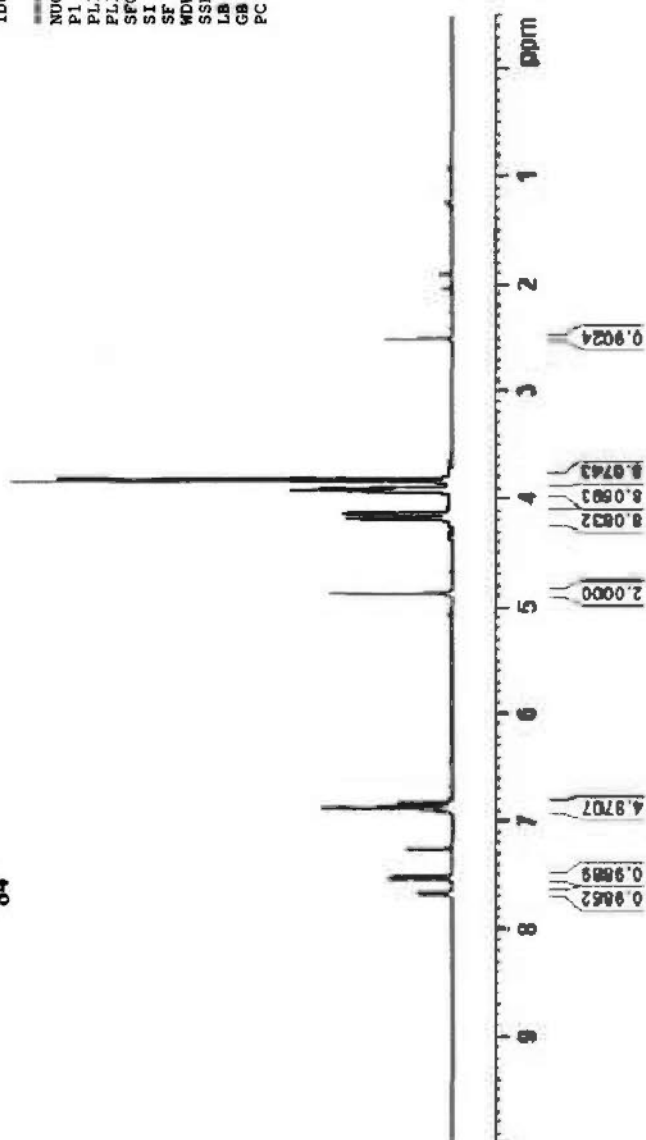
NAME peng-trownCO2propagrylestar

EXPNO 1
 PROCNO 1
 Date_ 20081108
 Time 14.43
 INSTRUM spect
 PROBH1 5 mm PADUL 13C
 PULPROG zg30
 TD 65536
 SOLVENT CDCl3
 NS 8
 DS 0
 SWH 10000.000 Hz
 FIDRES 0.152588 Hz
 AQ 3.2768500 sec
 RG 128
 DM 50.000 usec
 DE 6.50 usec
 TE 295.3 K
 D1 1.00000000 sec
 TD0 1

===== CHANNEL f1 =====
 NUC1 1H
 P1 14.83 usec
 PL1 0.00 dB
 PL1W 6.3143441 W
 SF01 400.1316005 MHz
 SI 65536
 SE 400.1300043 MHz
 MDW EM
 SSB 0
 LB 0.30 Hz
 GB 0
 PC 1.00



84



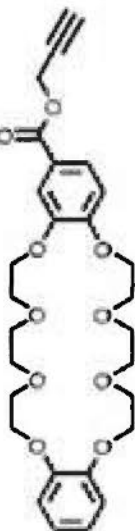
¹³C NMR spectrum of 84

pong-crownCO2propargylester [c]

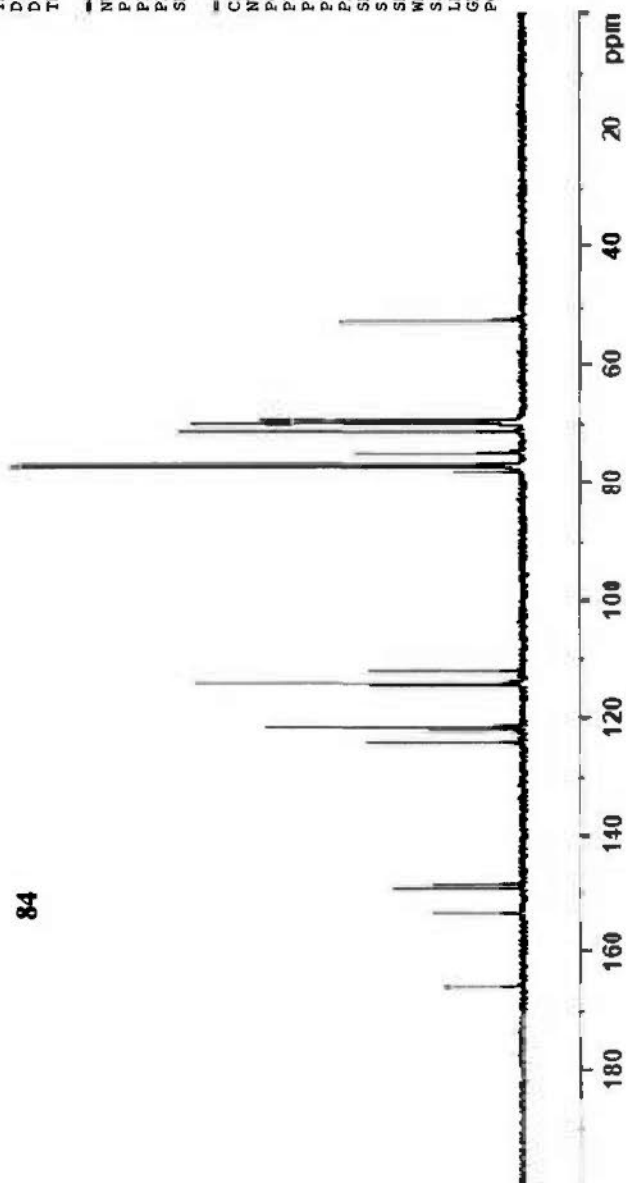
NAME
EXPNO 1
PROCNO 1
Date_ 20081108
Time 15.33
INSTRUM spect
PROBHD 5 mm PADUL 13C
PULPROG zgpgc
TD 131072
SOLVENT CDCl3
NS 1074
DS 0
SWH 29761.904 Hz
FIDRES 0.227065 Hz
AQ 2.2020595 sec
RG 203
DW 16.800 usec
DE 6.50 usec
TE 296.0 K
D1 1.00000000 sec
D11 0.03000000 sec
TDO 1

CHANNEL f1
NUC1 13C
P1 5.00 usec
PL1 -0.60 dB
PL1W 41.24164963 W
SFO1 100.6208180 MHz

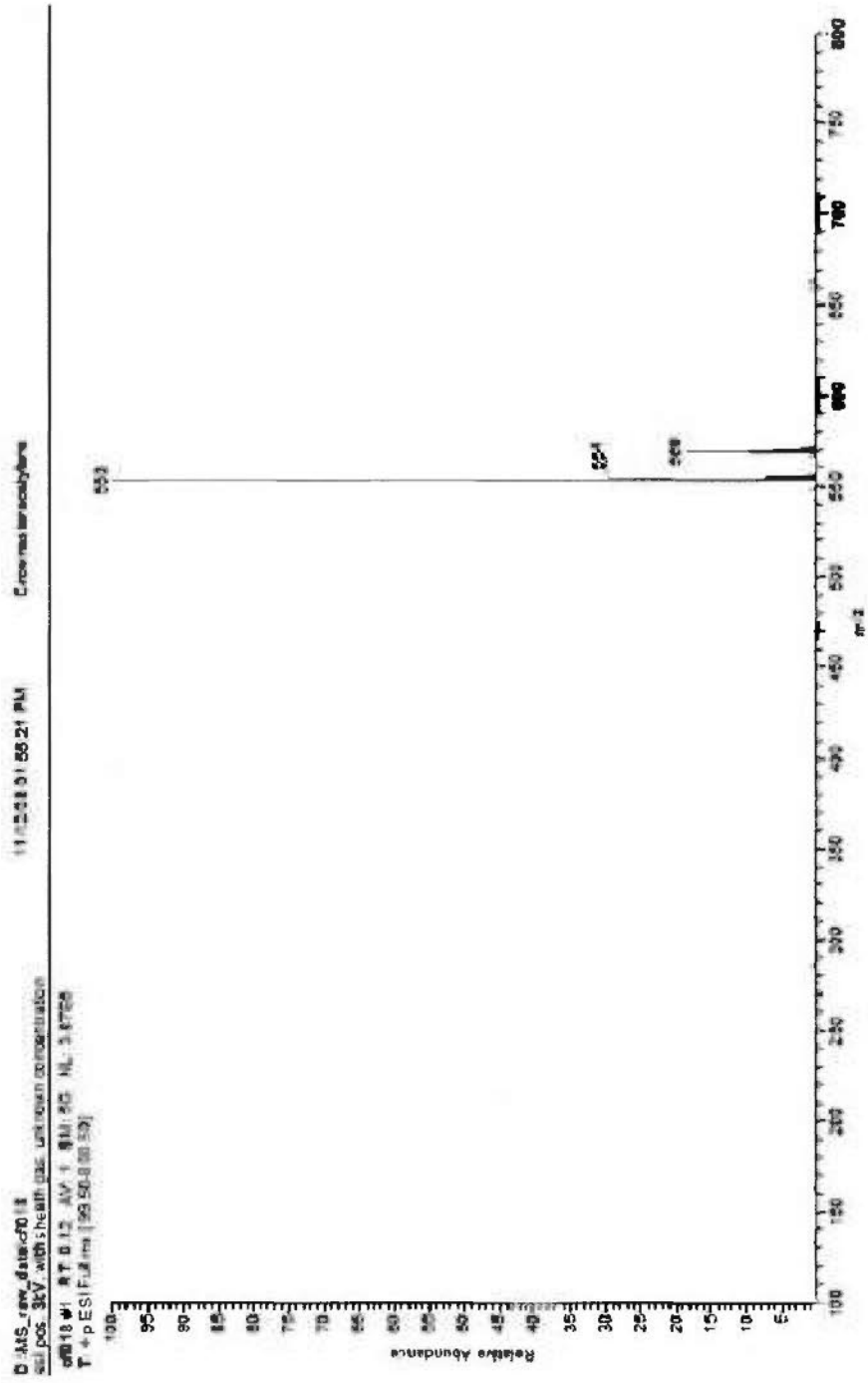
CHANNEL f2
CPDPRG2 waitz16
NUC2 1H
PCPD2 90.00 usec
PL2 0.00 dB
PL12 16.10 dB
PL2W 8.31434441 W
PL12W 0.20409293 W
SFO2 400.1320007 MHz
SI 131072
SF 100.6127595 MHz
WDW EM
SSB 0
LB 3.00 Hz
GB 0
PC 1.40



84



Mass spectrum of 84

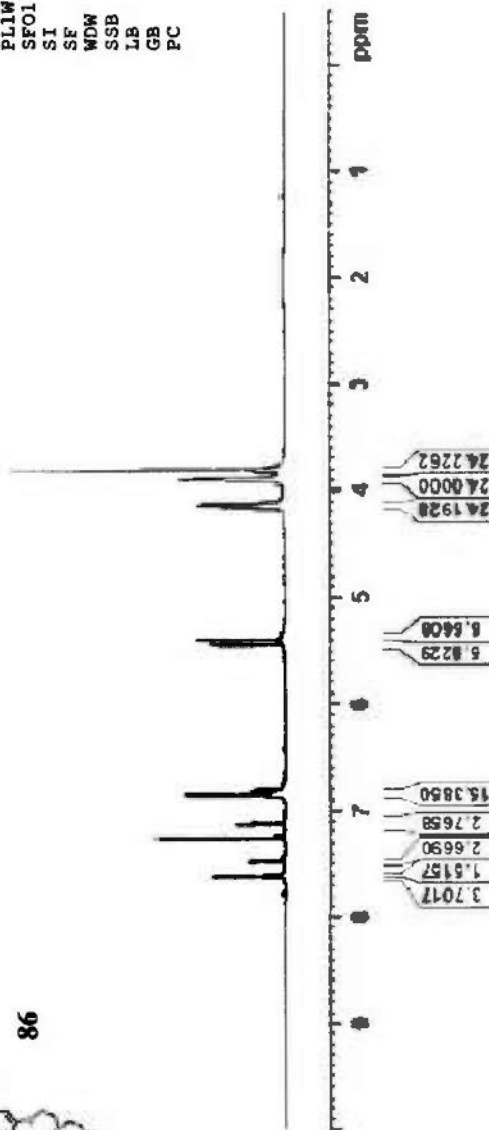
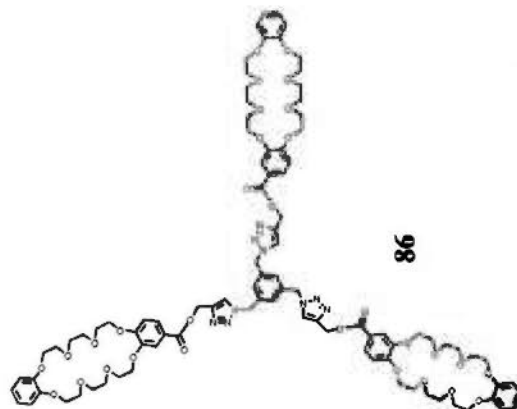
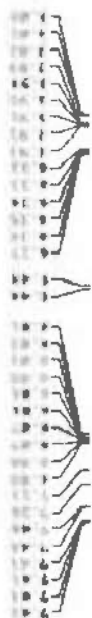


¹H NMR spectrum of 86

pong-crowntrimerclick

NAME 1
 EXPNO 1
 PROCNO 1
 Date 20081119
 Time 14.02
 INSTRUM spect
 PROBHD 5 mm PADUL 13C
 PULPROG zg
 TD 65536
 SOLVENT CDCl3
 NS 16
 DS 0
 SWH 10000.000 Hz
 FIDRES 0.152588 Hz
 AQ 3.2768500 sec
 RG 203
 DW 50.000 usec
 DE 6.50 usec
 TE 295.4 K
 D1 5.0000000 sec
 TD0 1

CHANNEL f1
 NUC1 1H
 P1 5.00 usec
 PL1 0.00 dB
 PL1W 8.31434441 W
 SF01 400.1316005 MHz
 SI 65536
 SE 400.1300045 MHz
 WDW EM
 SSB 0
 LB 0.30 Hz
 GB 0
 PC 1.00



¹³C NMR spectrum of 86

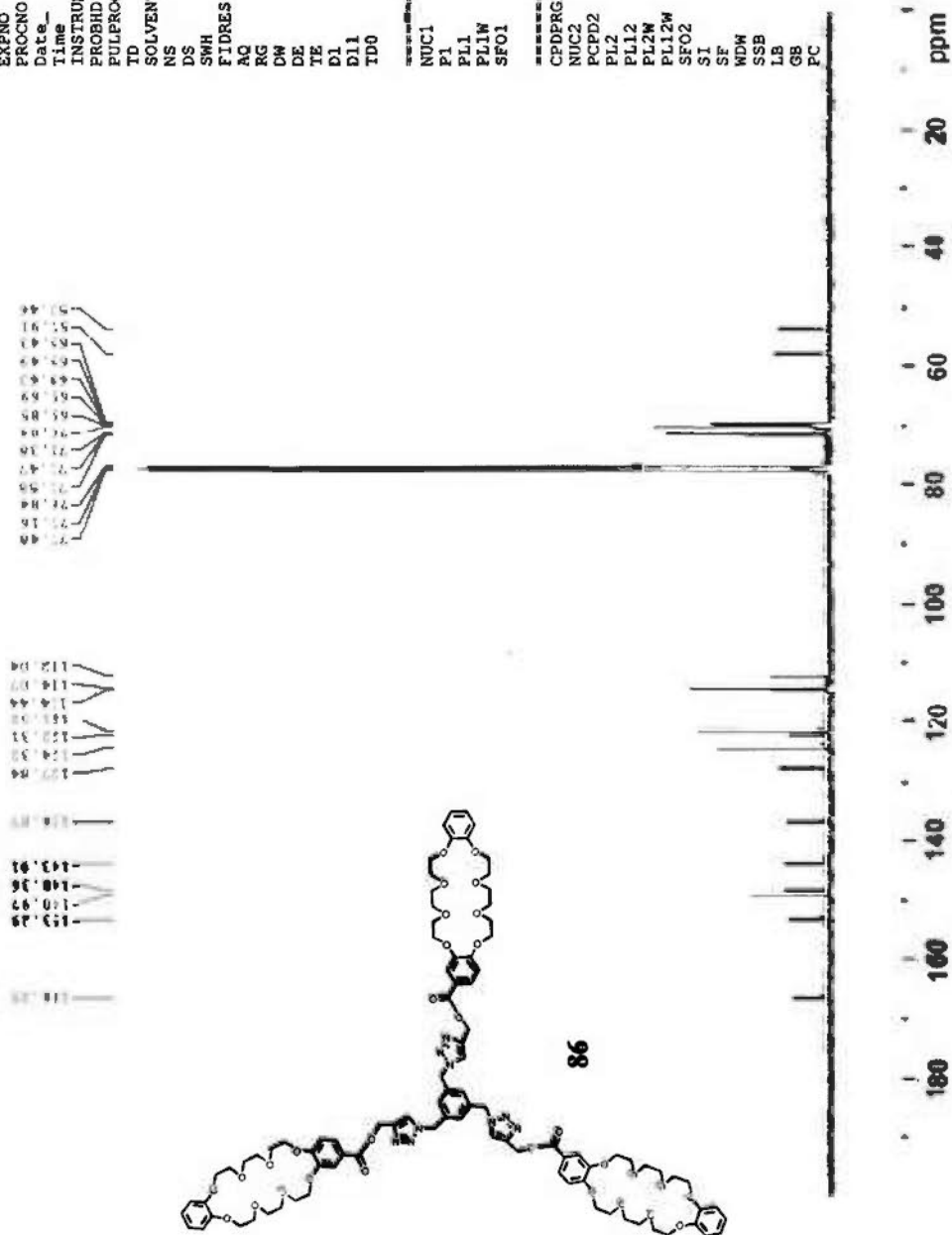
```

NAME      pong-crowntriacetic(C)
EXPNO    1
PROCNO   1
Date_    2008118
Time     21.03
INSTRUM  spect
PROBHD   5 mm PADUL 13C
PULPROG  zgpg
TD        131072
SOLVENT  CDCl3
NS        1327
DS        0
SWH       29761.904 Hz
FIDRES    0.227065 Hz
AQ        2.2020595 sec
RG        203
DW        16.800 usec
DE        6.50 usec
TE        295.0 K
D1        1.00000000 sec
D11       0.03000000 sec
TD0       1

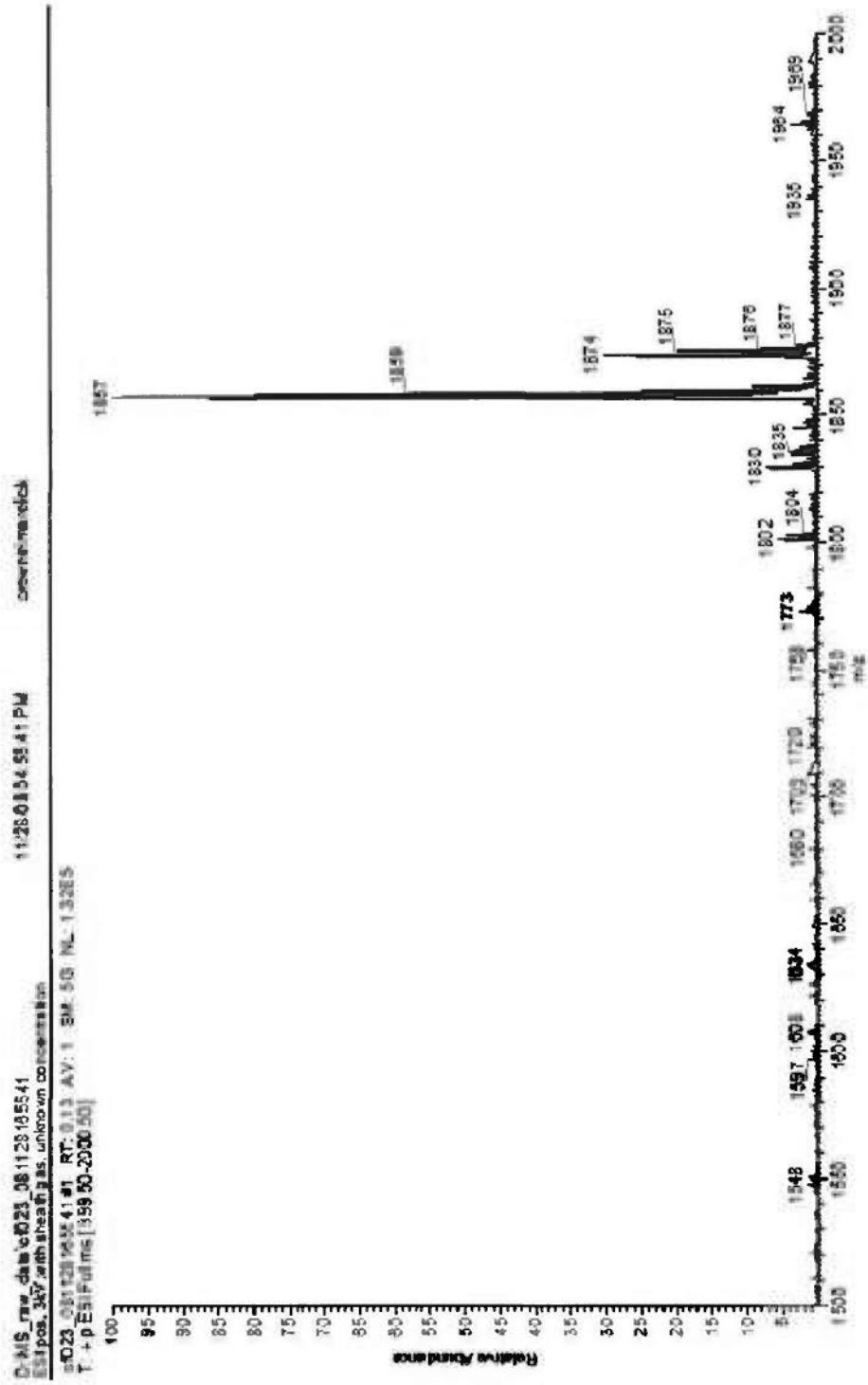
===== CHANNEL f1 =====
NUC1      13C
P1        5.00 usec
PL1       -0.60 dB
PL1W      41.24164963 W
SFO1      100.6208180 MHz

===== CHANNEL f2 =====
CPDPRG2   waltz16
NUC2      1H
PCPD2     90.00 usec
PL2       0.00 dB
PL12      16.10 dB
PL2W      8.31434441 W
PL12W     0.20409293 W
SFO2      400.1320007 MHz
SI        131072
SF        100.6127571 MHz
WDW       EM
SSB       0
LB        3.00 Hz
GB        0
PC        1.40

```



Mass spectrum of 86

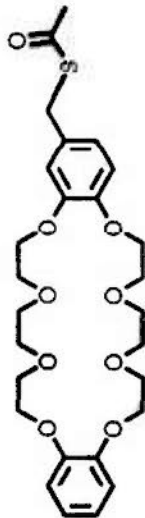


¹H NMR spectrum of 89

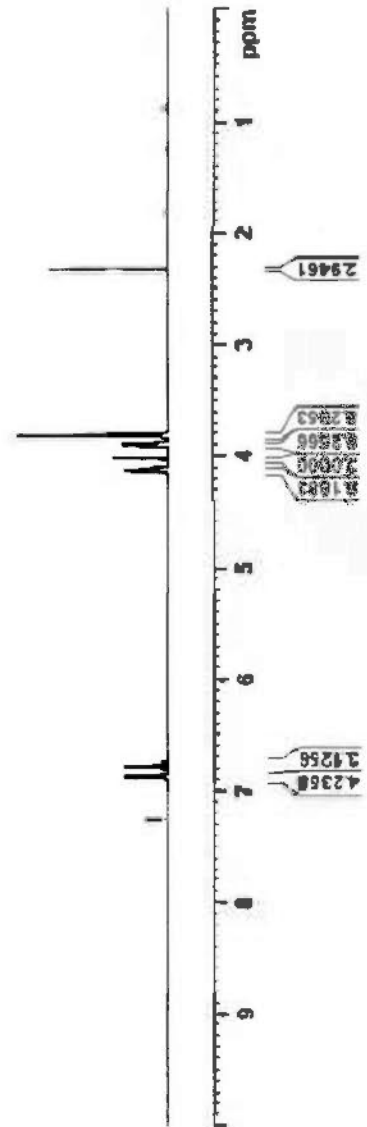
pong-CrownetherDB24C8-SM

NAME EXPNO
 PROCNO 1
 Date_ 20090625
 Time 14.47
 INSTRUM spect
 PROBHD 5 mm PADUL13C
 PULPROG zg30
 TD 65536
 SOLVENT CDC13
 NS 16
 DS 0
 SWH 10000.000 Hz
 FIDRES 0.152588 Hz
 AQ 3.2768500 sec
 RG 203
 DW 50.000 usec
 DE 6.50 usec
 TE 294.7 K
 D1 1.0000000 sec
 TD0 1

----- CHANNEL f1 -----
 NUC1 1H
 P1 14.83 usec
 PL1 0.00 dB
 PL1W 8.31434441 W
 SF01 400.1316005 MHz
 SI 65536
 SF 400.1300049 MHz
 WDM EM
 SSB 0
 LB 0.30 Hz
 GB 0
 PC 1.00



89

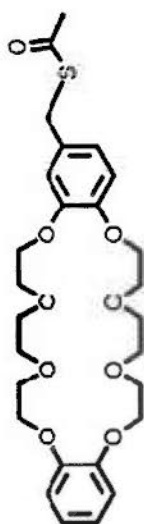
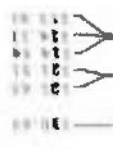


¹³C NMR spectrum of 89

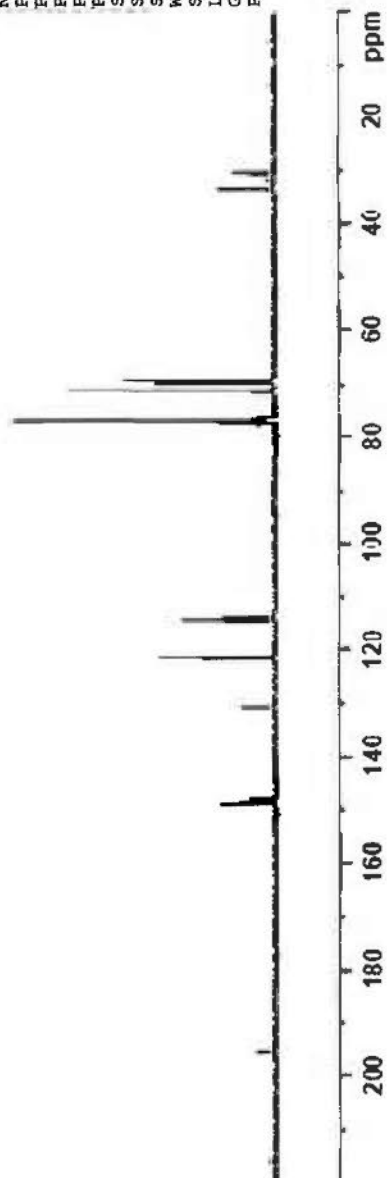
NAME pong-crownethersac [c]
 EXPNO 1
 PROCNO 1
 Date_ 20090625
 Time 14.50
 INSTRUM spect
 PROBHD 5 mm PADUL 13C
 PULPROG zgpg
 TD 131072
 SOLVENT CDCl3
 NS 542
 DS 0
 SWH 29761.904 Hz
 FIDRES 0.227065 Hz
 AQ 2.2020595 sec
 RG 203
 DM 16.800 usec
 DE 6.50 usec
 TE 295.1 K
 D1 1.00000000 sec
 D11 0.03000000 sec
 TD0 1

===== CHANNEL f1 =====
 NUC1 13C
 P1 5.00 usec
 PL1 -0.60 dB
 PL1W 41.24164963 W
 SFO1 100.6208180 MHz

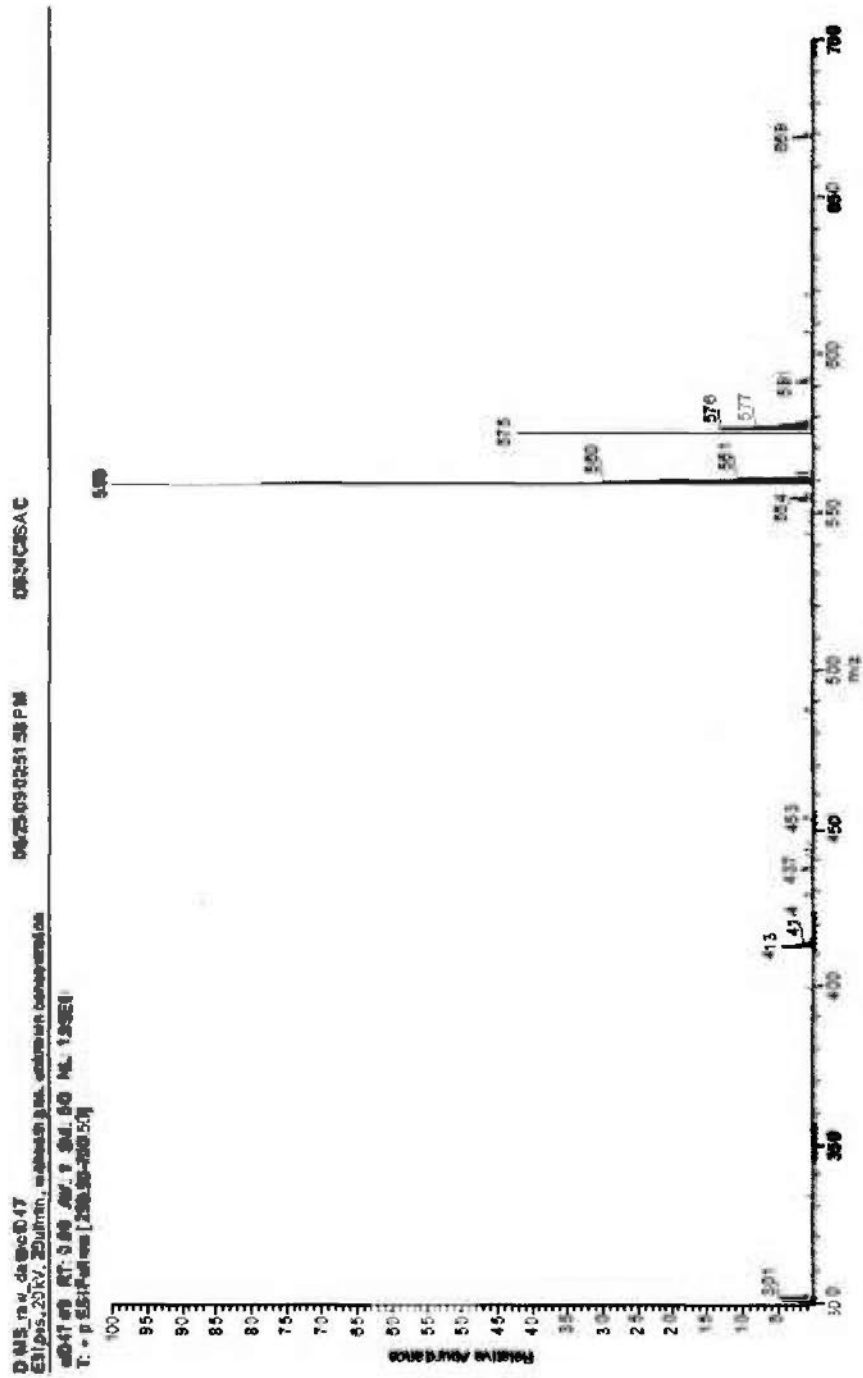
===== CHANNEL f2 =====
 CPDPRG2 waltz16
 NUC2 1H
 PCPD2 90.00 usec
 PL2 0.00 dB
 PL12 16.10 dB
 PL2W 8.31434441 W
 PL12W 0.20409293 W
 SFO2 400.1320007 MHz
 SI 131072
 SF 100.6127578 MHz
 WDW EM
 SSB 0
 LB 3.00 Hz
 GB 0
 PC 1.40



89



Mass spectrum of 89



¹H NMR spectrum of 90

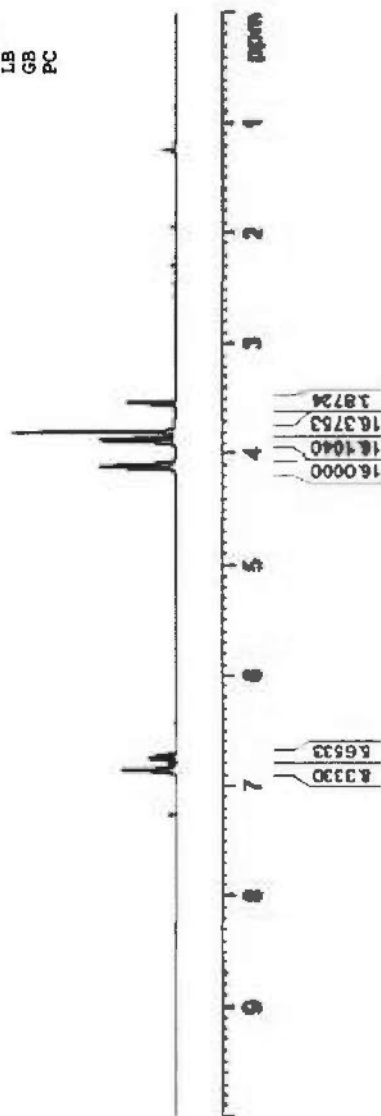
pong-CrownetherDB24C8-55

NAME
 EXPNO 1
 PROCNO 1
 Date_ 20090707
 Time 14.44
 INSTRUM spect
 PROBHD 5 mm PADUL 13C
 PULPROG zg30
 TD 65536
 ID CDC13
 SOLVENT 16
 NS 0
 DS 0
 SWH 10000.000 Hz
 FIDRES 0.152588 Hz
 AQ 3.2768500 sec
 RG 40.3
 DW 50.000 usec
 DE 6.50 usec
 TE 296.1 K
 D1 1.00000000 sec
 TD0 1

===== CHANNEL f1 =====
 NUC1 1H
 P1 14.83 usec
 PL1 0.00 dB
 PL1W 8.31434441 W
 SF01 400.1316005 MHz
 SI 65536
 SF 400.1300046 MHz
 WDW EM
 SSB 0
 LB 0.30 Hz
 GB 0
 PC 1.00



90

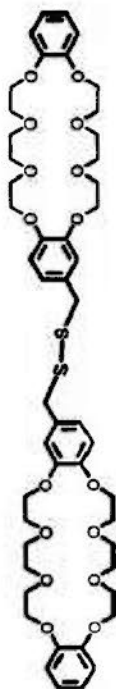


¹³C NMR spectrum of 90

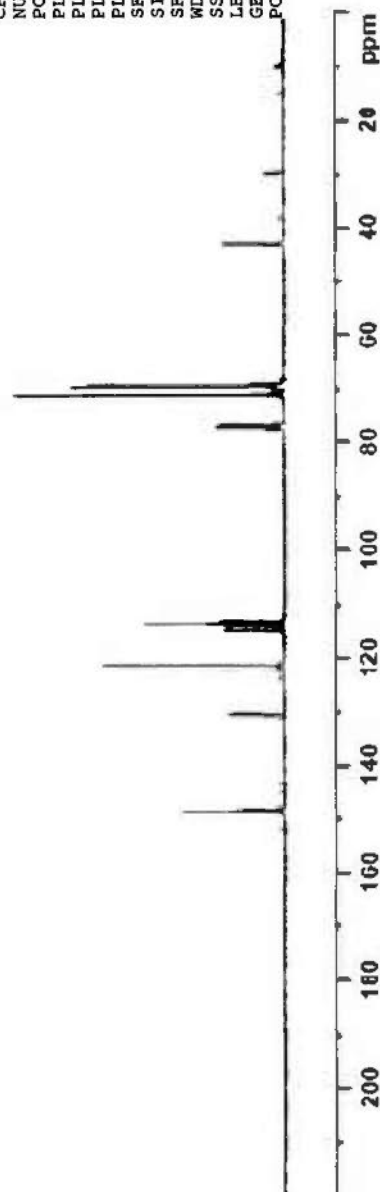
NAME pong-crownetherSS [c]
 EXPNO 1
 PROCNO 1
 Date_ 20090707
 Time_ 16.32
 INSTRUM spect
 PROBDH 5 mm PADUL 13C
 PULPROG zgdc
 TD 131072
 SOLVENT CDCl3
 NS 23
 DS 0
 SWH 29761.904 Hz
 FIDRES 0.227065 Hz
 AQ 2.2020595 sec
 RG 203
 OW 16.800 usec
 DE 6.50 usec
 TE 294.8 K
 D1 1.0000000 sec
 D11 0.0300000 sec
 TD0 1

===== CHANNEL f1 =====
 NUC1 13C
 P1 5.00 usec
 PL1 -0.60 dB
 PL1W 41.24164963 W
 SFO1 100.6208180 MHz

===== CHANNEL f2 =====
 CPDPRG2 waltz16
 NUC2 1H
 PCPD2 90.00 usec
 PL2 0.00 dB
 PL12 16.10 dB
 PL2W 8.31434441 W
 PL12W 0.20409293 W
 SFO2 400.1320007 MHz
 SI 131072
 SF 100.6127740 MHz
 WDW EM
 SSB 0
 LB 3.00 Hz
 GB 0
 PC 1.40



90



Mass spectrum of 90

